INTERFACIAL BEHAVIOURS OF SMART COMPOSITES

by

Chi-kin Poon

A thesis submitted in partial fulfillment of
the requirements for the degree of
Doctor of Philosophy
at The Hong Kong Polytechnic University

Department of Mechanical Engineering

2004

Certificate of Originality

I hereby declare that this thesis is my own work and that, to the best of my knowledge and belief, it reproduces no material previously published or written, nor material that has been accepted for the award of any other degree or diploma, except where due acknowledgement has been made in the text.

Chi-kin Poon

Abstract

The success of conventional fiber reinforced composites (FRC) relies on the quality of bonding between fibers and matrix. The excellent interfacial bond strength between shape memory alloy (SMA) inclusions and the host materials is also critically important for the success of SMA-composites. A review of literatures shows that there is a lack of theoretical models and experimental findings on the interfacial behaviours of the SMA-composites. Therefore, in the past, the operation limit as well as the ideal actuation condition of SMA inclusions could not be predicted accurately during the design stage. Some of the fabricated SMA-composite structures may therefore suffer a potential risk of sudden failure due to over-loading or over-actuation.

The theoretical models developed in this research provide a study basis for the prediction of internal stresses and interfacial strength of the SMA-composites. Martensite volume fraction is considered as a critical parameter which determines the material properties and shape memory effect (SME) of the SMA inclusions. The proposed model reproduce the SMA behaviour inside a substrate, evolutions of martensite volume fraction and elastic modulus of SMA, and the internal stresses along the embedded length in different loading and actuation scenarios. The concepts of 'constant martensite volume fraction region (CMR)' and 'constant axial stress region (CASR)' are proposed to justify the desired SMA actuation which ensures the uniform material properties and mechanical performance within a target region. The minimum required geometric factors for satisfying the CMR and CASR are estimated from the associated numerical analysis.

Three types of typical loading conditions and two possible actuation modes are identified to study the influence of loading-actuation scenarios on internal stress distributions and interfacial debond. The critical wire embedded length and matrix-to-wire radius ratio for achieving 'almost the same' mechanical response of different loading conditions are estimated from the corresponding parametric studies. The results suggest that the critical embedded length and the matrix-to-wire ratio are required to validate the loading condition employed in pullout test for determining the interfacial properties. In addition, mode-b actuation approach is found to be more effective for the initiation of the SME.

The energy approach is applied in the formulation of the interfacial debonding criterion. The total elastic strain energy on both the SMA wire and matrix cylinder is taken into account for the prediction of interfacial debond. Solutions of stress distributions in the partially debonded and the remaining bonded regions are derived with the considerations of externally applied stress, axial position and actuation temperature. These solutions are then substituted into the debonding criterion that results in the numerical solutions of normalised strain energy release rate against the applied load. The substantial improvement of the initial debond stress is predicted with the increase of the actuation temperature. A pre-load or initial applied stress is found to be necessary to compensate the additional recovery stress arising from SMA actuation before the further development of the strain energy release rate.

Single fibre pullout test is employed to validate the model developed in this study. Based on the knowledge obtained from the CMR and CASR analysis, the SMA wire/epoxy matrix cylinders with appropriate dimensions are fabricated for the test. In addition to the pullout test data measured by the MTS micro-force testing machine, the debonding processes are also closely monitored by using the high resolution digital video capturing system. Results are then compared with theoretical predictions. Both the critical stress at the initial debond and the debond stress development with the debonded length are found matching fairly well with the theoretical predictions.

The 'Optimum Actuation Condition (OAC)' that ensures the reinforcement of SMA composite but avoids the failure of composite interface due to over-actuation is also defined to optimize the application of SME in the composite structure within a safety actuation limit. Feasibility of OAC is studied with the consideration of different prestrain values. It is found that the higher the prestrain value, the more difficult the OAC control. A simplified OAC (SOAC) is also developed to provide an analytical solution of OAC and thus the ideal actuation temperature for achieving such specific actuation condition can be estimated more easily. It is found that the results of OAC and SOAC are compromised for the sufficient wire embedded length.

The stress distributions in the perfectly bonded and partially debonded SMA wire/matrix cylinder are simulated by using finite element analysis (FEA). The frictional contact surfaces at the debonded region are carefully defined and the nonlinear static analysis is employed to analyze the stress distributions inside the partially debonded two-cylinder models. The results indicate that both FEA and theoretical results agree well with each other especially in the perfectly bonded condition.

Buckling control of composites with embedded SMA wires is employed as application examples. The buckling resistance of SMA-reinforced laminated beam is measured from the buckling test. The results agree fairly well with the theoretical predictions and hence convince the applications of such theoretical model for the estimation of buckling resistance in the design stage of the SMA-composites.

Based on the overall developments, it appears that the proposed theoretical models and the approach of experimental study are the viable basis for the development of the SMA-composites as a new class of reliable materials for satisfying wide variety of engineering requirements. The concept of evolution of martensite volume fraction along the embedded SMA materials is particularly important for the predictions of mechanical response as well as material status of the SMA-composites.

Acknowledgement

I wish to express my most sincere appreciation and gratitude to my chief supervisor Dr. L.M. Zhou. His advice, encouragement and patience throughout the course of my research studies are very much appreciated. His exceptional insight into fracture mechanics and into interfacial behaviour of composites beyond mathematical formulas has always deeply fascinated me. I also wish to thank for all the support he gave me, and his family for their friendship.

I would like to thank my co-supervisors Dr. L.H. Yam and Dr. W. Jin for their advice and recommendations in various matters. They have given valuable comments and helps on this research. A special acknowledgement goes to Dr. K.T. Lau for his constructive suggestions on many experimental issues which allow me to validate the theoretical model successfully. I wish to thank the research students Mr. K.K. Cheung, Miss. F.T. Choi and Mr. C.P. Lee for their assistances on setting up the pullout test.

I am indebted to Dr. Y. Zheng for his recommendations on the finite element studies. His professional knowledge on the applications of FEA software gave me a great help on the development of two-cylinder models. I also wish to thank the technicians in the Laboratory of Applied Physics Department for technical support on the characterization of SMA materials.

I would like to thank my parents for instilling in me the importance of education at an early age and for supporting me through this long process. Finally, I wish to dedicate this thesis to my love Eva for her love and continuous encouragement.

Contents

List of Symbols and Abbreviations

a	Radius of SMA wire
b	Radius of matrix
b_c/a	Critical matrix-to-wire radius ratio
A	Austenite
M	Martensite
M^d	Detwinned martensite
M^t	Twinned martensite
σ	Stress or strength
σ_a	Applied stress on SMA wire
σ_r	Recovery stress
σ_{fb}	Axial stress on wire in the bonded region
σ_{fd}	Axial stress on wire in the debonded region
σ_{mb}	Axial stress on matrix in the bonded region
σ_{md}	Axial stress on matrix in the debonded region
σ_{cr}^s	Critical stress of detwinning (start)
σ_{cr}^f	Critical stress of detwinning (finish)
σ_t	Crack tip stress
σ_d^o	Initial debond stress
σ_d^p	Partial debond stress
σ_d^*	Maximum debond stress
$\Delta\sigma_{CMR}$	Difference of axial stress on SMA wire in CMR
τ_{mb}	Shear stress on matrix in the bonded region
τ_{md}	Shear stress on matrix in the debonded region
τ_i	Interfacial shear stress in the bonded region
τ_f	Interfacial shear stress in the debonded region
τ_M	Interfacial shear strength
μ	Coefficient of friction

q_o	Residual clamping stress
q_a	Interfacial radial clamping stress arising from applied load and SME
G_{ic}	Fracture toughness
N_{ic}	Normalized strain energy release rate
T_{so}^{M}	Transition temperature of martensite start in stress-free state
T_{fo}^{M}	Transition temperature of martensite finish in stress-free state
T_{so}^{A}	Transition temperature of austenite start in stress-free state
T_{fo}^{A}	Transition temperature of austenite finish in stress-free state
T_{OA}	Actuation temperature for the optimum actuation condition
C_A	Stress influence coefficient in austenitic state
C_M	Stress influence coefficient in martensitic state
G_{SMA}	Shear modulus of SMA
ν_f	Poison's ratio of SMA wire
ν_m	Poison's ratio of matrix
E_f	Elastic modulus of SMA
E_A	Elastic modulus of SMA in austenitic state
E_M	Elastic modulus of SMA in martensitic state
E_m	Elastic modulus of matrix
ξ	Martensite volume fraction ($= \xi_s + \xi_T$)
ξ_s	Stress-induced martensite volume fraction
ξ_T	Temperature-induced martensite volume fraction
$\Delta\xi_{CMR}$	Difference of martensite volume fraction in the targeted CMR
ε	Strain
ε_p	Prestrain value
ε_L	Maximum residual strain of SMA wire
Ω	Transformation tensor
θ	Thermal stress coefficient of SMA
β_m	Thermal expansion coefficient of matrix

T	Temperature
T_g	Glass transition temperature of matrix material
z_n	Position of the n-th element
m	Total number of step
L	Wire embedded length
L_{min}	Minimum wire embedded length
L_c	Critical wire embedded length
L_n	Normalized embedded length
l	Debonded length
γ	Volume ratio of wire to matrix $(a^2/(b^2-a^2))$
q_r	Interfacial radial stress
α	Modulus ratio of matrix to wire
λ	Reciprocal debond length in single fiber-matrix pullout model
U_t	Total elastic strain energy
U_b	Elastic strain energy in the bonded region
U_d	Elastic strain energy in the debonded region
CMR	Constant martensite volume fraction region
CASR	Constant axial stress region
OAC	Optimum actuation condition
SOAC	Simplified optimum actuation condition
SMA	Shape memory alloy
SME	Shape memory effect
SIM	Stress induced martensitic transformation

Chapter 1

Introduction

Shape memory alloys (SMAs) are intelligent materials that 'remember' their original shape. The properties of the SMA change markedly due to a phase transformation between a crystallographically more-ordered austenitic phase and a crystallographically less-ordered martensitic phase caused by the changes in temperature and stress. Nickel-titanium alloys have been found to be the most useful of all SMAs. Other shape memory alloys include copper-aluminum-nickel, copper-zinc-aluminum and iron-mangnaese-silcon alloys. The generic name for the family of nickel-titanium alloys is Nitinol. In 1961, Nitinol, which stands for Nickel Titanium Naval Ordnance Laboratory, was discovered to possess the unique property of having shape memory. William J. Buehler, a researcher at the Naval Ordnance Laboratory in White Oak, Maryland, was the one to discover this shape memory alloy.

SMAs in the shape of thin wires can be integrated in fiber reinforced polymer composites (FRC), yielding adaptive composites. Research findings generally agreed that the application of shape memory effect can modify the modal material properties as well as the internal stress distributions of the SMA-composites. Therefore, the mechanical response of those composite structures against external stimulus can be improved.

Over the years, many constitutive models have been proposed to represent the nonlinear behaviour of the SMA with hysteresis [1-3]. Numerous experimental findings agreed well with most of the theoretical models. However, the efforts for the control of the SMA-composite structures as well as their reliability are quite rare. Success of the

FRC highly relies on the strong interfacial bond between the constituents. There is no exception for the SMA-composites having physical limitation related to the quality of interfaces. A review of literatures, however, show that there is lack of theoretical studies or even experimental findings for characterizing the wire-matrix interface failure behaviour in such novel composite materials. If the influence of shape memory effect on the interfacial bond strength is not clarified, it is difficult to estimate the operation limit accurately and hence to optimize the performance of the SMA-composites.

In Chapter 2 of this thesis, the working principles of SMA inclusions and the role of interfacial bond strength in a SMA-composite are reviewed with particular attention to the risks of over-simplified constitutive models applied in some recent researches. Several typical configurations of SMA actuators in composite structures are identified and the advantages and limitations of different configurations are discussed. Some of the plausible improvement schemes for interfacial bond strength enhancement are also reviewed. A constitutive model of the SMA is incorporated with the general stress-strain relations to formulate the stress distribution solutions in Chapter 3. The evolutions of martensite volume fraction at the well-defined stress-temperature regions are critically discussed. Such 'evolution' mechanism is proposed and simulated by setting the recurrence relation between axial stress on the SMA wire and the martensite volume fraction. Chapter 4 focuses on the influence of various loading-actuation scenarios on the estimation of SMA's material properties. Evolution of internal stress distributions throughout the wire embedded length is also studied. Parametric studies are employed to clarify the critical geometric factors that validate the application of equivalent martensite volume fraction for the estimation of material properties. Two actuation modes, so called the 'mode-a' and 'mode-b', are clearly defined to distinguish the two typical actuation scenarios which may cause substantial derivation in the estimation of material properties. Using the energy approach, shape memory effect on the critical interfacial debond is evaluated in Chapter 5. Critical change of the strain energy release rate and thus effectiveness of the SMA actuation on the improvement of debonding behaviour are also presented. In Chapter 6, pullout tests of the SMA wire/epoxy matrix cylinders are performed to determine the interfacial properties. Comparison between experimental results and theoretical predictions of the debonding stresses at different actuation temperatures are employed to validate the theoretical model developed in the present study. Chapter 7 presents an important concept of the optimum actuation condition (OAC) in which the ideal actuation temperature can be estimated to prevent the interfacial debond due to the over-actuation of the embedded SMA wire actuators. A simplified OAC (SOAC), which provides an explicit solution, is also developed. The internal stress distributions in the SMA-composites for different debonding condition are analyzed by using finite element method (FEM) in Chapter 8. Two-dimensional axisymmetric models predefined with different debonded lengths are developed with specific assignment of surface meshing. The FEA results are used to validate the theoretical solutions of stress distributions as well as the application of equivalent martensite volume fraction. Chapter 9 is devoted to the buckling control of SMA-reinforced laminated slender beam. The simply support-simply support (SS) boundary condition is considered in the buckling test and the additional buckling resistance is measured to qualify the application of the SMA wire actuators in buckling control. It is followed, in Chapter 10, by a summary of the present works and several suggestions for future research.

Chapter 2

Working Principles and Applications of SMAs and SMA-Composites

2.1 Introduction

Shape-memory properties for nickel (Ni) and titanium (Ti) alloys with a composition of 53% to 57% of nickel by weight were discovered by Buehler and Wiley [4] in 1960s at the Naval Ordinance Laboratory (NOL); therefore, the term Nitinol is commonly used when referring to Ni-Ti-based shape memory alloys. In the past three decades, Ni-Ti alloys have been widely investigated due to their novel features and frequent use in engineering applications [5-8]. All of those alloys can be deformed severely with residual strains of 8-15% and then regain their original shape after a thermal cycle. This effect is typically known as the shape memory effect (SME) and the alloys exhibiting this novel phenomenon were named shape-memory alloys (SMA). It was later found that except for shape memory properties, at sufficiently high temperatures such materials also possess the special property of superelasticity. It allows the recovery from large deformation during mechanical loading-unloading cycles experienced at a constant temperature. As a consequence of superelastic and shape-memory properties, shape memory alloys lend themselves to a wide range of innovative applications. Unlike natural materials or even most engineering material systems that exhibit elastic properties and demonstrate plastic deformation after the critical yield point, shape memory alloys can undergo reversible solid-solid phase transformation between a crystallographically more ordered phase called austenite, and a crystallographically less ordered phase called martensite. The difference between the

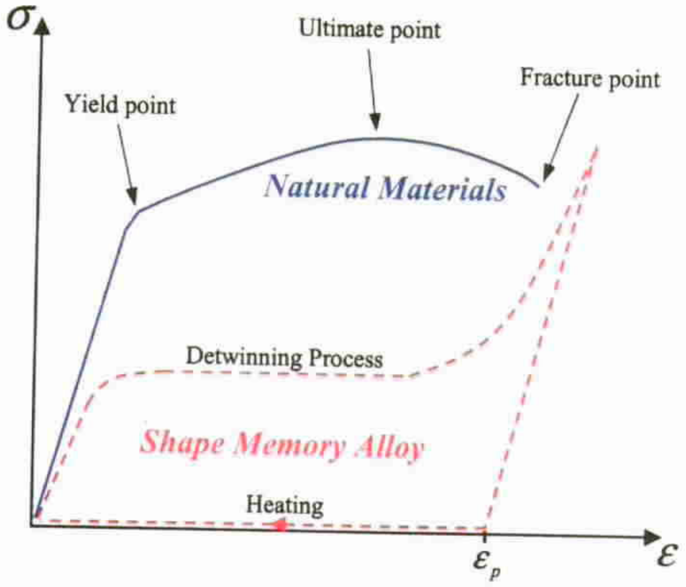

Figure 2.1 Differences between the typical stress-strain curves of natural materials and shape-memory alloys.

stress-strain responses of natural materials and SMA are schematically illustrated in Fig. 2.1.

The active and passive control of structures has been the subject of intense research over the past few decades. Many applications in modern engineering structures require an effective and reliable sensing and actuation system to refine the mechanical responses toward external stimuli. Numerous sensors and actuators were therefore proposed and developed to serve a wide range of control requirements. Techniques for the active control of structures often use hydraulics, and pneumatic as well as electric motors as the means of damping or positioning. For certain applications, although hydraulics systems can generate a relatively high actuation force, they are either too massive or their responses are too slow for particular areas, such as aviation industries or even space structures. Pneumatic systems can provide a much faster mechanical response, but they are also bulky and involve the installation of compressors and a pressure vessel near the application regions. As a result, compact electric motors are normally preferred in many control systems.

Structures externally attached with actuators (i.e., electric motors or hydraulic systems) and a series of gearing components have limited the flexibility of structural assembly and also the aerodynamic performance of vehicles and aircrafts. Therefore, researchers have aimed to further develop material systems or structures with built-in actuators to achieve active control by modifying material properties or even changing shapes. However, hydraulic systems and motors can no longer satisfy the dimensional requirements of modal properties as well as improve them. A new class of smart materials, which can serve the captioned requirements, has become critically important in the future development of engineering structures. Composite materials embedded with SMAs (SMA-composites) are a class of materials in which the intrinsic shape-memory effect can be used to achieve shape or vibration control, impact absorption, or even structural repairs. Recently proposed designs based on such materials range from self-expanding microstructures for treating body vessel occlusions to devices for the space structures and aircraft industries, such as antennas and hingeless flaps.

Success in SMA composite manufacturing has been limited by poor SMA/matrix bonding [9,10]. It is known that special surface treatment on the SMA hybrid composite interface is required to ensure effective load transfers between constituents so that the proper SMA composite shape control can be obtained. This paper reviews the previous experimental characterization of SMA behaviour, compares constitutive models and, finally, discusses the design and application of SMA hybrid composites.

2.2 SMA Behaviour

2.2.1 Phase Transformations

For the case of uniaxial stress, both the superelastic and shape memory effect follow from the SMA's ability to undergo reversible changes in the crystallographic symmetry-point-group. Such changes are the result of martensitic phase transformations, which are solid-solid displacive-diffusionless phase transformations between a crystallographically more ordered phase, called austenite (or the parent phase) and a crystallographically less ordered phase, called martensite.

In the kinematics point of view, a martensitic phase transformation is the change in atomic structure during the transformation process. The single martensite crystals generally have a platelet shape and such a plate formation is accompanied by a macroscopic deformation. In general, a change in shape with a surface relief can be observed using scanning electron microscopy (SEM), as shown in Fig. 2.2. Also, there exists a well-defined habit plane, which is the interface between austenite and martensite, as schematically illustrated in Fig. 2.3. As was recognized by Bain in 1924 [11], the formation of martensite plates cannot simply follow the single-crystal mechanism. Nowadays, it has been clarified that this mechanism introduces a major problem of accommodation arising from the misfit between martensite and the surrounding austenite. If there is no preferred direction for the formation of martensite plates, a series of crystallographically equivalent variants will be formed. This kind of product phase is then termed multiple-variant martensite, and is characterized by a twinned structure. If a preferred direction for the occurrence of a martensitic transformation is present, all the martensite plates will be formed along the favorable habit plane. It therefore forms a product phase with a detwinned structure that minimizes the misfit between martensite and the surrounding austenite. Therefore, this phenomenon is known as self-accommodation between microstructures, and the detwinned structure is termed single-variant martensite. The detailed discussions regarding crystallographic aspects, including possible self-accommodation mechanisms, can be found in many studies [12-15].

For Ni-Ti SMA, the critical phase transformation temperatures known as austenitic start T_{Ao}^{s}, austenitic finish T_{Ao}^{f}, martensitic start T_{Mo}^{s}, and martensitic finish T_{Mo}^{f} are strongly dependent on the material composition. To obtain a desired phase-transformation temperature range, a composition control of between 0.01-0.1% is required. However, the transformation temperatures are usually measured as quality control instead of relying on the chemical composition.

In general, the characteristics of SMA can be improved via a combination of cold-working and annealing. Cold-working is an effective way of increasing yield strength but, normally, the shape memory properties will be reduced [16]. Annealing can effectively restore the memory effect but decreases the yield stress. Therefore the amount of cold work and annealing determines the preference of a fabricated SMA material. Normally, cold works generate a high density of dislocations in the lattice structure, which restricts the mobility of twin boundaries. The annealing rearranges these dislocations into the relatively dislocation-free areas in which the twinned martensite can be mobile but surrounded by dislocation networks.

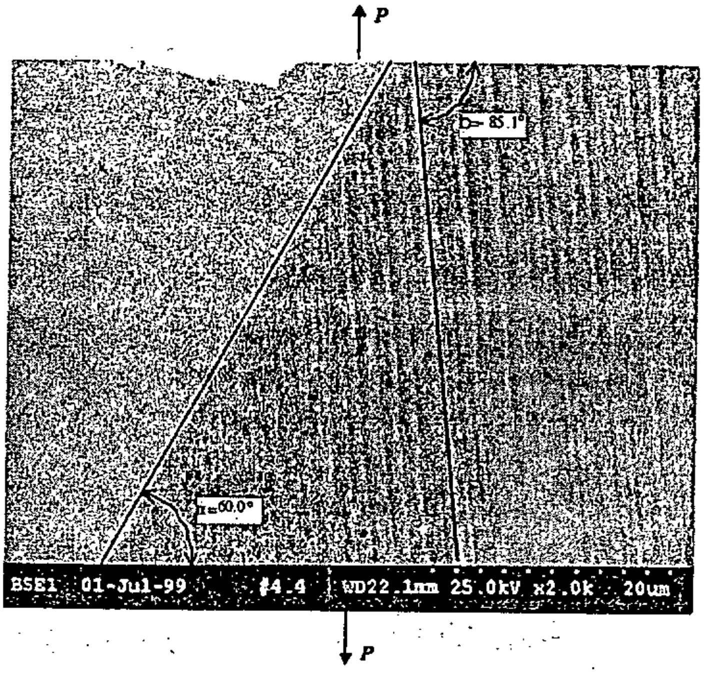

Figure 2.2 SEM image at 2000x shows a habit plane and twin plane orientations. Using these angles and the orientation of the specimen, the habit plane variant and corresponding variants composing the habit plane variant can be identified. [17]

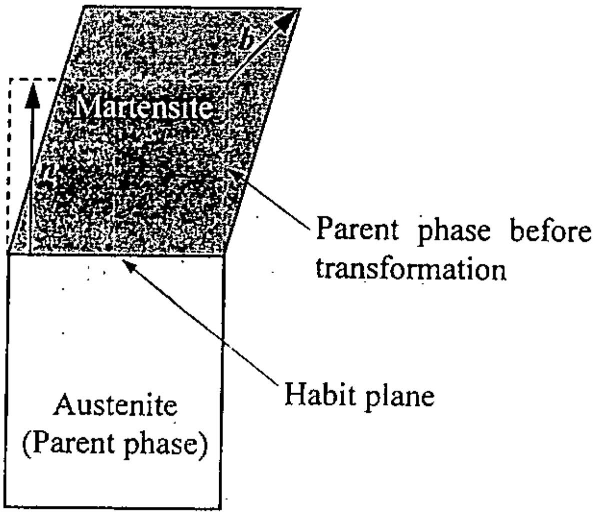

Figure 2.3 Formation of a single martensite plate in the unconstrained condition, where *b* is a unit vector in the direction of martensitic transformation and *n* is a unit vector normal to the variant plane.

2.2.2 Thermomechanical Properties

The amount of recoverable strain due to SMA heating as well as the size of the hysteresis loop are normally associated with several possible factors including the alloy composition, thermomechanical history, loading direction, and the types of loading [18]. If the applied strain is larger than the maximum allowable recovery strain of a selected SMA, the reversible martensitic transformation and dislocations due to plastic flow will interact. As a result, the recoverable memory strain will be reduced. For the complete phase transformation, which means the transformation between pure austenite and pure martensite, the maximum recoverable strain is of the order of 8%, with the hysteresis loop typically between 30°C and 50°C.

For applications that are subjected to cyclic loading, the stability of the shape memory effect and material properties become much more important [19-26]. Depending on the composition and the applied heat treatment, it is possible to obtain Ni-Ti alloys for which the properties associated with austenitic and martensitic phase transformations stabilize after several training cycles. In addition to the shape memory effect and superelasticity, Dalaey et al. [27] discovered another important phenomenon known as two-way shape memory (TWSM). This special behaviour appears via a series of cyclic thermomechanical transformations, i.e. training, which induces a favorable residual stress field within the SMA material. After training, stress-free cooling of austenite produces a transformation strain that is hysteretically recovered during the stress-free heating of the martensite.

2.2.3 Experimental Characterization of SMA Behaviour

Much research has been conducted on how to characterize the thermomechanical behaviour of SMA materials. Of the particular interest to this study are the constitutive modeling, transfer of internal stresses, and interfacial behaviour of SMA-composites. In order to facilitate the captioned studies, the most common type of shape memory alloy – Nitinol – is employed for all of the experimental tests and theoretical models. One of the first exhaustive experimental studies was reported by Cross et al. [5] in 1969. It was then followed by other thermomechanical characterizations and reliability studies [6,28-30], which have sought to fill the gap in knowledge about the technical specifications of nitinol and about the various ternary and quaternary alloys of nitinol [31,32]. However, most of those previous studies validate the behaviour of nitinol in limited temperature ranges. The complete nitinol response for a wide range of temperatures has been characterized in more recent studies [33-36]. Some other research groups have also examined the influence of strain rate on the mechanical response of nitinol [37-39].

In addition to the one-dimensional experimental testing of SMA wires and strips conducted in most of the previous studies, other studies have been conducted to examine the recovery action of two-dimensional SMA plates in different stress states. Furuya et al. was the pioneer in studying the influence of annealing temperature as well as heating rates on the force of recovery of 2-D nitinol plates [40]. In the next ten years, several experimental tests using combined tension and torsion were performed on SMA tubes [41]. In addition, Jacobus et al. [42] conducted a more through study that focused on the uniaxial compression, hydrostatic compression, and triaxial compression on transformation in SMAs.

2.3 Behaviour of SMA Inclusions

The mechanical properties of conventional types of fiber-reinforced matrix (FRM) composites are determined by a number of factors, including the strengths and moduli of the fiber and matrix; aspect ratio, fiber embedded length, volume fraction, uniformity, orientation of fibers and, more importantly, the adhesion at the fiber-matrix interfaces. Definitely, the success of FRM manufacturing relies strongly on high-quality interfacial bonding. This important requirement is not limited to conventional FRMs but also extends to SMA hybrid matrix composites. In the past decade, there has been a wealth of published research on issues of bonding relating to SMA-composites, to enhance the reliability of this novel material system. Some previous studies have focused on measuring the interfacial shear strength at the SMA composite interface while varying the surface treatment of SMA inclusions [43-46]. Some other research groups have proposed the use of coupling sleeves [47] or even mechanical fasteners [48] to enhance the interfacial bond. Paine and Rogers [49] developed a simple pullout test model for investigating stress and strain transfers from SMA wire to the surrounding matrix cylinder. Berman and White [50] also proposed a similar concentric cylinder model for predicting thermal and transformation residual stresses in SMA-composites, and suggested that the large residual stress may damage the interfacial bond in the curing process. Other experimental evidence has confirmed the existence of microcracking in matrix due to high residual stress during processing [51].

The more recent studies have investigated the phenomenon of internal stress transfer by using both the strain gauge measurement and photoelasticity [52,53]. They agree that the non-uniform phase transformation of SMA inclusions has important implications for designing and predicting the behaviour of embedded SMA actuators. In the latest research, Poon et al. [54] developed a two-cylinder model to predict the in-situ martensite volume fraction and, hence, the evolution of the material properties of SMAs as well as internal stress distributions. Both the experimental data and theoretical results confirmed the absence of transformation in the center portion of embedded SMAs. This phenomenon can be attributed to the constraints imposed by the surrounding matrix. Due to load transfer between the matrix and the stiffer SMA inclusions, axial stress in the SMA builds up from zero at the free embedded ends to the maximum value at the center [56,57]. In addition, Berman [57] addressed the problem of excessive residual hoop stresses that develop from the mechanical and/or thermal transformation of constrained SMA wires, leading to radial cracking around the embedded nitinol wires. Also, it has been confirmed that thermal and transformational residual stresses will directly influence the structural behaviour of SMA-composites. Since mechanical stress can induce phase transformation in SMAs, the modal properties of SMA-composites can be changed by an externally applied load.

2.4 Constitutive Models

When the SMA is restrained such that it cannot recover its strain, a very large recovery force can be developed in wire. Applying this novel mechanical response, prestrained SMA wire has been used to actively generate force or to turn the properties of a composite structure [58-60]. This phase transformation is also accompanied by a large change in resistivity, specific heat, the modulus of elasticity, and other properties of the materials. In structures with embedded SMAs, these changes can be harnessed to achieve a change in the modal properties for different applications [61,62]. Since the behaviour of SMA materials is primarily a function of three variables including stress, strain, and temperature, and their associated rates, a constitutive model that attempts to describe the material behaviour has to be a function of these variables.

The first constitutive model for the macroscopic behaviour of SMA was proposed by Tanaka [63] in 1986. The model is based on thermomechanics, where the second law of thermodynamics is written in terms of Helmholts free energy. It was assumed that the unidirectional strain, temperature, and martensite volume fraction are the state variables for the stress calculation. One may notice that the martensite volume fraction is a function of stress and temperature, which means that the recursive numerical solution has to be employed to determine both the stress and the martensite volume fraction in embedded SMA at the instant. In this model, exponential expression is selected to describe the martensite volume fraction in terms of temperature and stress.

Tanaka Model

This model associates the three important variables as given below,

$$\sigma - \sigma_o = E(\xi)(\varepsilon - \varepsilon_o) + \theta(T - T_o) + \Omega(\xi)(\xi - \xi_o) \tag{2.1}$$

where the state variables including stress σ, strain ε, and temperature T are described in terms of martensite volume fraction ξ. The subscript "o" represents the initial state of SMA; E, θ, and Ω refer to the modulus of elasticity, the thermal stress coefficient, and the phase transformation coefficient, respectively. The modulus E is considered a linear function of the martensite volume fraction as given below:

$$E(\xi) = E_A + \xi(E_M - E_A) \tag{2.2}$$

and

$$\Omega(\xi) = -\varepsilon_L E(\xi) \tag{2.3}$$

where ε_L the maximum recoverable strain is considered as a material constant. The martensite volume fraction described by the exponential function is modeled as

$$\xi = 1 - \exp\left[a_M\left(T_{so}^M - T\right) + b_M\sigma\right] \tag{2.4}$$

for austenite→martensite transformation and

$$\xi = \exp\left[a_A\left(T_{so}^A - T\right) + b_A\sigma\right] \tag{2.5}$$

for martensite→austenite transformation. a_M , a_A , b_M , and b_A are the empirical constants employed for the given SMA material. T_{so}^M and T_{so}^A refer to the martensitic start and austenitic start temperatures, respectively. After Tanaka's works, Liang and Rogers [64] formulated a constitutive model that considers the rate form of Tanaka's model. However, the exponential expressions are replaced by cosine functions to characterize the martensite volume fraction.

Liang and Rogers Model

The same form of constitutive equation has been used in this model. Although some of the constants are defined differently, the most essential components modified from the Tanaka model is the application of the cosine form to model the martensite volume fraction, as follows:

$$\xi = \frac{1-\xi_A}{2}\cos\left(a_M\left(T - T_{fo}^M\right) + b_M\sigma\right) \tag{2.6}$$

for austenite→martensite transformation at $C_M(T-T^M_{so}) < \sigma < C_M(T-T^M_{fo})$ and

$$\xi = \frac{\xi_M}{2}\left[\cos\left(a_A\left(T-T^A_{so}\right)+b_A\sigma\right)+1\right] \tag{2.7}$$

for martensite→austenite transformation at $C_A(T-T^A_{fo}) < \sigma < C_A(T-T^A_{so})$, where ξ_A and ξ_M are the initial martensite fractions for the corresponding transformation. The constants C_M and C_A are material properties that describe the relationship between temperature and critical stress, σ_{crit} to induce transformation, as illustrated in Fig. 2.4.

Although the Tanaka, and Liang and Rogers models agree well with the experimental findings, due to the absence of variables that differentiate between the twinned and detwinned variants of martensite, they can only reproduce some of the behaviour of SMA: phase transformation from martensite to austenite and vice versa, but fail to represent the overall shape memory effect.

Brinson Model

Based on the micromechanics of SMA material, Brinson [65] proposed separating marteniste volume fraction into two parts, as given below:

$$\xi = \xi_s + \xi_T \tag{2.8}$$

where ξ_T refers to the fraction of the material that is purely temperature-induced martensite with multiple variants, while ξ_s represents the fraction of the material that has been transform by stress into a single variant of martensite. This new arrangement allows the previously proposed constitutive equation to reproduce the behaviour of SMA at temperatures of below T_{so}^{M}, as well as above. Figure 2.5 schematically presents the variation with the temperature of the critical stresses for a transformation consistent with the separation of ξ into two stress- and temperature-induced components.

Using the new arrangement of martensite fraction, ξ, Eqn. 2.1 has been modified as follows:

$$\sigma-\sigma_o=E(\xi)\varepsilon-E(\xi_o)\varepsilon_o+\Omega(\xi)\xi_s-\Omega(\xi_o)\xi_{so}+\theta(T-T_o) \tag{2.9}$$

As for the major interest of this study on the internal stress distributions in SMA wire/matrix composites, the evolution of martensite volume fraction along the wire direction is modeled based on Brinson's constitutive law. Details of the transformation equations for different thermomechanical application scenarios are further discussed in the following sections.

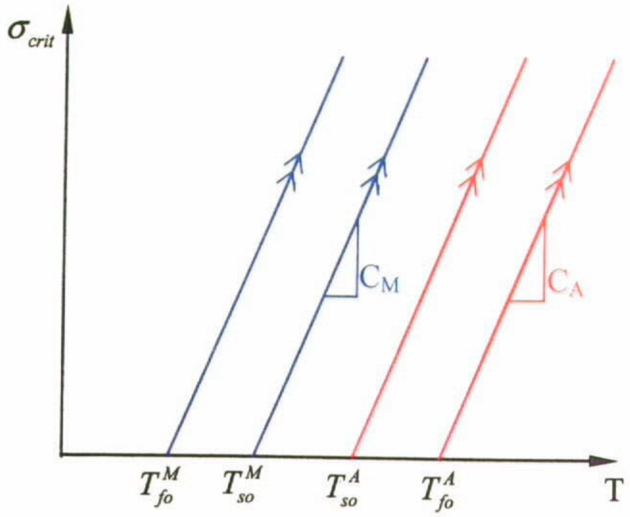

Figure 2.4 Critical stresses for transformations as a function of temperature. C_M and C_A are slopes of the $\sigma_{crit}(T)$ curves for the austenitic and martensitic phase transformation, respectively. [64]

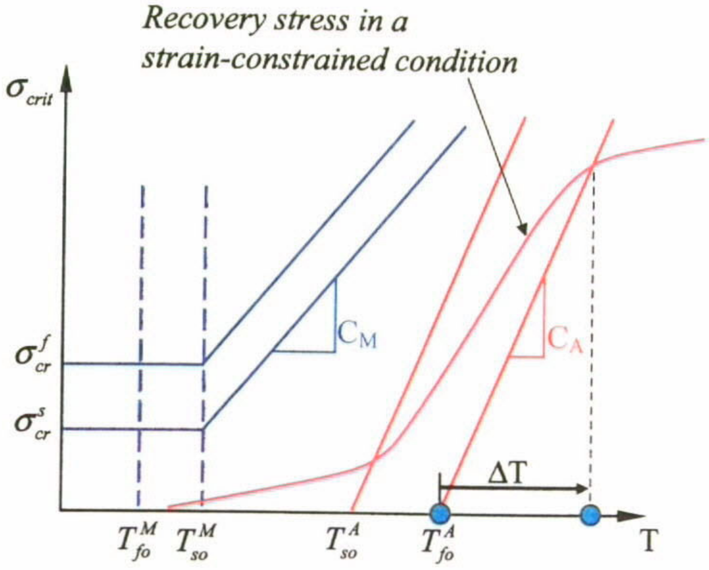

Figure 2.5 Critical stresses for phase transformations and the formation of detwinned martensite due to applied stress. [65]

2.5 Designs and Applications of SMA-Composites

2.5.1 Configurations of SMA in Composite Structures

Several plausible designs of SMA-reinforced composites have been proposed to satisfy a wide range of engineering requirements in the past decade. Most of these designs use the advance in SMA's recovery action to control the frequency, buckling resistance, and shape change of a structure. The three distinct configurations using SMA materials in a composite structure are: connecting the materials externally to the structure [58,66-69], inserting the materials in a composite structure via a sleeve [70,71] and embedding the materials directly in the composite structure [72-82].

2.5.2 Advantages and Limitations of Different Configurations

Externally attached with SMA Actuators

There have been several reported cases of using similar configurations of externally attached SMA actuators. The schematic of a flexible beam/plate externally attached with SMA actuator is illustrated in Fig.2.6a. A comprehensive feasibility study utilizing an externally attached SMA to control the vibrations of a cantilever beam had been performed by Baz et al. [58]. The results demonstrated the potential of using SMA as a viable means of damping out the vibrations of a beam. However, their work was not derived from a constitutive relation of SMAs. In addition to controlling vibrations,

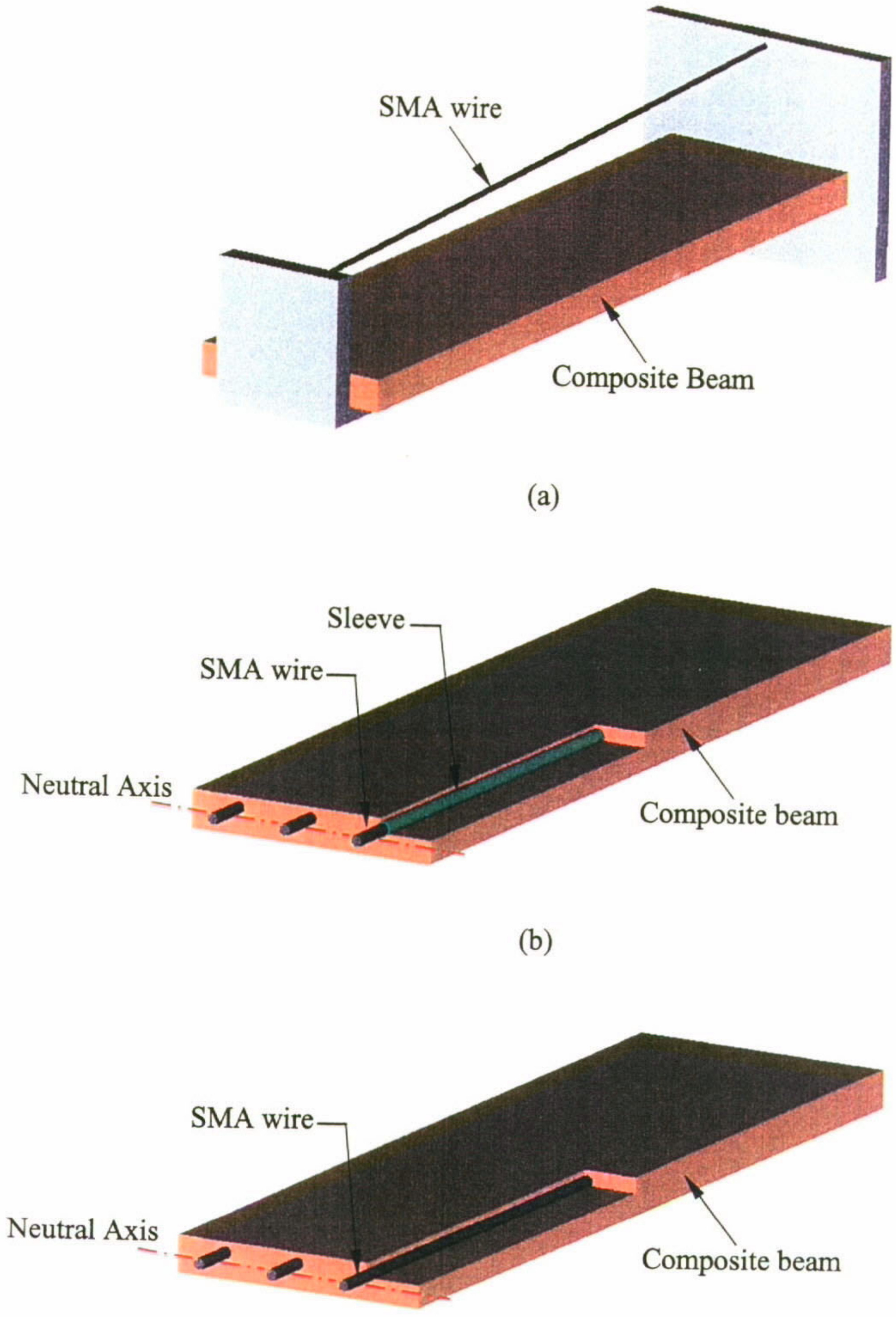

(a)

(b)

(c)

Figure 2.6 Schematic of flexible beam/plate (a) externally attached with a shape memory alloy wire actuator, (b) inserted with SMA wires via sleeves and (c) directly embedded with SMA wires

Chaudhry and Rogers [68] demonstrated the possibility of using this configuration to induce deflections of a beam and also the feasibility of shape control for a composite structure. Brand et al. [69] discussed a solution for a flexible beam and a constitutive model for SMA, but their works did not include coupling between the beam and SMA. The strong coupling between the nonlinear solution of a large deflection problem with an SMA constitutive model and electrical current control had been addressed by Steven G. Shu et al. [66], in which the actuation force applied to the beam is solely from the SMA actuator. Shu et al.'s work therefore demonstrated that the SMA actuator could be used to control the shape of a flexible structure. The external actuators also have better control authority since the actuator can be placed at a different offset distance from the beam. The moment, caused by SMA actuation, is therefore much greater than in a composite beam with an SMA wire embedded inside a composite beam. The actuation of an externally attached SMA wire actuator will not affect the flexural stiffness of the beam. Such a configuration also allows for the introduction of fast convection cooling, which is very important in shape-control applications that require a high-frequency response from SMA actuators. Although the so-called 'externally attached' approach provides a number of advantages, including in relation to the cooling problem of SMA-composites, this kind of configuration normally occupies more space and thus reduces the flexibility of the structural assembly as well as the aerodynamic performance of the whole structure.

SMA Wire Inserted Via Sleeve

Several research groups have tried to insert SMA wires into sleeves embedded in a flexible beam to control buckling, vibration, and bending behaviour. Baz et al. [71] used a finite element method on their experimental results, which compared well with the theory. They showed that the buckling load of a flexible fiberglass composite beam inserted with prestrained SMA wires can be increased by almost 300% over that of an uncontrolled beam. On the other hand, Chaudhry and Rogers [83] examined the basic concepts relating to the structural response to the embedded SMA wires. They verified the fundamental principle that no buckling takes place due to internal SMA actuators. Their findings confirmed the possibility of using SMA actuators to actively control the bending of structures. Epps and Chandra [84] also conducted both numerical and experimental studies of natural frequencies of composite beams with activated SMA wires. The eight-ply graphite-epoxy beams with embedded fused silica tubes filled with 'dummy' steel wire were fabricated using an autoclave molding technique. After curing the composite beam, the steel wires were replaced with prestrained SMA wires. The numerical study reported that the outstanding improvement of first frequency can be obtained by inserting 25 SMA wires with a diameter of 0.5mm into a graphic-epoxy beam. The typical configuration of their SMA hybrid composite models is shown in Fig.2.6b.

Embedding Directly into Composite Structure

Considering the issue of fabricating SMA-composites, it is crucial to maintain the prestrain level of the embedded SMA wire inside a composite structure. Failure to control the amount of cold work applied on SMA during the fabrication process results in the derivation of an actual mechanical response from the designed specification. Certainly, inserting prestrained SMA wires via a sleeve inside a composite can minimize "unwanted" cold work (other than the target prestrain value), which may derivate the expected SMA properties in the initial state as well as the prestrain value and, hence, the final performance of a SMA-composite could be totally different from the expectation. If the clearance between the sleeve and the SMA wire is sufficiently large, the prestrained wire can be inserted into the sleeve after the curing of a composite structure without using any fixture to maintain the wire's alignment during the curing process. In the other words, it is more convenient to use such an approach to inserting wire when fabricating SMA-composites.

Although this approach ensures the properties of the SMA actuator, it cannot be used to modify the modal properties of a whole composite structure. For example, since the actuation of SMA is considered to generate a pair of compressive forces on both ends of a structure, there is no means to change the elastic modulus of a composite. Therefore, numerous studies have focused on the design and fabrication of smart composites directly embedded with prestrained SMA wires in recent years.

Rogers and Baker [82] directly embedded SMA wires in a graphic-epoxy composite beam to control its frequency. In that experimental study, the beam and SMA wires were independently clamped. When the SMA wires were heated, the beam was subjected to an axial force due to the shape memory effect and the elastic constraints provided by the host matrix. They demonstrated a 200% increase in the natural frequency of a graphic-epoxy beam by using 15% volume fraction of SMA wires. Song and Sun [72] established a micromechanical model to simulate the thermomechanical behaviour of an aluminum matrix composite with SMA reinforcement under uniaxial tension. They quantitatively investigated the influence of the shape and volume fraction of SMA inclusions on the overall behaviour as well as on the internal stress evolution inside the aluminum composite. However, the issue of debonding between the aluminum matrix and SMA material was ignored. Considering the interfacial debonding in terms of the shear strength between the constituents, when interfacial shear stress develops on the critical shear strength, debonding occurs immediately and propagates throughout the embedded length with a further increase in applied stress. Psarras et al. [85] suggested that the interface between the SMA wire and the polymer matrix must be sufficiently strong to be able to transmit stresses to the adjacent material. They also successfully applied the technique of laser Raman spectroscopy to measure the stress, strain, and temperature distribution at the vicinity of the SMA wire in the aramid fibers during actuation of the SMA wires. After Psarras's work, Moore and Bruck [86], and Shimamoto et al. [53] applied the digital image correlation (DIC) technique and the photoelasticity technique, respectively, to measure the internal stress and strain distribution of SMA reinforced structures. Moore and Bruck reported substantial differences between the deformations near the end and the one near the middle of the length of the specimen. That is in direct contrast to the isostrain assumptions used in a simple actuation model developed by Blonk and Lagoudas [87]. Their numerical and experimental results also indicated that one-way SMA wires experience inelastic strains during large strain recovery in the flexible polyurethanes that substantially reduced the level of the actuation strain. Similarly, Shimamoto et al. reconfirmed the active reinforcement of the SMA wire hybrid smart composite by using the technique of photoelasticity. They also confirmed that the recovery strain increases with the increase of prestrain and fiber volume fraction, while the modulus of the longitudinal elasticity of the SMA-composite decreases with increasing temperature. However, they did not attempt a further interpretation of the reduction of the elastic modulus due to SMA actuation.

2.5.3 Drawbacks from the Over-simplification of Constitutive Models

Numerous studies in recent years have focused on the design and reliability of SMA wire hybrid polymer matrix composites. Depending on the particular engineering problem, many specific SMA configurations, activation approaches, training schemes for SMA wires, manufacturing processes, and some theoretical studies for the control of mechanical responses have been proposed, as was briefly reviewed in the previous sections. However, since the phase transformation of SMA materials is sensitive to applied stress and temperature and the internal stress distributions are also functions of material properties and geometric factors of constituents, these lead to a strong coupling between the constitutive equations of SMA and the internal stress distributions.

2.5.3.1 Decoupling of Constitutive Models

In order to facilitate performance predictions and reliability studies, some researchers, including Lee and Jeong [88], Moore and Bruck [86], and Wang [89], have simplified the problems with constant material properties throughout the embedded wire at defined operating conditions. Lee and Jeong assumed that the whole SMA wire (including the center portion and embedded ends) exhibits phase transformation at an instant. In other words, in a specific condition with a given actuation temperature, the elastic modulus is expected to be consistent along the embedded portion. Similarly, Moore and Bruck proposed the use of a elastic modulus deduced from the SMA's constitutive model for predicting interfacial debonding stress. Wang further simplified the constitutive model into two distinct operating conditions, which means that the embedded SMA material was assumed to be at either at a purely martensitic or austenitic phase corresponding to the stage before or after transformation. Certainly, this is a plausible way to decouple the constitutive equations into two distinct components: the shape memory effect (or the recovery stress/strain) and the stress transmission throughout the surrounding matrix. However, this assumption leads to the loss of critical information associated with the evolution of the martensite volume fraction ξ and, hence, to an over-estimation of the recovery stress and elastic modulus of SMA in the actuated condition. As discussed in the previous section, ξ is considered a governing parameter for determining SMA properties. It can be changed in different stress states and actuation temperatures. Failure to incorporate the influence of the internal stress distribution in constitutive models will lead to a failure to reproduce the appropriate stage of SMA for predicting mechanical response.

2.5.3.2 Assumption of Constant Transformation Temperatures

In addition to the over-simplification of the constitutive model, another unreasonable assumption that has frequently been employed in many feasibility studies of SMA-composites [78,86,88 and 90,] is the stress-independent transformation temperatures. Referring to Fig.2.4 and Fig. 2.5 for the typical phase diagram of SMA material, the four transformation temperatures must be the functions of stress on SMA. Considering the embedded SMA wire that is subjected to the strain-constrained condition, the self-generated recovery stress increases the transformation temperatures. Depending on the values of C_A, both the austenitic start and finish transformation temperatures can be increased substantially with the increasing recovery stress due to thermal expansion. Lee and Jeong [88] incorrectly assumed the same transformation temperatures for both the embedded and unrefined SMA wire, which yielded an over-estimation of the mechanical response of SMA-composites. Li et al. [90] and Schrooten et al. [78] also made the same mistake; the first in a study of phase transformation behaviour under the constraint of a hard substrate, and the second in a comparison between the generation of recovered stresses in SMA wires and composites. They assumed that the austenitic phase transformation starts immediately when the actuation temperature increases upon the austenitic start temperature, T_{so}^{A} (where T_{so}^{A} is the transformation temperature at the stress-free condition obtained from measuring DSC). This led to an incorrect identification of the shape memory effect in their experimental results and theoretical predictions, respectively. Slightly different from the captioned mistakes, Wang [89] individually estimated the performances of SMA wire hybrid epoxy matrix composites at a purely martensitic phase and austenitic phase. Although this study focused on the two extreme scenarios of operation without examining issues relating to temperature, it was basically impossible to achieve the pre-defined condition with a purely austenitic phase in a strain-constrained condition. Since the austenitic finish temperature increases with residual stress on wire, an extremely high temperature (i.e., $T_{fo}^{A} + \Delta T$) may be required to complete the austenitic transformation as schematically illustrated in Fig. 2.5. For the application of epoxy matrix, the actuation level of the embedded SMA has to be controlled below the glass transition temperature of epoxy (typical value ~ 120°C); otherwise, the epoxy matrix goes from a hard, glass-like state to a rubber-like state. However the austenitic finish temperature T_{fo}^{A} for the actuator-type SMA materials is normally designed to be from 65°C to 75°C. A further increase in the actuation temperature to achieve a purely austenitic phase may reach the glass transition temperature and, hence, reduce the material properties of epoxy. Therefore, Wang's numerical results are difficult to validate via an experimental study.

2.5.4 Interfacial Bond Strength of SMA Wire-Matrix Composites

2.5.4.1 Improvement Scheme of Interfacial Bond Strength

The bonding strength of the SMA-reinforced composites is an important factor that controls the overall mechanical performance of a smart composite structure. Many studies have reported that debonding may happen at a prestrained SMA wire/epoxy matrix interface when the embedded SMA materials are heated up [91,92 and 93]. These phenomena result in a reduction in the desirable strength of a smart composite, particularly for purposes of structural buckling and vibration control. This is due to the shortening of the effective stress transfer length of the structure. To functionally achieve excellent controllability of an adaptive structure, there is no doubt that the bonding quality of the SMA/matrix interface is crucial unless mechanical fasteners or coupling sleeves are used.

Numerous experimental studies been devoted to enhancing the quality of the bonding that occurs between the SMA inclusions and matrix materials to further improve the reliability of this new class of smart composites. Beckel and Sottos [94] conducted a serious study of wire adhesion on different substrates, such as the polymer matrix and metal matrix. They examined the influence of hand sanding, sand blasting and chemical etching on the SMA wire in order to improve the quality of the interface [95]. Gabry et al. [96] revealed the surface treatments which, when applied strongly, modify the external surface of the wire. They determined the parameters that characterize the vertical distribution of the roughness and the wire morphology.

In a more recent study, Umezak [97] fabricated the epoxy resin plates embedded with spiral SMA wire, which successfully demonstrated the ability to control a crack closure force of a smart composite structure with a crack formation. After Umezak's work, Lau et al. [91] developed a new configuration of an SMA actuator for structural reinforcement. The bonding properties between twisted wires and epoxy matrix cylinders were studied experimentally through microscopical and fractographical observations as well as wire pullout tests. However, Lau's work focused only on the morphological effect at room temperature (before the SMA actuation); thus, there is no way to characterize the behaviour of interfacial debonding during the SMA actuation.

2.5.4.2 Theoretical Analysis of the Strength of the Interfacial Bond

There is no doubt that using mechanical fasteners to fax both of the SMA actuators inside a matrix can minimize or even eliminate interfacial debonding due to the over-actuation of SMA or poor bonding quality between constituents. However, because the installation of these mechanical devices may further increase the body load of the composite, additional machining and assembly procedures are also necessary. This therefore greatly reduces the flexibility of using SMA-composites from the design point of view. As discussed in the previous section, there are many plausible, distinct solutions to improving the overall mechanical strength of an SMA-reinforced composite structure. Except for the application of fasteners and/or a coupling sleeve, most of the other methods require post-processing on the SMA inclusions in order to improve surface roughness before the formation of SMA-composites.

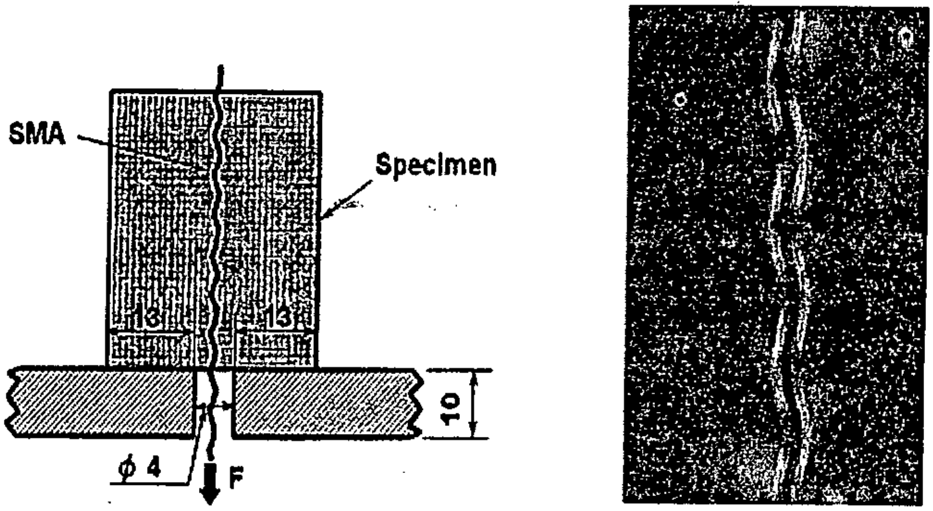

Figure 2.7 Schematic illustration of a composite plate embedded with spiral SMA wire (after Umezak et al.)[97]

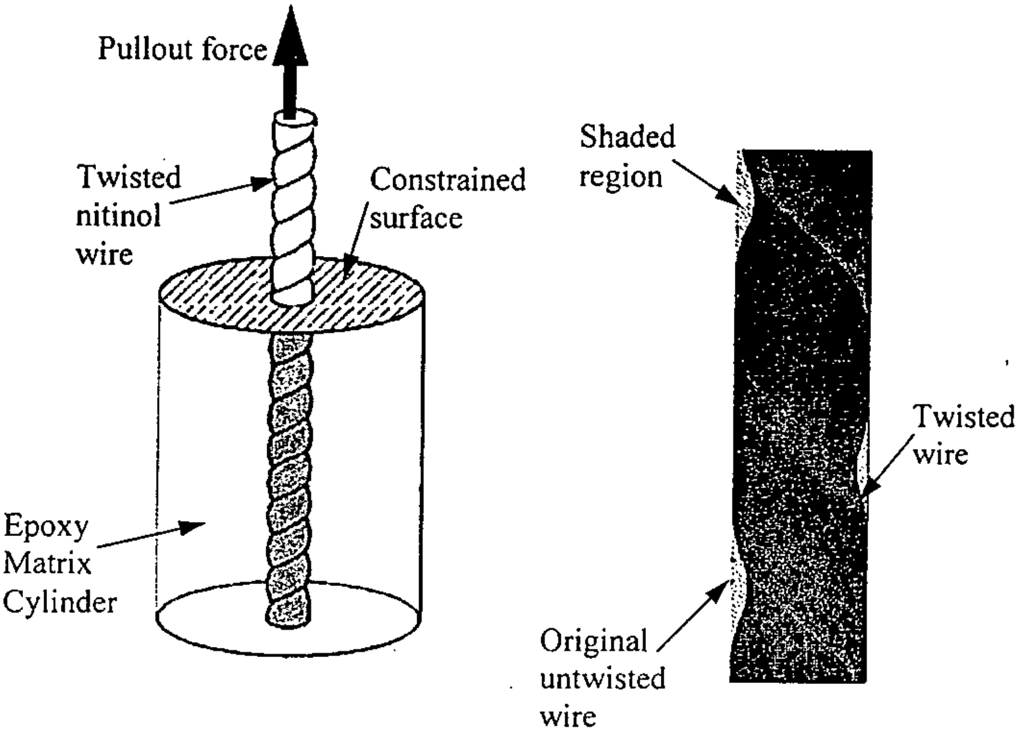

Figure 2.8 Schematic illustration of the epoxy matrix cylinder embedded with twisted SMA wire (after Lau et al.) [91]

In order to expedite the design process including selecting materials, confirming ideal actuation scenarios and geometric relations between SMA actuators and the matrix, etc., it is crucial to develop a theoretical model that can estimate all of these parameters in the design stage. In addition to the strong coupling between the SMA's constitutive models and internal stress distributions, the fracture mechanics of the interface in SMA-composites is another critical problem that has to be solved prior to the success of the design and fabrication of this novel material system.

Lagoudas and Tadjbakhsh [81] are pioneers who developed an approximate cylindrical to transfer loads from the SMA fiber to the host medium, based on the cylindrical shear-lag model [98]. According to this model, the axial strain of the host medium and the partial shape recovery of SMA takes place through the deformation of a shear layer surrounding the SMA fiber (Fig. 2.9). Because of the constraints imposed by the host medium, a self-equilibrated internal stress state will develop instead, and the prestrain ε_p will only be partially recovered. The constitutive equations for the SMA fiber and the cylindrical rod are given by

$$\sigma_f = E_f \frac{dw_1}{dz} - E_f \varepsilon_p \tag{2.10}$$

$$\sigma_m = E_m \frac{dw_2}{dz} \tag{2.11}$$

$$\tau = G_m \frac{\partial w}{\partial r} \tag{2.12}$$

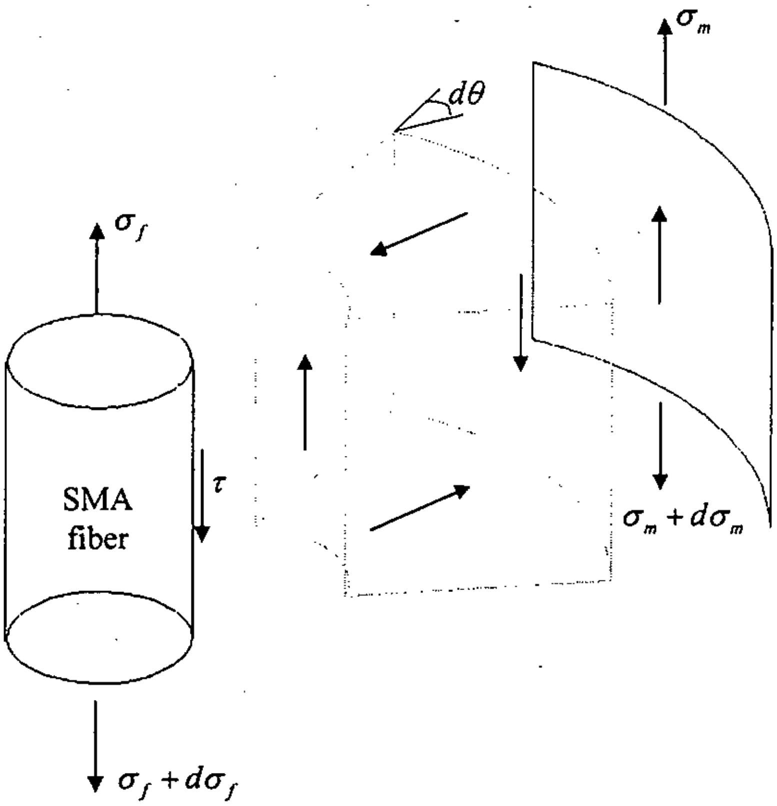

Figure 2.9 Shear-lag model for transferring loads from SMA fiber to the host medium

where E_f is the elastic modulus of the SMA fiber in the austenitic phase, and E_m and G_m are the elastic modulus and shear modulus of the host medium, respectively. The axial displacements of the fiber and host medium are denoted by $w_1(z,\theta)$, $w_2(z,\theta)$, respectively, and of the shear layer by $w(z,r,\theta)$. One may notice that the proposed constitutive equations only represent the extreme case with a purely austenitic phase through the whole SMA actuator, which means that the recovery action due to the phase transformation is totally completed at a high temperature. In addition, the thermal expansion on the host medium was also ignored. This contradicts the assumption of a completed austenitic phase transformation that is normally achieved at relatively higher actuation temperatures ($T > T_{fn}^{A}$). Therefore, this approximate model can only simulate a very limited "on" and "off" mode of operation of the SMA composite structures.

Berman and White [51] addressed the problem of residual stress arising from the difference in thermal expansion between the SMA and host material, and the stresses generated from the SMA transformations during the fabrication process. In their studies, a combined thermal and transformation expansion β_{SMA} was proposed to simulate the properties of embedded SMA wire.

$$\beta_{SMA}(T_i) = \frac{\bar{\varepsilon}(T_{i-1}) - \bar{\varepsilon}(T_i)}{\Delta T_i} \tag{2.13}$$

with

$$\xi(T_i) = 1 - \frac{\bar{\varepsilon}(T_i)}{\varepsilon_{rec}} \tag{2.14}$$

where $\bar{\varepsilon}$ and ε_{rec} are the average wire strain over a given temperature interval and maximum recoverable strain, respectively. ξ represents the martensite volume fraction and ΔT_i is the temperature interval. They obtained the mechanical properties of SMA as a function of temperature by first calculating the martensite volume fraction ξ as a function of temperature and then using the rule of mixture relations:

$$E_{SMA} = \xi E_M + (1-\xi) E_A \tag{2.15}$$

$$G_{SMA} = \xi G_M + (1-\xi) G_A \tag{2.16}$$

where E_{SMA} and G_{SMA} are the elastic modulus and shear modulus of SMA, respectively. The parameters with subscripts of "M" and "A" represent the corresponding properties at the purely martenistic and austenitic phases, respectively. In addition to the SMA properties, the thermal expansion properties of epoxy coating were also considered in the model. Therefore, the influence of the shape memory effect and thermal expansion on the development of internal stress can be estimated. Since their research focused on the residual stress developed during a cooling down of the SMA composite from the processing condition, the hoop stress at the interface, arising from the difference in thermal shrinkage between the constituents, was thus considered to be the critical stress component that induced radial cracks in the surrounding composite. However, this model can neither simulate the internal stress distributions in the wire direction nor the bond strength of an SMA composite.

The modeling of internal stress distributions is critically important for predicting the performance of SMA-composites, such as estimating the maximum recovery stress and modal properties of the whole composite structure, However, the influence of stress distributions on SMA properties (e.g., elastic modulus) has not been considered in Berman and White's works, which implies that there is nothing that can be used to conduct a feasibility study. On the other hand, when wire is heated up for a shape change or structural reinforcement, the wire will experience maximum strain and stress recovery in the axial direction instead of in the radial direction. It is therefore more reasonable to induce interfacial debonding in the axial direction rather than radial cracking in the surrounding matrix.

In addition to the models developed by Lagoudas and Tadjbakhsh, and Berman and White, some other research teams have used traditional models that were developed for studies of conventional composite structures, in order to the determine the interfacial strength of the particular structure. Gabry et al. [96] used Grezczuck's theory [99] to model the distribution of shear stress along the SMA wire. They gave the expression of interfacial shear stress τ as follows:

$$\tau(x) = F_d \frac{\alpha}{2\pi r}\left[\coth(\alpha \cdot L)\cosh(\alpha \cdot x) - \sinh(\alpha \cdot x)\right]$$

$$\text{with} \quad \alpha = \sqrt{2\pi \frac{G_m}{\ln(\frac{r}{R})} \left[\frac{1}{\pi r^2 E_f} - \frac{1}{\pi R^2 E_m} \right]} \tag{2.17}$$

where G_m represents the shear modulus of the matrix, and r and R refer to the radius of the wire and matrix cylinder, respectively. E_f and E_m are the elastic modulus of the wire and matrix, while L is the length of the embedded wire. Certainly, this could be the easiest way to estimate the distribution of interfacial shear stress along the wire(in x-direction). However, they over-simplified the problem by using the elastic modulus of SMA at the initial state in Eqn. 2.17 to predict interfacial shear stress. As a result, there was no means to represent the effect of phase transformations on stress distributions.

Similarly, Moore and Bruck suggested a simple model that is associated with both the loading arising from the recovery action of SMA wire F_A and the strength of the interfacial bond τ_d as given below:

$$F_A = 2\pi r^2 \sqrt{E_f G_i / r} \tanh(n l_e / r) \tag{2.18}$$

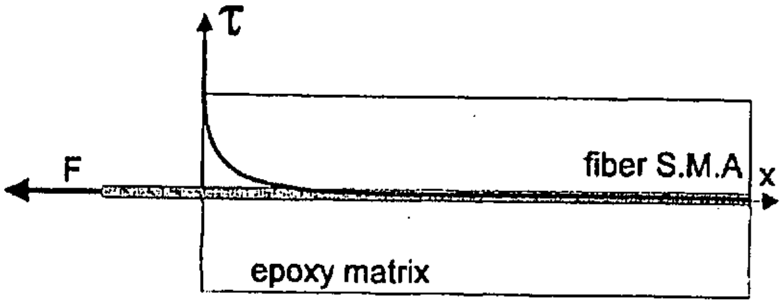

Figure 2.10 Evolution of the shear stress induced in the SMA fiber-epoxy matrix cylinder (after Gabry et al. [96]).

and $$\tau_d = n\sqrt{E_f G_i / r} \tag{2.19}$$

where G_i is the interfacial work of the fracture, E_f and r are the elastic modulus and radius of the SMA wire, le represents the length of the embedded wire, and n is a function of the dimensional constants and material properties. In order to determine the bond strength of the specimens embedded with SMA wire before any further experimental study, a pullout test was performed to obtain the bond strength τ_d. The corresponding maximum recovery stress was then calculated from Eqn.2.18. It was found that the calculated result is much lower than the data reported by the manufacturer of the wires. Therefore, the bond strength was confirmed as strong enough to sustain the maximum actuation of SMA. However, both Eqns.2.18 and2.19 are definitely not associated with issues of phase transformation. In the other words, they cannot be directly applied to project the results of different actuation temperatures.

In a more recent study, Wang [89] proposed a simple model to estimate the minimum volume fraction requirement of SMA wire in the composite patches to repair structural damage. The specific requirement evaluated from the criterion of bonding strength is given as:

$$\varepsilon_{SMA} \leq \frac{\tau_c}{E_{SMA}} \tag{2.20}$$

where ε_{SMA} and E_{SMA} represent the prestrain value and elastic modulus of SMA, and τ_c is he interfacial strength obtained from the pullout test. In the calculation, SMA had been considered at another purely martensite or austenite phase corresponding to the stage before or after transformation. Again, this assumption over-simplified the behaviour of SMA. It cannot represent the change in E_{SMA} due to stress-induced martensitic transformation (SIM) during the pullout test. Also, as previously discussed for the phase transformation phenomenon of a strained constrained wire in a composite structure, austenitic transformation has to be finished at a temperature much higher than T_{fo}^{A} – the austenite finish temperature. Strictly speaking, it is almost impossible to achieve a purely austenitic phase is for actuator-type SMA materials in the constrained condition. Therefore, the E_{SMA} value is over-estimated in Eqn.2.20.

2.6 Summary

The problems discussed in the captioned paragraphs have highlighted a few of the typical drawbacks of over-simplification in the formation of constitutive models and evaluation of interfacial bond strength. A failure to associate the internal stress distributions with SMA behaviour in the strained-constrained condition will lead to a failure to develop an appropriate solution to predict the performance of SMA-composites as well as make it difficult to carry out a study on their reliability. It is therefore critically important to address these problems to provide the basis for a study of the design and analysis of SMA wire hybrid matrix composites.

Chapter 3

Internal Stress Distributions in SMA-Composites

3.1 Introduction

Research on the application of shape memory alloys in composite materials has been gaining momentum over the past decade. Numerous designs and fabrication processes of composite structures built-in with SMAs in the form of wires, short fibers, thin film as well as particulates have been proposed by different research groups [102-106]. Since the recovery action of embedded SMAs induced by elevated temperature could change the modal properties and the mechanical responses of the whole structure, the SMA-reinforced composite becomes one of the most attractive candidates of smart structures for satisfying a wide variety of engineering requirements. Many papers have examined SMA constitutive response and hence the development of SMA-composites so as to realize the control of shape change [106,107], buckling [108,109], vibration [110,111], structural damage [112] as well as damping properties of structures [102]. In order to successfully develop these kinds of novel material systems, it is crucial to quantitatively clarify the correlations between all the potential external stimulus, actuation temperatures, evolutions of material properties and mechanical responses of constituents.

Due to the changes of material properties as well as the modal response of actuated SMA-composites, feasibility and reliability studies of those novel material systems reasonably rely on the thorough knowledge of non-linear relationship between the phase transformation criteria of SMA and the evolution of internal stresses. The principle aim of this chapter is therefore to develop a recurrence relation between internal stress distributions and evolution of martensite volume fraction on the SMA during actuation. This theoretical model is developed based on the two sets of fundamental governing equations: the constitutive law for shape memory effect (SME) and basic stress-strain relations for stress transmission throughout the constituents. Solutions of internal stresses on constituents are therefore modeled with two distinguished contributions of thermomechanical effect and SME. Results indicate substantial changes of the internal stresses in different actuation and loading scenarios. Relationship between interfacial shear stress and actuation temperature also gives us important hints to predict the ideal actuation temperature which is able to maximize the structural enhancement and meanwhile avoid interfacial failure due to over-actuation. In addition, influence of geometric factors on the development of maximum axial stress on SMA wire is analyzed and presented in this chapter. Results are particularly important for ensuring the utilization of SME for mechanical response improvement in the composite structures.

3.2 Fundamental Governing Equations

3.2.1 Constitutive Law of Shape Memory Effect

A simple SMA-matrix cylinder model, actuated by means of electrical resistive heating as shown in Fig. 3.1, is employed to evaluate the correlations discussed in the previous section. Parametric studies with different applied loads, actuation temperatures and geometric factors are required to systematically evaluate the evolution of internal stresses. In addition, constitutive law of the SMA is also necessary to be considered to simulate the SME inside the model. In the past two decades, a fundamental constitutive model proposed and modified by Tanaka [64], Liang and Rogers [65] and Brinson [66] has been extensively applied to study the thermomechanical behaviour [103,113] of SMA actuators. Fairly good agreement between experimental results and theoretical predictions has been reported in many literatures. Based on the pre-defined thermomechanical history and the given initial conditions, the instantaneous material properties and mechanical responses of the SMA are readily determined from the constitutive model using the information of applied stress and actuation temperature in the particular moment. Therefore, mechanical responses or degree of shape change of the SMA component can be predicted accurately in the design stage. However for the SMA-polymer hybrid composites, due to the stress transmission across interface between constituents, information of stress and temperature on the embedded portion of the SMA cannot be determined explicitly. Boundary conditions can only provide the exact values of stress and temperature at the embedded ends ($z = 0$ and $z = L$). In the other words, instantaneous martensite volume fraction and hence the material properties and mechanical response are only available on these specific positions. Therefore, it is critical to develop a theoretical model, which is able to clarify the instantaneous behaviour of constituents along the embedded length, for the prediction of internal stresses of the SMA-composites.

In 1986, Tanaka [64] proposed a constitutive model to describe the thermomechanical behaviour of the SMA. Four years later, Liang and Rogers [65] modified Tanaka's model by introducing a cosine function to represent the martensite fraction as a function of stress and temperature during transformation, which agreed well with numerous experimental results. However, due to the absence of variable for differentiating the 'twinned' and 'detwinned' variants of martensite, there is no means to

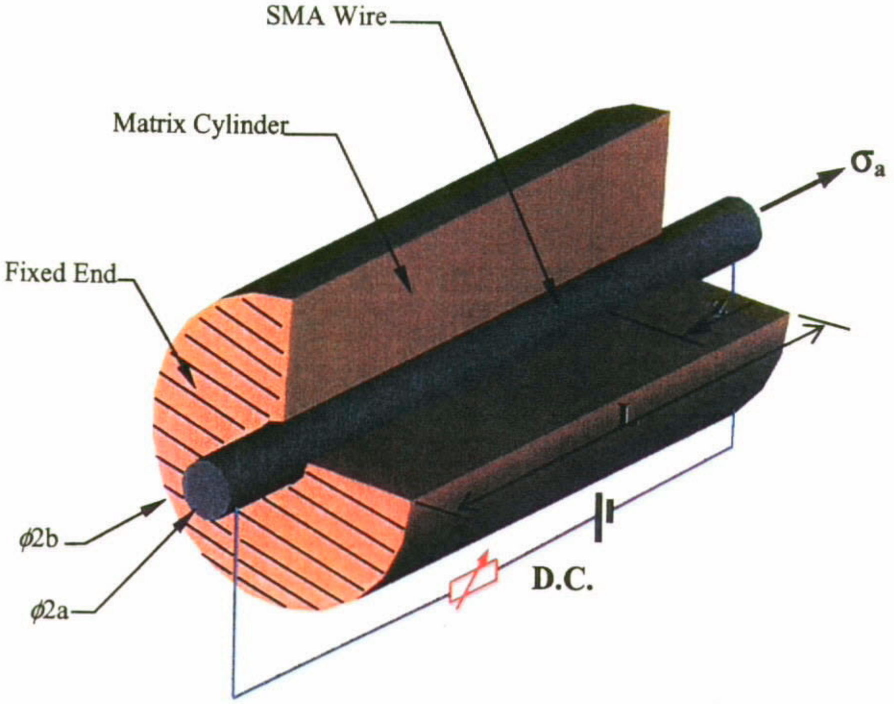

Figure 3.1 Schematic of SMA-matrix cylinder model with fixed matrix bottom and external applied stress, σ_a on wire end in z-axis.

capture SMA material behaviour at $T < M_s$ when any temperature-induced martensite is present. Brinson [65] addressed the problem by separating the martensite variable ξ into stress-induced ξ_s and temperature-induced ξ_T components in the modified model. The resulting constitutive equation together with some necessary material functions are summarized as following,

$$\sigma - \sigma_o = E_f(\xi)\varepsilon - E_f(\xi_o)\varepsilon_o + \Omega(\xi)\xi_S - \Omega(\xi_o)\xi_{So} + \theta(T - T_o) \tag{3.1}$$

$$\Omega(\xi) = -\varepsilon_L E_f(\xi) \tag{3.2}$$

$$E_f(\xi) = \xi(E_M - E_A) + E_A \tag{3.3}$$

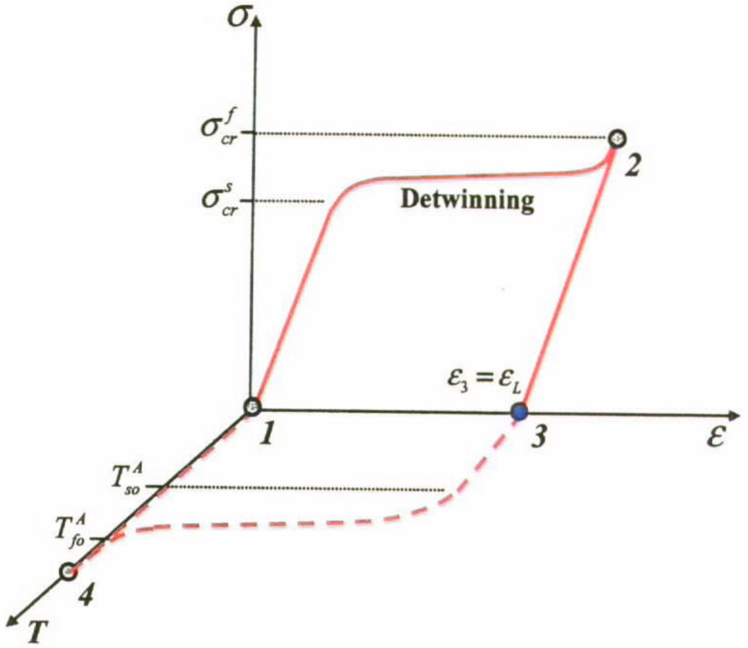

Figure 3.2 Development of maximum residual strain, ε_L at $T < T_{so}^{A}$ (1-2-3) and strain recovery path for temperature increased over T_{fo}^{A} and $\sigma = 0$ (3-4-1).

where σ_o, ε_o, ξ_o and T_o represent the values of stress, strain, martensite and temperature at initial condition, respectively. E_f, Ω and θ are modulus of elasticity, transformation tensor and thermal stress coefficient for the SMA material. The maximum residual strain ε_L, which is also considered as material constant, can be achieved by using externally applied load to convert all of the austenite or twinned martensite to detwinned martensite at $T < T_{so}^{A}$.

As schematically illustrated in Fig. 3.2, if the whole SMA wire is maintained at a temperature-induced martensite state (i.e. $\xi_T = 1$ or $\xi_s = 0$) in the stress free condition and when the axial load is increased from zero (at point 1) to the critical stress σ_{cr}^{s} variants will start to detwin and hence a long plateau can be observed. Such detwinning process completes at point 2 and the stress-induced martensite volume fraction increases to unity

(ξ = ξ_s = 1) at the instant. Elastic strain will be restored upon unloading and only the maximum residual strain, ε_L remains at point 3. Such residual strain may be recovered through a thermal cycle 3-4-1 in a stress-free condition. In the perfectly bonded condition, it is assumed that the strain of the embedded SMA wire is absolutely constrained by the surrounding matrix. Therefore, the strain-constrained condition with $\varepsilon = \varepsilon_o = \varepsilon_p$ has to be satisfied in Eqn. 3.1. Substituting Eqns. 3.2 and 3.3 into Eqn. 3.1, constrained recovery stress σ_r can be obtained as

$$\sigma_r = E_f(\xi)(\varepsilon_p - \varepsilon_L \xi_S) + \theta(T - T_o) \tag{3.4}$$

where ε_p represents the prestrain value of the SMA which governs the maximum recovery stress due to austenitic phase transformation.

3.2.2 Stress-strain Relations Incorporated with SME

In addition to the actuation temperature, numerous experimental findings have confirmed that the pre-strain value (or the residual strain after unloading), ε_p of the embedded SMA wire fundamentally governs the overall mechanical performance of the SMA-composites. Therefore the value of ε_p, which is a critical parameter to simulate the recovery action inside matrix, has to be chosen carefully in the numerical modeling. As an example, after certain unwanted cold works during manufacturing process or transportation, it is normally impossible to explicitly determine the

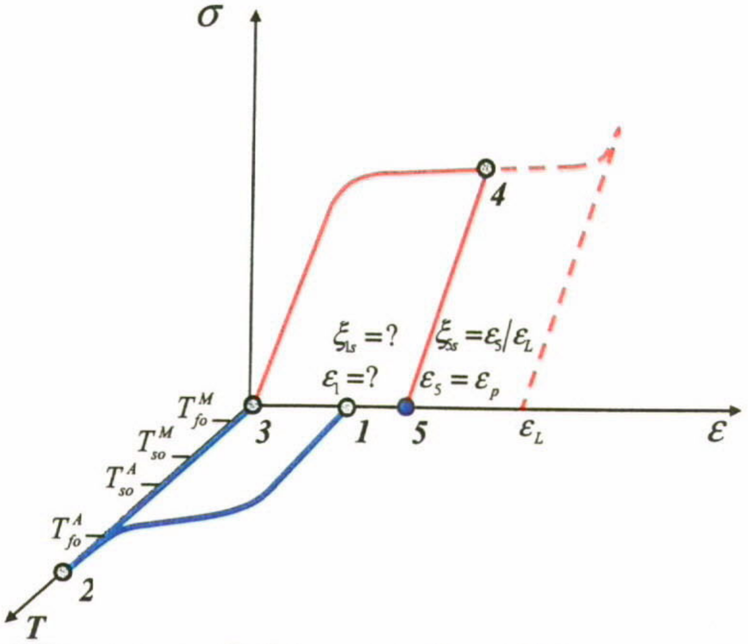

Figure 3.4 Sequence applied to pre-strain a NiTi wire (originally with unknown residual strain, ε_1) to the desired residual strain, ε_p.

pre-strained value as well as instantaneous properties of the SMA. Therefore, it is necessary to recover this residual strain and make sure that the pure temperature-induced martensite state ($\xi = \xi_T = 1$) is attained using a thermal cycle 1-2-3 as shown in Fig. 3.4. For the simplicity, this specific thermal cycle is termed as 'SMA reset-cycle' in this study. After the reset-cycle, the SMA wire will be loaded from point 3 to point 4 and then completely unloaded to point 5. The residual strain ε_5 should be considered as the final pre-strained level ε_p and the stress-induced martensite volume fraction can be estimated by using the following equation,

$$\xi_s = \frac{\varepsilon_p}{\varepsilon_L} \tag{3.5}$$

Figure 3.1 schematically illustrates that a prestrained SMA wire is embedded at the center of a coaxial cylindrical matrix with total length L. Material properties of the SMA

Table. 3.1 Dimensions and material properties of constituents for the SMA-composite..

a (mm)	b (mm)	ε_p (%)	ε_L (%)	E_A (GPa)	E_M (GPa)	E_m (GPa)	C_A (MPa/°C)	C_M (MPa/°C)
0.125	5	2	8	40	20	2.3	28	20

σ_{cr}^{s} $(T<T_{so}^{M})$ (MPa)	σ_{cr}^{f} $(T<T_{so}^{M})$ (MPa)	T_{so}^{A} (°C)	T_{fo}^{A} (°C)	T_{so}^{M} (°C)	T_{fo}^{M} (°C)	θ (MPa/°C)	T_o (°C)	v_f	v_m
120	200	40	75	33	18	5.5	25	0.33	0.35

employed as numerical examples are summarized in Table 3.1. DC power supply is directly connected to the wire ends so as to facilitate the resistive heating for SMA actuation. It is also assumed that there is no temperature derivation along the wire, and temperature differences between SMA and its surrounding matrix in both the transverse and radial directions are ignored. Combining Eqn. 3.4 into the general stress-strain relations of constituents, governing equations between stresses and strains for the embedded SMA wire are given by

$$\varepsilon_f^z(r,z,\sigma_a,T)=\frac{1}{E_f(z,\sigma_a,T)}\left[\sigma_f^z(z,\sigma_a,T)-\nu_f\left(\sigma_f^r(z,\sigma_a,T)+\sigma_f^\theta(z,\sigma_a,T)\right)\right]-\left(\varepsilon_p-\varepsilon_L\xi_s\right)-\frac{\theta}{E_f(z,\sigma_a,T)}(T-T_o) \tag{3.6}$$

$$\varepsilon_f^\theta(r,z,\sigma_a,T)=\frac{1}{E_f(z,\sigma_a,T)}\left[\sigma_f^\vartheta(z,\sigma_a,T)-\nu_f\left(\sigma_f^r(z,\sigma_a,T)+\sigma_f^z(z,\sigma_a,T)\right)\right]+\nu_f[\varepsilon_p(1-\xi_s)+\frac{\theta}{E_f(z,\sigma_a,T)}(T-T_o)] \tag{3.7}$$

where σ_a represents the externally applied stress acting on the SMA wire's end ($z = 0$). Recalling Eqn. 3.3, modulus of elasticity of the SMA $E_f(\xi)$ is a function ξ. However the martensite volume fraction ξ, determined by its thermomechanical history, is a function of stress and temperature on the SMA. Obviously, axial stress on the SMA wire is dependent of applied stress σ_a and axial position z. Therefore $E_f(\xi)$ can be rewritten as $E_f(z, \sigma_a, T)$ so as to highlight the evolution of ξ and hence the SMA's material properties inside the matrix.

Based on the assumption of constant temperature distribution throughout constituents, when the SMA wire is actuated to temperature T, the surrounding matrix should also experience the same temperature in the steady state. As a result, thermal expansion on the matrix cylinder has to be considered to form the governing equations as shown below

$$\varepsilon_m^z(r,z,\sigma_a,T)=\frac{1}{E_m}\left[\sigma_m^z(z,\sigma_a,T)-\nu_m\left(\sigma_m^r(z,\sigma_a,T)+\sigma_m^\theta(z,\sigma_a,T)\right)\right]+\beta_m(T-T_o) \tag{3.8}$$

$$\varepsilon_m^\theta(r,z,\sigma_a,T)=\frac{1}{E_m}\left[\sigma_m^\theta(z,\sigma_a,T)-\nu_m\left(\sigma_m^r(z,\sigma_a,T)+\sigma_m^z(z,\sigma_a,T)\right)\right]+\beta_m(T-T_o) \tag{3.9}$$

where β_m is the thermal expansion coefficient of matrix material. ν_f and ν_m are the Poisson's ratio of the SMA and matrix respectively.

3.3 Evolution of Internal Stresses for $T < T_{so}^A$ and $\sigma < \sigma_M^s(T)$

The condition that the SMA wire and matrix remain in contact during the deformation requires $\varepsilon_f^\theta(a,z,\sigma_a,T) = \varepsilon_m^\theta(a,z,\sigma_a,T)$. Therefore, the interfacial radial stress $q_r(z, \sigma, T)$ arising from Poisson contraction between constituents is obtained by

$$q_r(z,\sigma_a,T)=\frac{\alpha(z,\sigma_a,T)\nu_f\sigma_f^z(z,\sigma_a,T)-\nu_m\sigma_m^z(z,\sigma_a,T)+E_m(G_b(T)-\nu_f G_a(z,\sigma_a,T))}{\alpha(z,\sigma_a,T)(1-\nu_f)+2\gamma+1+\nu_m} \tag{3.10}$$

where

$$E_f(z,\sigma_a,T)=\xi(z,\sigma_a,T)(E_M-E_A)+E_A \tag{3.11}$$

$$\alpha(z,\sigma_a,T)=\frac{E_m}{E_f(z,\sigma_a,T)} \tag{3.12}$$

$$G_a(z,\sigma_a,T)=-\frac{\theta(T-T_o)}{E_f(z,\sigma_a,T)}+\varepsilon_p(\xi(z,\sigma_a,T)-I) \tag{3.13}$$

$$G_b(T)=\beta_m(T-T_o) \tag{3.14}$$

$$\gamma=\frac{a^2}{b^2-a^2} \tag{3.15}$$

It should be noted that ξ is a constant at $T < T^A_{so}$ and $\sigma < \sigma^s_M(T)$. As a result, E_f and α should be considered as constants in Eqns. 3.11-3.13. G_a and G_b are products of the SME and thermal expansion respectively. The general relation between interfacial shear stress, $\tau_i(z, \sigma_a, T)$ and axial strains on constituents is given as

$$\frac{d\tau_i(z,\sigma,T)}{dz}=\frac{aE_m[\varepsilon^z_m(b,z,\sigma,T)-\varepsilon^z_f(a,z,\sigma,T)]}{(I+\nu_m)[2\gamma b^2\ln(b/a)-a^2]} \tag{3.16}$$

and using the assumption of average axial stresses on the SMA wire and matrix respectively in radial direction, mechanical condition between externally applied stress and internal stress distributions can be derived as

$$\sigma_a=\sigma^z_f(z,\sigma_a,T)+\frac{I}{\gamma}\sigma^z_m(z,\sigma_a,T) \tag{3.17}$$

where γ ($=a^2/(b^2-a^2)$) is a volume ratio of wire to matrix. To simplify the analysis it is assumed that the axial stresses in the fiber and the matrix are taken as the average of the fiber and the matrix stresses in the r-direction, in which $\sigma_f^z(z) = 2/a^2 \int_0^a \sigma_f^z(r,z)rdr$ and $\sigma_m^z(z) = 2\gamma/a^2 \int_a^b \sigma_m^z(r,z)rdr$. This assumption is considered appropriate for the model cylindrical composite having a fiber embedded in a relative large matrix as in a practical fiber pullout experiment. It is expected in reality that the variation of the axial matrix stress with regard to the radial direction is substantial only near the fiber free end where all stress components are concentrated, but it diminishes with distance away from this region. In addition, the equilibrium condition describing the stress transfer between the SMA wire and matrix is

$$\frac{d\sigma_f^z(z,\sigma_a,T)}{dz} = -\frac{2}{a}\tau_i(z,\sigma_a,T) \tag{3.18}$$

Combining Eqns. 3.6, 3.8, 3.10, 3.16 and 3.17, a second order differential equation for axial stress on the SMA wire can be obtained by

$$\sigma_f^{z''}(z,\sigma_a,T) = \psi_1(z,\sigma_a,T)\sigma_f^{z}(z,\sigma_a,T) + \psi_1(z,\sigma_a,T)\psi_3(z,\sigma_a,T)\sigma_f^{z}(z,\sigma_a,T) + \psi_2(z,\sigma_a,T) \tag{3.19}$$

where ψ_1, ψ_2 and ψ_3 are functions of geometric factors, material properties, position in axial direction, applied stress and actuation temperature and given by:

$$\psi_1(z,\sigma_a,T) = \frac{2\varphi[\alpha(1-2k(z,\sigma_a,T)\nu_f) + \gamma(1-2k(z,\sigma_a,T))\nu_m]}{E_m} \tag{3.20}$$

$$\psi_2(z,\sigma_a,T) = 2\varphi[G_a(z,\sigma_a,T) - G_b(T) - 2k(z,\sigma_a,T)(G_b(T) + \nu_f G_a(z,\sigma_a,T))] \tag{3.21}$$

$$\psi_3(z,\sigma_a,T)=\frac{2\gamma(2k(z,\sigma_a,T)\nu_m-1)}{\alpha(1-2k(z,\sigma_a,T)\nu_f)+\gamma(1-2k(z,\sigma_a,T)\nu_m)} \tag{3.22}$$

where $k(z,\sigma,T)=\frac{\alpha(z,\sigma,T)\nu_f+\gamma\nu_m}{\alpha(z,\sigma,T)\left(1-\nu_f\right)+2\gamma+1+\nu_m}$ and $\varphi=\frac{E_m}{(1+\nu_m)\left[2\gamma b^2\ln(b/a)-a^2\right]}$.

For the constant value of ξ, $\psi_1$and ψ_3 are simply the constants with given geometric factors and material properties. Also, ψ_2 represents the thermal effects on constituents due to resistive heating of SMA.

Figure 3.5 shows a typical phase diagram for SMA materials. In a stress-free condition, austenitic phase transformation will only occur when the SMA has been heated to above the austenite start temperature – T_{so}^{A}. In addition, stress induced martensitic transformation (SIM) can be initiated when the applied stress on SMA is higher than $\sigma_M^s(T)$. Therefore, if the actuation temperature is controlled at $T < T_{so}^{A}$ and the applied stress on SMA is restricted below $\sigma_M^s(T)$, both the 'total' and 'stress-induced' martensite fraction, ξ and ξ_s will remain unchanged. In the other words, the constant material properties of SMA should be considered throughout the embedded length. Nonetheless, referring to Eqn. 1, recovery stress is linearly increased with temperature due to thermal elasticity (i.e. $\theta(T - T_o)$). Therefore, solving Eqn. 3.19 with the following boundary equations,

$$\sigma_f^z(0,\sigma_a,T)=\sigma_a \tag{3.23}$$

$$\sigma_f^z(L,\sigma_a,T)=0 \tag{3.24}$$

solutions of internal stresses ($\sigma_f^z(z,\sigma_a,T)$, $\sigma_m^z(z,\sigma_a,T)$, $\tau_m^{rz}(z,\sigma_a,T)$ and $\tau_i(z,\sigma_a,T)$) at $T < T_{so}^A$ and $\sigma_a < \sigma_M^s(T)$ can be obtained as following,

$$\sigma_f^z(z,\sigma_a,T)=\frac{(\psi_4(T)+\psi_3\sigma_a)\sinh\sqrt{\psi_1}z+(\psi_4(T)+\sigma_a+\psi_3)\sinh\sqrt{\psi_1}(L-z)}{\sinh\sqrt{\psi_1}L}-(\psi_4(T)+\psi_3\sigma_a) \tag{3.25}$$

$$\sigma_m^z(z,\sigma_a,T)=-\gamma\left\{\frac{(\psi_4(T)+\psi_3\sigma_a)\sinh\sqrt{\psi_1}z+(\psi_4(T)+\sigma_a+\psi_3)\sinh\sqrt{\psi_1}(L-z)}{\sinh\sqrt{\psi_1}L}-\psi_4(T)-(1+\psi_3)\sigma_a\right\} \tag{3.26}$$

$$\tau_m^{rz}(r,z,\sigma_a,T)=\frac{\gamma(b^2-r^2)\sqrt{\psi_1}\left[(\psi_4(T)+\psi_3\sigma_a+\sigma_a)\cosh\sqrt{\psi_1}(L-z)-(\psi_4(T)+\psi_3\sigma_a)\cosh\sqrt{\psi_1}z\right]}{2r\sinh\sqrt{A_1}L} \tag{3.27}$$

$$\tau_i(z,\sigma_a,T)=\frac{a\sqrt{\psi_1}\left[(\psi_4(T)+\psi_3\sigma_a+\sigma_a)\cosh\sqrt{\psi_1}(L-z)-(\psi_4(T)+\psi_3\sigma_a)\cosh\sqrt{\psi_1}z\right]}{2\sinh\sqrt{A_1}L} \tag{3.28}$$

where $\psi_4 = \psi_2/\psi_1$ is also a function of actuation temperature. It is important to emphasize that all of the ψ's are independent of phase transformation for $T < T_{so}^A$. Plots of axial stress on SMA wire, $\sigma_f^z(z,\sigma,T)$ and interfacial shear stress, τ_i at 25°C and 40°C are shown in Figs. 3.6 and 3.7 respectively.

In Fig. 3.6, solid line represents the axial stress on SMA wire which is subjected to a constant applied stress σ_a = 1GPa and T = 25°C. Material properties of SMA remain unchanged at the instant. The plot indicates that the axial stress monotonically decreases from loading end (z = 0) to free end (z = L). Definitely, identical results can also be obtained by using the previously developed theoretical model [114] for internal stresses of fiber-matrix cylinder with constant material properties of constituents. However, if the wire has been heated to 40°C (< T_{so}^A), axial stresses on wire will increase

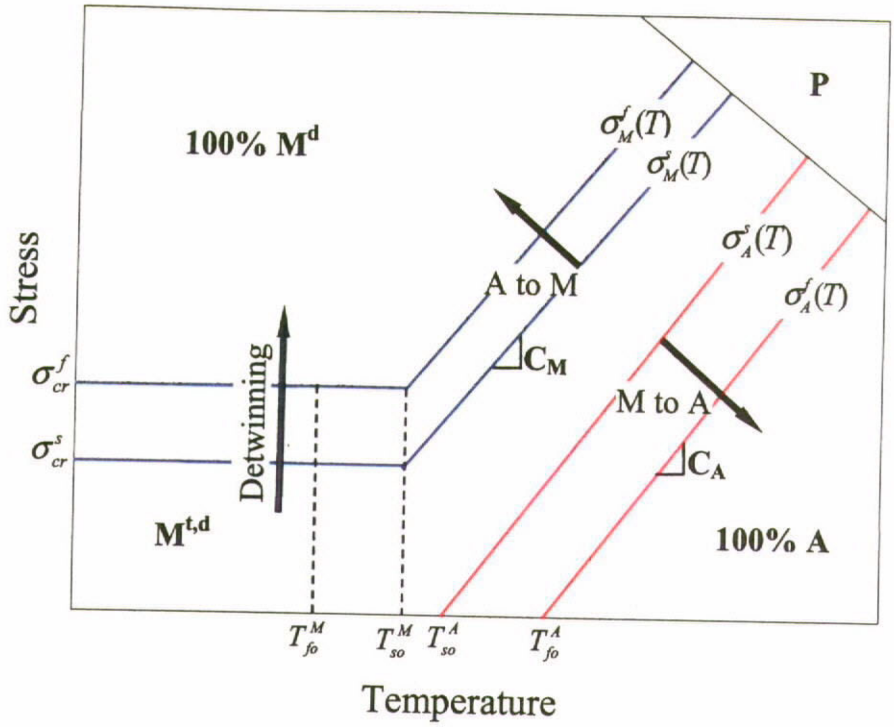

Figure 3.5 Typical phase diagram of shape memory alloy.

slightly along the embedded length except the two end points. This phenomenon is independent of phase transformation but a result of thermal effect on both constituents – recovery stress of SMA increases in linear manner with temperature (i.e. $\theta(T\text{-}T_o)$) and the thermal expansion occurred in matrix. As shown in Fig. 3.7, the interfacial shear stress monotonically decreases in *z*-direction at $T = 25°\text{C}$ but increases slightly at $z = L$ when the temperature increased to 40°C.

Based on the results for $T < T_{so}^A$ as shown in Fig. 3.6, it can be imagined that if the SMA wire is heated to a temperature above T_{so}^A in a no-load condition ($\sigma_a = 0$), austenitic transformation is expected to start at both embedded ends where the axial stresses on wire have to be zero as given in the boundary conditions ($\sigma_f^z(0,\sigma,T) = \sigma_a = 0$, $\sigma_f^z(L,\sigma,T) = 0$). As a result, value of ξ is no longer to be a constant but decreases toward both ends.

If an external stress is then apply on the SMA wire's end ($z = 0$), The SIM may occur and start from loading end to converse austenite to stress-prefer variants again. In the other words, the martensite volume fraction and hence the material properties of the SMA should change accordingly.

As previously discussed, the martensite volume fraction, ξ is a function of stress and temperature. Considering that the SMA wire is subjected to a constant actuation temperature ($T > T_o$) and if the stress values on wire at different axial positions 'z' can be determined, the critical parameter ξ and hence the material properties as well as evolutions of internal stresses can be estimated.

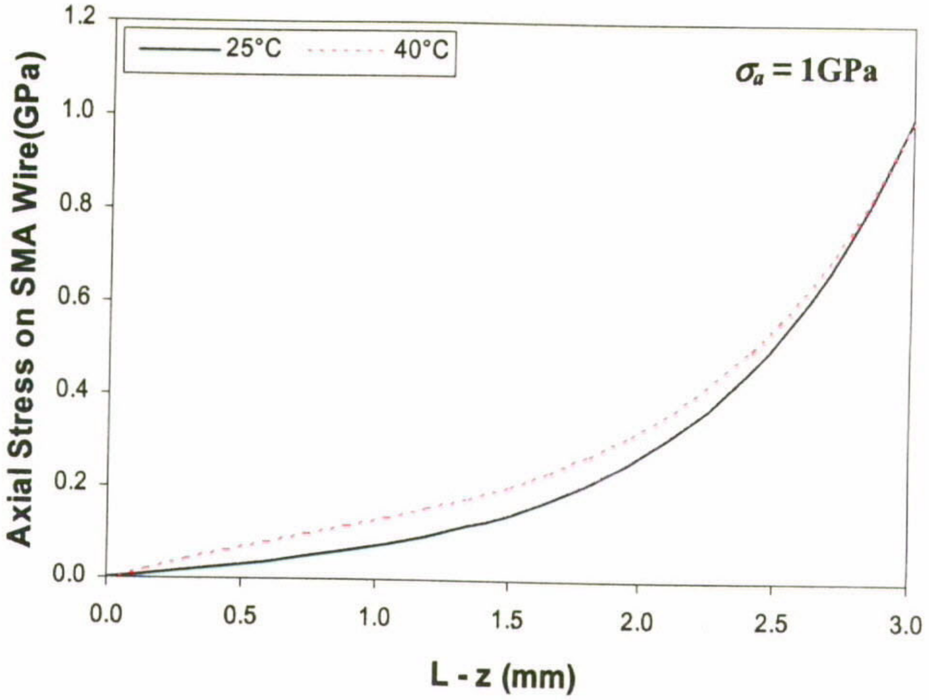

Figure 3.6 Plots of axial stress on SMA wire $\sigma_f^z(z,\sigma_a,T)$. (for σ_a = 1GPa; T = 25°C and 40°C respectively)

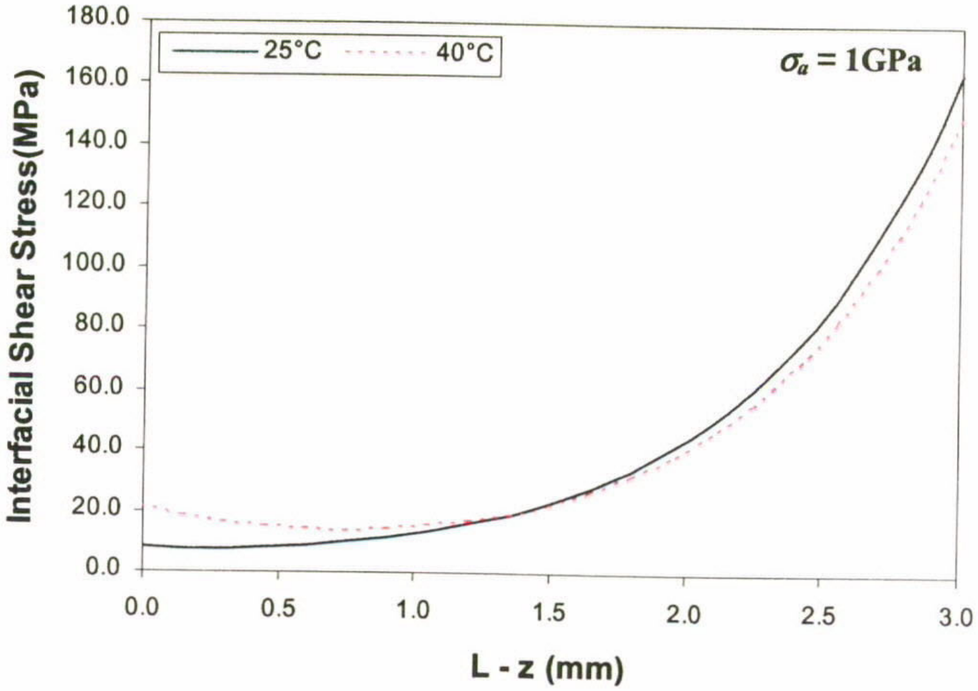

Figure 3.7 Plots of interfacial shear stress $\tau_i(z,\sigma_a,T)$. (for σ_a = 1GPa; T = 25°C and 40°C respectively)

3.4 Evolution of Internal Stresses for $T > T_{so}^A$

It should be noted that the material properties of the SMA wire and surrounding matrix remain unchanged throughout the embedded length at $T < T_{so}^A$. Therefore, referring to Eqn. 3.25 for the solution of axial stress on the SMA wire, the actuation condition '$T < T_{so}^A$' is purposely specified to ensure the validity of such stress solution with constant material properties. Although ψ_2 and ψ_4 are functions of temperature, the governing parameter ξ remains unchanged before the austenitic transformation. Therefore, the linear elastic property of the SMA is valid throughout the embedded length.

Considering the SMA-matrix cylinder model in the microscopic point of view and if the cylinder is divided into finite pieces of small elements with length $\Delta z = L/m$ as shown in Fig. 3.9, derivations of internal stresses within an element are assumed negligible. In the other words, both the internal stress and temperature are constants and hence the constant martensite fraction can be determined for any single element. As a result, the constant material properties can be substituted into Eqn 3.25 to calculate the appropriate axial stresses on the next element.

As illustrated in Fig. 3.9b, constant value of ξ_o in the 1-st element can be obtained from the initial condition of $\sigma_f^z(0, \sigma_a, T) = \sigma_a$ and actuation temperature T. Therefore the corresponding material properties of the 1-st element can be determined. Applying these information (including σ_a, T and ξ_o) into Eqn. 3.25, it is able to calculate $\sigma_f^z(z_1, \sigma_a, T) = \sigma_1$, which is the axial stress applying on the 2-nd element. Again, the values of σ_1, T and $\xi_1 = \xi(z_1, \sigma_a, T)$ in the 2-nd element can be used to predict σ_2 and so on. Equation 3.25 is then reformed into a recurrence equation as in Eqn 3.29 to predict the appropriate axial stress value for next element. If $\sigma_f^z(z_n, \sigma_a, T)$ for the n-th element is lower than $\sigma_M^s(T)$, the martensite fraction remains unchanged. However, if $\sigma_M^s(T) < \sigma_f^z(z_n, \sigma_a, T) < \sigma_M^f(T)$, the stress induced martensitic (SIM) transformation occurs and pure martensite state ($\xi =$ 1) will be attained when $\sigma_f^z(z_n, \sigma_a, T) > \sigma_M^f(T)$.

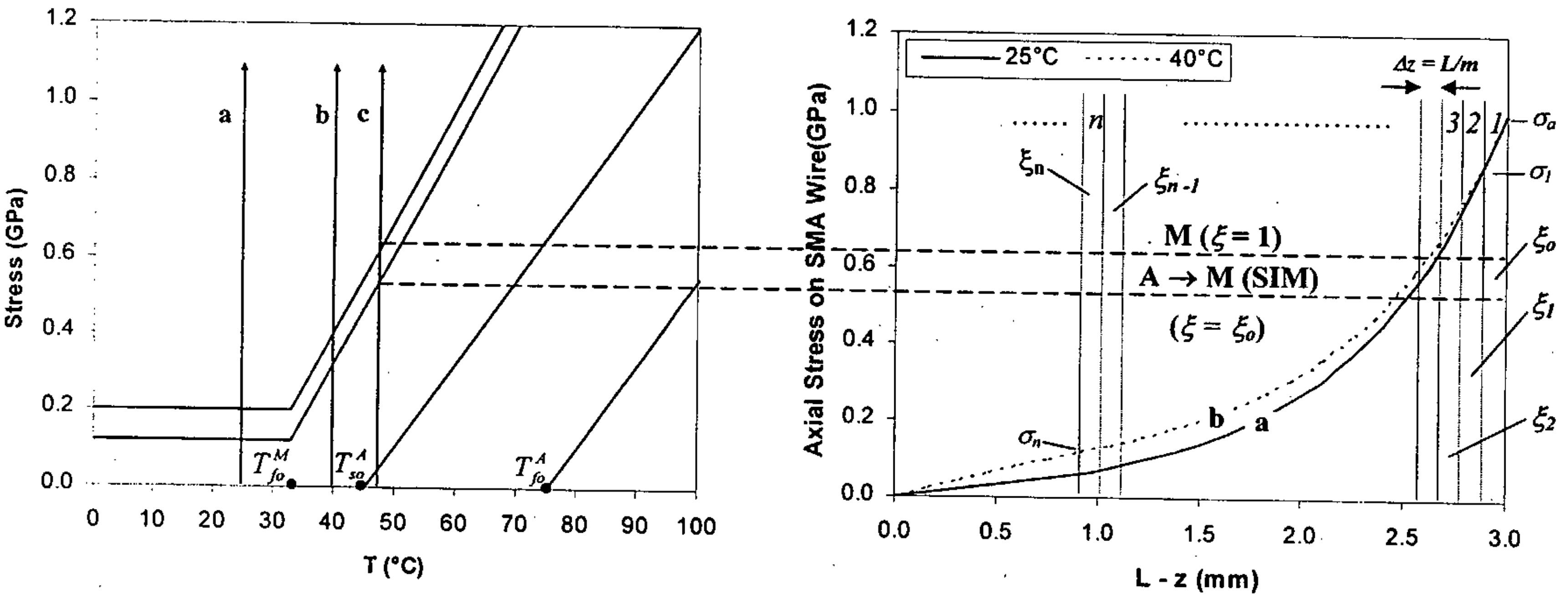

(a)

(b)

Figure 3.9 a) Illustration of different loading scenarios on phase diagram of selected SMA material. Path a: $T = T_o$ ($\xi=\xi_o$ throughout the path); Path b: $T_o<T<T^A_{so}$ ($\xi=\xi_o$ throughout the path); Path c: $T > T^A_{so}$ (ξ increase to '1'). b) Schematic illustration of parameters in recurrence relation. ('m' is the total number of elements).

3.4.1 Recurrence Relation

Applying the concept of recurrence relation described above, Eqn. 3.25 can be rewritten into following recurrence equation,

$$\sigma_f^z(z_n,\sigma_a,T)=\frac{[\psi_3(\sigma_{n-1},T)\sigma_a+\psi_4(\sigma_{n-1},T)]\sinh\left[\sqrt{\psi_1(\sigma_{n-1},T)}(L/m)\right]+(\sigma_{n-1}+\psi_3(\sigma_{n-1},T)\sigma_a+\psi_4(\sigma_{n-1},T))\sinh\left[\sqrt{\psi_1(\sigma_{n-1},T)}L(1-n/m)\right]}{\sinh\left[\sqrt{\psi_1(\sigma_{n-1},T)}L(1-(n-1)/m)\right]}$$
$$-\left(\psi_3(\sigma_{n-1},T)\sigma_{n-1}+\psi_4(\sigma_{n-1},T)\right) \tag{3.29}$$

where $\sigma_f^z(z_n,\sigma_a,T)$ (= σ_n) is the axial stress acting on the n+1th element and $z_n = n(L/m)$ for n = 1, 2...m. m is the total number of elements and controls the resolution of this stress solution.

Considering that the SMA wire is actuated prior to the application of axial load on wire end, the evolution of martensite volume fraction in z-direction should be evaluated in the following sequence:

Step - a

SMA Actuation in No-Load Condition ($\sigma_a = 0$)

(Martensite → Austenite)

For $C_A(T-T_{fo}^A) < \sigma_f^z(z_n,0,T) < C_A(T-T_{so}^A)$ and $T > T_{so}^A$

$$\xi_a(z_n,0,T)=\frac{\xi_o}{2}\left\{\cos\left[a_A\left(T-T_{so}^A-\frac{\sigma_f^z(z_n,0,T)}{C_A}\right)\right]+1\right\} \tag{3.30}$$

and $$\xi_a(z_n,0,T)=\begin{vmatrix}\xi_o & \textit{for} & \sigma_f^z(z_n,0,T)\geq C_A\left(T-T_{so}^A\right)\\ 0 & \textit{for} & \sigma_f^z(z_n,0,T)<C_A\left(T-T_{fo}^A\right)\end{vmatrix} \tag{3.31}$$

$$\xi_{sa}(z_n,0,T)=\xi_{so}-\frac{\xi_{so}}{\xi_o}(\xi_o-\xi_a(z_n,0,T)) \tag{3.32}$$

$$\xi_{Ta}(z_n,0,T)=\xi_{To}-\frac{\xi_{To}}{\xi_o}(\xi_o-\xi_a(z_n,0,T)) \tag{3.33}$$

Step - b

Axial Stress Applied on the Actuated SMA Wire

(Austenite → Martensite)

For $\sigma_{cr}{}^{s} + C_M(T\text{-}T_{so}^{M}) < \sigma_f^z(z_n, \sigma_a, T) < \sigma_{cr}{}^{f} + C_M(T\text{-}T_{so}^{M})$ and $T > T_{so}^{A}$

$$\xi_{sb}(z_n,\sigma_a,T)=\frac{1-\xi_{sa}(z_n,0,T)}{2}\cos\left\{\frac{\pi}{\sigma_{cr}^{s}-\sigma_{cr}^{f}}\left[\sigma_f^z(z_n,\sigma_a,T)-\sigma_{cr}^{f}-C_M\left(T-T_{so}^{M}\right)\right]\right\}+\frac{1+\xi_{sa}(z_n,0,T)}{2} \tag{3.34}$$

$$\xi_{Tb}(z_n,\sigma_a,T)=\xi_{Ta}(z_n,0,T)-\frac{\xi_{Ta}(z_n,0,T)}{1-\xi_{sa}(z_n,0,T)}\left[\xi_{sb}(z_n,\sigma_a,T)-\xi_{sa}(z_n,0,T)\right] \tag{3.35}$$

$$\xi_b(z_n,\sigma_a,T)=\xi_{sb}(z_n,\sigma_a,T)+\xi_{Tb}(z_n,\sigma_a,T) \tag{3.36}$$

where the total martensite volume fraction, ξ equals to $\xi_a(z_n, \sigma_a, T)$ for $\sigma_a = 0$ and $\xi_b(z_n, \sigma_a, T)$ for $\sigma_a > 0$. In step-a, ξ_a, ξ_{sa} and ξ_{Ta} represent the evolution of total, stress-induced and temperature-induced martensite volume fractions respectively on the SMA wire under zero applied stress (σ_a = 0GPa) and constant temperature ($T > T_{so}^{A}$). In according to the predefined loading scenario, external load will be applied on the SMA wire end until the constant temperature has been reached throughout the SMA wire. Therefore, $\xi_a(z_n, 0, T)$, $\xi_{sa}(z_n, 0, T)$ and $\xi_{Ta}(z_n, 0, T)$ should be considered as initial values in step-b to predict the evolution of martensite fraction due to externally applied stress σ_a. Using the boundary condition of $\sigma_f^z(0, \sigma_a, T) = \sigma_o = \sigma_a$ as an initial value in the captioned recurrence relation Eqn. 3.29, σ_n can be obtained and then substituted into Eqns. 3.30 – 3.36 to estimate the corresponding value of $\xi(z_n, \sigma_a, T)$ and hence the parameters ψ_1, ψ_2, ψ_3 and ψ_4. As a result, Eqn. 3.29 is considered as solution of axial stress for $T > T_{so}^{A}$. It has to be emphasized here that all the parameters ψ_i (i=1,2,3,4) are the complicated functions of material properties, geometric constants, externally applied stress as well as actuation temperature. Using the equilibrium condition expressed in Eqn. 3.18, solution of τ_i can be obtained by differentiating σ_f^z with respect to z as shown below,

$$\tau_i(z_n,\sigma_a,T)=\frac{-\{\psi_3(\sigma_{n-1},T)\sigma+\psi_4(\sigma_{n-1},T)\}\cosh[\sqrt{\psi_1(\sigma_{n-1},T)}(L/m)]+(\sigma_{n-1}+\psi_3(\sigma_{n-1},T)\sigma_a+\psi_4(\sigma_{n-1},T))\cosh[\sqrt{\psi_1(\sigma_{n-1},T)}L(1-n/m)]}{2\sinh[\sqrt{\psi_1(\sigma_{n-1},T)}L(1-(n-1)/m)]} \tag{3.37}$$

3.5 Stress Distributions in Constituents

3.5.1 No-Load Condition

Figures 3.10 and 3.11 illustrate the distributions of axial stress, $\sigma_f^z(z_n,0,T)$ on the SMA wire and interfacial shear stress, $\tau_f^z(z_n,0,T)$ in a no-load condition. T_o = 25°C is considered as initial temperature for both constituents. The actuation temperatures of 40°C, 60°C and 80°C are employed to compare the influence of recovery action on the internal stress distributions. Referring to Eqn. 3.17, σ_f^z and σ_m^z are linearly co-related with a constant coefficient of γ. These two stress components act in opposite directions for $\sigma_a = 0$ so as to satisfy the equilibrium requirement. It is therefore reasonable for σ_f^z and σ_m^z to have similar distribution profiles but develop with opposite sign. Therefore only the plots of $\sigma_f^z(z_n,\sigma_a,T)$ and $\tau_i(z_n,\sigma_a,T)$ are presented in this study.

According to the restrictions specified in boundary conditions, both the loading and embedded ends of the SMA wire are subjected to zero axial stress. The maximum axial stress for different actuation temperatures is found at a mid-point of embedded length,

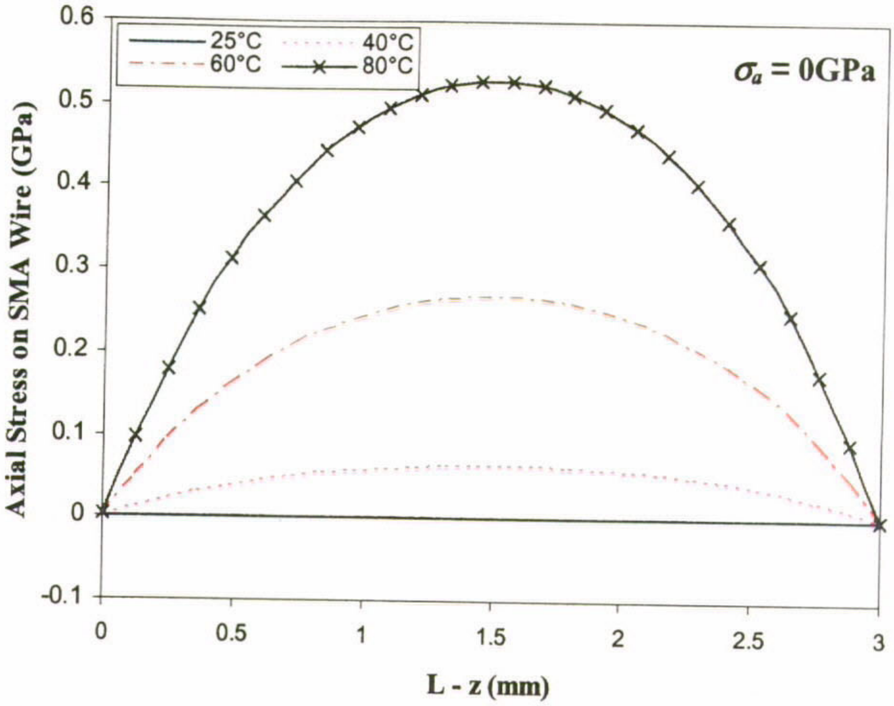

Figure 3.10 Plots of axial stress on SMA wire $\sigma_f^z(z,\sigma_a,T)$. (for σ_a = 0GPa; T = 25°C, 40°C, 60°C and 80°C respectively)

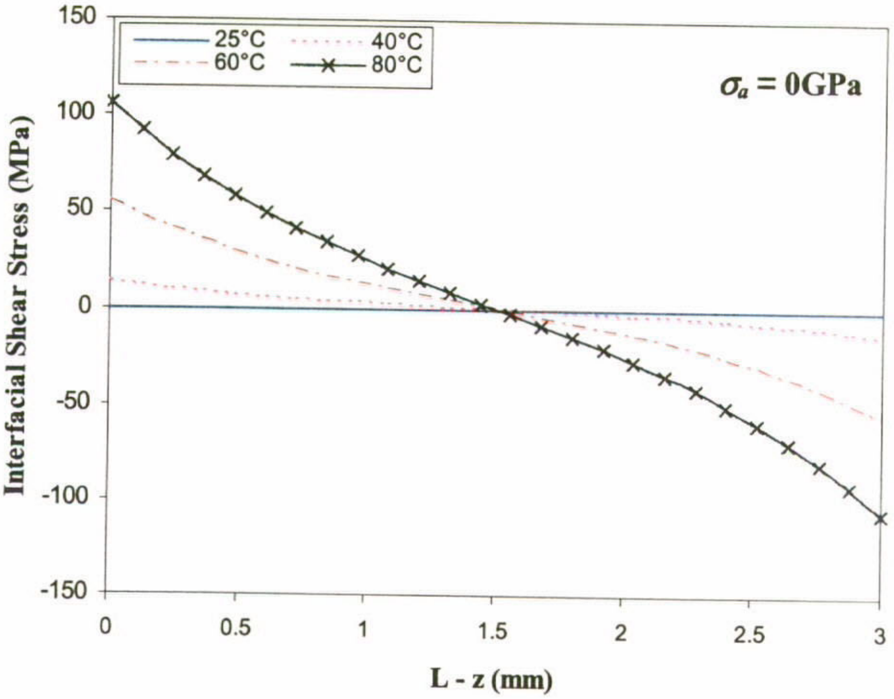

Figure 3.11 Plots of interfacial shear stress $\tau_i(z,\sigma_a,T)$. (for σ_a = 0GPa; T = 25°C, 40°C, 60°C and 80°C respectively)

which implies that the highest stress recovery due to SMA-actuation can be attained or the maximum reinforcement can be achieved at the center proportion. One may notice that the recovery action should only start when temperature is increased upon T_{so}^{A}. However due to thermal expansion of both constituents, axial stress on SMA wire is increased slightly at $T = 40^{\circ}\mathrm{C}$ ($<T_{so}^{A}$). Problem of matrix material softening due to the high actuation temperature is beyond the concern of this study. Therefore, the actuation should be restricted below the glass transition temperature of T_g (~120°C for epoxy) and a reasonable range of operation temperatures (up to 80°C) is employed to facilitate the numerical examples in this study.

Plots of the interfacial shear stress distribution in no-load condition are also shown in Fig. 3.11. When the SMA wire is heated up, increase of interfacial shear at both embedded ends can be found in the same magnitude but opposite direction. The highest magnitudes of $\tau_i(z_n, \sigma_a, T)$ at both ends diminish toward the center of embedded length. Therefore, the interfacial cracks tend to start instantaneously from the two ends while the shear stress at $z = L/2$ is always zero.

3.5.2 Constant Load Condition

It is assumed that the embedded SMA wire is firstly heated to a target temperature T and then an axial load σ_a is applied on the SMA wire end. Solution of axial stress on SMA wire obtained for the no-load condition could be used as initial condition to evaluate the influence of external load on the steadily actuated SMA-composite. Plots of $\sigma_f^z(z_n, \sigma_a, T)$ and $\tau_i(z_n, \sigma_a, T)$ for SMA-matrix cylinder subjected to a constant applied stress, $\sigma_a = 500\mathrm{MPa}$ are shown in Figs. 3.12 and 3.13. When the actuation temperature is

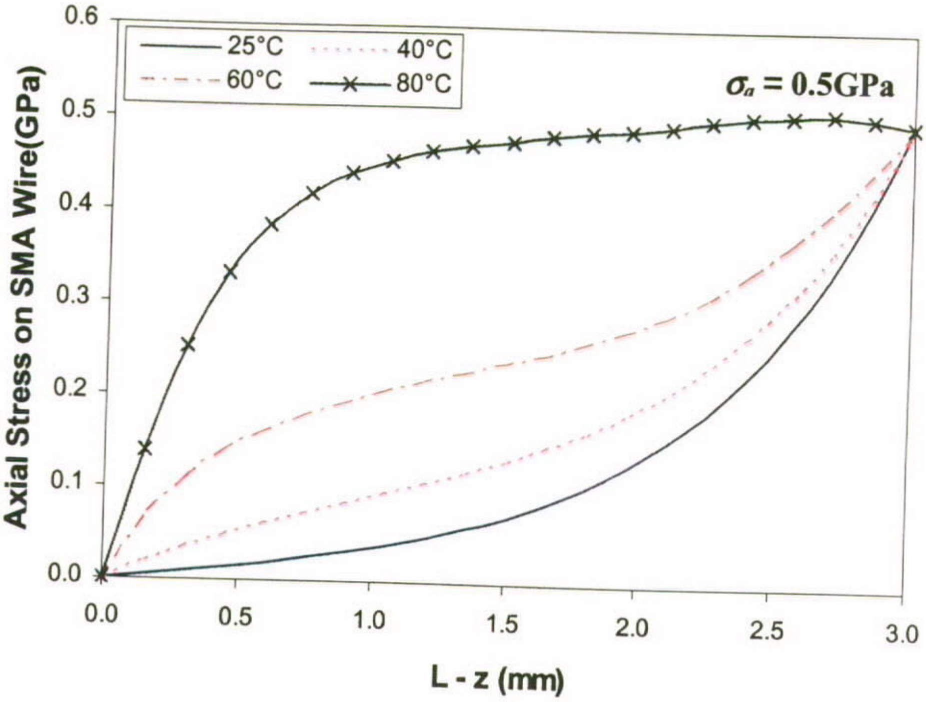

Figure 3.12 Plots of axial stress on SMA wire $\sigma_f^z(z,\sigma_a,T)$. (for $\sigma_a = 0.5$GPa; T = 25°C, 40°C, 60°C and 80°C respectively)

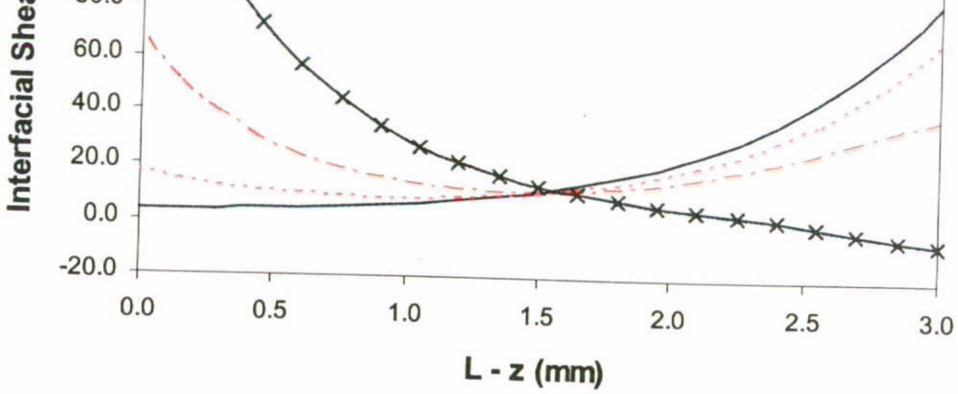

Figure 3.13 Plots of interfacial shear stress $\tau_i(z,\sigma_a,T)$. (for $\sigma_a = 0.5$GPa; T = 25°C, 40°C, 60°C and 80°C respectively)

relatively low ($T = 40^{o}C < T_{so}^{A}$), axial stress drops monotonically toward the embedded end. If the wire has been heated to a 60°C, axial stresses along the wire are generally increased except the two end points. However, when the actuation temperature is increased to 80°C, applied load cannot dominate the stress distribution. The highest axial stress still appears on the center portion ($0 < z < L$) instead of loading end ($z = 0$). Referring to Eqn. 3.18, interfacial shear stress, τ_i is found directly proportion to the slope of axial stress, σ_f^z. Therefore, any change of σ_f^z can be reflected in the solution of τ_i.

Figure 3.13 shows that the τ_i at loading end could be reduced by over 50% (from 82.2MPa to 40.4MPa) when the SMA wire has been heated from 25°C to 60°C. This moderation in interfacial shear can effectively delay the start of interfacial crack. When the actuation temperature has been further increased upon 80°C, moderation of τ_i at loading end ($z = 0$) could be increased substantially and τ_i becomes the highest at free end ($z = L$). The prediction shows a high potential for interfacial debond start at free end instead of loading end in a high actuation condition. This potential problem is therefore defined as a risk of over-actuation. When the actuation temperature is increased to a level between 40°C and 60°C, interfacial shear at both ends $\tau_i(L, \sigma_a, T)$ and $\tau_i(0, \sigma_a, T)$ should be more or less the same. In such particular situation, interfacial shear stress is moderated but can also avoid the starting of interfacial crack at free end due to over actuation. It is defined that the SMA-composite which is heated to the specific actuation temperature T_{OA}, so that the identical value of τ_i is attained at both embedded ends (i.e. $\tau_i(L, \sigma_a, T) = \tau_i(0, \sigma_a, T)$), is operated in an optimum actuation condition (OAC). If the activation temperature is higher then T_{OA}, the composite is considered as over-actuated.

As previously discussed, part of the SMA wire experiences austenitic transformation due to resistive heating. However, when the externally applied stress is relatively high ($\sigma_a > \sigma_{cr}^{s}(T)$), stress induced martensitic transformation will start in part of the SMA wire. Considering that the wire has been heated to 60°C and then an axial load of 1GPa was applied at wire end, the axial stress distribution with a 'step' change nearby the loading end can be observed in Fig. 3.14a. This change can be explained by using the phase diagram in Fig. 3.9a. If σ_a is increased to 1GPa at $T = 60$°C, the loading path passes through the $\sigma_{cr}^{s}(T)$ and $\sigma_{cr}^{f}(T)$ and eventually reaches the 100% martensite zone. Plots of σ_f^z in 58°C and 62°C actuation temperature are employed to highlight the evolution of this change. Part-pan of this sudden change is enlarged and shown in Fig. 3.14b. When $\sigma_f^z < \sigma_{cr}^{s}(T)$ for 0.25mm $< z <$ 3mm, material properties of SMA wire in this region remain unchanged and the SIM only starts until $\sigma_f^z(z, \sigma_a, T) > \sigma_{cr}^{s}(T)$ and finishes at $\sigma_{cr}^{f}(T)$. Therefore, the martensitic transformation should be completed in the range of 0mm $< z <$ 0.1mm and the material properties become constants for $z >$ 0.2mm.

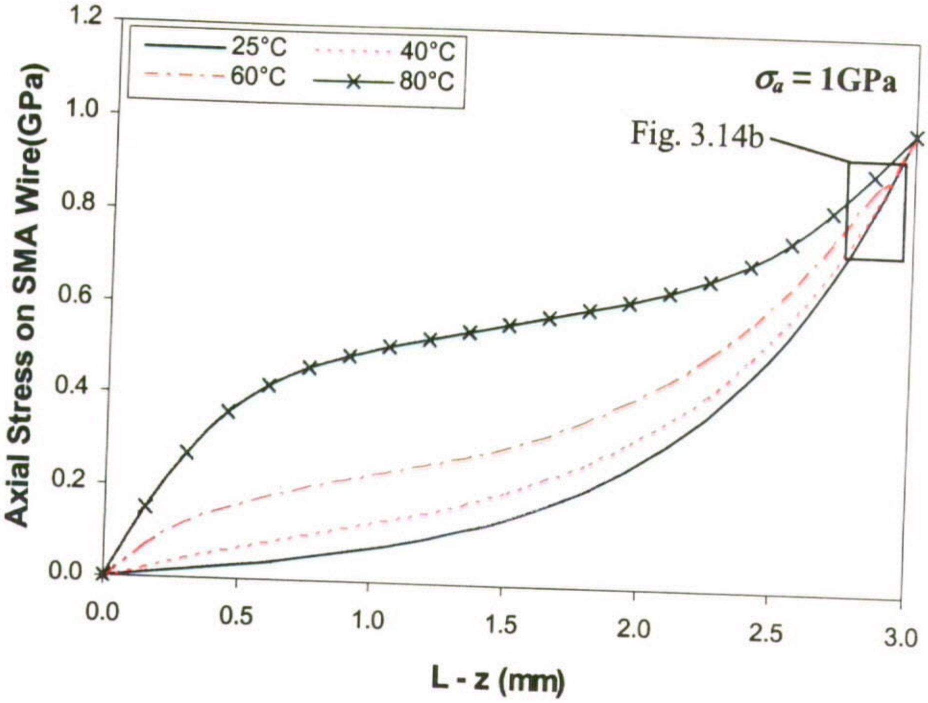

Figure 3.14a Plots of axial stress on SMA wire $\sigma_f^z(z,\sigma_a,T)$. (for σ_a = 1GPa; T = 25°C, 40°C, 60°C and 80°C respectively)

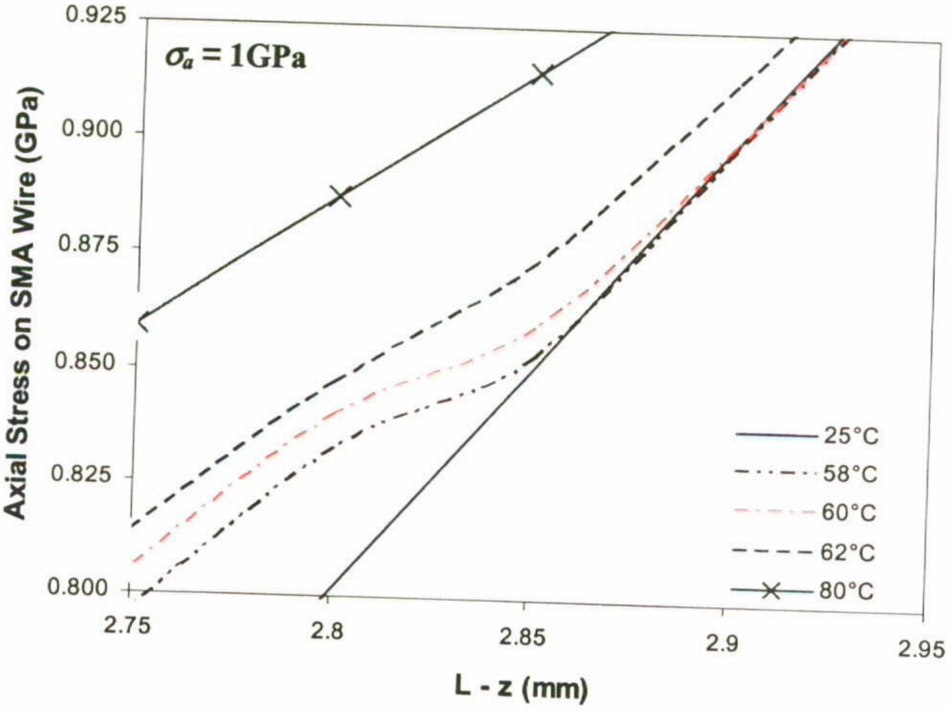

Figure 3.14b Part-pan of axial stress $\sigma_f^z(z,\sigma_a,T)$, which highlights the effect of SIM in internal stress distribution.

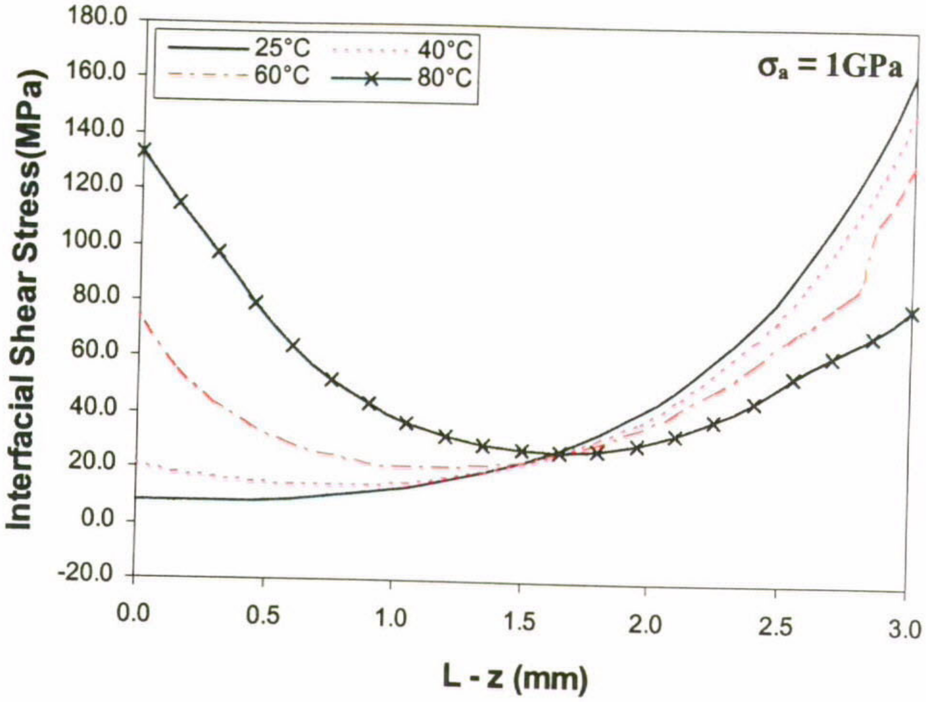

Figure 3.15 Plots of interfacial shear stress $\tau_i(z,\sigma_a,T)$. (for σ_a = 1GPa; T = 25°C, 40°C, 60°C and 80°C respectively)

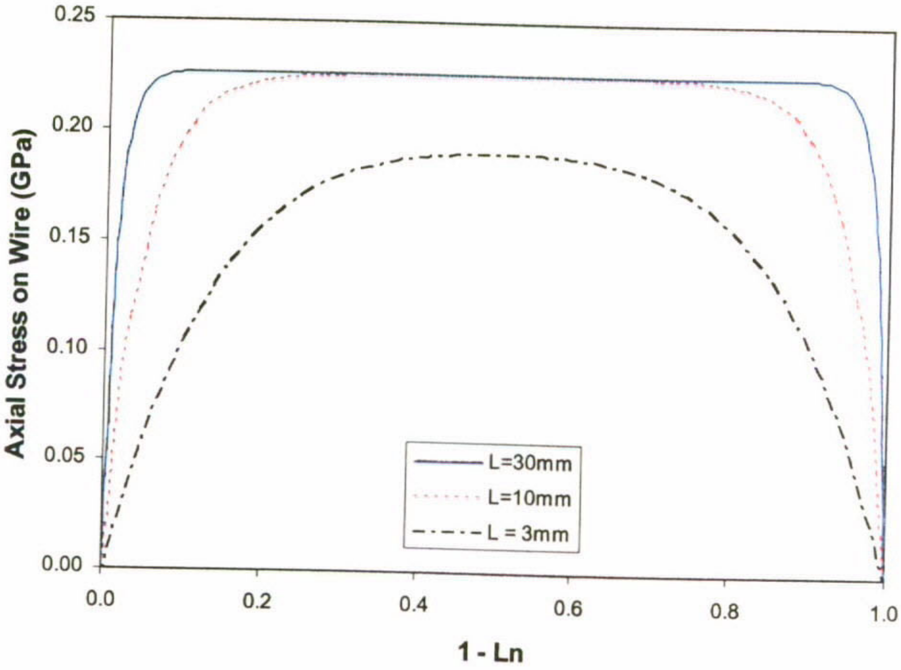

Figure 3.16 Plots of axial stress on SMA wire $\sigma_f^z(z,0,T)$, for T = 60°C; L = 3mm, 10mm and 30mm respectively. Axial stresses are saturated at 0.226GPa for long embedded length.

3.6 Constant Axial Stress Development

In order to highlight the shape memory effect on internal stress distributions, short embedded length (L = 3mm) was employed in the previous analysis. However, the stress distribution profiles have not been fully developed in such short embedded length. Considering the plots of internal stresses under actuation temperature 60°C for the L = 3mm, 10mm and 30mm respectively as shown in Fig. 3.16, where $L_n = z/L$ is the normalized embedded length employed for qualitative comparison between the plots, the results clearly indicate that when b/a = 40 and L = 30mm, a long plateau region at about 0.226GPa occupies over 80% of embedded length but only about 40% of embedded length reaches the same plateau for L = 10mm. Obviously, the one with L = 3mm can never touch the plateau. It implies that if the embedded length is long enough, maximum recovery stress on the SMA wire for the corresponding actuation temperature can be attained inside a composite and hence the stress recovery induced in the SMA can be fully utilized to improve the mechanical responses in composite structures.

Referring to the symmetric profiles obtained in Fig. 3.16, σ_f^z at $z = L/2$ should be considered as the maximum stress value. Therefore, in order to estimate the minimum required embedded length for achieving maximum axial stress inside a composite due to SMA actuation, it is crucial to evaluate the relationship between $\sigma_f^z(L/2,0,T)$ and L as illustrated in Fig. 3.17. For T = 60°C, axial stress on the SMA wire saturates at the maximum value of 0.226GPa when $L \geq$ 10mm for b/a = 40. Similarly, when the embedded length is fixed at 30mm, saturation of maximum axial stress will occur for $b/a \geq 25$ as illustrated in Fig. 3.18.

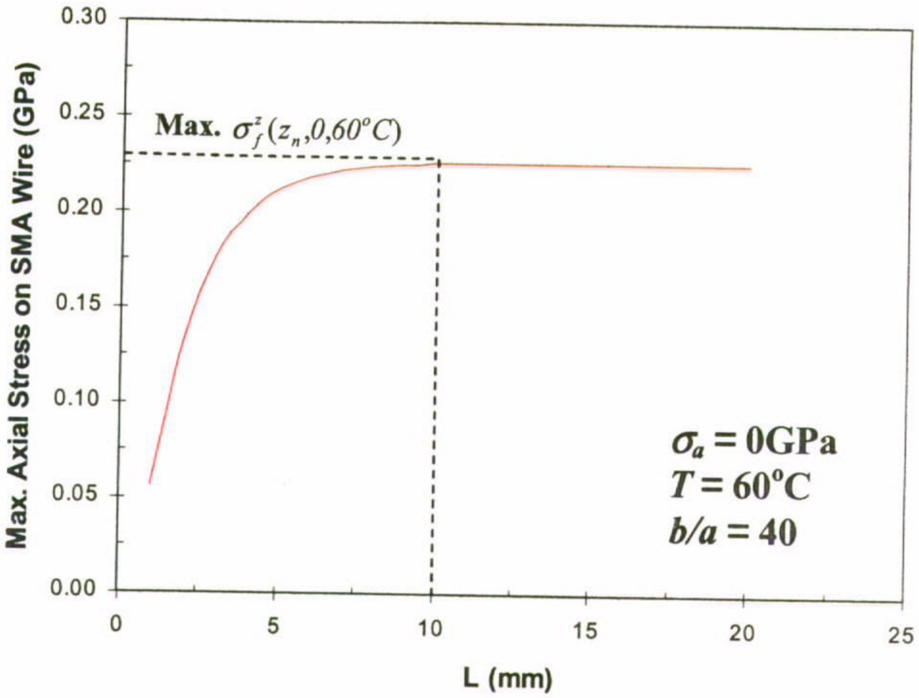

Figure 3.17 Plot of maximum axial stress on SMA wire $\sigma_f^z(L/2,0,T)$ versus against total embedded length L for b/a = 40.

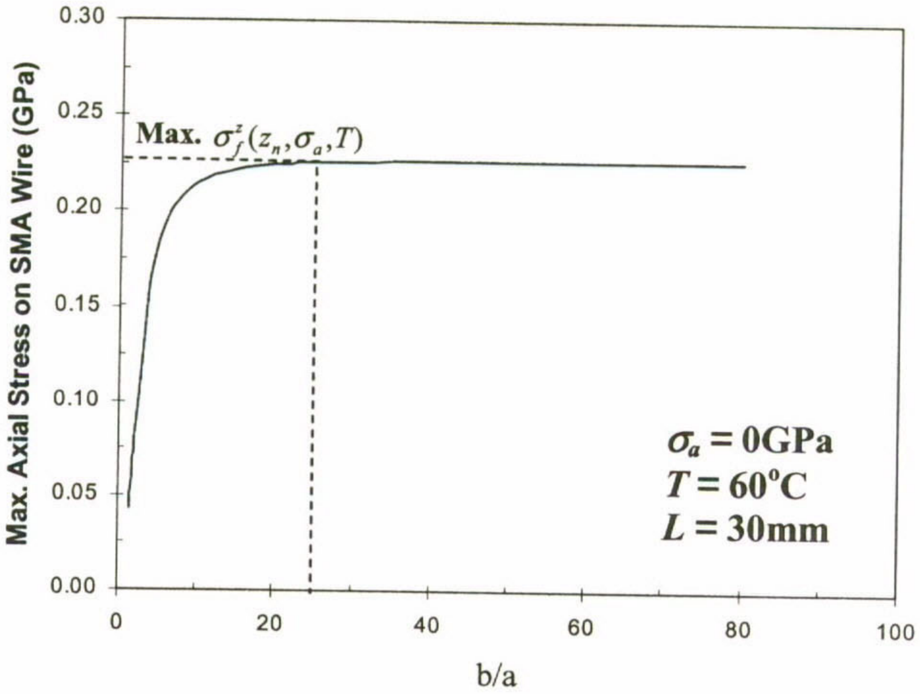

Figure 3.18 Plot of maximum axial stress on SMA wire $\sigma_f^z(L/2,0,T)$ versus against b/a ratio for L = 30mm.

3.7 Summary

In this chapter, evolution of martensite volume fraction due to SMA actuation and applied load had been predicted by using recurrence relation between axial stress and position z along the wire. This prediction clarified the SMA's material properties along the embedded length. Under the constant load condition, identical values of interfacial shear stress τ_i at two embedded ends (z = 0 and L) can be attained at the specific actuation temperature. This specific actuation mode, defined as Optimum Actuation Condition (OAC), ensures the moderation of interfacial shear at loading end and avoids interfacial debond due to over-actuation. Physical meanings and development of analytical solutions for OAC will be further discussed in Chapter 7. When the externally applied stress is higher than critical stress $\sigma_{cr}^{s}(T)$, 'step-shape' stress distribution profile is found in the solutions of σ_f^z and τ_i. This is the result of stress induced martensitic transformation (SIM) of actuated SMA wire. It should be noted that the changes of martensite volume fraction and hence the material properties due to the SIM do affect the stress transfer throughout the matrix cylinder.

In addition, effects of total embedded lengths, L and wire-matrix radius ratio, b/a on the development of maximum axial stress were also investigated. Results confirm the increase of maximum axial stress with the increase of L or b/a ratio. Also, the minimum values of these geometric constants required for achieving maximum axial stress on the SMA wire can be predicted. This prediction is particularly useful for ensuring constant internal stresses and material properties of embedded SMA can be attained. Performance of the SMA composite, after modification of its modal properties, can be determined by simply considering the constant properties of matrix and SMA inclusions only.

Chapter 4

Effect of Loading-actuation Scenarios

4.1 Introduction

This chapter focuses on the influences of loading conditions and actuation modes on evolution of material properties and internal stress distributions in SMA-reinforced composites. Despite the effects of loading-actuation scenarios on the composite structures and due to the stress transmission between the SMA wire and its surrounding matrix, it is basically impossible to achieve the so-called 'uniformly distributed' internal stresses along the SMA inclusions and matrix. For a typical SMA-composite material with the embedded prestrained SMA wires in the longitudinal direction, when a wire is subjected to an externally applied load at its embedded end, different sections of the wire are probably suffering different levels of internal stress and hence response differently to the applied temperature. Based on the specific thermomechanical properties of SMAs, the fundamental parameter – martensite volume fraction which determines the status of phase transformation, is defined as a function of stress and temperature. Both the modulus of elasticity and constrained recovery stress can be clarified by using the instantaneous values of stress-induced and temperature-induced martensite volume fractions. Changes of these relations can be simulated by using many previously proposed constitutive models; and the phase transformation temperatures that govern the start and finish of transformation processes are clearly presented in a typical phase diagram as shown in Fig. 3.5. In the other words, based on the known values of stress and temperature on a piece of SMA material, its material properties and mechanical responses are readily estimated by using those constitutive models. However, for the embedded SMA wire, internal stresses cannot be explicitly determined. Therefore, we need to clarify the coupled relation between the internal stresses and the martensite volume fractions prior the prediction of SMA's material properties and mechanical responses.

Numerous theoretical models have been proposed for the prediction of ideal prestrain values, volume ratio between wire and matrix, orientations of SMA inclusions as well as the desired actuation temperatures so as to optimize the performance of SMA-composites. For the simplicity, material properties of constituents were normally assumed as constants in the feasibility studies of SMA reinforced structures. The SMA inclusions were considered as in either purely martensitic or purely austenitic state throughout the embedded length. Using this simple idea, predictions of modal properties as well as the mechanical responses of the actuated SMA-composites have been reported in numerous literatures in the past decade.

Due to the different application purposes, composite structures are probably subjected to different types of mechanical loadings. Three types of typical loading conditions are therefore identified and applied on the SMA-matrix cylinder model in order to study their influences on internal stress distributions. Obviously, when the embedded SMA wire is subjected to constant actuation, axial stress on the SMA wire should not be a constant even for the no-load condition. Therefore, martensite volume fraction could be changed along the embedded length at different loading conditions.

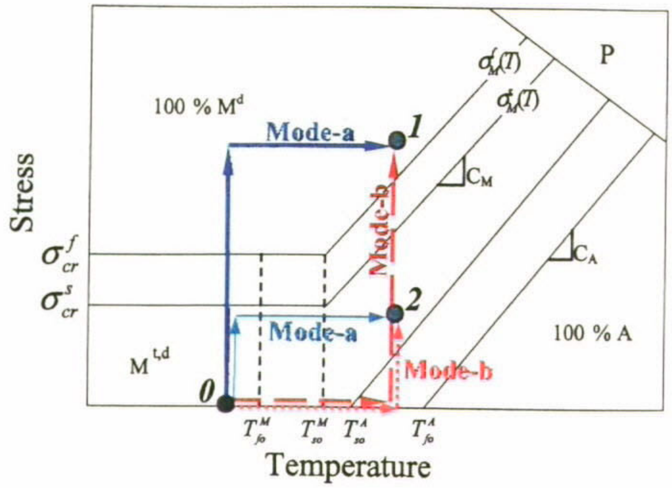

Figure 4.1 Two possible loading-actuation scenarios for the applications of SMA-composites. (Mode-a: Loaded then actuate; Mode-b: Actuated then load)

Referring to the loading-actuation paths (Mode-a and Mode-b) as shown in Fig. 4.1, the total martensite volume fraction ξ must be equal to 1 at destination point 1. However, values of ξ are definitely not the same at point 2 for different loading and actuation sequences. Therefore, except loading conditions, sequence of loading and actuation can also influence the effectiveness of phase transformations in SMA and hence the mechanical responses can be totally different.

4.2 Effect of Loading Conditions on Internal Stress Distribution

4.2.1 Typical Loading Conditions

Depending on the application requirements, there are many possible loading methods which may lead to the failure of composite structures. Therefore, it is crucial to study the influences of typical pull-out loading conditions on the internal stress development inside a composite. With the knowledge on this critical issue can help to

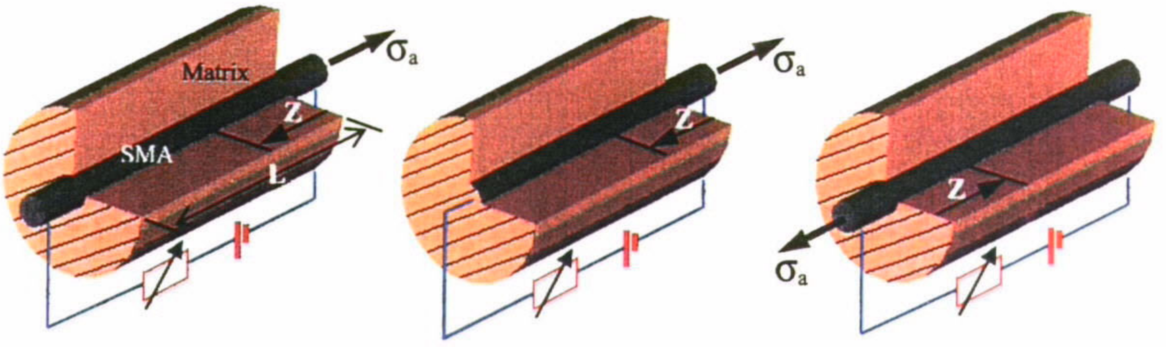

(a) (b) (c)

Figure 4.2 Schematics of pull-out loading conditions for the SMA-matrix cylinders. a) Type I: the fixed matrix bottom, b) Type II: the fixed matrix and SMA wire bottom and c) Type III: the restrained matrix top.

decide an appropriate configuration for experimental study of interfacial properties, such as the required size of fiber-matrix specimens and the ideal loading method. Especially for a composite hybridized with functional materials – shape memory alloys, which is usually designed for tackling several specific engineering requirements, evolution of material properties and the effectiveness of SMA actuation can be directly affected by the loading conditions. Therefore, it is necessary to clarify the influence of loading methods on stress development in the constituents which in turn control the mechanical response of the actuated SMA and the debond stresses. Three types of typical loading methods have been identified as shown in Fig. 4.2. Both types I and II have a free matrix top at the loading side while it has been restrained for type III. Doubtlessly, the type I and type II loading conditions are more appropriate to be employed for describing the condition when a matrix crack propagates in the perpendicular direction of wire-matrix interface. However, type III is frequently used in fiber pull-out tests for traditional fiber-matrix composites. Therefore, there is an urged need to clarify the requirements that ensures the validity of type III loading condition being used in experimental studies with the SMA actuation. In this chapter, it is assumed that the SMA-matrix cylinder model is subjected to a constant axial stress on wire's end before actuation unless otherwise specified.

Figure 3.1 shows the type I loading condition being used to study the internal stress evolutions in the constituents. Therefore, Eqns. 3.25 to 3.28 should be considered as solutions of internal stresses for $T < T_{so}^A$ and $\sigma_a < \sigma_M^s(T)$. However due to the differences in loading methods, equilibrium condition Eqn. 3.17 is only valid for type I and II. It has to be changed for type III as given below

$$\gamma\sigma_f^s(z,\sigma_a,T)+\sigma_m^s(z,\sigma_a,T)=0 \qquad (4.1)$$

Substituting Eqns. 3.17 and 4.1 into 3.16 for types I&II and type III loading methods respectively, the second order differential equations for axial stress on the SMA wire are obtained as

$$\sigma_f^{s''}(z,\sigma_a,T)=\psi_1(z,\sigma_a,T)\sigma_f^s(z,\sigma_a,T)+\psi_1(z,\sigma_a,T)\psi_3(z,\sigma_a,T)\sigma_a+\psi_2(z,\sigma_a,T) \qquad (4.2)$$

for types I and II, and

$$\sigma_f^{s''}(z,\sigma_a,T)=\psi_1(z,\sigma_a,T)\sigma_f^s(z,\sigma_a,T)+\psi_2(z,\sigma_a,T) \qquad (4.3)$$

for type III. Referring to the loading methods specified in Fig. 4.2, boundary conditions for the corresponding types of loading are readily identified and summarized in Table 4.1. Applying these boundary conditions into Eqns. 4.2 and 4.3, solutions of axial stresses and shear stresses on constituents and at interface are given by

$$\sigma^z_{f2}(z,\sigma_a,T)=\frac{(\psi_4(T)+\psi_3\sigma_a+\sigma_a)\cosh\sqrt{\psi_1(T)}(L-z)}{\cosh\sqrt{\psi_1}L}-(\psi_4(T)+\psi_3\sigma_a) \tag{4.4}$$

$$\sigma^z_{m2}(z,\sigma_a,T)=-\gamma(\psi_4(T)+\psi_3\sigma_a+\sigma_a)\left\{\frac{\cosh\sqrt{\psi_1}(L-z)}{\cosh\sqrt{\psi_1}L}-1\right\} \tag{4.5}$$

$$\tau_{m2}(z,\sigma_a,T)=\frac{\gamma(b^2-r^2)\sqrt{\psi_1}}{2r}\frac{\left[\left(\psi_4(T)+\psi_3\sigma_a+\sigma_a\right)\sinh\sqrt{\psi_1}(L-z)\right]}{\cosh\sqrt{\psi_1}L} \tag{4.6}$$

$$\tau_{i2}(z,\sigma_a,T)=\frac{a\sqrt{\psi_1}}{2}\frac{\left[\left(\psi_4(T)+\psi_3\sigma_a+\sigma_a\right)\sinh\sqrt{\psi_1}(L-z)\right]}{\cosh\sqrt{\psi_1}L} \tag{4.7}$$

for type II and

$$\sigma^z_{f3}(z,\sigma_a,T)=\frac{(\psi_4(T)+\sigma_a)\sinh\sqrt{\psi_1}(L-z)+\psi_4(T)\sinh\sqrt{\psi_1}z}{\sinh\sqrt{\psi_1}L}-\psi_4(T) \tag{4.8}$$

$$\sigma^z_{m3}(z,\sigma_a,T)=-\gamma\left[\frac{(\psi_4(T)+\sigma_a)\sinh\sqrt{\psi_1(T)}(L-z)+\psi_4(T)\sinh\sqrt{\psi_1}z}{\sinh\sqrt{\psi_1}L}-\psi_4(T)\right] \tag{4.9}$$

$$\tau_{m3}(z,\sigma_a,T)=\frac{\gamma(b^2-r^2)\sqrt{\psi_1}}{2r}\frac{\left[\left(\psi_4(T)+\sigma_a\right)\cosh\sqrt{\psi_1}(L-z)-\psi_4(T)\cosh\sqrt{\psi_1}z\right]}{\sinh\sqrt{\psi_1}L}, \tag{4.10}$$

$$\tau_{i3}(z,\sigma_a,T)=\frac{a\sqrt{\psi_1}}{2}\frac{\left[\left(\psi_4(T)+\sigma_a\right)\cosh\sqrt{\psi_1}(L-z)-\psi_4(T)\cosh\sqrt{\psi_1}z\right]}{\sinh\sqrt{\psi_1}L} \tag{4.11}$$

for type III. It should be noted that Eqns. 4.4 to 4.11 represent the solutions of internal stress distributions for $T < T^A_{so}$ only. Recalling the discussion in Section 3.4 for the evolution of material properties and mechanical responses of the embedded SMA wires, Eqns. 4.4 and 4.8 have to be rewritten into the following recurrence equations,

$$\sigma_{f2}^{z}(z_n,\sigma_a,T)=\frac{(\psi_4(\sigma_{n-1},T)+\psi_3(\sigma_{n-1},T)\sigma_a+\sigma_{n-1})\cosh\sqrt{\psi_1(\sigma_{n-1},T)}L(1-n/m)}{\cosh\sqrt{\psi_1(\sigma_{n-1},T)}L(1-(n-1)/m)}-(\psi_4(\sigma_{n-1},T)+\psi_3(\sigma_{n-1},T)\sigma_a) \tag{4.12}$$

$$\sigma_{f3}^{z}(z_n,\sigma_a,T)=\frac{(\psi_4(\sigma_{n-1},T)+\sigma_a)\sinh\sqrt{\psi_1(\sigma_{n-1},T)}L(1-n/m)+\psi_4(\sigma_{n-1},T)\sinh\sqrt{\psi_1(\sigma_{n-1},T)}(L/m)}{\sinh\sqrt{\psi_1(\sigma_{n-1},T)}L(1-(n-1)/m)}-\psi_4(\sigma_{n-1},T) \tag{4.13}$$

Here, Eqns. 4.12 and 4.13 reproduce the evolutions of axial stresses on the embedded SMA wires in type II and III loading conditions respectively. The parameter n represents the *n*-th element in *z*-direction and m is the number of elements which controls the resolution of the predicted results. As illustrated in Fig. 4.1 for the possible actuation modes of the SMA-composites, substantial difference in the internal stress evolutions may be obtained for the same type of loading condition but different mode of actuation. In order to highlight the influence of loading methods in the current section, the SMA wires are assumed to be subjected to a constant applied load prior to the SMA actuation.

4.2.2 Evaluation of SMA's Material Properties

4.2.2.1 Evolution of Martensite Volume Fraction

Substituting $\sigma_{f1}^{z}(z_n,\sigma_a,T)$, $\sigma_{f2}^{z}(z_n,\sigma_a,T)$ and $\sigma_{f3}^{z}(z_n,\sigma_a,T)$ into Eqns. 3.30 to 3.32 for type I, II and III loading methods respectively and using a constant value of σ_a ($\neq 0$), evolutions of martensite volume fraction ξ_{1a}, ξ_{2a} and ξ_{3a} can be estimated. Since the recovery action of embedded SMA could be restricted by its surrounding matrix, stiffness of matrix is certainly taking an important role in the effectiveness of stress transmission in constituents. Depending on the design purposes, prestrained SMA is sometimes embedded into an elastomeric material with modulus of elasticity E_m = 5.51MPa [88] for shape change control or sometimes employed as an actuator inside a hard substrate (Aluminum) with E_m = 69GPa [90] so as to achieve structural reinforcement. Epoxy is the typical matrix material for composite structure and its modulus of elasticity is normally around 2 to 4 GPa. Therefore the parametric studies with E_m = 0.1GPa and 2.3 GPa are considered in the plots of martensite volume fraction against L-z in Figs. 4.3 to 4.5 in order to demonstrate the effect of matrix stiffness on phase transformation of the embedded SMA.

Plots a and b in Fig. 4.3 highlight the influence of externally applied load, σ_a on evolution of total martensite volume fraction, ξ with E_m = 0.1GPa while the results for E_m = 2.3GPa are shown in plots c and d in Fig. 4.3 to 4.5. Considering Fig. 4.3 for type-I loading method and mode-a actuation (Ia-condition), due to the austenitic phase transformation at high temperature, the decreases of ξ with the increase of the temperature can be generally observed in all four plots. Although recovery force can also be generated in low actuation levels ($T_o < T < T_{so}^A$), phase transformation will not start and ξ remains unchanged for 40°C in all cases. This recovery action is in fact the result of thermal expansion instead of austenitic transformation. Therefore, the changes of ξ will only start at $T > T_{so}^A$. When T = 60°C, ξ decreases to 0.5 and 0.65 at free end ($z = L$) and loading end ($z = 0$) respectively, while the ξ is reduced to 0.82 only at around the center portion. The reason for having this uniformly distributed martensite volume fraction is the fact of uneven stress distribution in different loading conditions. Both the

Table 4.1 Boundary conditions for type-I, II and III loading conditions

Type I	**Type II**	**Type III**
$\sigma_f^z(0,\sigma_a,T)=\sigma_a$ $\sigma_f^z(L,\sigma_a,T)=0$ $\sigma_m^z(0,\sigma_a,T)=0$	$\sigma_f^z(0,\sigma_a,T)=\sigma_a$ $\sigma_m^z(0,\sigma,T)=0$	$\sigma_f^z(0,\sigma_a,T)=\sigma_a$ $\sigma_f^z(L,\sigma_a,T)=0$ $\sigma_m^z(0,\sigma_a,T)/\gamma=-\sigma_a$

boundary condition and matrix stiffness govern the stress development in constituents. For example, at the free end ($z = L$) in type-I loading condition, austenitic transformation will always start and finish at T_{so}^A and T_{fo}^A. Referring to the phase diagram as shown in Fig. 3.8a, when $\sigma_a = 0$ GPa and $T = 60°\mathrm{C}$ ($= (T_{so}^A + T_{fo}^A)/2$), 50% of original quantity of martensite should transform to austenite. Similarly, since the loading end ($z = 0$) is continuously subjected to an axial stress 0.1GPa, the austenitic start and finish temperature will shift to 49.6°C and 79.6°C respectively. As a result, the value of ξ at $z = 0$ is reasonably reduced to 0.65 instead of 0.5 as illustrated in Fig. 4.3a.

In addition, since the recovery action is restricted by matrix cylinder, the temperature induced recovery stress is then increased at center portion. The austenitic phase transformation is resisted by its self-recovery action and only a small amount of martensite can change to austenite. It is for sure that the ability of M→A transformation in the embedded proportion can be improved by using higher actuation temperature. But this improvement for a composite with hard substrate is relatively poor as indicated in Figs. 4.3c and d with $E_m = 2.3$ GPa. Referring to the plots for 60°C and 80°C, one may notice that the values of ξ are relatively consistence along the embedded length. However the reduction of ξ is much lower than that in the case with soft matrix even for the same actuation temperature. This observation convinces the possibility of the SMA wire to attain constant material properties over the embedded proportion and the maximum value of ξ under actuation can be difference for different matrix materials.

It should be noticed that only the free end point can exhibit phase transformation effectively while the relatively high axial stress loading side ($0 < z < L/2$) resist the transformation. Therefore, the profile of ξ-distribution is not symmetric about the center point ($z = L/2$) but shifts slightly toward the loading end.

Figure 4.3b shows the distributions of ξ in SMA-matrix cylinder with $\sigma_a = 0.5$GPa and $E_m = 0.1$GPa. The axial stress on the SMA wire is too high to start austenitic transformation at loading end. Therefore, ξ remains unchanged at the loading side and starts to decrease monotonically until $L - z < 6$mm. Due to stress free requirement at $z = L$, although the applied stress is four times higher than that in plots a and c of Fig. 4.3, ξ is reduced to 0.5 again at 60°C. Similarly, purely austenitic state can be reached at free end for $T = 80$°C. Constant values of ξ for $T = 60$°C and 80°C at center portion of embedded length can be observed as shown in Fig. 4.3d. Comparing the plots between Figs. 4.3c and d, the two plots exhibit the same profile on the free end side. Since the hard substrate ensures the effective stress transmission between the SMA wire and matrix, the applied load on the wire can be transmitted to the matrix effectively. As a result, effect of axial load on phase transformation is not significant at free end side.

Figures 4.4 and 4.5 present the ξ distributions in type-II and III loading methods respectively. Theoretical predictions for type-III loading and mode-a actuation (IIIa-condition) are more or less the same as those in Fig. 4.3 for the similarity between type-I and III loading methods. Substantial difference of ξ distributions can be observed in Fig. 4.4. Based on the fixed wire and matrix bottom ends requirement, the highest axial stress arising from SMA actuation appears at $z = L$. As a result, in a low-load condition (Figs. 4.4a and c), the austenitic phase transformation can take place effectively at loading end instead of embedded end. Therefore, ξ drops to 0 at z = 0 while it maintains at 0.65 at $z = L$. If the SMA wires were pre-loaded to σ_a = 0.5GPa and then heated to 60°C (Figs. 4.4b and d), both the embedded and loading ends are subjected to high axial stress. As a result, phase transformation temperatures are increased and only small amount of martensite at embedded end can change to austenite.

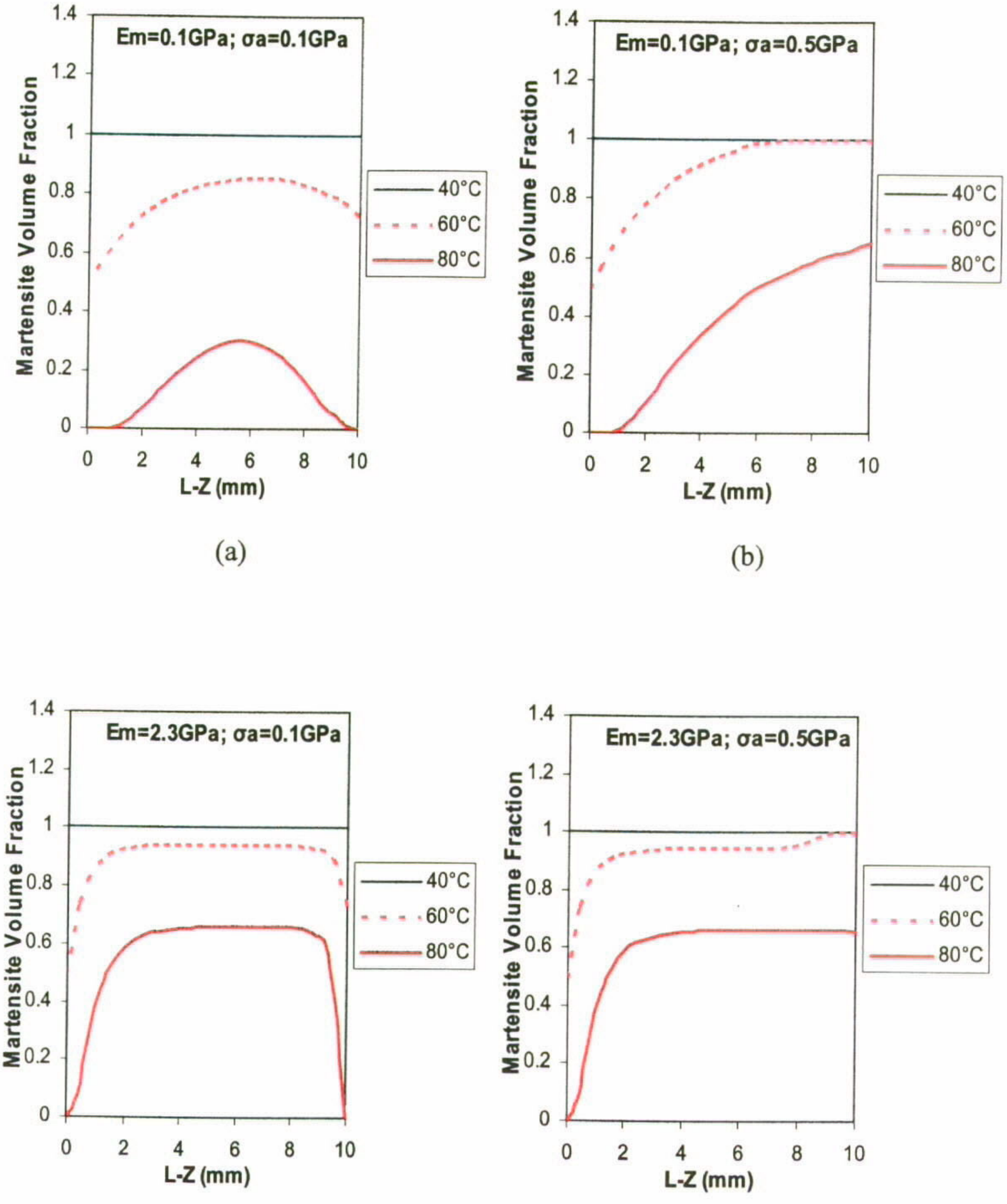

(a) (b)

(c) (d)

Figure 4.3 Evolutions of martensite volume fraction on the embedded SMA wire in type-I loading condition and mode-a actuation. a) $E_m = 0.1\text{GPa}$ and $\sigma_a = 0.1\text{GPa}$; b) $E_m = 0.1\text{GPa}$ and $\sigma_a = 0.5\text{GPa}$; c) $E_m = 2.3\text{GPa}$ and $\sigma_a = 0.1\text{GPa}$ and d) $E_m = 2.3\text{GPa}$ and $\sigma_a = 0.5\text{GPa}$.

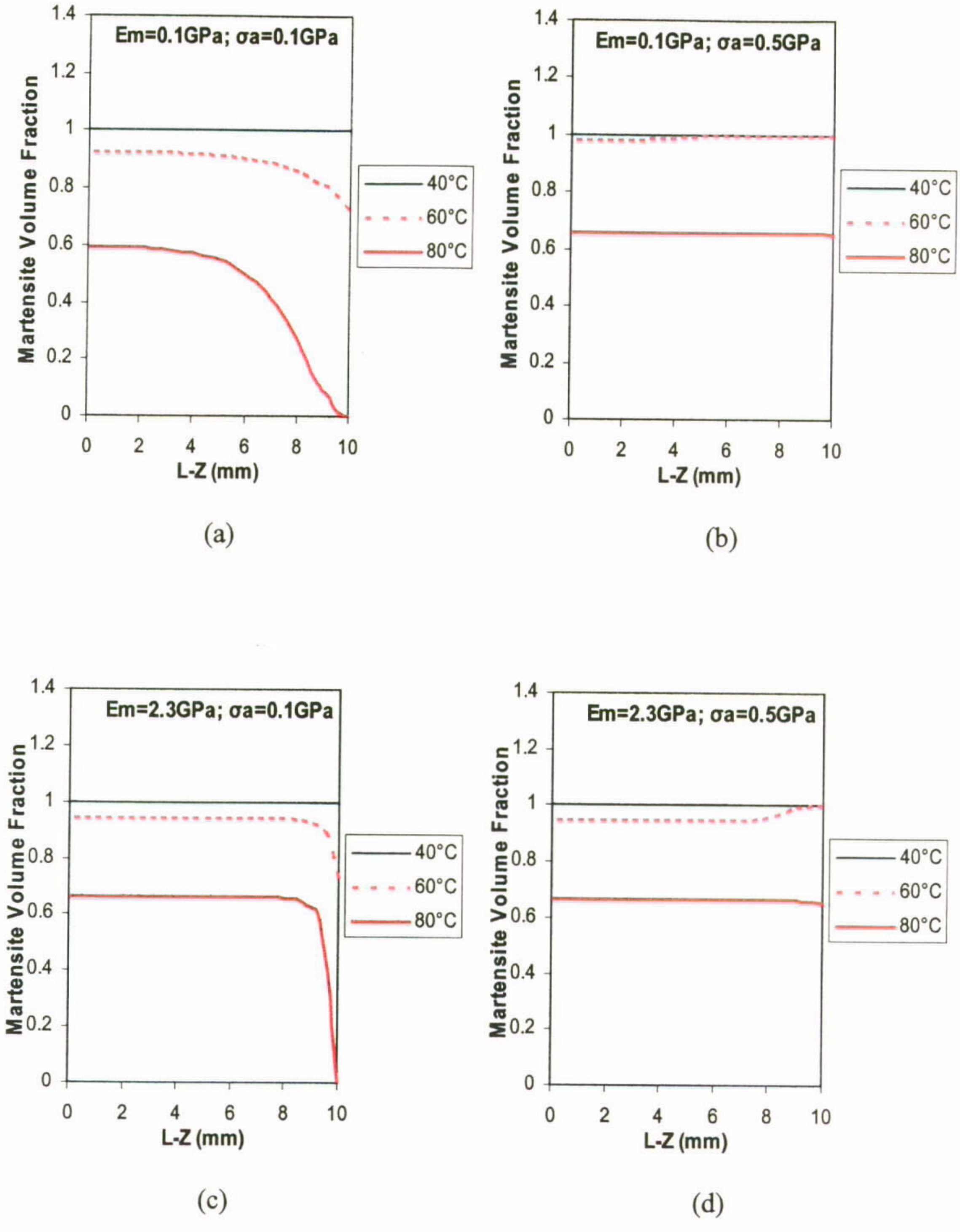

(a) (b)

(c) (d)

Figure 4.4 Evolutions of martensite volume fraction on the embedded SMA wire in type-II loading condition and mode-a actuation. a) E_m = 0.1GPa and σ_a = 0.1GPa; b) E_m = 0.1GPa and σ_a = 0.5GPa; c) E_m = 2.3GPa and σ_a = 0.1GPa and d) E_m = 2.3GPa and σ_a = 0.5GPa.

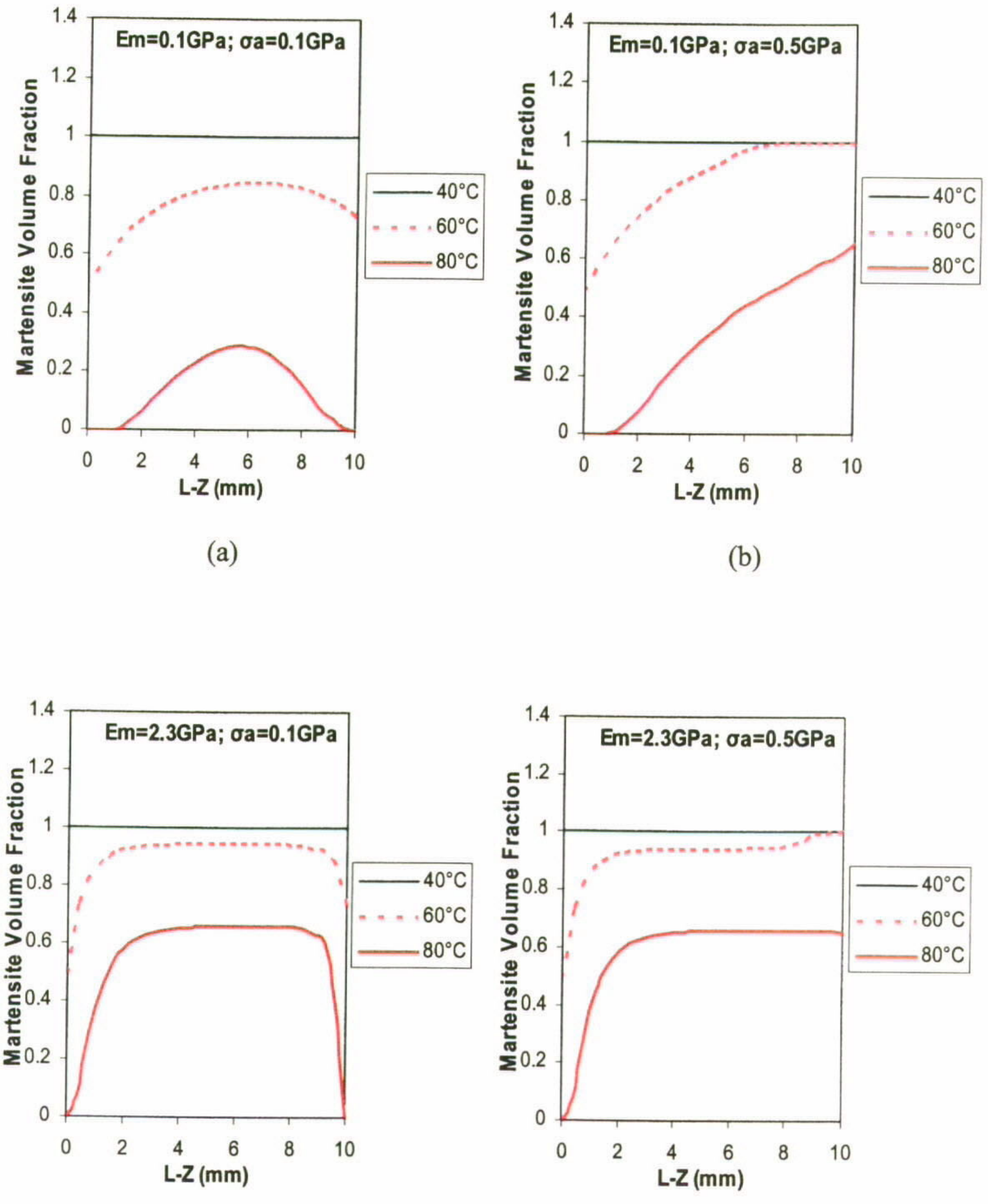

(a) (b)

(c) (d)

Figure 4.5 Evolutions of martensite volume fraction on the embedded SMA wire in type-III loading condition and mode-a actuation. a) E_m = 0.1GPa and σ_a = 0.1GPa; b) E_m = 0.1GPa and σ_a = 0.5GPa; c) E_m = 2.3GPa and σ_a = 0.1GPa and d) E_m = 2.3GPa and σ_a = 0.5GPa.

4.2.2.2 Evolution of Modulus of Elasticity

It is emphasized here that the modulus E_f given in Eqn. 3.11 is assumed to be a linear function of the martensite volume fraction in the Tanaka [1] and Liang and Rogers [2] as well as Brinson's [3] constitutive models. Based on the proposed recurrence relation for evolutions of martensite volume fraction, distributions of modulus E_f along the SMA wire for types I, II and III loading conditions are readily determined by substituting ξ_{1a}, ξ_{2a} and ξ_{3a} into Eqn 3.11.

Plots of E_{f1a}, E_{f2a} and E_{f3a} are shown in Figs. 4.6, 4.7 and 4.8 respectively. They reproduce the actual status of embedded SMA wire in different conditions of loading and actuation. Due to the linear relation between E_f and ξ, it is not surprise for E_f plots having similar distribution profile as ξ in different temperatures. Figure 4.6 shows the E_f-distribution in Ia-condition. Since austenitic phase transformation occurs effectively at the two embedded ends in low-load condition (σ_a = 0GPa) and also the modulus of SMA in austenite state is much higher than that in martensite state (E_A = 40GPa and E_M = 20GPa), the plots of E_f distribution are the curves opening upward. This implies that the embedded SMA wire may not be stiffened effectively especially for the composite with hard substrate. Considering the plots in Fig. 4.6a and 4.6c, when T = 80°C, modulus E_f can be increased to 32GPa at $z = L/2$ for E_m = 0.1GPa while it can only be raised to 25GPa for E_m = 23GPa. In terms of modal properties improvement, effectiveness of SMA actuation is definitely rely on the matrix stiffness. Figures 4.6a and b show the plots for σ_a = 0.5GPa. When E_m = 0.1GPa, modulus E_f at T = 80°C decreases monotonically toward the loading end. However, if the wire has been heated to 60°C, first half of the embedded wire remains soft with E_f = E_M = 20GPa and start to be stiffened until $L - z < 6$mm. Similar results including a long plateau can be observed in Fig. 4.6d. It implies that the SMA wire is relatively difficult to exhibit austenitic phase transform when it is embedded inside a hard substrate. Similarly, Figs. 4.7 and 4.8 show the predictions of E_f evolution in IIa and IIIa conditions. Changes of E_{f1a} and E_{f2a} distributions can be explained from the corresponding ξ evolutions.

As previously discussed for the prediction of mechanical responses of the SMA-reinforced composites, modulus of elasticity of SMA inclusions is normally assumed to be uniformly distributed inside the matrix. Based on the proposed recurrence relations in this study, plots of E_f distributions presented in Figs. 4.6 to 4.8 strongly disagree with that assumption. However, both ξ and E_f evolution plots demonstrate the possibility for attaining plateau states in some specific configurations. It motivates the study of appropriate geometric relations between constituents for achieving constant material properties of SMA inside a composite. It is crucial to emphasis here that even though the constant SMA properties can be attained, the values of ξ and E_f inside a composite should always be lower than those predicted for a SMA wire without embedment. It is due to the recover stress developed in strain-constrained condition inside a composite that increases the phase transformation temperatures.

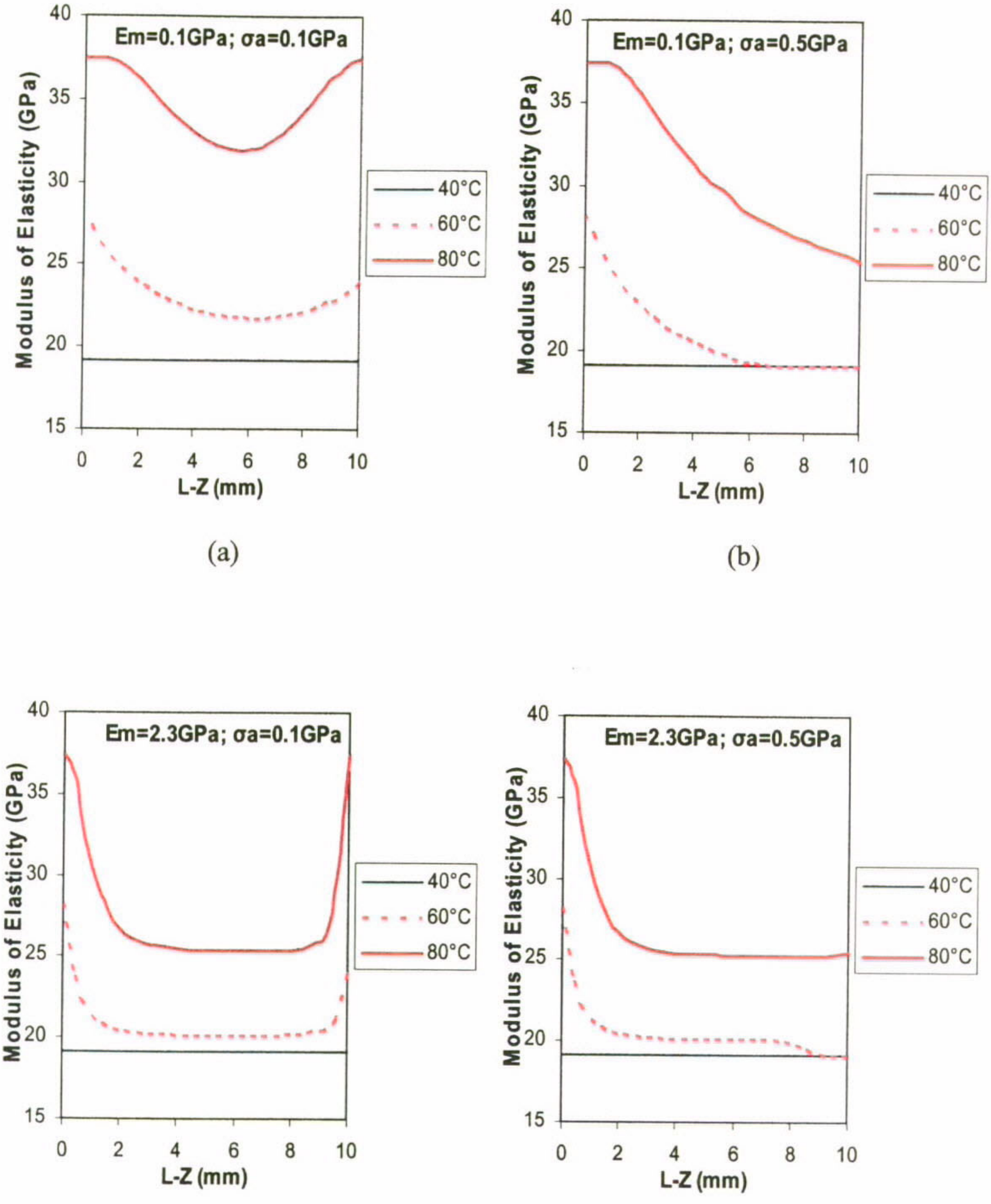

(a) (b)

(c) (d)

Figure 4.6 Evolutions of modulus of elasticity of the embedded SMA wire in type-I loading condition and mode-a actuation, E_{f1a}. a) $E_m = 0.1$GPa and $\sigma_a = 0.1$GPa; b) $E_m = 0.1$GPa and $\sigma_a = 0.5$GPa; c) $E_m = 2.3$GPa and $\sigma_a = 0.1$GPa and d) $E_m = 2.3$GPa and $\sigma_a = 0.5$GPa.

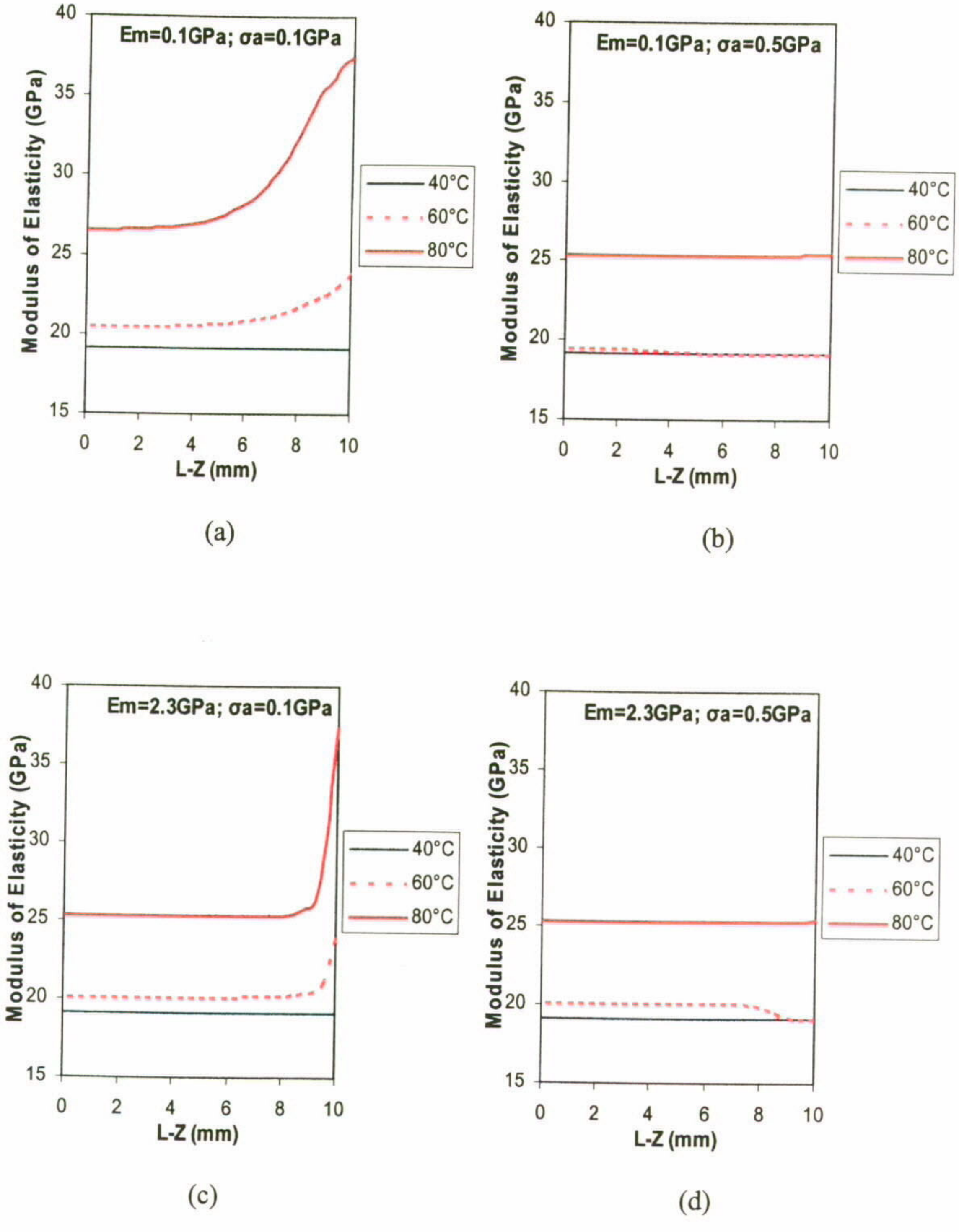

(a) (b)

(c) (d)

Figure 4.7 Evolutions of modulus of elasticity of the embedded SMA wire in type-II loading condition and mode-a actuation, E_{f2a}. a) E_m = 0.1GPa and σ_a = 0.1GPa; b) E_m = 0.1GPa and σ_a = 0.5GPa; c) E_m = 2.3GPa and σ_a = 0.1GPa and d) E_m = 2.3GPa and σ_a = 0.5GPa.

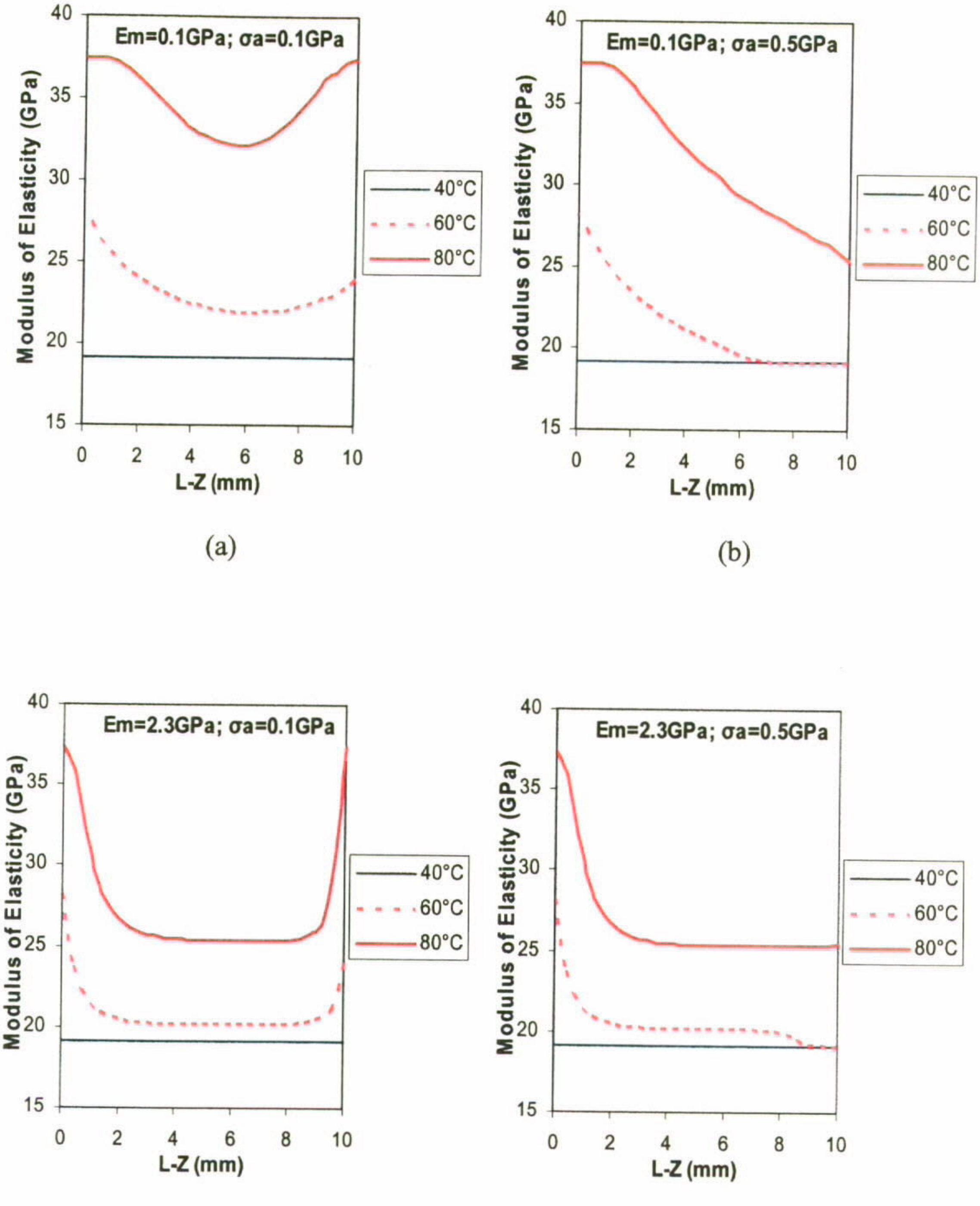

(a) (b) (c) (d)

Figure 4.8 Evolutions of modulus of elasticity of the embedded SMA wire in type-III loading condition and mode-a actuation, E_{f3a}. a) $E_m = 0.1$GPa and $\sigma_a = 0.1$GPa; b) $E_m = 0.1$GPa and $\sigma_a = 0.5$GPa; c) $E_m = 2.3$GPa and $\sigma_a = 0.1$GPa and d) $E_m = 2.3$GPa and $\sigma_a = 0.5$GPa.

4.2.2.3 Estimation of Critical Geometric Factors

In order to design a SMA-reinforced composite with appropriate dimensions for satisfying different types of mechanical requirements, such as vibration control or buckling resistance, it is critically important to estimate the modal properties of the composite structure during the SMA actuation. With the knowledge of ξ evolution in different loading conditions (i.e. Ia, IIa and IIIa), it is possible to estimate the minimum required geometric relations for achieving uniformly distributed ξ over certain portion of the embedded length as schematically demonstrated in Fig. 4.9 (the effective zone for satisfying constant martensite fraction is defined as 'constant martensite volume fraction region (CMR)'). In the other words, the constant SMA properties and hence the modal properties of a composite can be evaluated to predict its mechanical response over a specified or targeted region. Procedures for the estimation of critical geometric factors including total embedded length L and b/a ratio are presented in the following steps:

Step 1: Prediction of L_{min}

For the general application requirement, constant material properties have to be attained at center portion of the SMA composite structure. In the other word, constant value of ξ at $z = L/2$ has to be achieved to realize the CMR. By using the radius of matrix cylinder b = 1.25mm (or b/a = 10) and the necessary material properties summarized in Table 3.1, the plots of $\xi_{1a}(z=L/2)$, $\xi_{2a}(z=L/2)$ and $\xi_{3a}(z=L/2)$ against L are obtained and shown in Fig. 4.10. When T = 60°C, σ_a = 0.5GPa and E_m = 2.3GPa, constant values of $\xi_{ia}(z=L/2)$ can be attained for $L \geq$ 28mm for all the three types of loading conditions. The minimum required embedded length is defined as L_{min}. Both curves of $\xi_{1a}(z=L/2)$ and

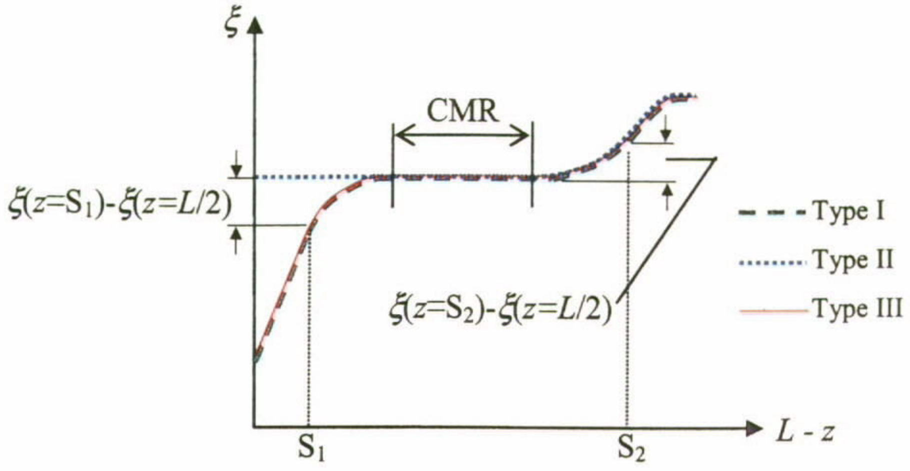

Figure 4.9 Schematic illustration for the 'constant ξ region' in the plots of martensite volume fraction distribution on SMA wire. (CMR: Constant martensite volume fraction region)

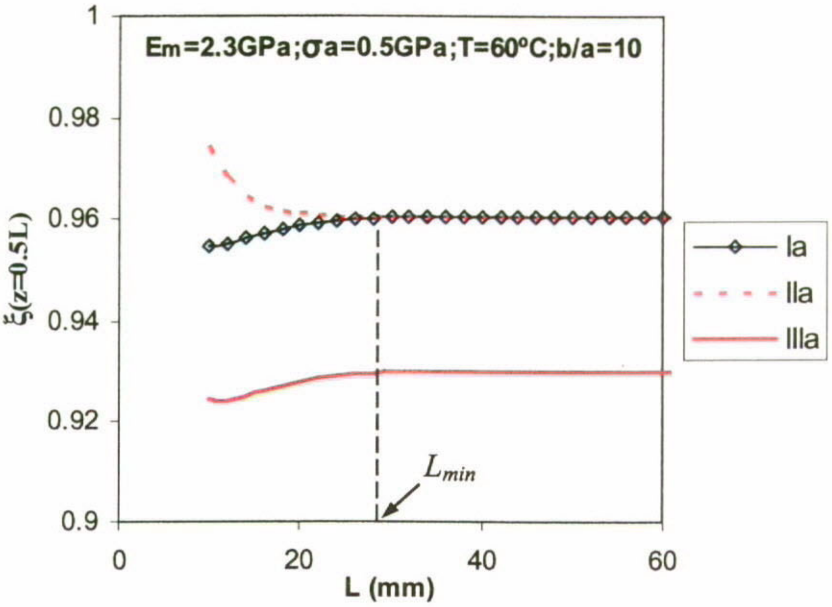

Figure 4.10 Plot of total marteniste volume fraction at mid-point, $\xi(z = 0.5L)$ versus against total embedded length, L in mode-a actuation. ($L_{min} = 28$mm)

$\xi_{2a}(z=L/2)$ are developed to the same constant level except the plot for type-III. It implies that the constant value of ξ at center point can be achieved until $L \geq 28$mm. It should be noted that the CMR only represents a point in this circumstance. It can be further developed into a plateau region by using longer embedded length ($L > 28$mm). Therefore the second step is to evaluate the relation between wire's embedded length and proportion of the CMR.

Step 2: Prediction of L_c

Depending on the types of loading method being used on a structure, position of the CMR could be different from type to type. In addition, stress free condition on wire's end in type-I and III loading conditions restricts the development of the CMR throughout the whole embedded length. Therefore, it is not practical to have CMR = L. The length of CMR = $0.6L$ (i.e. $S_2 - S_1 = 60\%L$) in the center portion is hence targeted for the evaluation of critical embedded length L_c. In the other words, values of ξ_i should remain unchanged between $z = S_1$ and $z = S_2$. In order to satisfy the requirement of CMR = $0.6L$, the following mathematical relation has to be achieved.

$$\Delta\xi_{CMR} = \left|\xi(z=S_1) - \xi(z=0.5L)\right| + \left|\xi(z=S_2) - \xi(z=0.5L)\right| = 0 \qquad (4.14)$$

If the CMR is exactly located at center portion, then $S_1 = (1\text{-N})L/2$ and $S_2 = (1\text{+N})L/2$ should be used, where N represents the required proportion of total embedded length for achieving CMR. Figure 4.11 shows the plots of Eqn. 4.14. The differences between martensite volume fractions become negligible for $L \geq 54$mm. Therefore, if the total embedded length is longer than $L_c = 54$mm, CMR = $0.6L$ can be guaranteed.

Step 3: Prediction of b_c/a

Type-III loading method is commonly used in experimental study for determining the interfacial properties of traditional fiber-matrix composites. The validity of this loading condition applied in pullout test has been clarified by Zhou et al [114]. Critical value of b/a ratio has been evaluated for constant material properties of constituents. However, material properties of the embedded SMA wire in CMR may not be necessarily the same for different loading methods. Therefore, in order to make sure the compatibility of type-III loading in experimental study for the mechanical responses of the SMA-composites, material properties at CMRs for type-I, II and III loading conditions must be the same within a targeted region. Figure 4.12 shows the plots of $\xi_1 - \xi_3$ at $z = L_c/2$ against b/a for $T = 60°C$. It can be found that the difference of ξ becomes negligible when $b/a \geq 37$. Therefore the critical radius of matrix is $b_c = 37a$ while the critical embedded length is $L_c = 50mm$ for achieving CMR in all the three types of loading with equivalent material properties over the 60% of total embedded length.

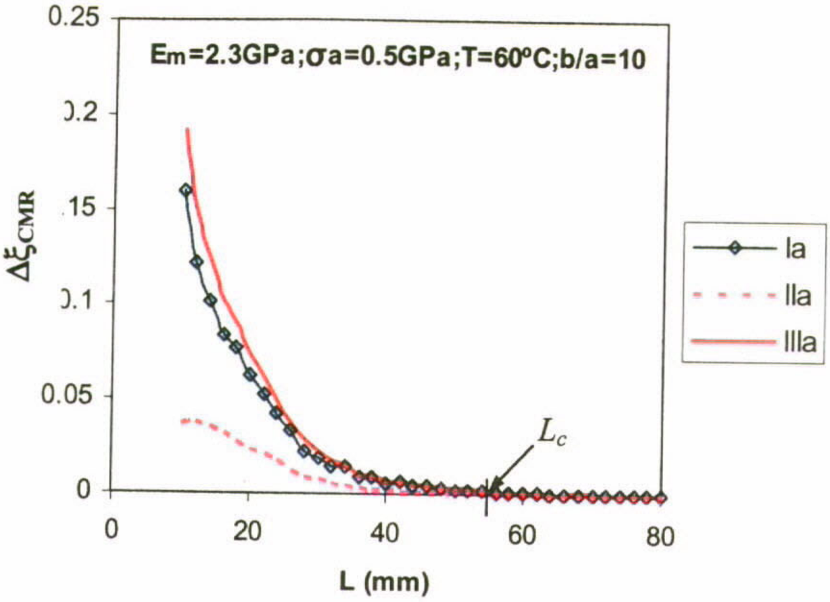

Figure 4.11 Evaluation of critical embedded length, L_c for achieving constant martensite volume fraction over the embedded portion of $z = 0.2L$ to $0.8L$ in mode-a actuation. ($L_c = 54$mm)

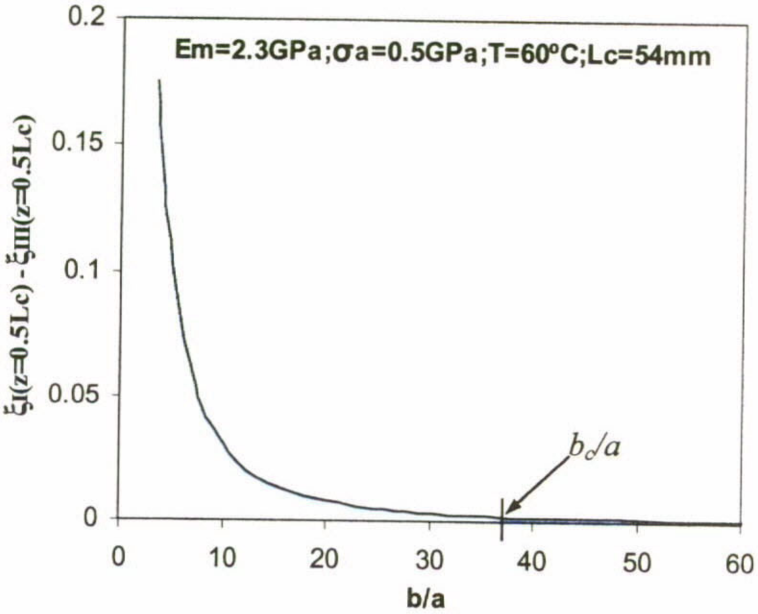

Figure 4.12 Evaluation of critical b_c/a ratio for satisfying the identical and constant martensite volume fraction in all the type-I, II and III loading conditions and mode-a actuation. ($b_c/a = 37$)

4.2.2.4 Evolution of Internal Stresses

Equations 3.25, 4.12 and 4.13 reproduce the evolutions of axial stresses on the SMA wire for type-I, II and III loading conditions respectively. Surface plots of these stress distributions $\sigma_{fia}(z, \sigma_a, T)$ at different actuation temperature T are shown in Figs. 4.13 to 4.15. It is considered in the calculations that the externally applied stress σ_a is equal to 0.5GPa. All the necessary material properties being used in the following numerical examples are summarized in Table 3.1 unless otherwise specified in the corresponding figures.

Effects of geometric factors (i.e. L and b/a) and matrix stiffness on internal stress distributions are demonstrated in Figs. 4.16 to 4.18. Figure 4.16a shows the typical plots of axial stress distributions for different types of loading while all the three plots demonstrate the 'constant axial stress region (CASR)' in center portion. However, when the matrix stiffness is reduced to 0.1GPa, derivations between the three plots increase substantially and the axial stress for type-II loading is always higher than that of the others as shown in Fig. 4.16b. Similarly, derivations due to size effects are illustrated in Figs. 4.17a and b. The derivations of internal stress distributions can be promoted by using shorter embedded length while the stress levels of the CASR in different loading condition are governed by b/a ratio. Therefore, in addition to the evaluation of the CMR for modal property estimation within a specified region, there is an urged need to clarify the dimensional requirement for achieving the CASR.

To estimate the critical embedded length L_c and b_c/a ratio for the CASR, the similar steps as described in Section 4.2.2.3 should be used.

Step 1: Prediction of L_{min}

The minimum required embedded length, L_{min} can be estimated by comparing the plots of $\sigma_{f1}^{z}(L/2, \sigma_a, T)$, $\sigma_{f2}^{z}(L/2, \sigma_a, T)$ and $\sigma_{f3}^{z}(L/2, \sigma_a, T)$ against L as shown in Fig. 4.a. The plots are developed to the constant levels when $L \geq 30$mm.

Step 2: Prediction of L_c

Referring to Fig. 3.15 for the axial stress distributions in the no-load condition (σ_a = 0GPa), it can be found that the identical stress value at $z = 0.2L$ and $z = 0.8L$ can be obtained before the constant axial stress at $z = L/2$ can be attained. Therefore the critical embedded length L_c has to be longer than L_{min} so as to make sure the constant axial stress can be attained. Using the similar approach for the prediction of L_c for the CMR in the targeted region ($0.2L < z < 0.8L$), the following equation has to be satisfied,

$$\Delta\sigma_{CMR} = \left|\sigma_{fi}^{z}\left(S_1, \sigma_a, T\right) - \sigma_{fi}^{z}\left(L/2, \sigma_a, T\right)\right| + \left|\sigma_{fi}^{z}\left(S_2, \sigma_a, T\right) - \sigma_{fi}^{z}\left(L/2, \sigma_a, T\right)\right| = 0 \quad (4.15)$$

Figure 4.18b indicates that the $\Delta\sigma_{CMR}$ becomes negligible when $L \geq 50$mm. In the other words, the CASR can be achieved when the total embedded length is longer than L_c = 50mm.

Step 3: Prediction of b_c/a

Figure 4.19 shows that the derivation between $\sigma_{f1}^{z}(L_c/2, \sigma_a, T)$ and $\sigma_{f3}^{z}(L_c/2, \sigma_a, T)$ can be ignored if $b/a \geq 40$ when L_c = 50mm. Therefore, if the SMA matrix cylinder is fabricated with $L > L_c$ and $b > b_c$, the CASR over the 60% of the embedded length can be obtained for all the three types of loading conditions.

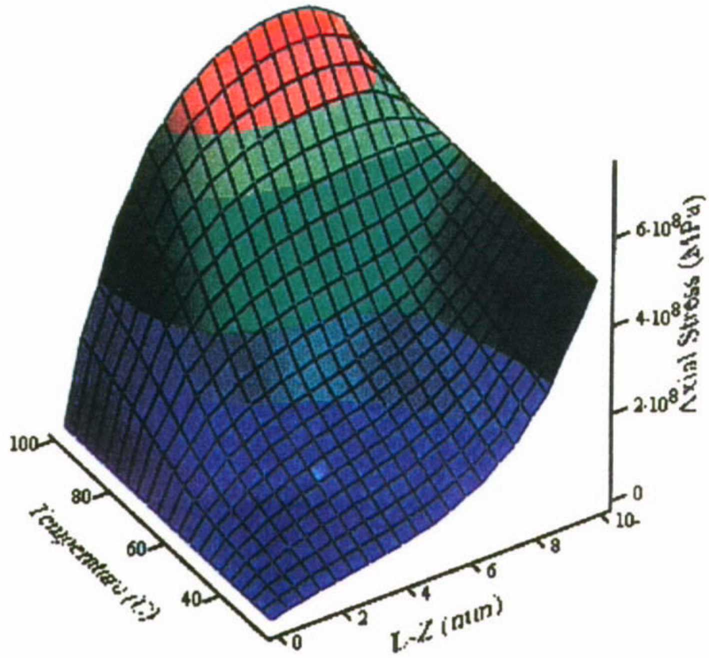

Figure 4.13 Axial Stress Distribution (Type-I loading method & Mode-a actuation)

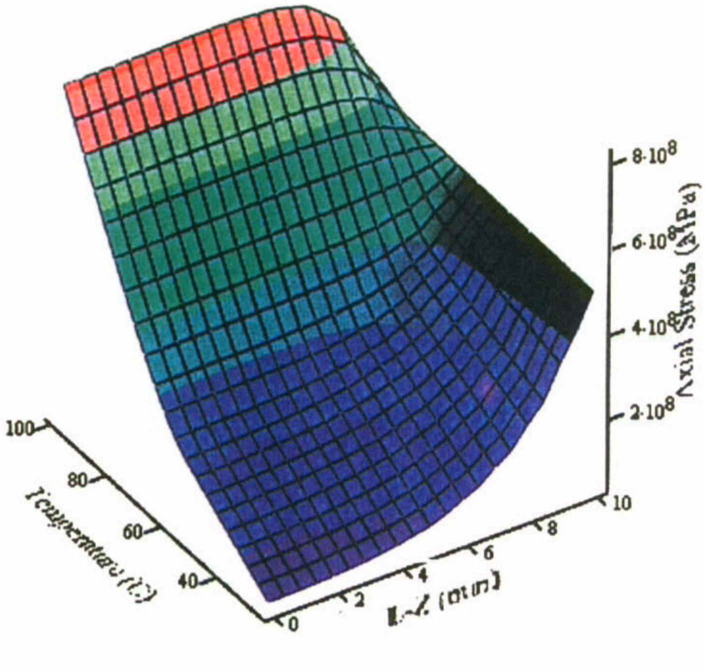

Figure 4.14 Axial Stress Distribution (Type-II loading method & Mode-a actuation)

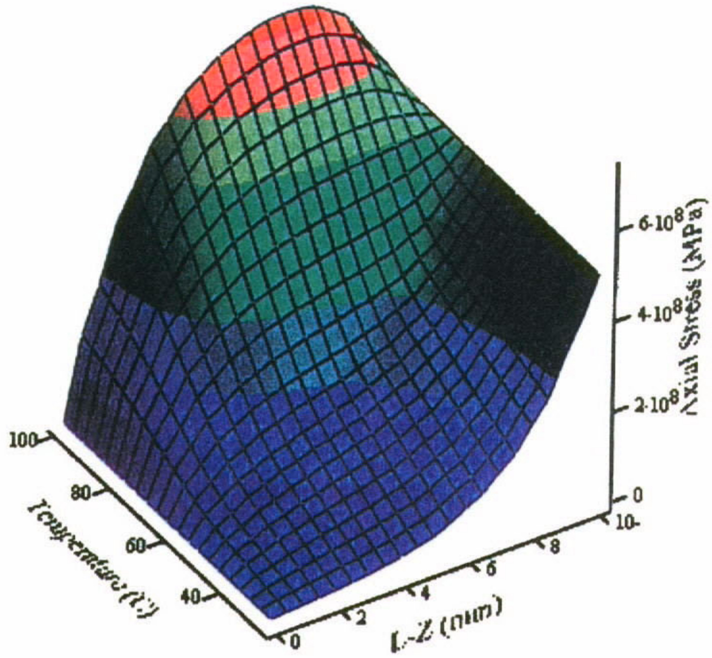

Figure 4.15 Axial Stress Distribution (Type-III loading method & Mode-a actuation)

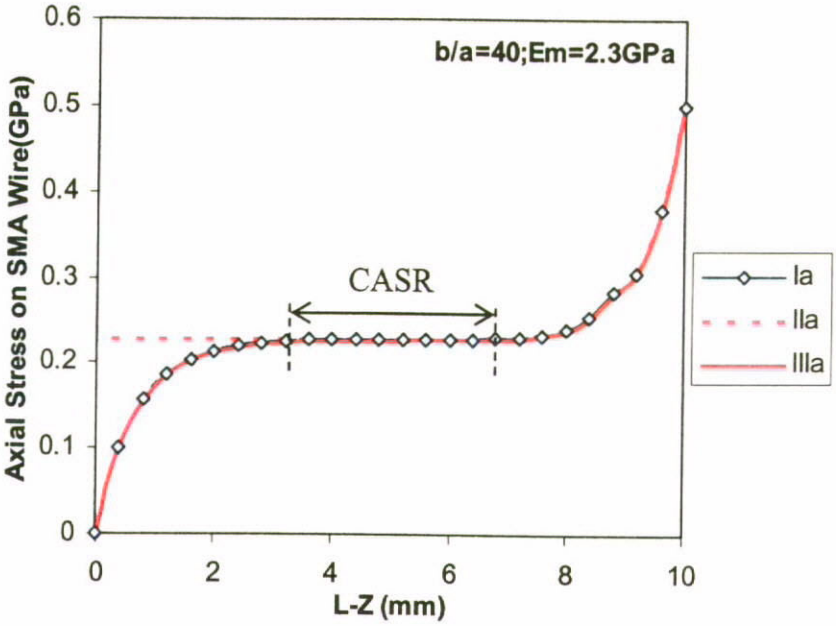

Figure 4.16a Axial stresses distribution for type-I, II and III loading condition. (CASR: Constant axial stress region)

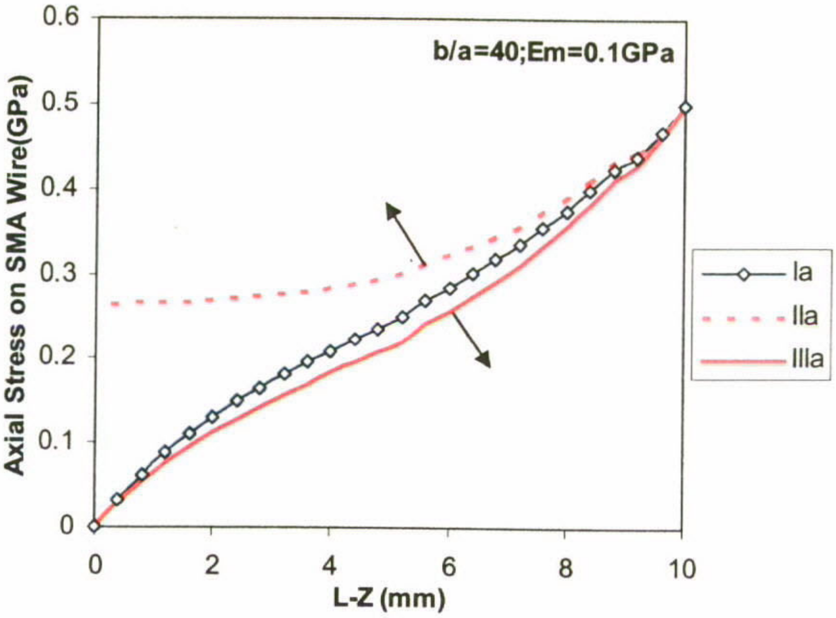

Figure 4.16b Axial stress distributions on SMA wire for $E_m = 0.1\text{GPa}$.

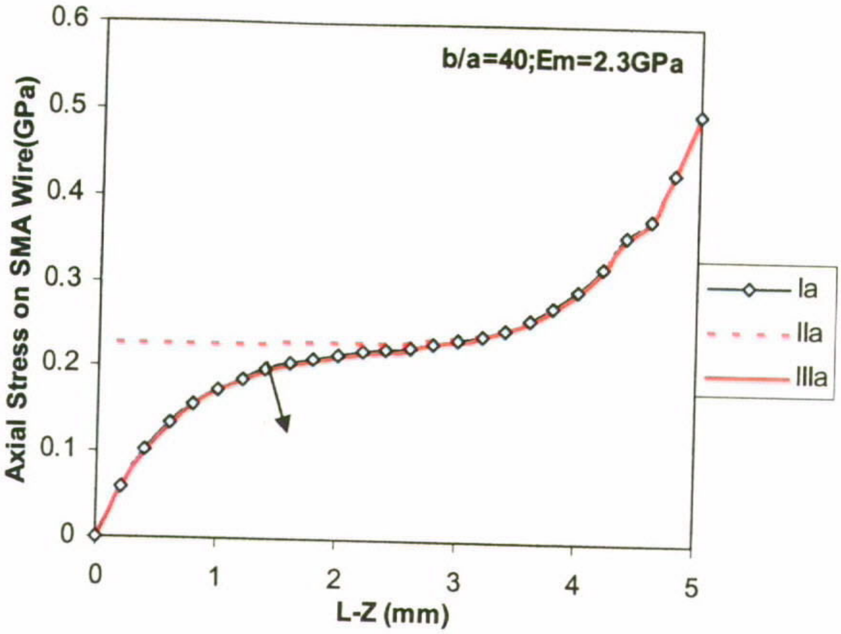

Figure 4.177a Effect of short embedded length on axial stress distributions.

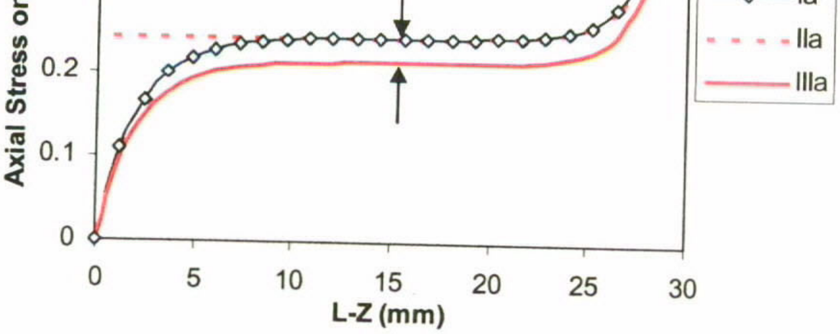

Figure 4.187b Effect of low b/a ratio on axial stress distributions.

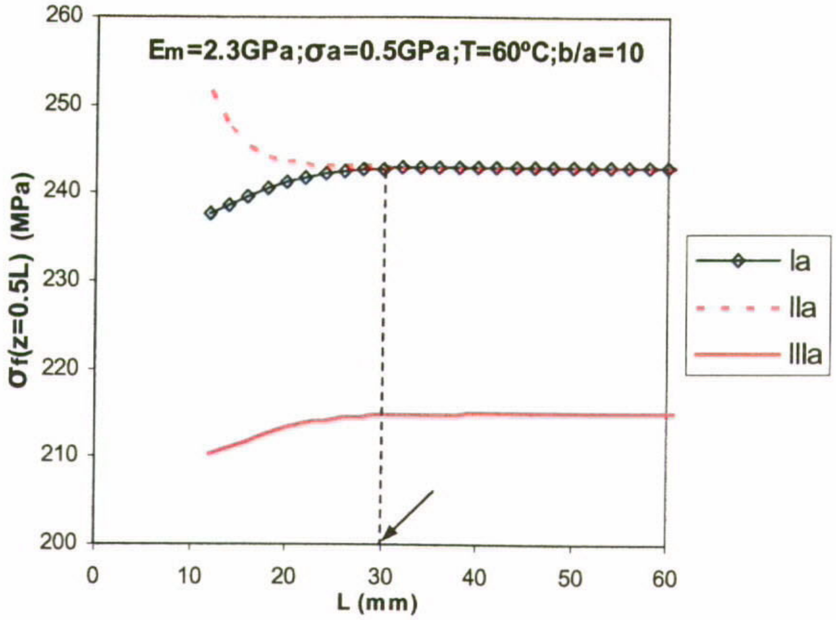

Figure 4.18a Plot of axial stress on SMA wire at mid-point, $\sigma_f^z(z=L/2)$ versus against total embedded length, L. (L_{min} = 30mm)

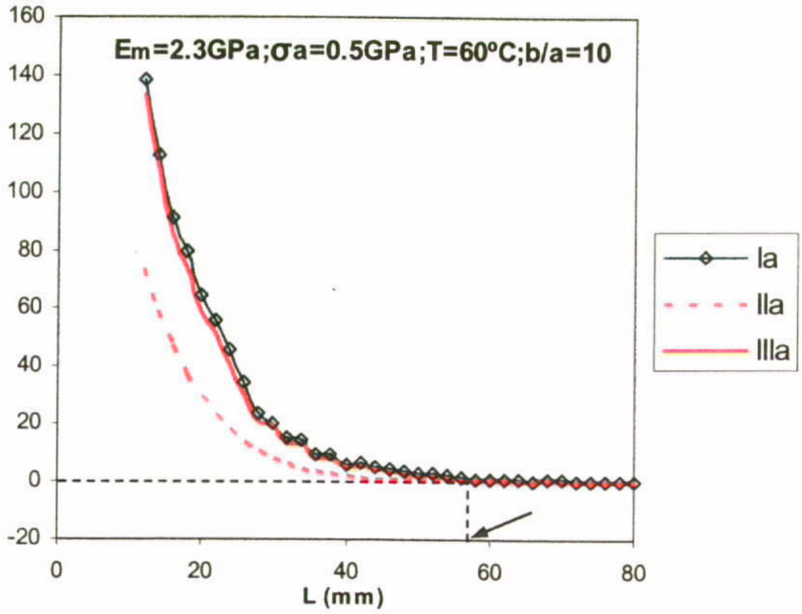

Figure 4.18b Evaluation of critical embedded length, L_c for achieving constant axial stress on SMA wire over the embedded portion of $z = 0.2L$ to $0.8L$. ($L_c = 56$mm)

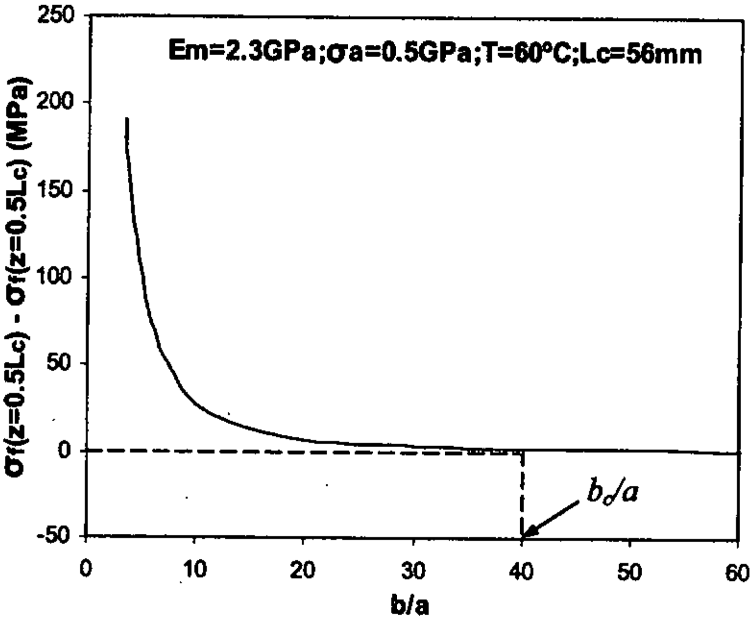

Figure 4.19 Evaluation of critical b/a ratio for satisfying the identical and constant axial stress on SMA wire in all the type I, II and III loading conditions. ($b_c/a = 40$)

4.3 Effect of Actuation Modes on Internal Stress Distributions

4.3.1 Mode-a and Mode-b SMA Actuation

As briefly discussed in Section 4.1 for the possible actuation modes of the SMA-reinforced composites, evolution of martensite volume fraction of the SMA wire inside a composite can be totally different for different actuation scenarios. In this section, the SMA actuations are classified into the following two basic modes:

***Mode-a**: SMA wire is actuated under a constant applied load on wire's end.*

***Mode-b**: SMA wire is actuated prior to the application of axial load on wire's end.*

These two actuation scenarios were schematically illustrated in Fig. 4.1. The point 1 and 2 are destinations of different loading-actuation paths and point 0 represents the starting point of each path. Initial value of total martensite volume fraction $\xi_o = 1$ is assumed for simplicity. In the case that the SMA material is activated to point 1 along the mode-a actuation path, it will never exhibit austenitic phase transformation and hence ξ remains unchanged. However, if it arrives the same destination by following mode-b actuation path, part of microstructures in the SMA will firstly exhibit austenitic phase transformation in a low stress level (i.e. $\xi = \xi_o \rightarrow \xi < \xi_o$). When the applied stress is increased upon $\sigma_M^f(T)$ and reaches the point 1, ξ increases to 1 again due to stress-induced martenitic transformation (SIM).

It should be noted that the captioned discussions for mode-a and b actuations are valid for the SMA-matrix cylinder model at wire's loading end ($z = 0$) only. As previously discussed for the internal stress distributions, axial stress on the SMA wire at $z > 0$ can be difference (i.e. $\sigma_f^z(z,\sigma_a,T) \neq \sigma_f^z(0,\sigma_a,T)$). Therefore, the destination of actuation paths may shift downward to point 2 at any arbitrary position in z-dircetion. Again, the SMA exhibits no phase transformation in mode-a actuation while the reduced ξ, due to austenitic transformation along the mode-b actuation path, remains unchanged at point 2. It explains the reason for SMA-composites having different mechanical responses in mode-a and mode-b actuation.

4.3.2 Evaluation of SMA's Material Properties in Mode-b Actuation

4.3.2.1 Evolution of Martensite Volume Fraction

Mode-b actuation requires heating the SMA wire in a no-load condition. External load will be only applied on the wire's end until the target temperature is attained, which implies that the initial stress on the SMA wire σ_{ao} must be zero. Recalling the evaluation sequence proposed in Section 3.4.1, evolution of ξ, ξ_s and ξ_T in a no-load condition can be obtained in 'step-a'. Solutions of ξ_{sa} and ξ_{Ta} are therefore employed as initial values in 'step-b' for the estimation of ξ distribution. It should be noted that if the SMA wire is initially subjected to a constant applied load, σ_{ao} as schematically illustrated in Fig. 4.19 (*0* → *1*), the actuation scenario should be considered as a combined mode of a and b. The ξ distribution in this combined actuation mode can be evaluated by simply substituting the initial stress σ_{ao} into step-a instead of using $\sigma_{ao} = 0$ for mode-b actuation. The loading-actuation path *0* → *2* represents another typical combined mode of actuation. Definitely, there is no difficulty to evaluate ξ distribution by using similar approach.

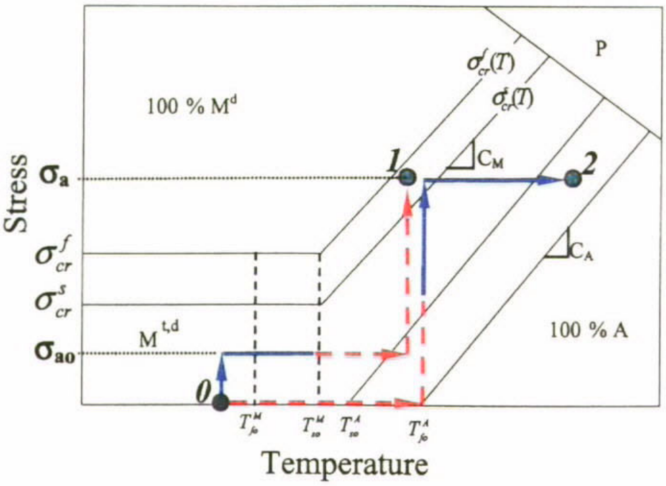

Figure 4.19 Schematic illustration of combined actuation modes.

However, the most essential element is the identification and application of actuation mode. Since the mode-a actuation has been studied in the previous section, only the mode-b will be focused in the current section.

Solutions of ξ can be obtained by substituting the recurrence equations (Eqns. 3.29, 4.12 and 4.13) into Eqns. 3.30 to 3.36. Plots of $\xi_b(z, \sigma_a, T)$ with mode-b actuation for type-I, II and III loading methods are shown in Figs. 4.20, 4.21 and 4.22 respectively.Figures 4.20a and b show the ξ distributions with σ_a = 0.5GPa and 1GPa respectively for E_m = 0.1GPa. It can be observed that the distribution profiles shown in the two figures are more or less the same, only the plot for σ_a = 0.1GPa at 60oC shows shape change nearby the loading end. Referring to Fig. 3.18a for the plot of phase diagram using all the employed material properties summarized in Table 3.1, it can be found that $\sigma_{cr}^{f}(T)$ = 0.983GPa at T = 60°C. Therefore, the martensite volume fraction at $z = 0$ is changed to 1 due to the SIM. However, if the temperature is increased upon 80°C, austenitic phase transformation completes at both embedded ends (z = 0 and L) and $\sigma_{cr}^{f}(80^{\circ}C)$ = 1.56GPa. As a result, ξ = 0 at loading end remains unchanged. Similar distribution profiles can be found in Figs. 4.20c and d for E_m = 2.3GPa. Obviously, long plateaus at the same attitude for the identical actuation temperature can be observed in the figures and the plots demonstrate the fairly ideal symmetric profiles. It implies that the ξ distribution is not sensitive to the externally applied load in mode-b actuation. Comparing to the results in Fig. 4.3 for the mode-a actuation, ξ distribution is relatively more sensitive to the externally applied load. In addition to the significant changes of ξ distribution, the relatively poor symmetric profiles can also be observed even for the low applied load (σ_a = 0.1GPa).

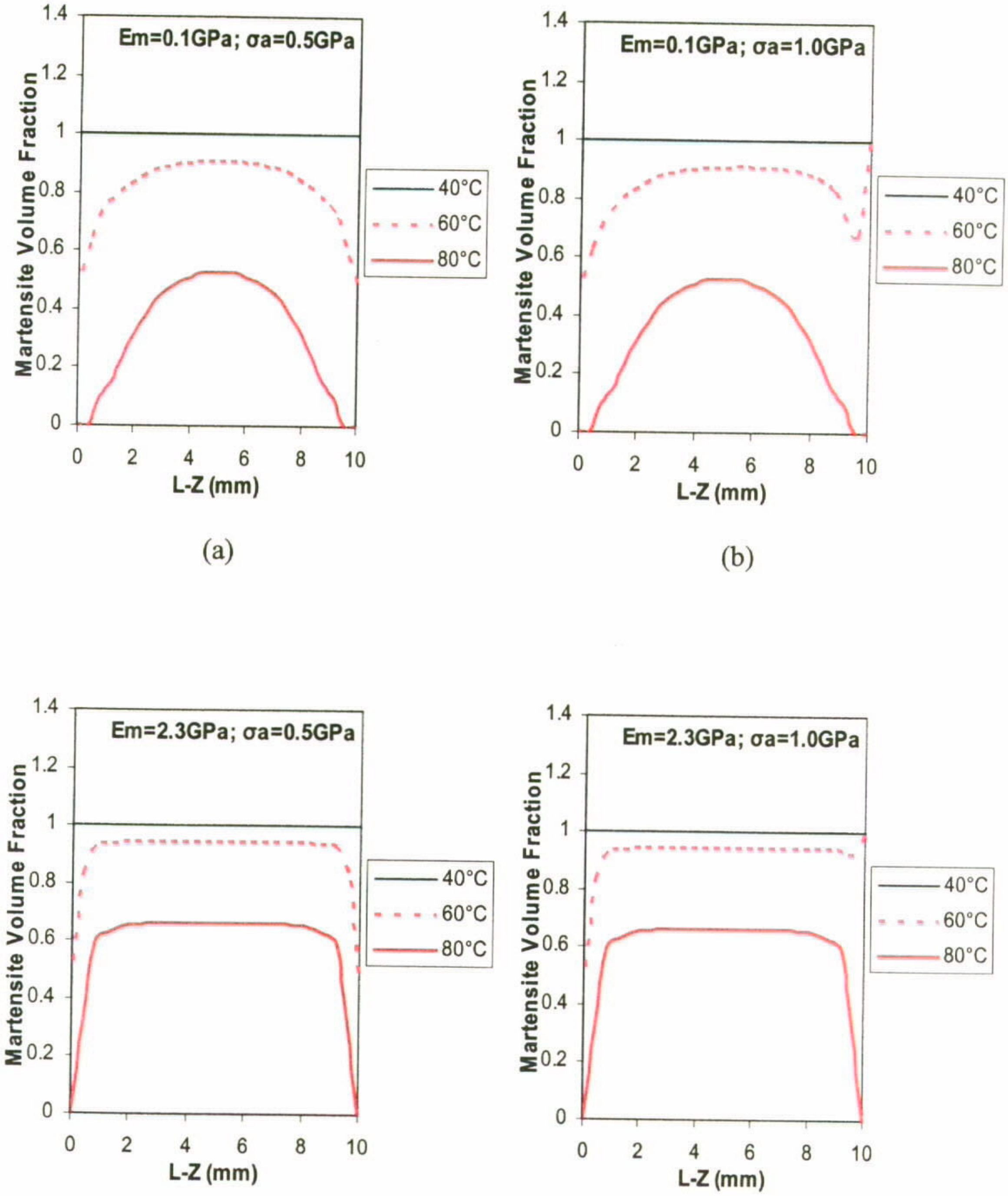

(a) (b)

(c) (d)

Figure 4.20 Evolutions of martensite volume fraction on the embedded SMA wire in type-I loading condition and mode-b actuation. a) $E_m = 0.1$GPa and $\sigma_a = 0.5$GPa; b) $E_m = 0.1$GPa and $\sigma_a = 1$GPa; c) $E_m = 2.3$GPa and $\sigma_a = 0.5$GPa and d) $E_m = 2.3$GPa and $\sigma_a = 1$GPa.

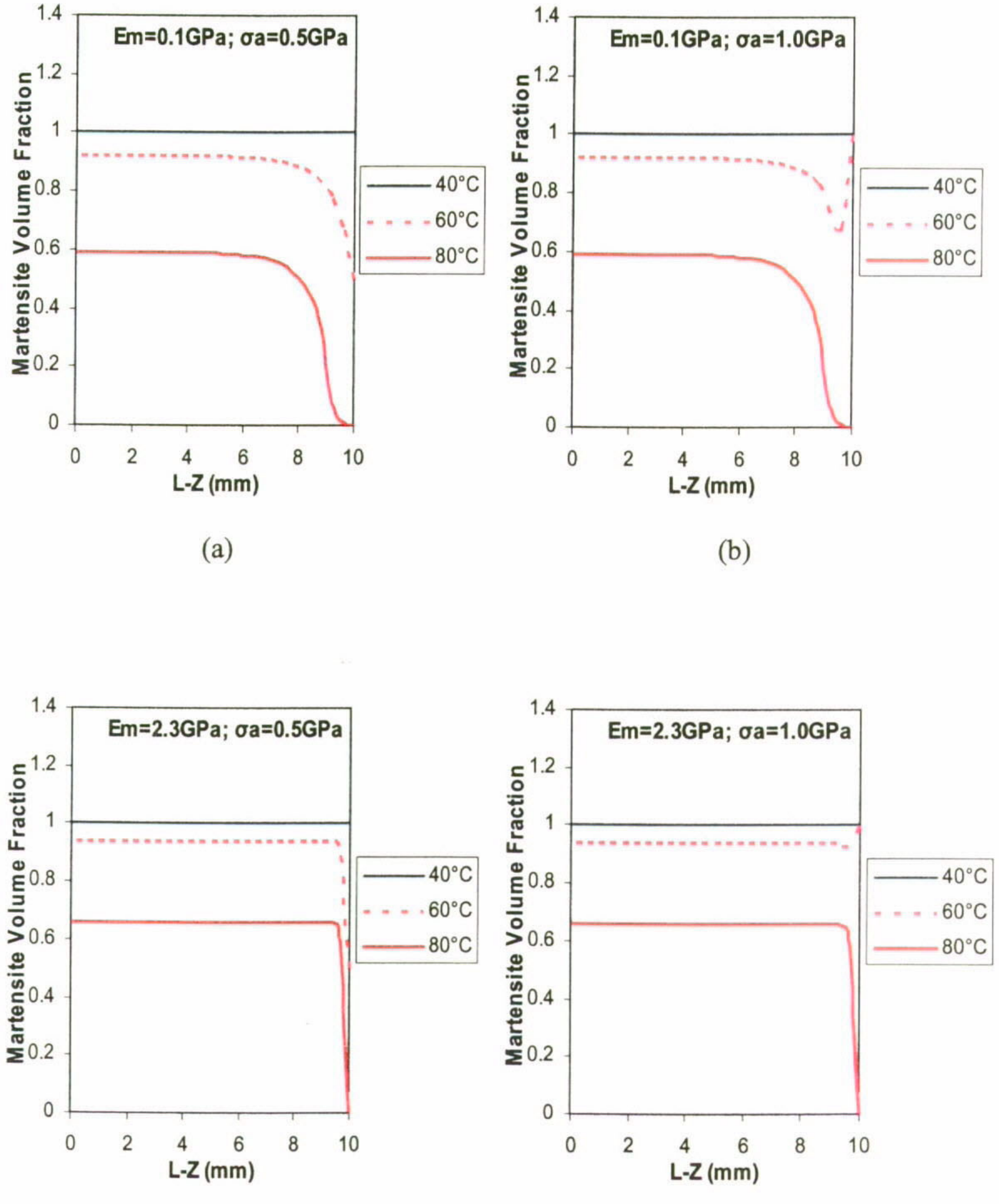

(a) (b)

(c) (d)

Figure 4.21 Evolutions of martensite volume fraction on the embedded SMA wire in type-II loading condition and mode-b actuation. a) $E_m = 0.1$GPa and $\sigma_a = 0.5$GPa; b) $E_m = 0.1$GPa and $\sigma_a = 1$GPa; c) $E_m = 2.3$GPa and $\sigma_a = 0.5$GPa and d) $E_m = 2.3$GPa and $\sigma_a = 1$GPa.

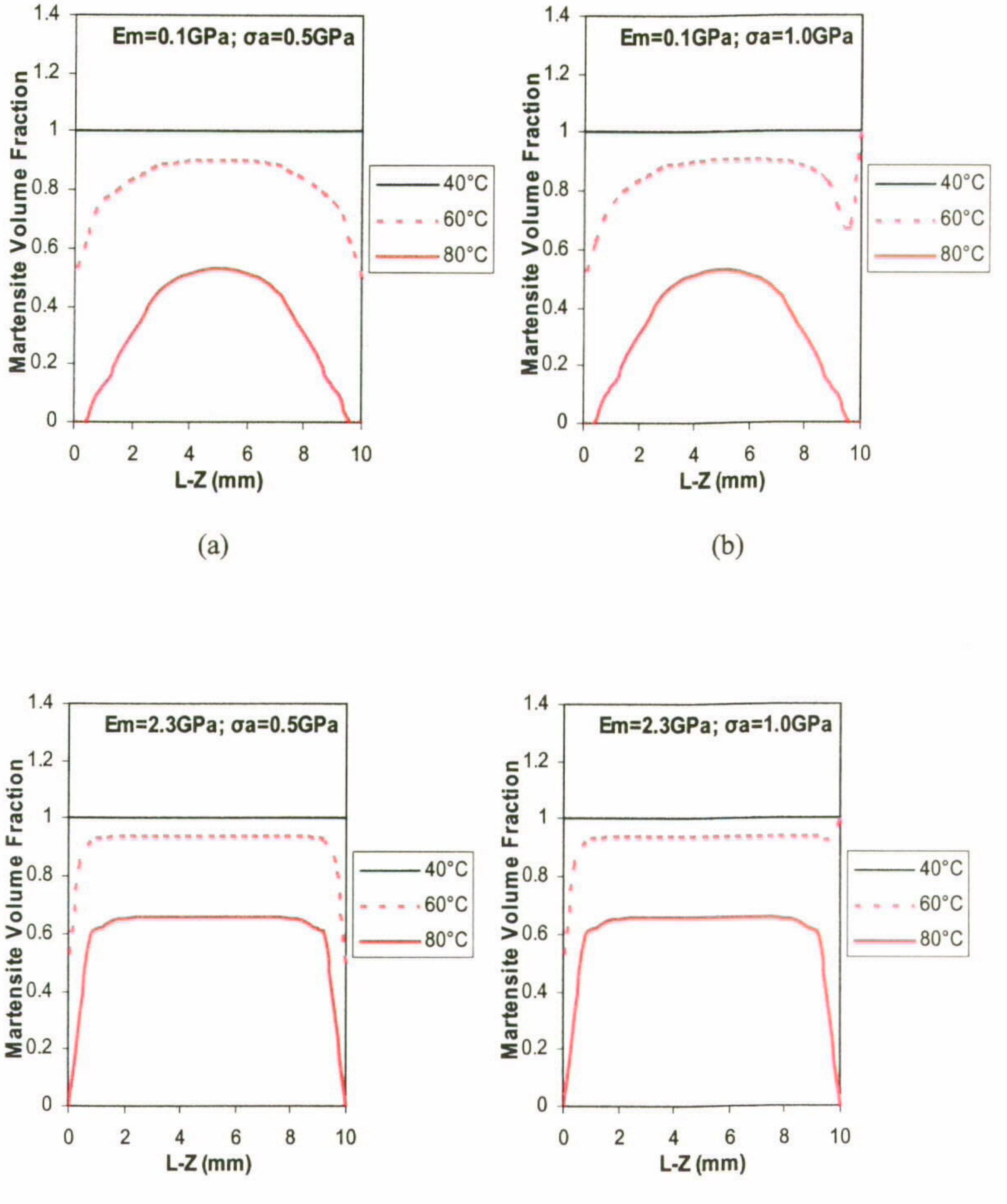

(a) (b)

(c) (d)

Figure 4.22 Evolutions of martensite volume fraction on the embedded SMA wire in type-III loading condition and mode-b actuation. a) $E_m = 0.1$GPa and $\sigma_a = 0.5$GPa; b) $E_m = 0.1$GPa and $\sigma_a = 1$GPa; c) $E_m = 2.3$GPa and $\sigma_a = 0.5$GPa and d) $E_m = 2.3$GPa and $\sigma_a = 1$GPa.

Figure 4.21 shows the ξ distributions for type-II loading methods under mode-b actuation. Shape changes for the high load condition (σ_a = 1GPa) at 60°C also exist in Figs. 4.21b and d. Comparing with Fig. 4.4 for the same type of loading in mode-a actuation, the ξ distribution looks more uniform for σ_a = 0.5GPa. However, austenitic phase transformation cannot be initiated effectively as shown in Fig. 4.4b. Both the plateau states for 60°C and 80°C are higher than those for the same matrix stiffness and axial load in mode-b actuation (Fig. 4.21a), which means the shape memory effect is more effective and the austenitic transformation can be initiated more easily in mode-b actuation.

Figure 4.22 presents the results for type-III loading in mode-b actuation. It shows almost the same results as obtained in Fig. 4.20 for the similar boundary conditions between type-I and type-III loading conditions.

4.3.2.2 Evolution of Modulus of Elasticity

The modulus of elasticity of SMA, E_f is a critical parameter governing mechanical responses of the SMA-composites and directly reflects the influence of ξ evolution during the actuation. As discussed in previous sections for the linear relation between E_f and ξ, modulus E_f is readily determined by using Eqn. 3.11. Figures 4.23 to 4.25 present the distributions of E_{f1b}, E_{f2b} and E_{f3b} for different types of loading in mode-b actuation respectively. Due to the similar ξ distributions obtained for type-I and III loading methods, it is not surprise for E_{f1b} and E_{f3b} distributions showing similar profiles in Figs.4.23a and c respectively. In type-I loading condition, when σ_a = 0.5GPa, symmetric

E_f distribution profiles can be obtained for all the targeted actuation temperatures. Increase of matrix stiffness can lengthen the constant E_f regions but resist the austenitic phase transformation. Therefore, the plateau region maintains at a lower attitude for higher matrix stiffness. In Fig. 4.23, plots a and c show symmetric distribution profiles in different actuation temperatures. As previously discussed for the mode-a actuation, if $\sigma_a = 0.5\text{GPa}$ and $T = 60°\text{C}$, austenitic phase transformation at loading end can be completely restricted as shown in Figs. 4.6b and c. Modulus E_f at loading end remains unchanged even at $T = 60°\text{C} > T_{so}^{A}$. However, the same applied load in mode-b actuation can never affect the E_f evolution. Figures 4.23b and d demonstrate the changes of E_f at loading end for $\sigma_a = 1\text{GPa}$. Considering that embedded wire has been heated to 60°C before the application of axial load in mode-b actuation, ξ should be firstly reduced and E_f is therefore increased. When the applied load is increased to 1GPa, the SIM starts and the austenite transforms to stress-induced martensite again. Similar results are obtained as illustrated in Figs. 4.24b, 4.24d, 4.25b and 4.25d.

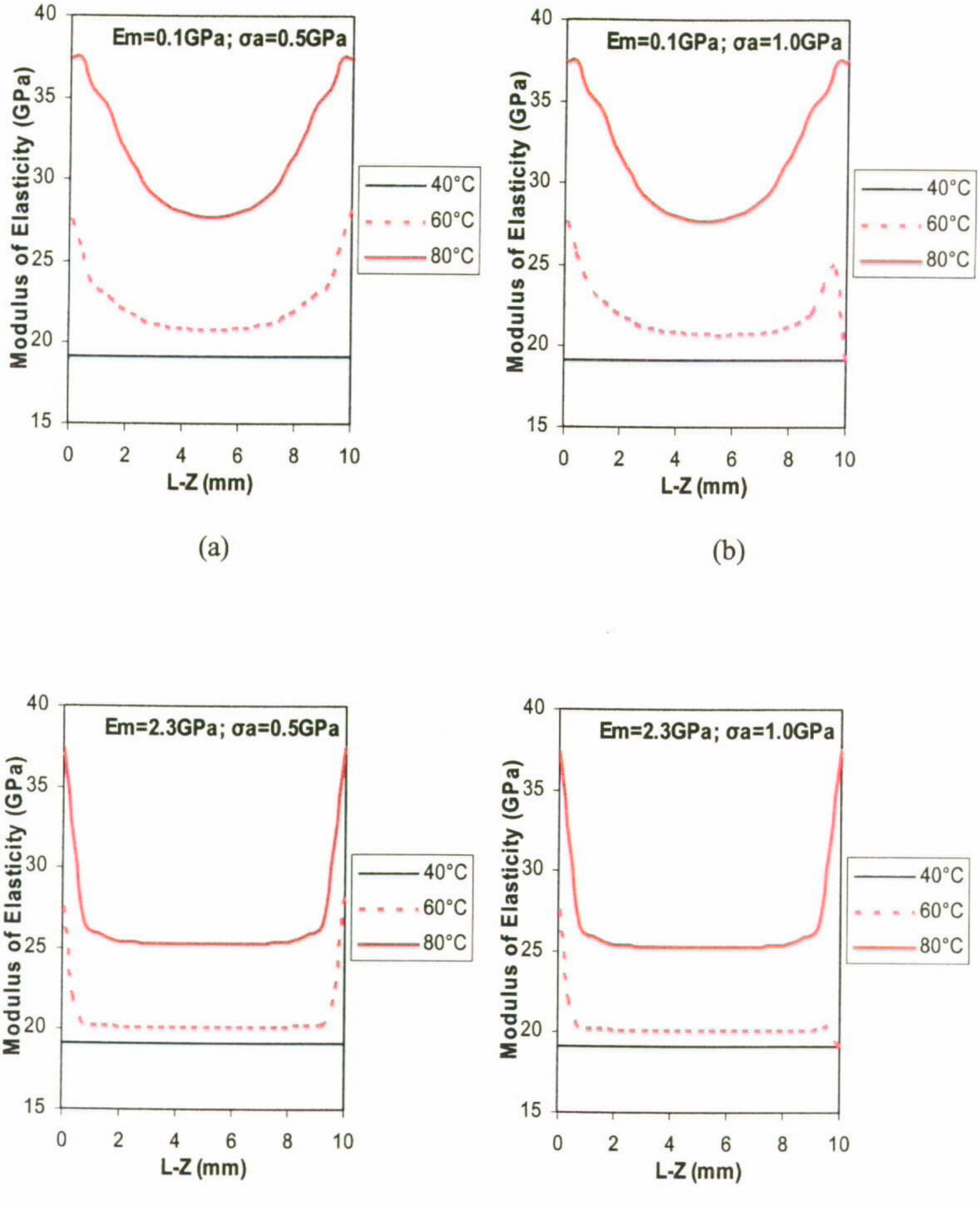

(a) (b)

(c) (d)

Figure 4.23 Evolutions of modulus of elasticity of the embedded SMA wire in type-I loading condition and mode-b actuation. a) E_m = 0.1GPa and σ_a = 0.5GPa; b) E_m = 0.1GPa and σ_a = 1GPa; c) E_m = 2.3GPa and σ_a = 0.5GPa and d) E_m = 2.3GPa and σ_a = 1GPa.

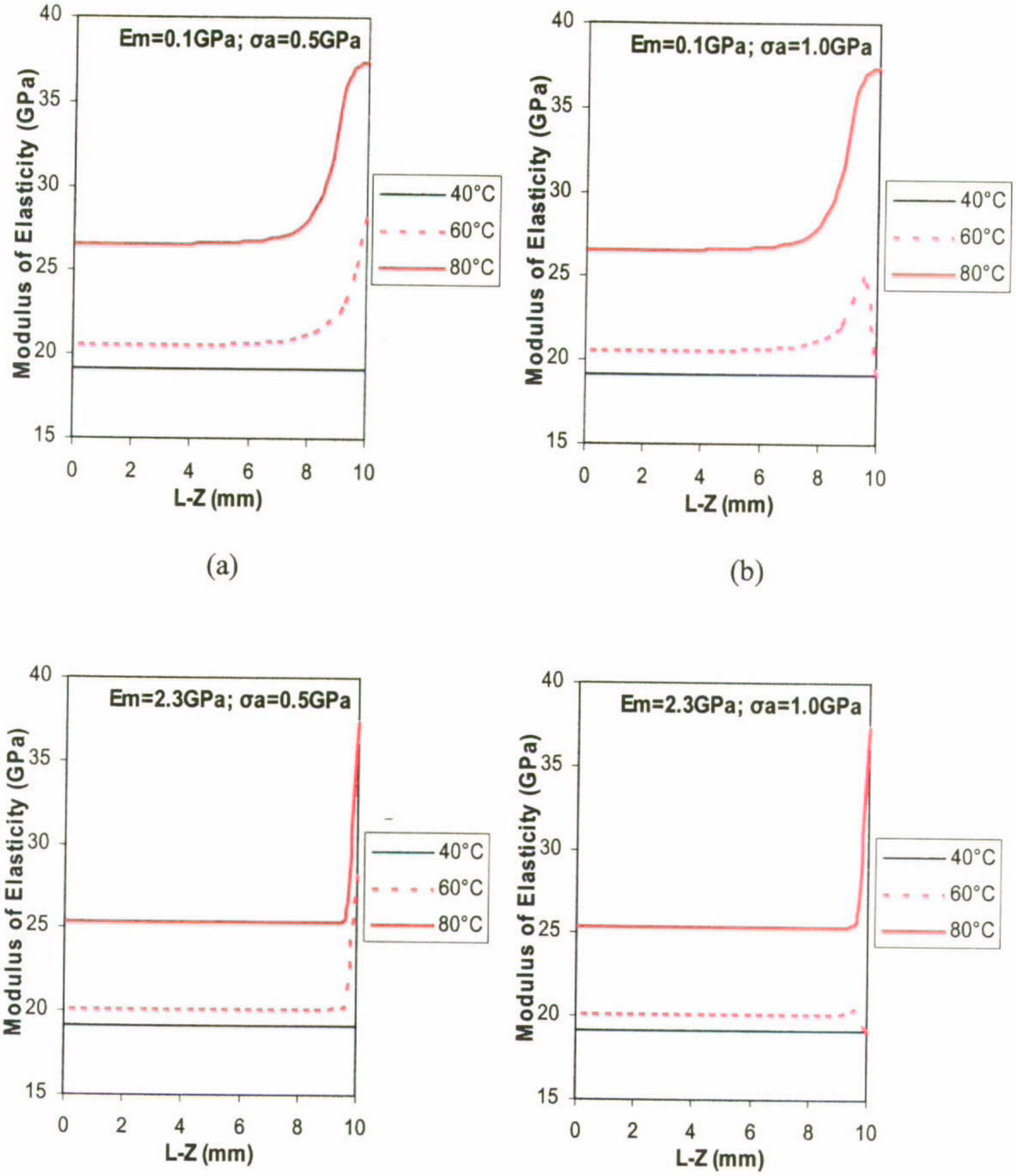

(a) (b)

(c) (d)

Figure 4.24 Evolutions of modulus of elasticity of the embedded SMA wire in type-II loading condition and mode-b actuation. a) E_m = 0.1GPa and σ_a = 0.5GPa; b) E_m = 0.1GPa and σ_a = 1GPa; c) E_m = 2.3GPa and σ_a = 0.5GPa and d) E_m = 2.3GPa and σ_a = 1GPa.

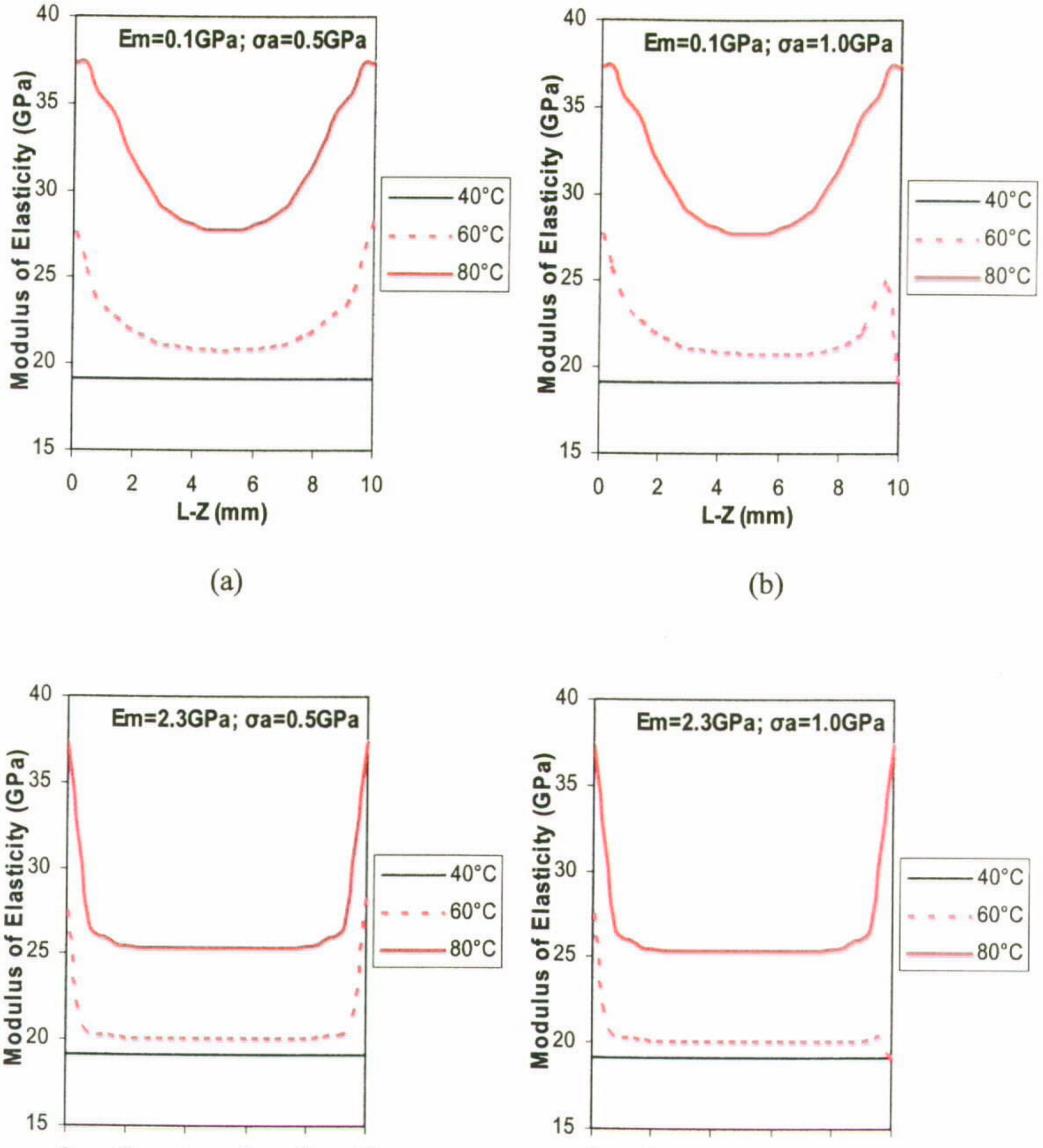

(a) (b)

(c) (d)

Figure 4.25 Evolutions of modulus of elasticity of the embedded SMA wire in type-III loading condition and mode-b actuation. a) E_m = 0.1GPa and σ_a = 0.5GPa; b) E_m = 0.1GPa and σ_a = 1GPa; c) E_m = 2.3GPa and σ_a = 0.5GPa and d) E_m = 2.3GPa and σ_a = 1GPa.

4.3.2.3 Estimation of Critical Geometric Factors

Again, using the step 1 to 3 described in Section 4.2.2.3 for the prediction of critical geometric factors, L_{min}, L_c and b_c/a can be obtained from Figs. 4.26 to 4.28 respectively. When $E_m = 2.3\text{GPa}$, $\sigma_a = 0.5\text{GPa}$, $T = 60°\text{C}$ and $b/a = 10$, plots of ξ_1, ξ_2 and ξ_3 approach to a constant level for $L \geq 25\text{mm}$ as shown in Fig. 4.26. Therefore the minimum required embedded length, L_{min} for type I, II and III loading condition in mode-b actuation to achieve constant ξ at $z = L/2$ is 25mm. Similarly, Fig. 4.27 shows that $\Delta\xi_{CMR}$ becomes negligible when $L \geq 45\text{mm}$. However, the constant values of ξ for all the types of loading are independent of b/a ratio as indicated in Fig. 4.28. There is no difference between them for $L \geq L_c$. Therefore, $L \geq L_c$ is the only requirement for satisfying the CMR over 60% of total embedded length in the center portion.

4.3.2.4 Evolution of Internal Stresses

Figures 4.29 to 4.31 present the surface plots of axial stress distributions of type-I, II and III loading conditions in mode-b actuation. In the figures, a long plateau can be observed in different actuation temperatures and the constant stress levels attained along the embedded length at any particular temperature is much higher than that in mode-a actuation. It implies that the more effective and stable SMA actuation can be obtained by actuating the SMA wire before the application of external load. This finding is critical important for the design of SMA-reinforced composites. Depending on the application requirements, mode-b actuation is definitely able to provide a more stable stress distribution along a composite and can also generate higher recovery stress for satisfying the purposes of shape change as well as modal property improvement.

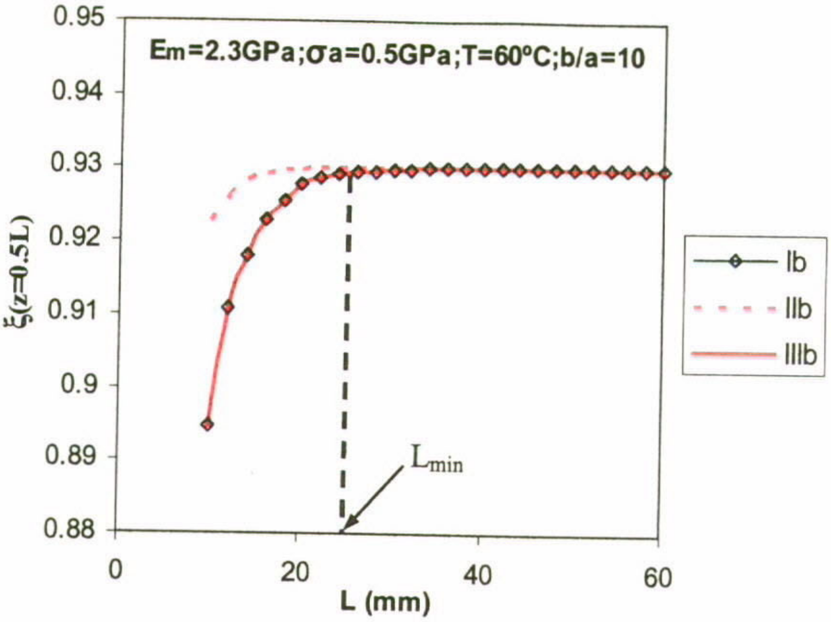

Figure 4.26 Evaluation of the minimum required embedded length for satisfying constant martensite volume fraction at mid-point, (i.e. $\xi(z=L/2)$ = constant). (L_{min} = 25mm)

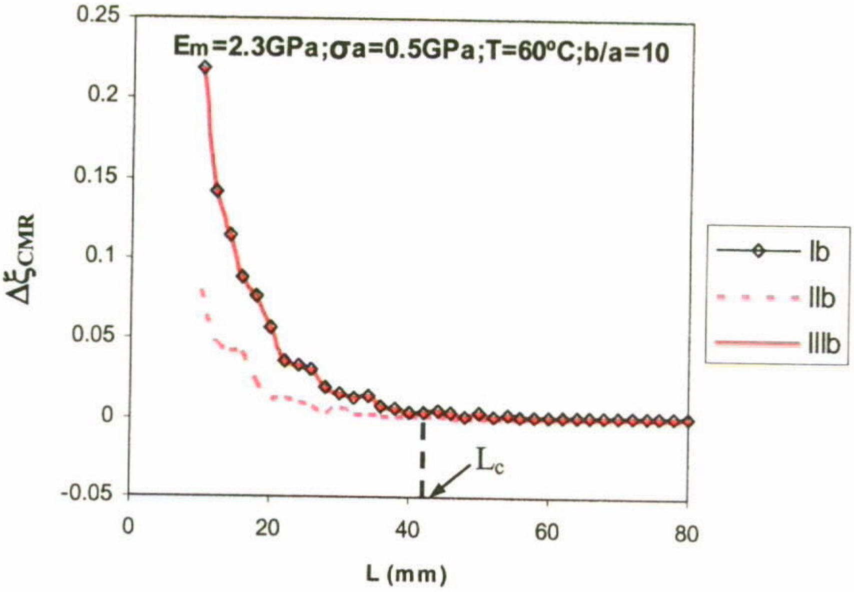

Figure 4.27 Evaluation of critical embedded length, L_c for achieving constant martensite volume fraction over the 60% of embedded length in center portion, (i.e. $\xi(z)$ = constant for $0.2L \leq z \leq 0.8L$). (L_c = 42mm)

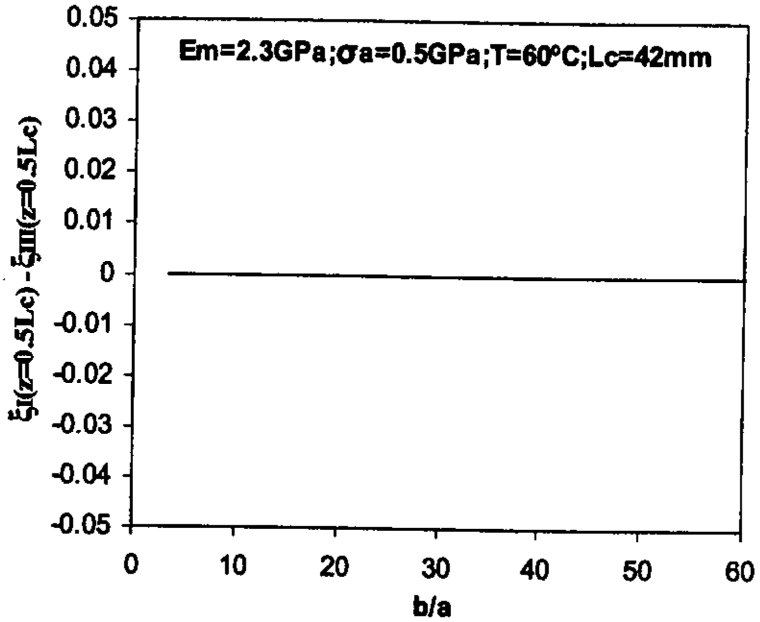

Figure 4.28 Evaluation of critical b/a ratio for satisfying the identical and constant martensite volume fraction in all the type I, II and III loading conditions.

Although the surface plots indicate better performance for mode-b actuation, it is crucial to clarify the validity of type-III loading method in pullout test for the study of interfacial behaviour. Plots of axial stress distributions on the SMA wire for type-I, II and III loading conditions at $T = 60^{\circ}C$ are shown in Figs. 4.32 to 4.35. Considering that when modulus of matrix $E_m = 2.3GPa$ and total embedded length $L = 10mm$, the constant axial stress region can be obtained as shown in Fig. 4.32. However, if the soft matrix material is used to fabricate SMA composite, effect of loading method on stress distribution can be significant. Figure 4.33 shows that the stress distribution profiles for type-I, II and III loading methods develop separately, which implies different mechanical responses could be obtained for very low modulus of matrix in different types of loading. In addition, influences of total embedded length and *b/a* ratio on axial stress development are shown in Figs. 4.34 and 4.35 respectively. Comparing to Fig. 4.32, if all the geometric factors and material properties remain unchanged but the total embedded length is reduced by half, derivation between the stress distributions could be increased substantially as shown in Fig. 4.34. This result implies that the longer the total embedded length, the closer the stress level in axial direction. However, if *b/a* ratio is reduced to 10, even though the embedded length is increased to 30mm, the constant axial stress region (CASR) for type-III loading method depart from the others as shown in Fig. 4.35. Therefore, there is an urged need to clarify critical geometric factors so as to ensure all types of loading can satisfy the identical axial stress over a targeted region.

Using the similar approach as described in Section 4.2.2.4 the minimum required embedded length as well as critical geometric factors for satisfying CASR in mode-b actuation can be obtained from the plots in Figs. 4.36 to 4.38. The estimated results for L_{min}, L_c and b_c/a are 26mm, 45mm and 37 respectively. Comparing to the plots shown Figs. 4., 4. and 4, longer embedded length and bigger matrix cylinder are required for achieving CASR on the same target region (60% of embedded length in center portion) in mode-a actuation. Therefore, it can be concluded that the mode-b actuation ensures the effectiveness of the SMA actuation in a composite structure. If the embedded SMA wire is heated up prior to the application of externally applied load, internal stresses developed inside a composite should be more uniform and the stress level could be much higher than that attained in mode-a actuation.

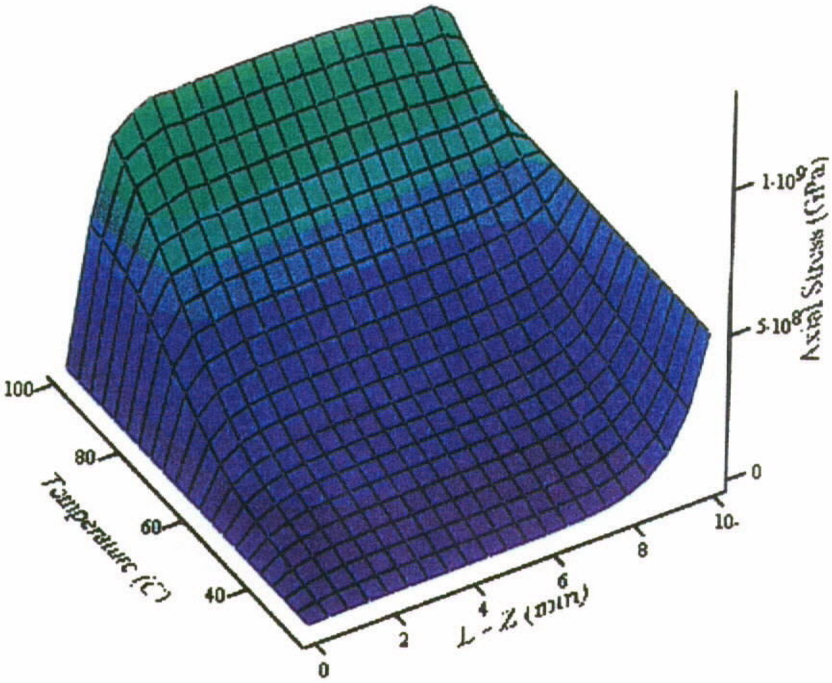

Figure 4.29 Axial Stress Distribution (Type I & mode b)

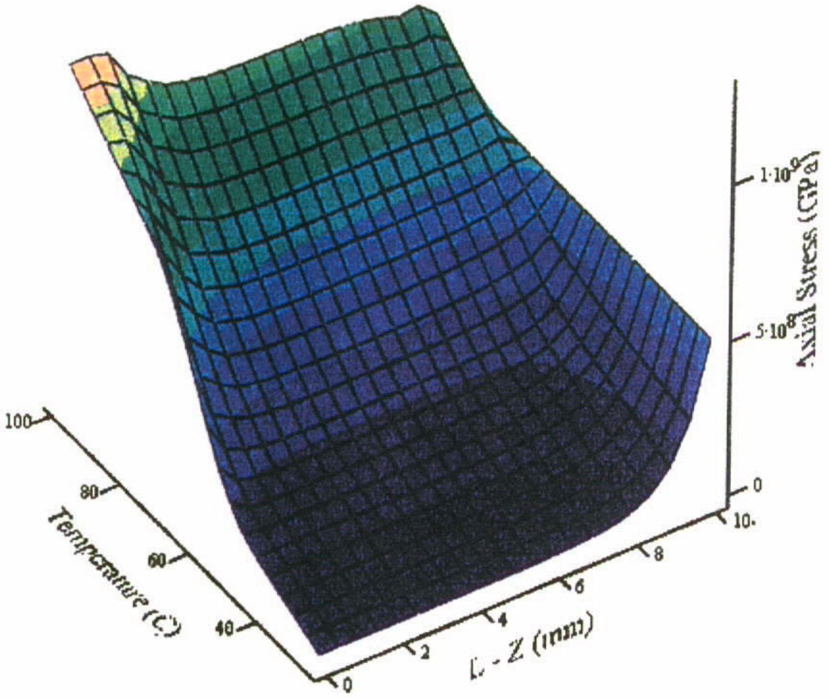

Figure 4.30 Axial Stress Distribution (Type II & mode b)

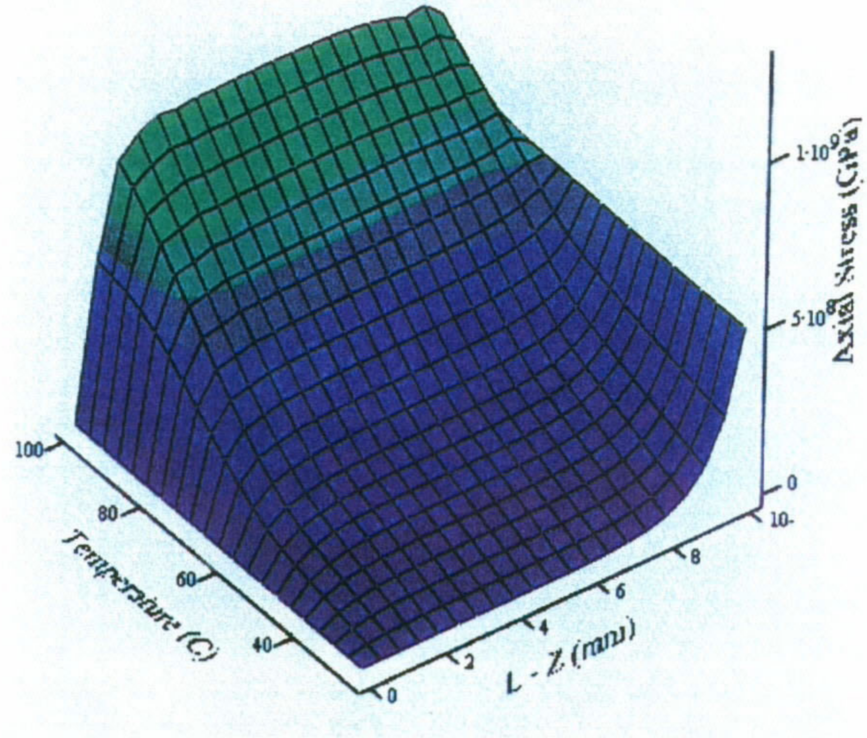

Figure 4.31 Axial Stress Distribution (Type III & mode b)

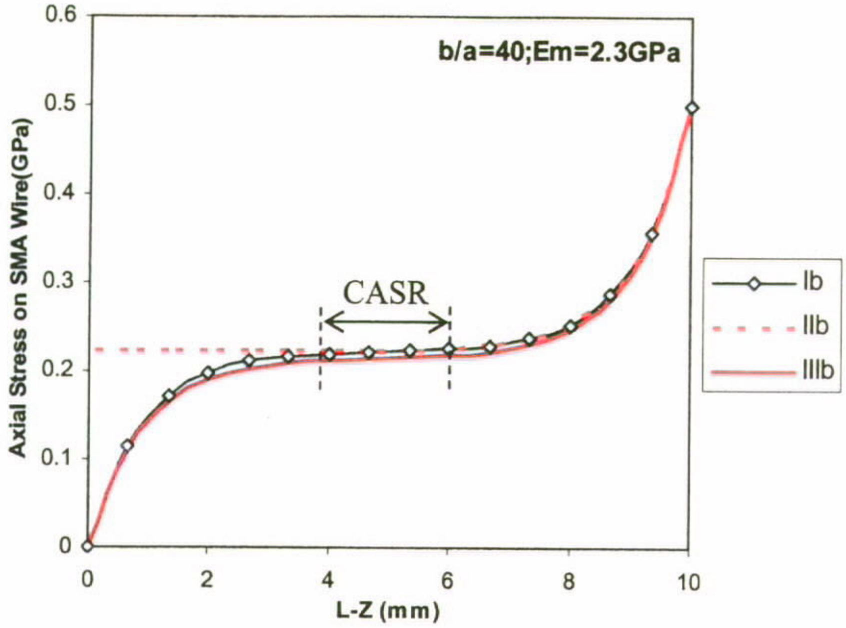

Figure 4.32 Axial stress distribution for type-I, II and III loading condition in mode-b actuation. (CASR: Constant axial stress region)

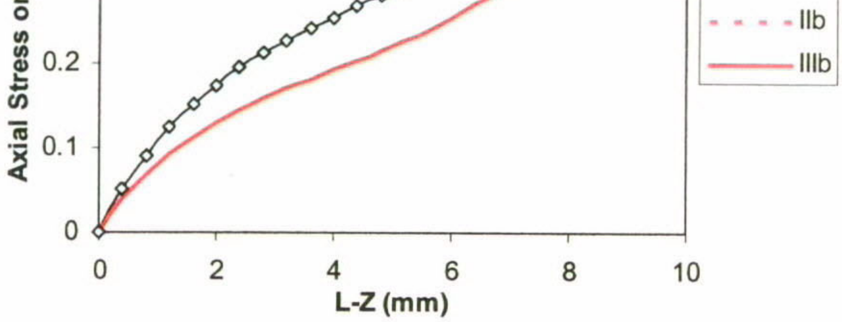

Figure 4.33 Axial stress distributions on SMA wire for $E_m = 0.1$GPa in mode-b actuation.

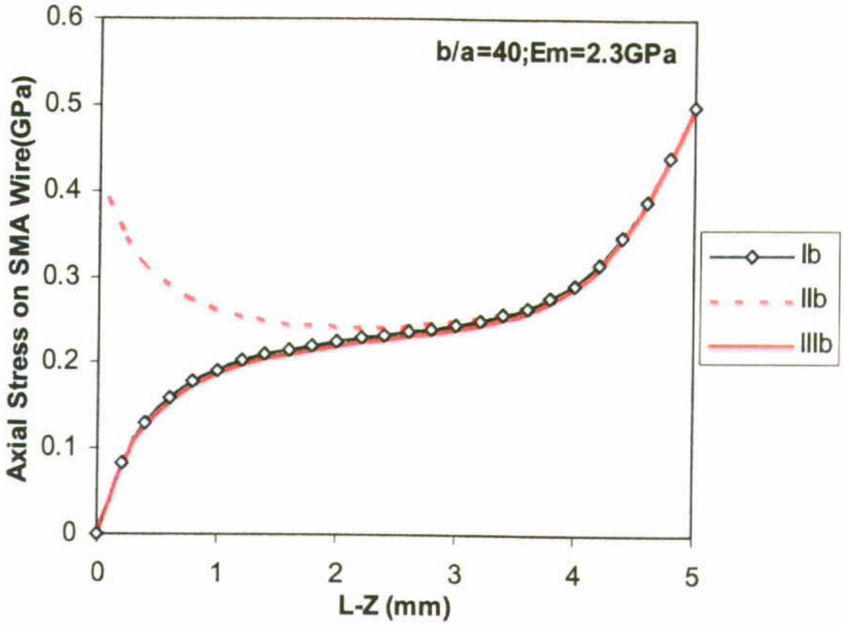

Figure 4.34 Effect of short embedded length on axial stress distributions in mode-b actuation.

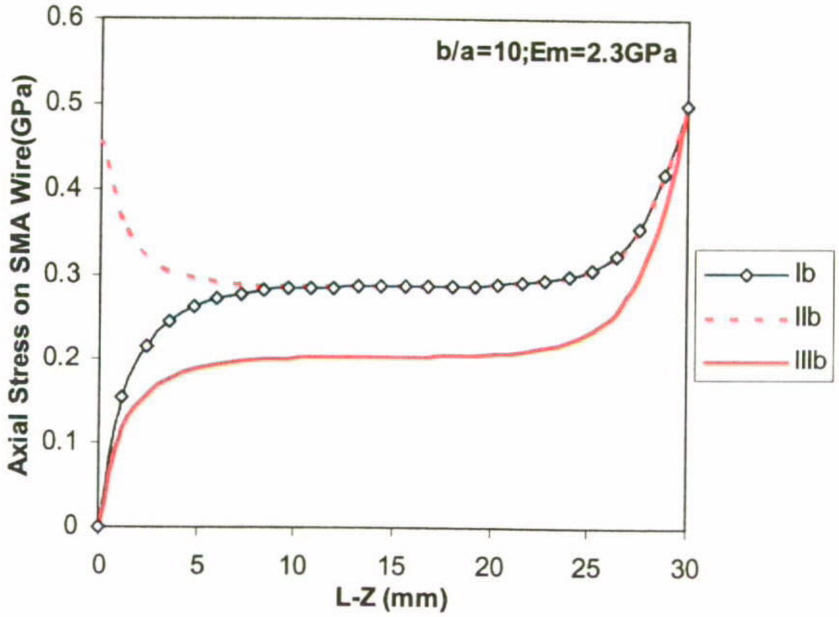

Figure 4.35 effect of low b/a ratio on axial stress distributions in mode-b actuation.

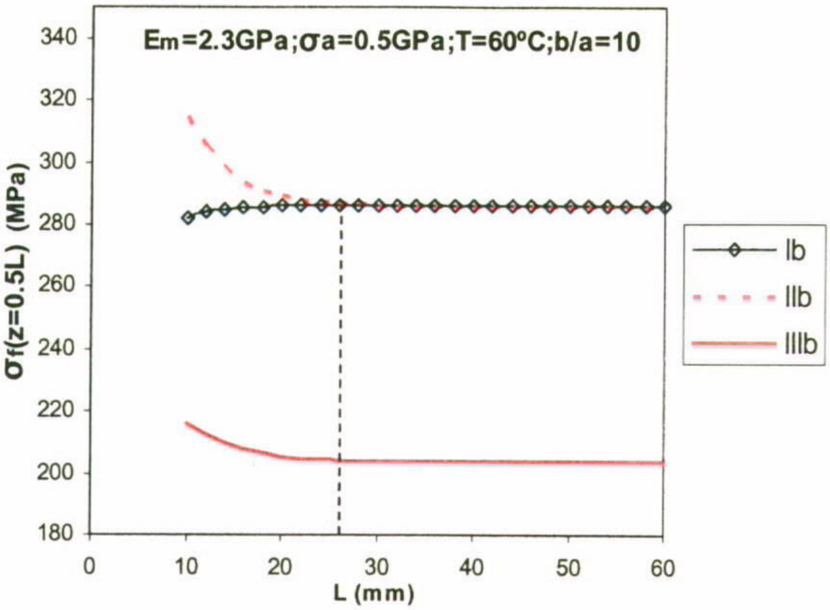

Figure 4.36 Plot of axial stress on SMA wire at mid-point, $\sigma_f^z(z = L/2)$ versus against total embedded length, L. (L_{min} = 26mm)

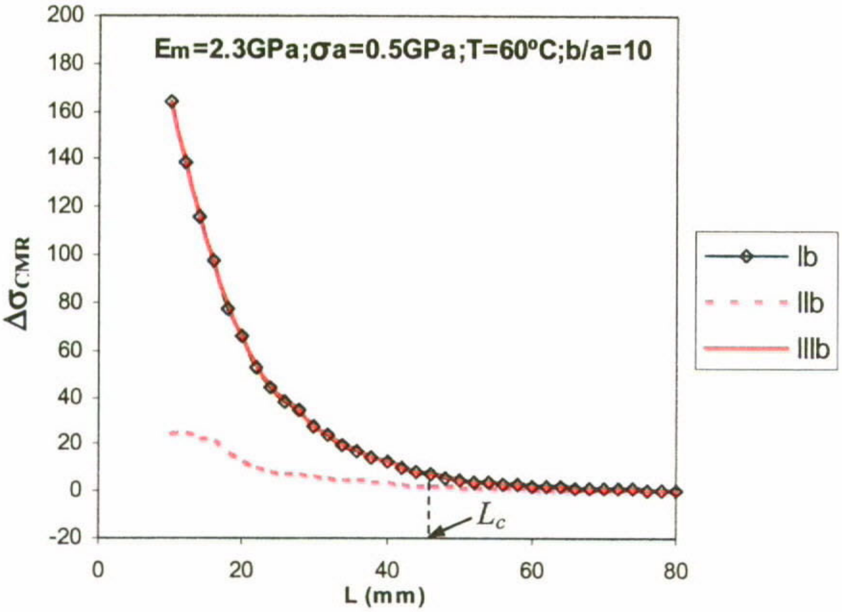

Figure 4.37 Evaluation of critical embedded length, L_c for achieving constant axial stress on SMA wire over the embedded portion of $z = 0.2L$ to $0.8L$. (L_c = 45mm)

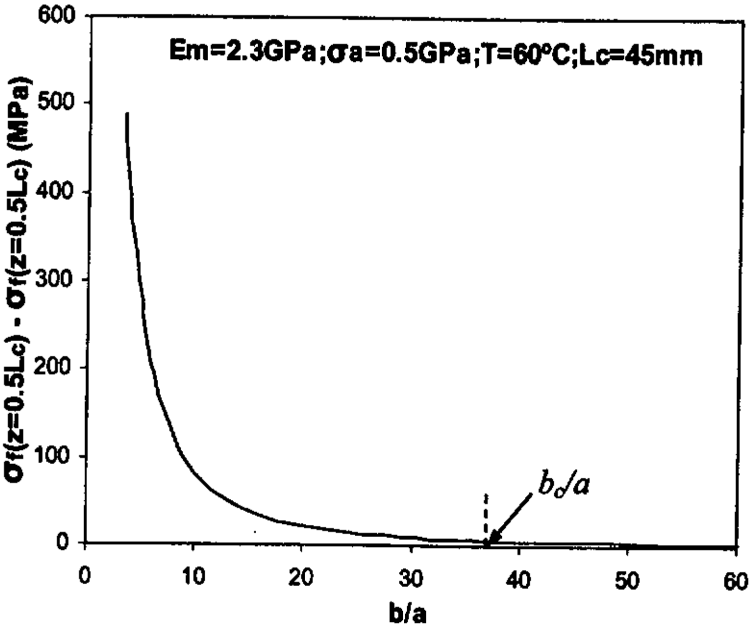

Figure 4.38 Evaluation of critical *b/a* ratio for satisfying the identical and constant axial stress on SMA wire in all the type I, II and III loading conditions. ($b_c/a = 37$)

4.4 Summary

Three types of loading conditions and two modes of the SMA actuations have been defined as the typical loading-actuation scenarios for the SMA-composites. The parametric studies on the influence of geometric factors suggested that the competence of type III loading condition in the fiber pullout test could be achieved if the critical embedded length and matrix-to-wire ratio have been satisfied. Besides, mode-a and mode-b actuations have been identified as the two major actuation modes for SMA inclusions. The shape memory effect (SME) was found more effective and the austenitic transformation could be initiated more easily in mode-b actuation. In addition, the important concepts of constant martensite volume fraction region (CMR) and constant axial stress region (CASR) have been proposed for ensuring that the uniformly distributed material and mechanical properties can be attained at the targeted region on the SMA-composites.

Chapter 5

Effects of SMA Actuation on Interfacial Debond

5.1 Introduction

A phenomenon of great significant in fiber composite technology for application in engineering construction of many load bearing primary structures is the stress transfer between fiber and matrix across the interface. Apart from the elastic stress transfer at the bonded region, another important phenomenon in fiber matrix composite is the stress transfer by means of friction, which is governed by Coulumb friction law after the interfacial debond. However, conventional types of fiber reinforced composites can only survive against external stimuli passively with constant material properties. SMA reinforced composites can work actively against external loads by generating intrinsic recovery stress and modifying their modal properties. Nevertheless, effectiveness of stress transfer from SMA wire to its surrounding matrix strongly depends on quality and nature of bonding at interface region, which are also important to justify the load-bearing capability of fiber-matrix composites.

From the stress-transfer point of view, theoretical analysis dealing with the internal stresses at interface region are of special interest which provides study bases on how the mechanical responses and fracture behaviour of the SMA-composites are affected by interfacial properties, actuation modes as well as loading geometries.

Using the mechanical model previously developed by Zhou et al [115], interfacial properties such as fracture toughness, friction coefficient and residual clamping stress for the typical fiber-matrix composites can be obtained successfully. However, as discussed in the previous Chapters for the internal stress distributions in wire length, the SMA actuation can change the distribution profile and hence the modal properties of a structure. Material properties of actuated SMA in composite structure can be totally different in various loading-actuation scenarios. In addition, due to the heat absorptions of both wire and matrix, influence of thermal expansion on stress state at interface region is no longer to be a negligible issue. A new set of internal stress solutions for both the bonded and debonded regions is therefore critically important in the fracture mechanics approach to calculate the total strain energy stored in constituents due to the applied load and the SMA actuation.

This chapter focuses on the formulation of total elastic strain energy stored in SMA wire and matrix. The strain energy release rate normalized with the constant interfacial fracture energy is employed to determine interfacial debond criterion.

5.2 Interfacial Debond Criterion

When interfacial debond occurs in the SMA-reinforced composite, the specific debonding criterion has to be satisfied. In the present study, the general fracture mechanics approach is employed such that the differentiation of total elastic strain energy U_t stored in constituents with respect to the debond length l is equated to the interfacial fracture toughness, G_{ic} as illustrated below,

$$G_{ic} = \frac{1}{2\pi a}\left[\frac{\partial U_t}{\partial l}\right] \tag{5.1}$$

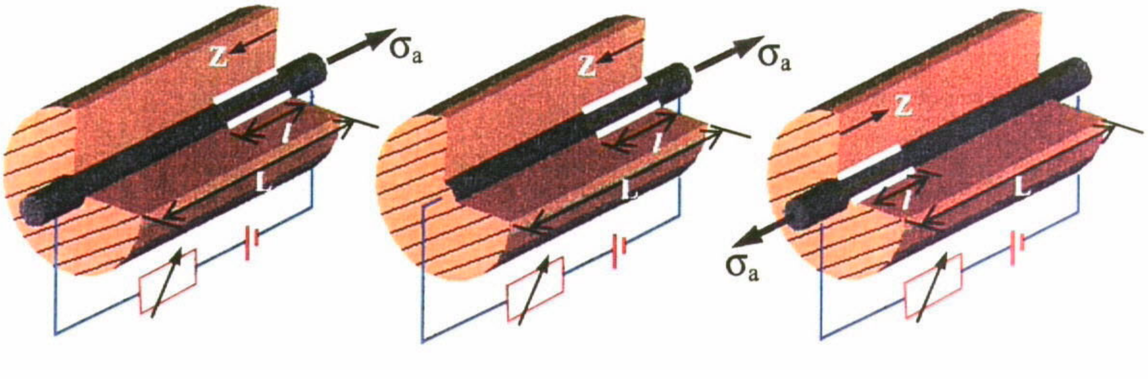

(a) (b) (c)

Figure 5.1 Schematic illustration of partial debonded SMA-matrix cylinder in (a) Type I, (b) Type II and (c) Type III loading conditions.

where the interfacial fracture toughness G_{ic}, is considered as a material constant before SMA actuation. ∂l can be considered as an extremely short debonded length located at crack tip while the embedded length is divided into two separated parts known as bonded and debonded regions as shown in Fig. 5.1. Therefore the formation of U_t requires the consideration of strain energies stored in constituents in both the bonded and debonded region.

5.2.1 Total Elastic Strain Energy

As previously discussed for the possibility of interfacial debond due to over-actuation of embedded SMA wire, the debondings in type I and III loading methods do not necessarily appear at the loading end. However in the ideal operating conditions, problems of over-actuation has to be avoided and recovery action of SMA is always considered as additional mechanism which works against the interfacial debond due to externally applied load. Therefore, it is reasonable to consider the crack propagation from loading end towards the embedded end as shown in Fig. 5.1.

Table 5.1 Boundary conditions for type-I, II and III loading conditions

	Type I	Type II	Type III
Debonded region	$\sigma_f^z(0,\sigma_a,T)=\sigma_a$ $\sigma_m^z(0,\sigma_a,T)=0$	$\sigma_f^z(0,\sigma_a,T)=\sigma_a$ $\sigma_m^z(0,\sigma_a,T)=0$	$\sigma_f^z(0,\sigma_a,T)=\sigma_a$ $-\frac{1}{\gamma}\sigma_m^z(0,\sigma_a,T)=0$
Bonded region	$\sigma_f^z(l,\sigma_a,T)=\sigma_{l1}$ $\sigma_f^z(L,\sigma_a,T)=0$	$\sigma_f^z(l,\sigma_a,T)=\sigma_{l2}$	$\sigma_f^z(l,\sigma_a,T)=\sigma_{l3}$ $\sigma_f^z(L,\sigma_a,T)=0$

The total elastic strain energy can be obtained by considering the energy components of U_{di} and U_{bi} in debonded and bonded regions as given below,

$$U_{ti}=U_{di}+U_{bi} \tag{5.2}$$

where

$$U_{di}=\int_0^l\int_0^a\frac{\left(\sigma_{fdi}^z(z,\sigma_a,T)\right)^2}{E_f}\pi rdrdz+\int_0^l\int_a^b\left[\frac{\left(\sigma_{mdi}^z(z,\sigma_a,T)\right)^2}{E_f}+\frac{2\left(1+\nu_m\right)\left(\tau_{mdi}(z,\sigma_a,T)\right)^2}{E_m}\right]\pi rdrdz \tag{5.3}$$

and

$$U_{bi}=\int_l^L\int_0^a\frac{\left(\sigma_{fbi}^z(z,\sigma_a,T)\right)^2}{E_f}\pi rdrdz+\int_l^L\int_a^b\left[\frac{\left(\sigma_{mbi}^z(z,\sigma_a,T)\right)^2}{E_f}+\frac{2\left(1+\nu_m\right)\left(\tau_{mbi}(z,\sigma_a,T)\right)^2}{E_m}\right]\pi rdrdz \tag{5.4}$$

U_{di} and U_{bi} represent the elastic strain energy stored in constituents in the bonded and debonded regions respectively. Assuming that the interfacial debond is developed to a finite value of l, then the boundary conditions for the stress solutions in different types of loading methods are summarized in Table 5.1. σ_{li} (for i = 1, 2 and 3) is defined as crack tip stress at the z = l for type-I, II and III loading methods. It means that both the stress solutions at the junction between the bonded and debonded regions must be continue and equals to σ_{li}.

5.2.1.1 Stress Solutions in Debonded Region

In the debonded region, frictional slip occurs at the interface where the stress transfer is assumed satisfying the coulomb friction law for a constant coefficient of friction μ [99, 116 and 117],

$$\tau_f(z,\sigma_a,T) = -\mu\left(q_o + q_a(z,\sigma_a,T)\right) \tag{5.5}$$

where $\tau_f\left(z,\sigma_a,T\right)$ is the interfacial frictional shear stress. q_o is the residual clamping stress due to matrix shrinkage and differential thermal contraction of constituents. $q_a(z,\sigma_a,T)$ is the interfacial radial stress arising from applied load and shape memory effect as given in Eqn. 3.10.

In addition, recalling Eqn. 3.18 for the equilibrium condition describing the stress distribution between the SMA wire and matrix, the interfacial shear stress $\tau_i(z,\sigma_a,T)$ should be replaced with $\tau_f(z,\sigma_a,T)$ which representing frictional shear stress in debonded region as given below,

$$\frac{d\sigma^z_{fd1}(z,\sigma_a,T)}{dz} = -\frac{2}{a}\tau_i(z,\sigma_a,T) \tag{5.6}$$

Substituting Eqn. 5.5 into Eqn. 5.6 and using the boundary conditions given in Table 5.1, solutions of axial and shear stresses for the debonded region can be obtained as

$$\sigma^z_{fd1}(z,\sigma_a,T) = \sigma_a - \omega(z,\sigma_a,T)\left(\sigma^*_1(z,\sigma_a,T) - \sigma_a\right)\left[\exp\left(\lambda(z,\sigma_a,T)z\right) - 1\right] \tag{5.7}$$

$$\sigma^z_{md1}(z,\sigma_a,T) = \gamma\omega(z,\sigma_a,T)\left(\sigma^*_1(z,\sigma_a,T) - \sigma_a\right)\left[\exp\left(\lambda(z,\sigma_a,T)z\right) - 1\right] \tag{5.8}$$

$$\tau^{z}_{md1}(z,\sigma_a,T)=\frac{\gamma\lambda(z,\sigma_a,T)\omega(z,\sigma_a,T)\left(b^2-r^2\right)}{2r}\left(\sigma^{*}_{1}(z,\sigma_a,T)-\sigma_a\right)\exp\left(\lambda(z,\sigma_a,T)z\right) \tag{5.9}$$

$$\tau_{f1}(z,\sigma_a,T)=\frac{a\lambda(z,\sigma_a,T)\omega(z,\sigma_a,T)}{2}\left(\sigma^{*}_{1}(z,\sigma_a,T)-\sigma_a\right)\exp\left(\lambda(z,\sigma_a,T)z\right) \tag{5.10}$$

for type-I loading method,

$$\sigma^{z}_{fd2}(z,\sigma_a,T)=\sigma^{z}_{fd1}(z,\sigma_a,T) \tag{5.11}$$

$$\sigma^{z}_{md2}(z,\sigma_a,T)=\sigma^{z}_{md1}(z,\sigma_a,T) \tag{5.12}$$

$$\tau^{z}_{md2}(z,\sigma_a,T)=\tau^{z}_{md1}(z,\sigma_a,T) \tag{5.13}$$

$$\tau^{z}_{f2}(z,\sigma_a,T)=\tau^{z}_{f1}(z,\sigma_a,T) \tag{5.14}$$

for type-II loading method and

$$\sigma^{z}_{fd3}(z,\sigma_a,T)=\sigma_a-\left(\sigma^{*}_{3}(z,\sigma_a,T)-\sigma_a\right)\left[\exp\left(\lambda(z,\sigma_a,T)z\right)-1\right] \tag{5.15}$$

$$\sigma^{z}_{md3}(z,\sigma_a,T)=-\gamma\sigma_a+\gamma\left(\sigma^{*}_{3}(z,\sigma_a,T)-\sigma_a\right)\left[\exp\left(\lambda(z,\sigma_a,T)z\right)-1\right] \tag{5.16}$$

$$\tau^{z}_{md3}(z,\sigma_a,T)=\frac{\gamma\lambda(z,\sigma_a,T)\left(b^2-r^2\right)}{2r}\left(\sigma^{*}_{3}(z,\sigma_a,T)-\sigma_a\right)\exp\left(\lambda(z,\sigma_a,T)z\right) \tag{5.17}$$

$$\tau_{f3}(z,\sigma_a,T)=\frac{a\lambda(z,\sigma_a,T)}{2}\left(\sigma^{*}_{3}(z,\sigma_a,T)-\sigma_a\right)\exp\left(\lambda(z,\sigma_a,T)z\right) \tag{5.18}$$

for type-III loading method, where

$$\sigma_1^*(z,\sigma_a,T)=\sigma_2^*(z,\sigma_a,T)=-\frac{q_o}{\omega(z,\sigma_a,T)k(z,\sigma_a,T)}-\frac{\eta(z,\sigma_a,T)}{\omega(z,\sigma_a,T)}E_T(z,\sigma_a,T) \tag{5.19}$$

$$\sigma_3^*(z,\sigma_a,T)=-\frac{q_o}{k(z,\sigma_a,T)}-\eta(z,\sigma_a,T)E_T(z,\sigma_a,T) \tag{5.20}$$

$$\omega(z,\sigma_a,T)=\frac{\alpha(z,\sigma_a,T)v_f}{\alpha(z,\sigma_a,T)v_f+\gamma v_m} \tag{5.21}$$

$$k(z,\sigma_a,T)=\frac{\alpha(z,\sigma_a,T)v_f+\gamma v_m}{\alpha(z,\sigma_a,T)\left(1+v_f\right)+2\gamma+v_m+1} \tag{5.22}$$

$$\eta(z,\sigma_a,T)=\frac{\omega(z,\sigma_a,T)}{\alpha(z,\sigma_a,T)v_f} \tag{5.23}$$

$$E_T(z,\sigma_a,T)=E_m\left(G_b(T)+v_fG_a(z,\sigma_a,T)\right) \tag{5.24}$$

$$\lambda(z,\sigma_a,T)=\frac{2\mu k(z,\sigma_a,T)}{a} \tag{5.25}$$

5.2.1.2 Stress Solutions in Bonded Region

Equations 3.25 to 3.28 and 4.4 to 4.11 represent the stress solutions before interfacial debond which means l = 0 for three types of loading methods. However, considering the present of finite debonded length l in z-direction, the boundary condition of $\sigma_f^*(0,\sigma_a,T)=\sigma_a$ given in Table 4.1 has to be replaced by $\sigma_f^*(l,\sigma_a,T)=\sigma_a$ as given in Table 5.1. The crack tip stress, σ_{li} for the corresponding type of loading methods is given in Eqns. 5.7, 5.11 and 5.15 respectively. Therefore, the stress solutions in perfectly bonded region ($l \leq z \leq L$) are readily obtained as following,

$$\sigma^{z}_{pb1}(z,\sigma_a,T)=\frac{\left(\psi_3(z,\sigma_a,T)\sigma_a+\psi_4(z,\sigma_a,T)\right)\left[\sinh\sqrt{\psi_1(z,\sigma_a,T)}\left(L-z\right)-\sinh\sqrt{\psi_1(z,\sigma_a,T)}\left(l-z\right)\right]+\sigma_{l1}(z,\sigma_a,T)\sinh\sqrt{\psi_1(z,\sigma_a,T)}(L-z}{\sinh\sqrt{\psi_1(z,\sigma_a,T)}\left(L-l\right)}$$
$$-\psi_3(z,\sigma_a,T)\sigma_a-\psi_4(z,\sigma_a,T)$$

(5.26)

$$\sigma^{z}_{mb1}(z,\sigma_a,T)=\gamma\left\{\begin{array}{l}\dfrac{\left(\psi_3(z,\sigma_a,T)\sigma_a+\psi_4(z,\sigma_a,T)\right)\left[\sinh\sqrt{\psi_1(z,\sigma_a,T)}\left(l-z\right)-\sinh\sqrt{\psi_1(z,\sigma_a,T)}\left(L-z\right)\right]-\sigma_{l1}(z,\sigma_a,T)\sinh\sqrt{\psi_1(z,\sigma_a,T)}\left(L-z\right)}{\sinh\sqrt{\psi_1(z,\sigma_a,T)}\left(L-l\right)}\\+\left(1+\psi_3(z,\sigma_a,T)\right)\sigma_a+\psi_4(z,\sigma_a,T)\end{array}\right\}$$

(5.27)

$$\tau^{rz}_{mb1}(z,\sigma_a,T)=\frac{\gamma\left(b^2-r^2\right)\sqrt{\psi_1(z,\sigma_a,T)}}{2r\sinh\sqrt{\psi_1(z,\sigma_a,T)}\left(L-l\right)}\left\{\begin{array}{l}\left(\psi_3(z,\sigma_a,T)\sigma_a+\psi_4(z,\sigma_a,T)\right)\left[\cosh\sqrt{\psi_1(z,\sigma_a,T)}\left(L-z\right)-\cosh\sqrt{\psi_1(z,\sigma_a,T)}\left(l-z\right)\right]\\+\sigma_{l1}(z,\sigma_a,T)\cosh\sqrt{\psi_1(z,\sigma_a,T)}\left(L-z\right)\end{array}\right\}$$

(5.28)

$$\tau_{l1}(z,\sigma_a,T)=\frac{a\sqrt{\psi_1(z,\sigma_a,T)}}{2\sinh\sqrt{\psi_1(z,\sigma_a,T)}\left(L-l\right)}\left\{\begin{array}{l}\left(\psi_3(z,\sigma_a,T)\sigma_a+\psi_4(z,\sigma_a,T)\right)\left[\cosh\sqrt{\psi_1(z,\sigma_a,T)}\left(L-z\right)-\cosh\sqrt{\psi_1(z,\sigma_a,T)}\left(l-z\right)\right]\\+\sigma_{l1}(z,\sigma_a,T)\cosh\sqrt{\psi_1(z,\sigma_a,T)}\left(L-z\right)\end{array}\right\}$$

(5.29)

for type-I loading method,

$$\sigma^{z}_{pb2}(z,\sigma_a,T)=\frac{\left(\psi_3(z,\sigma_a,T)\sigma_a+\psi_4(z,\sigma_a,T)+\sigma_{l2}(z,\sigma_a,T)\right)\cosh\sqrt{\psi_1(z,\sigma_a,T)}\left(L-z\right)}{\cosh\sqrt{\psi_1(z,\sigma_a,T)}\left(L-l\right)}-\psi_3(z,\sigma_a,T)\sigma_a-\psi_4(z,\sigma_a,T)$$

(5.30)

$$\sigma^{z}_{mb2}(z,\sigma_a,T)=-\gamma\left\{\frac{\left(\psi_3(z,\sigma_a,T)\sigma_a+\psi_4(z,\sigma_a,T)+\sigma_{l2}(z,\sigma_a,T)\right)\cosh\sqrt{\psi_1(z,\sigma_a,T)}\left(L-z\right)}{\cosh\sqrt{\psi_1(z,\sigma_a,T)}\left(L-l\right)}-\left(1+\psi_3(z,\sigma_a,T)\right)\sigma_a-\psi_4(z,\sigma_a,T)\right\}$$

(5.31)

$$\tau^{rz}_{mb2}(z,\sigma_a,T)=\frac{\gamma\left(b^2-r^2\right)\sqrt{\psi_1(z,\sigma_a,T)}\left(\psi_3(z,\sigma_a,T)\sigma_a+\psi_4(z,\sigma_a,T)+\sigma_{f2}(z,\sigma_a,T)\right)\sinh\sqrt{\psi_1(z,\sigma_a,T)}\left(L-z\right)}{2r\cosh\sqrt{\psi_1(z,\sigma_a,T)}\left(L-l\right)} \tag{5.32}$$

$$\tau_{i2}(z,\sigma_a,T)=\frac{a\sqrt{\psi_1(z,\sigma_a,T)}\left(\psi_3(z,\sigma_a,T)\sigma_a+\psi_4(z,\sigma_a,T)+\sigma_{f2}(z,\sigma_a,T)\right)\sinh\sqrt{\psi_1(z,\sigma_a,T)}\left(L-z\right)}{2\cosh\sqrt{\psi_1(z,\sigma_a,T)}\left(L-l\right)} \tag{5.33}$$

for type-II loading method and

$$\sigma^{z}_{fb3}(z,\sigma_a,T)=\frac{\left(\psi_4(z,\sigma_a,T)+\sigma_{f3}(z,\sigma_a,T)\right)\sinh\sqrt{\psi_1(z,\sigma_a,T)}\left(L-z\right)-\psi_1(z,\sigma_a,T)\sinh\sqrt{\psi_1(z,\sigma_a,T)}\left(l-z\right)}{\sinh\sqrt{\psi_1(z,\sigma_a,T)}\left(L-l\right)}-\psi_4(z,\sigma_a,T) \tag{5.34}$$

$$\sigma^{z}_{mb3}(z,\sigma_a,T)=-\gamma\left\{\frac{\left(\psi_4(z,\sigma_a,T)+\sigma_{f3}(z,\sigma_a,T)\right)\sinh\sqrt{\psi_1(z,\sigma_a,T)}\left(L-z\right)-\psi_4(z,\sigma_a,T)\sinh\sqrt{\psi_1(z,\sigma_a,T)}\left(l-z\right)}{\sinh\sqrt{\psi_1(z,\sigma_a,T)}\left(L-l\right)}-\psi_4(z,\sigma_a,T)\right\} \tag{5.35}$$

$$\tau^{rz}_{mb3}(z,\sigma_a,T)=\frac{\gamma\left(b^2-r^2\right)\sqrt{\psi_1(z,\sigma_a,T)}\left(\psi_4(z,\sigma_a,T)+\sigma_{f3}(z,\sigma_a,T)\right)\cosh\sqrt{\psi_1(z,\sigma_a,T)}\left(L-z\right)-\psi_4(z,\sigma_a,T)\cosh\sqrt{\psi_1(z,\sigma_a,T)}\left(l-z\right)}{2r\sinh\sqrt{\psi_1(z,\sigma_a,T)}\left(L-l\right)} \tag{5.36}$$

$$\tau_{i3}(z,\sigma_a,T)=\frac{a\sqrt{\psi_1(z,\sigma_a,T)}\left[\left(\psi_4(z,\sigma_a,T)+\sigma_{f3}(z,\sigma_a,T)\right)\cosh\sqrt{\psi_1(z,\sigma_a,T)}\left(L-z\right)-\psi_4(z,\sigma_a,T)\cosh\sqrt{\psi_1(z,\sigma_a,T)}\left(l-z\right)\right]}{2\sinh\sqrt{\psi_1(z,\sigma_a,T)}\left(L-l\right)} \tag{5.37}$$

for type-III loading method respectively.

Referring to Section 4.3.2 for the evolution of SMA's material properties in mode-b actuation, one may notice that the total martensite volume fraction, ξ, which governing the SMA's material properties, attains a constant level at center portion of embedded length. Long plateaus can be observed as shown in plots c and d in Figs. 4.21 to 4.23. Figure 4.28 further clarifies the critical embedded length, L_c required for achieving constant martensite volume fraction over the center portion of embedded length. Using the same material properties as summarized in Table. 3.1 as numerical example in the current study, if the wire embedded length is longer than L_c (i.e. 42mm), the martensite volume fraction along the embedded wire can be assumed as constant and independent of externally applied load. Therefore, the ξ–evolution can be reduced to a simple function of temperature as given below,

$$\xi(z;\sigma_a,T)=\xi(L/2,0,T)=\tilde{\xi} \qquad \text{for } L>L_c \tag{5.38}$$

where $\tilde{\xi}$ represents the equivalent martensite volume fraction distributing along the embedded length for $L > L_c$ in actuation temperature T. Since the $\tilde{\xi}$ governs all the material properties of SMA, coefficients in all the stress solutions (from Eqn. 5.7 to 5.37) can be reduced to the equivalent functions denoted with '~'on the top of them.

Substituting Eqns. 5.7–5.37 into Eqns. 5.3 and 5.4 for the corresponding types of loading methods, the strain energy stored in both SMA wire and matrix due to the applied load and SMA actuation can be obtained. Finally, the interfacial debond criterion of the SMA-matrix composite can be derived by substituting the U_t into Eqn. 5.1 as given below,

$$G_{ic}=\frac{1}{2\pi a}\left[\tilde{B}_i\sigma_a^{\,2}+\tilde{C}_i\left(\tilde{\sigma}_i^{\bullet}-\sigma_a\right)\sigma_a+\tilde{D}_i\left(\tilde{\sigma}_i^{\bullet}-\sigma_a\right)^2+\tilde{L}_i\sigma_a+\tilde{M}_i\left(\tilde{\sigma}_i^{\bullet}-\sigma_a\right)+\tilde{N}_i\right] \tag{5.39}$$

where i = 1, 2 and 3 for the corresponding type of loading methods. $\tilde{B}_i$, $\tilde{C}_i$, $\tilde{D}_i$, $\tilde{L}_{i1}$, $\tilde{M}_{i2}$ and $\tilde{N}_{i3}$ are the equivalent functions of material constants, geometric factors in actuation temperatures, T as given below,

$$\tilde{B}_1 = \left\{ \begin{aligned} &\tilde{b}_2 - \left(\tilde{b}_2 - \tilde{b}_1\tilde{\psi}_1\right)\left[1 + \tilde{\psi}_3\left(1 + \tilde{\psi}_3\right)\left(2 - 2\cosh\tilde{\phi} + \tanh\tilde{\phi}\sinh\tilde{\phi}\right)\right]\tilde{\phi}\coth\tilde{\phi} \\ &+ \left[2\tilde{\psi}_3\left(1 + \tilde{\psi}_3\right)\tilde{b}_2 - \left(1 + 2\tilde{\psi}_3\right)\tilde{b}_3\right]\left(1 - \cosh\tilde{\phi}\right) \end{aligned} \right\} \operatorname{csch}^2\tilde{\phi} - \tilde{b}_4 \quad (5.40)$$

$$\tilde{C}_1 = \tilde{\omega} e^{\tilde{\lambda} l}\left[\left(\frac{d\tilde{H}_1}{dl} - \frac{\pi a^2}{\tilde{E}_f}\right)\left(1 - e^{-\tilde{\lambda} l}\right) + \tilde{\lambda}\tilde{H}_1\right] \quad (5.41)$$

$$\tilde{D}_1 = \tilde{\omega}^2 e^{2\tilde{\lambda} l}\left\{ \left[\begin{aligned} &\left(1 - e^{-\tilde{\lambda} l}\right)^2\left(\tilde{b}_2\cosh^2\tilde{\phi} - \left(\tilde{b}_2 - \tilde{b}_1\tilde{\psi}_1\right)\tilde{\phi}\coth\tilde{\phi}\right) \\ &+ \tilde{\lambda}\left(1 - e^{-\tilde{\lambda} l}\right)\left(\left(\tilde{b}_2 + \tilde{b}_1\tilde{\psi}_1\right)\sinh 2\tilde{\phi} - \left(\tilde{b}_2 - \tilde{b}_1\tilde{\psi}_1\right)\tilde{\phi}\right) \Big/ 2\sqrt{\tilde{\psi}_1} \end{aligned} \right] \cosh^2\tilde{\phi} + \tilde{b}_1\tilde{\lambda}^2 \right\}$$

(5.42)

$$\tilde{H}_1 = \frac{\operatorname{csch}\tilde{\phi}}{\sqrt{\tilde{\psi}_1}}\left\{ \begin{aligned} &\left[\left(1 + \tilde{\psi}_3\right)\left(\left(\tilde{b}_2 - \tilde{b}_1\tilde{\psi}_1\right)\left(1 + \tilde{\phi}\operatorname{csch}\tilde{\phi}\right) + 2\tilde{b}_1\tilde{\psi}_1\right) - \tilde{b}_3\right]\left(1 - \cosh\tilde{\phi}\right) \\ &- \left(\tilde{b}_2 - \tilde{b}_1\tilde{\psi}\right)\left(1 - \tilde{\phi}\coth\tilde{\phi}\right) - 2\tilde{b}_1\tilde{\psi}_1 \end{aligned} \right\}$$

(5.43)

$$\tilde{L}_1 = \tilde{h}_{11} + \tilde{h}_{12} + \tilde{i}_{13}\tilde{h}_{13} \quad (5.44)$$

$$\tilde{M}_1 = \tilde{i}_{11} + \tilde{i}_{12} + \tilde{h}_{13}\tilde{j}_{13} \quad (5.45)$$

$$\tilde{N}_1 = \tilde{j}_{11} + \tilde{j}_{12} + \tilde{h}_{13}\tilde{\psi}_4 \quad (5.46)$$

$$\tilde{h}_{11} = \left[2\tilde{\psi}_3\tilde{\chi}_a\sqrt{\tilde{\psi}_1}\sinh\tilde{\phi}\left(\tilde{\phi} - \sinh\tilde{\phi}\right) + \tilde{\chi}_a\sqrt{\tilde{\psi}_1}\tilde{\phi}\sinh\tilde{\phi}\right] \Big/ \left(\cosh\tilde{\phi} + 1\right)^2 \quad (5.47)$$

$$\tilde{i}_{11} = \tilde{\chi}_a\tilde{\omega}\left[\tilde{\lambda} e^{\tilde{\lambda} l}\left(\tilde{\phi} - \sinh\tilde{\phi}\right) + \sqrt{\tilde{\psi}_1}\left(e^{\tilde{\lambda} l} - 1\right)\tilde{\phi}\left(\coth\tilde{\phi} - \operatorname{csch}\tilde{\phi}\right)\right] \Big/ \left(\cosh\tilde{\phi} + 1\right) \quad (5.48)$$

$$\tilde{j}_{11} = \tilde{\psi}_4\tilde{\chi}_a\sqrt{\tilde{\psi}_1}\sinh\tilde{\phi}\left(\tilde{\phi} - \sinh\tilde{\phi}\right) \Big/ \left(\cosh\tilde{\phi} + 1\right)^2 \quad (5.49)$$

$$\tilde{h}_{12} = \tilde{h}_{11}\frac{\tilde{\chi}_b}{\tilde{\chi}_a} \quad (5.50)$$

$$\tilde{i}_{12} = \tilde{i}_{11}\frac{\tilde{\chi}_b}{\tilde{\chi}_a} \tag{5.51}$$

$$\tilde{j}_{12} = \tilde{j}_{11}\frac{\tilde{\chi}_b}{\tilde{\chi}_a} \tag{5.52}$$

$$\tilde{h}_{13} = -\tilde{\chi}_c\left(2\tilde{\psi}_3+1\right)\sqrt{\tilde{\psi}_1}\tilde{\phi}\sinh\tilde{\phi}\Big/\left(\cosh\tilde{\phi}+1\right)^2 \tag{5.53}$$

$$\tilde{i}_{13} = \tilde{\chi}_c\tilde{\omega}\left[-\tilde{\lambda}e^{\tilde{\lambda}l}\sinh\tilde{\phi}\left(\sinh\tilde{\phi}-\tilde{\phi}\right)+\sqrt{\tilde{\psi}_1}\tilde{\phi}\left(1-\cosh\tilde{\phi}\right)\left(1-e^{\tilde{\lambda}l}\right)\right]\Big/\left(\cosh\tilde{\phi}+1\right)\sinh\tilde{\phi} \tag{5.54}$$

$$\tilde{j}_{13} = \tilde{h}_{13}\frac{\tilde{\psi}_4}{2\tilde{\psi}_3+1} \tag{5.55}$$

for type-I loading method,

$$\tilde{B}_2 = \left\{\left(1+\tilde{\psi}_3\right)\left[\left(\tilde{b}_2-\tilde{b}_1\tilde{\psi}_1\right)\tilde{\phi}\tanh\tilde{\phi}-\tilde{b}_2\right]+\tilde{b}_3\right\}\left(1+\tilde{\psi}_3\right)\operatorname{sech}^2\tilde{\phi}-\tilde{b}_4 \tag{5.56}$$

$$\tilde{C}_2 = \tilde{\omega}e^{\tilde{\lambda}l}\left[\left(\frac{d\tilde{H}_2}{dl}-\frac{\pi a^2}{\tilde{E}_f}\right)\left(1-e^{-\tilde{\lambda}l}\right)+\tilde{\lambda}\tilde{H}_2\right] \tag{5.57}$$

$$\tilde{D}_2 = \tilde{\omega}^2e^{2\tilde{\lambda}l}\left\{\left(1-e^{-\tilde{\lambda}l}\right)\begin{bmatrix}\left(\tilde{\lambda}\big/\sqrt{\tilde{\psi}_1}+\left(1-e^{-\tilde{\lambda}l}\right)\tanh\tilde{\phi}\right)\left(\tilde{b}_2-\tilde{b}_1\tilde{\psi}_1\right)\tilde{\phi} \\ +\tilde{\lambda}\left(\tilde{b}_2+\tilde{b}_1\tilde{\psi}_1\right)\sinh 2\tilde{\phi}\big/2\sqrt{\tilde{\psi}_1}-\left(1-e^{-\tilde{\lambda}l}\right)\tilde{b}_2\sinh^2\tilde{\phi}\end{bmatrix}\operatorname{sech}^2\tilde{\phi}+\tilde{\lambda}^2\tilde{b}_1\right\} \tag{5.58}$$

$$\tilde{H}_2 = \left[\tilde{b}_3-\left(1+\tilde{\psi}_2\right)\left(\tilde{b}_2+\tilde{b}_1\tilde{\psi}_1\right)\right]\tanh\tilde{\phi}-\left(1+\tilde{\psi}_2\right)\left(\tilde{b}_2-\tilde{b}_1\tilde{\psi}_1\right)\tilde{\phi}\operatorname{sech}^2\tilde{\phi} \tag{5.59}$$

$$\tilde{L}_2 = \tilde{h}_{21}+\tilde{h}_{22}+\tilde{h}_{23} \tag{5.60}$$

$$\tilde{M}_2 = \tilde{i}_{21} + \tilde{i}_{22} + \tilde{i}_{23} \tag{5.61}$$

$$\tilde{N}_2 = \tilde{j}_{21} + \tilde{j}_{22} + \tilde{j}_{23} \tag{5.62}$$

$$\tilde{h}_{21} = 2\,\tilde{g}_a \tilde{\psi}_4 \left[\left(1+\tilde{\psi}_3\right)\tilde{\phi} \tanh\tilde{\phi} - \tilde{\psi}_3 \sinh^2\tilde{\phi}\right] \Big/ \cosh^2\tilde{\phi} \tag{5.63}$$

$$\tilde{i}_{21} = \tilde{\psi}_4 \tilde{g}_a \tilde{\omega} \left[\tilde{\lambda} e^{\tilde{\lambda} l} \cosh\tilde{\phi}\left(\sinh\tilde{\phi}\cosh\tilde{\phi} - \tilde{\phi}\right) - 2\sqrt{\tilde{\psi}_1}\,\tilde{\phi}\sinh\tilde{\phi}\left(e^{\tilde{\lambda} l} - 1\right)\right] \Big/ \sqrt{\tilde{\psi}_1}\cosh^3\tilde{\phi} \tag{5.64}$$

$$\tilde{j}_{21} = \tilde{\psi}_4{}^2 \tilde{g}_a \sinh\tilde{\phi}\left(\tilde{\phi} - \sinh\tilde{\phi}\cosh\tilde{\phi}\right) \Big/ \cosh^3\tilde{\phi} \tag{5.65}$$

$$\tilde{h}_{22} = 2\tilde{g}_a \gamma^2 \tilde{\psi}_4 \left(1+\tilde{\psi}_3\right) \tanh\tilde{\phi}\left(\tilde{\phi} - \sinh\tilde{\phi}\right) \Big/ \cosh\tilde{\phi} \tag{5.66}$$

$$\tilde{i}_{22} = \gamma^2 \frac{\tilde{g}_b}{\tilde{g}_a} \tilde{i}_{21} \tag{5.67}$$

$$j_{22} = \gamma^2 \frac{g_b}{g_a} j_{21} \tag{5.68}$$

$$\tilde{h}_{23} = \frac{\tilde{g}_c}{\gamma^2 \tilde{g}_b} \tilde{h}_{22} \tag{5.69}$$

$$\tilde{i}_{23} = \frac{\tilde{\psi}_4 \tilde{g}_c \tilde{\omega}}{\cosh^2\tilde{\phi}} \left[2\left(\tilde{\phi}\tanh\tilde{\phi} - \sinh^2\tilde{\phi}\cosh^2\tilde{\phi}\right)\left(1 - e^{\tilde{\lambda} l}\right) + \frac{\tilde{\lambda} e^{\tilde{\lambda} l}}{\sqrt{\tilde{\psi}_1}} \sinh^2\tilde{\phi}\left(\tilde{\phi} - \sinh\tilde{\phi}\cosh\tilde{\phi}\right)\right] \tag{5.70}$$

$$\tilde{j}_{23} = \tilde{\psi}_4{}^2 \tilde{g}_c \sinh\tilde{\phi}\left(\tilde{\phi} - \sinh\tilde{\phi}\cosh^3\tilde{\phi}\right) \Big/ \cosh^3\tilde{\phi} \tag{5.71}$$

for type-II loading method and

$$\tilde{B}_3 = \tilde{b}_2 + \left[\tilde{b}_2 - \left(\tilde{b}_2 - \tilde{b}_1\tilde{\psi}_1\right)\tilde{\phi}\coth\tilde{\phi}\right]\operatorname{csch}^2\tilde{\phi} \tag{5.72}$$

$$\tilde{C}_3 = 2\tilde{b}_2\left\{1 - e^{\tilde{\lambda}l}\begin{bmatrix}\sinh^2\tilde{\phi} + \tilde{\lambda}\left(\tilde{b}_2 + \tilde{b}_1\tilde{\psi}_1\right)\sinh 2\tilde{\phi}/2\sqrt{\tilde{\psi}_1} + 2\tilde{b}_2\left(1 - e^{-\tilde{\lambda}l}\right) \\ -\left(\tilde{\lambda}/2\sqrt{\tilde{\psi}_1} + 2\left(1 - e^{-\tilde{\lambda}l}\right)\coth\tilde{\phi}\right)\left(\tilde{b}_2 - \tilde{b}_1\tilde{\psi}_1\right)\tilde{\phi}\end{bmatrix}\operatorname{csch}^2\tilde{\phi}_1\right\} \tag{5.73}$$

$$\tilde{D}_3 = \tilde{b}_1\tilde{\lambda}^2 e^{2\tilde{\lambda}l} - \tilde{C}_3 + \left(1 - e^{\tilde{\lambda}l}\right)\left\{\tilde{b}_2 + \left[\tilde{b}_2 - \left(\tilde{b}_2 - \tilde{b}_1\tilde{\psi}_1\right)\tilde{\phi}\coth\tilde{\phi}\right]\operatorname{csch}^2\tilde{\phi}\right\} \tag{5.74}$$

$$\tilde{L}_3 = \left(1 + \frac{\tilde{g}_b}{\tilde{g}_a}\gamma^2\right)\tilde{h}_{31} + \tilde{h}_{32} \tag{5.75}$$

$$\tilde{M}_3 = \left(1 + \frac{\tilde{g}_b}{\tilde{g}_a}\gamma^2\right)\tilde{i}_{31} + \tilde{i}_{32} \tag{5.76}$$

$$\tilde{N}_3 = \left(1 + \frac{\tilde{g}_b}{\tilde{g}_a}\gamma^2\right)\tilde{j}_{31} + \tilde{j}_{32} \tag{5.77}$$

$$\tilde{h}_{31} = \tilde{\chi}_a\sqrt{\tilde{\psi}_1}\tilde{\phi}\left(\cosh\tilde{\phi} - 1\right)/\left(\cosh\tilde{\phi} + 1\right)\sinh\tilde{\phi} \tag{5.78}$$

$$\tilde{i}_{31} = \tilde{\chi}_a\left[\tilde{\lambda}e^{\tilde{\lambda}l}\left(\sinh\tilde{\phi} - \tilde{\phi}\right)/\left(\cosh\tilde{\phi} + 1\right) - h_{31}\left(e^{\tilde{\lambda}l} - 1\right)\right] \tag{5.79}$$

$$\tilde{j}_{31} = \tilde{\psi}_4\tilde{\chi}_a\sqrt{\tilde{\psi}_1}\sinh\tilde{\phi}\left(\tilde{\phi} - \sinh\tilde{\phi}\right)/\left(\cosh\tilde{\phi} + 1\right)^2 \tag{5.80}$$

$$\tilde{h}_{32} = -\frac{\tilde{\chi}_3}{\tilde{\chi}_1}\tilde{h}_{31} \tag{5.81}$$

$$\tilde{i}_{32} = -\frac{\tilde{\chi}_3}{\tilde{\chi}_1}\tilde{i}_{31} \tag{5.82}$$

$$\tilde{j}_{32} = -\tilde{\chi}_c\tilde{\psi}_4\sqrt{\tilde{\psi}_1}\tilde{\phi}\sinh\tilde{\phi}/\left(\cosh\tilde{\phi} + 1\right)^2 \tag{5.83}$$

for type-III loading method, where

$$\tilde{\phi} = \sqrt{\tilde{\psi}_1}\left(L - l\right) \tag{5.84}$$

$$\tilde{\psi}_4 = \frac{\tilde{\psi}_2}{\tilde{\psi}_1} \tag{5.85}$$

$$\tilde{\chi}_a = \tilde{g}_a \tilde{\psi}_4 \Big/ \sqrt{\tilde{\psi}_1} \tag{5.86}$$

$$\tilde{\chi}_b = \tilde{\psi}_4 \tilde{g}_b \gamma^2 \Big/ \sqrt{\tilde{\psi}_1} \tag{5.87}$$

$$\tilde{\chi}_c = \tilde{g}_c \tilde{\psi}_4 \sinh^2 \tilde{\phi} \Big/ \sqrt{\tilde{\psi}_1} \tag{5.88}$$

$$\tilde{g}_a = \pi a^2 / 2\tilde{E}_f \tag{5.89}$$

$$\tilde{g}_b = \pi\left(b^2 - a^2\right) / 2\tilde{E}_m \tag{5.90}$$

$$\tilde{g}_c = b_1 \tilde{\psi}_1 / \sinh^2 \tilde{\phi} \tag{5.91}$$

$$b_1 = \pi\gamma^2\left(1 + \nu_m\right)\left[b^4 \ln\left(b/a\right) - \left(3b^2 - a^2\right)\left(b^2 - a^2\right)/4\right] \Big/ 2E_m \tag{5.92}$$

$$\tilde{b}_2 = \pi a^2\left(\tilde{\alpha} + \gamma\right) / 2E_m \tag{5.93}$$

$$\tilde{b}_3 = \pi a^2\left[\left(\tilde{\alpha} + \gamma\right)\tilde{\psi}_3 + \gamma\right] \Big/ E_m \tag{5.94}$$

$$\tilde{b}_4 = \pi a^2\left[\tilde{\alpha}\left(\tilde{\psi}_3{}^2 - 1\right) + \gamma\left(1 + \tilde{\psi}_3{}^2\right)\right] \Big/ 2E_m \tag{5.95}$$

Solving Eqn. 5.39 for σ_a, the applied axial stress acting on SMA wire in a partial deboned condition can be obtained as given below,

$$\sigma_{di}^{p} = \frac{\tilde{\Omega}_{bi} + \sqrt{\tilde{\Omega}_{bi}{}^{2} - 4\tilde{\Omega}_{ai}\left(\tilde{\Omega}_{ci} - 2\pi a G_{ic}\right)}}{2\tilde{\Omega}_{ai}} \tag{5.96}$$

where

$$\tilde{\Omega}_{ai} = -\tilde{B}_i - \tilde{C}_i + \tilde{D}_i \tag{5.97}$$

$$\tilde{\Omega}_{bi} = -\tilde{C} + 2\tilde{D}_i\tilde{\sigma}_i^{*} - \tilde{L}_i + \tilde{M}_i \tag{5.98}$$

$$\tilde{\Omega}_{ci} = \tilde{D}_i\tilde{\sigma}_i^{*2} + \tilde{M}_i\tilde{\sigma}_i^{*} + \tilde{N}_i \tag{5.99}$$

It should be noted that except the constant value of interfacial fracture toughness G_{ic}, all the Ω's are functions of actuation temperature. It implies that the partial debond stress, σ_{di}^{p} has been reduced to a function of temperature, T for the given initial conditions of the SMA, material properties of constituents and geometric factors of the SMA-matrix cylinder.

5.3 Critical Changes of Strain Energy Release Rate

The energy components U_{di} and U_{bi} stated in Eqns. 5.3 and 5.4 represent the elastic strain energies stored in constituents due to externally applied load and the SMA actuation. When the embedded wire is subjected to relatively high applied load in a low actuation temperature ($T < T_{fo}^{A}$), the SMA wire can be considered as a general metallic fiber with constant material properties inside a matrix cylinder. Only the tensile stress and strain will be generated on the SMA wire and matrix. As a result, U_t represents the strain energy due to tensile load in the low actuation condition. In a high actuation condition, the recovery stress (compressive) of SMA becomes dominant to take up the major role for generating compressive strain in constituents and hence the extra applied load is required compensate such intrinsic compressive stress results from the SMA actuation. In the sense of energy development in mode-b actuation, the strain energy arising from this recovery action will be minimized by the initial applied stress prior to the development of total elastic strain energy due to tensile load.

Certainly, this phenomenon is quite obvious and able to explain the resistant of interfacial debond in the SMA-reinforced composites. However the critical applied stress, which is required to compensate the strain energy due to the SMA actuation, has to be predefined prior the application of Eqn. 5.1 for the prediction of interfacial debond stress. Recalling Eqn. 3.18 for the equilibrium condition between interfacial shear stress, τ_i and axial stress on SMA wire, σ_f^z, one may notice that τ_i is linearly related to the rate of change of σ_f^z in the wire direction. When $d\sigma_f^z/dl = 0$, τ_i will be reduced to zero. Referring to the surface plot of axial stress distribution on the SMA wire for type-III and mode-b loading-actuation scenario, a long plateau developed from loading end to about z = 9mm is found at T = 76°C for σ_a = 0.5GPa. It implies that the τ_i is minimized to zero at 9mm < z < 0mm. Therefore, the following criterion has to be satisfied for the study of fracture energy development in the SMA-matrix cylinder,

$$N_{ic} = -\frac{dU_{ii}/dl}{2\pi a G_{ic}} \qquad for \qquad \sigma_a < \sigma_{fb3}^z(L/2,T) \qquad (5.100)$$

$$N_{ic} = \frac{dU_{ii}/dl}{2\pi a G_{ic}} \qquad for \qquad \sigma_a \geq \sigma_{fb3}^z(L/2,T) \qquad (5.101)$$

where $N_{ic}(i = 1,2 \text{ and } 3)$ are the normalized strain energy release rates for type-I, II and III loading conditions. $\sigma^{s}_{fb3}(L/2,T)$ represents the residual stress on wire induced by the SMA actuation at z = $L/2$, and is also considered as the average stress level for the plateau of axial stress distribution. $\sigma_a < \sigma^{s}_{fb3}(L/2,T)$ represents the specific condition with recovery stress dominating the strain energy development. Therefore dU_{ii}/dl is decreased with increase of σ_a and a negative sign appears in Eqn. 5.100. It contradicts to the dU_{ii}/dl arising from tensile load (i.e. $\sigma_a \geq \sigma^{s}_{fb3}(L/2,T)$) as described in Enq. 5.101 in which the normalized strain energy release rate N_{ic} is always increased with σ_a.

Plots of N_{ic} for type-I, II and III loading conditions at 25°C (initial temperature), 40°C and 60°C as a function of applied stress, σ_a are shown in Fig. 5.2. Again, all the material properties and geometric constants summarised in Table 3.1 are employed as numerical examples in this chapter. Based on the predictions of critical embedded length, L_c required for achieving constant martensite volume fraction and axial stress on SMA wire in the center portion (i.e. CMR and CASR) as described in Chapter 4, L = 50mm and ε_p = 2% are employed in the following studies unless otherwise specified. It should be noted that the results for type-I and type-II loading conditions are basically the same in a wide range of actuation temperatures. Only the plots for type-III loading condition demonstrate minor derivation from the others. The N_{ic}–plots for all the three loading methods show the similar responses toward the SMA actuation.

In Fig. 5.2a, the curves for type-I and type-II loading conditions develop to unity at σ_a = 582MPa while the type-III is always higher than the others for a given applied stress and reach the unity at 577MPa. This result shows the typical development profiles of potential energy release rates for the fiber-matrix cylinder with constant material properties in a simple pullout test. All the critical stresses for satisfying unity of N_{ic} represent the initial debond stress, σ_d^o of the corresponding loading condition. When the embedded SMA is heated at $T = 40°\mathrm{C}$, minor improvements of σ_d^o (591MPa for Type-I and II; 584MPa for Type-III) can be obtained as shown in Fig. 5.2b. Although the austenitic start temperature, T_{so}^A (= 40°C in the stress-free condition) is just satisfied, and no substantial changes of material properties as well as phase transformation should be induced in such low actuation level, recovery action due to thermal expansion of SMA (i.e. $\theta(T\text{-}T_o)$) works against the applied stress. Therefore, additional stress is required to compensate such recovery stress prior the development of critical potential strain energy for interfacial debond and as a result, the initial debond stresses are increased. One may notice that the curves do not start from zero, which means the elastic strain energy release rate is not zero in stress-free condition. This phenomenon can also be observed from the plots of N_{ic} at $T = 60°\mathrm{C}$. In Fig. 5.2c, the curves are clearly separated into two sections with turning points at 0.23GPa for type-I and II and0.22GPa for type-III loading condition. When the applied stress increases toward the so-called turning point in a constant actuation temperature, the elastic strain energy release rate due to SMA's recovery action could be gradually reduced and reach the energy equilibrium condition with $N_{ic} = 0$. The elastic strain energy arising from tensile load increases again until the applied stress is further increased beyond the turning point.

As described in the previous section, critical stress of this turning point could be defined as $\sigma_{fbi}^{t}(L/2,T)$. When temperature increases, this critical stress will be increased accordingly and the whole curve may shift toward right-hand side and reach unity at a higher stress level.

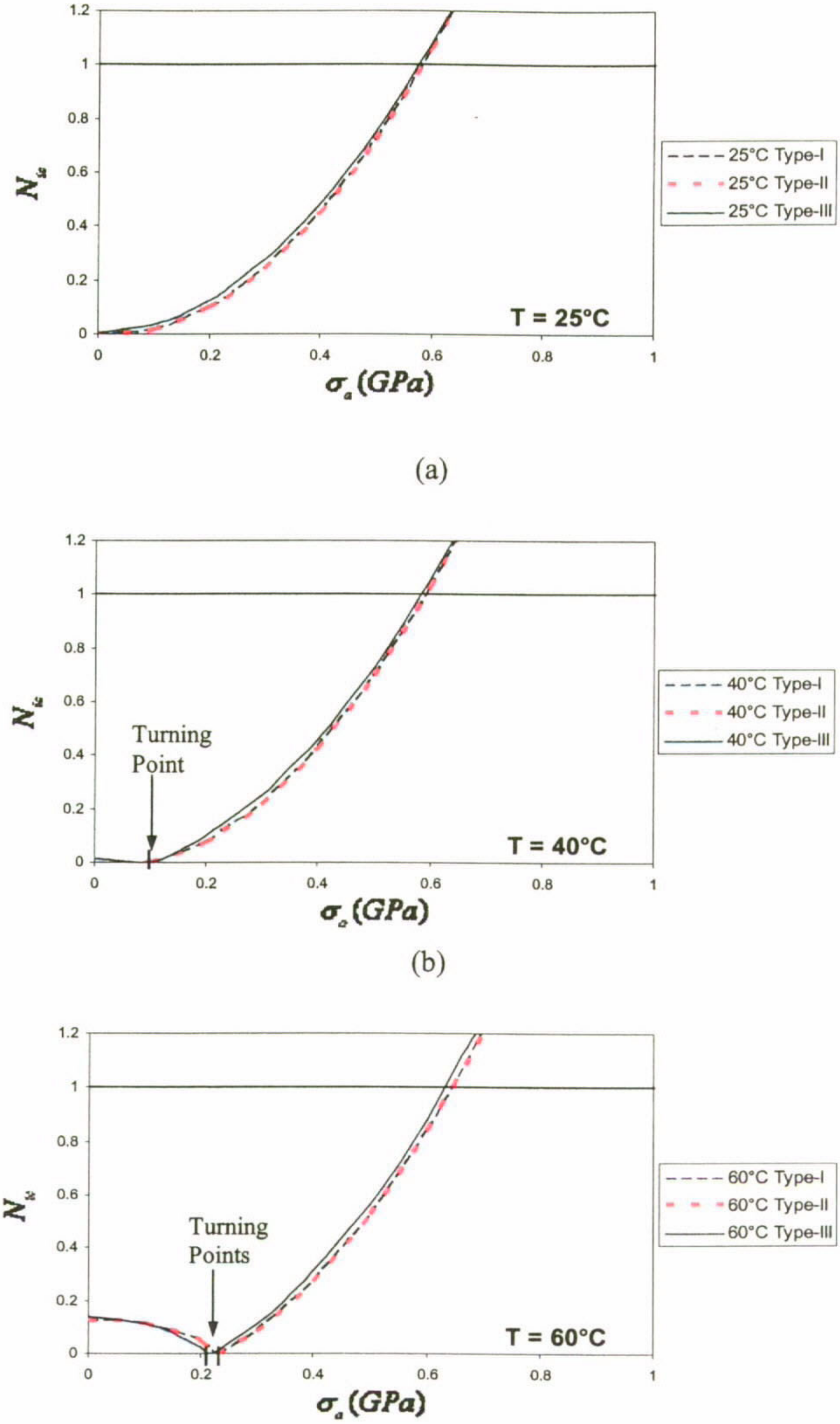

(a)

(b)

(c)

Figure 5.2 Plots of normalized strain energy release rate, N_{ic} ($= dU_t/dl/2\pi a G_{ic}$) for the type-I, II and III loading conditions in mode-b actuation at (a) 25°C (initial temperature), (b) 40°C and (c) 60°C.

Type-III loading method is typically employed in pullout test for the study of interfacial properties and debond stresses. Therefore, it is more essential to study the shape memory effect on interfacial debond in type-III loading condition. Figure 5.3 shows the three-dimensional plots of normalized strain energy release rate against actuation temperatures. It can be clearly found that the turning points are not aligned linearly on the stress-temperature plane. The critical stress increases linearly with temperature in the low actuation level but the rate of change of critical stress suddenly increases at about 60°C. This phenomenon is the result of austenitic phase transformation of the embedded SMA. One should notice that the phase transformation starts at the temperature higher than T_{so}^{A} in stress-free condition. It is in fact due to the residual stress generated in constituents during SMA actuation that shifts up the austenitic start temperature.

Figure 5.4 shows the plots of N_{ic} against the applied load for different actuation temperatures. It should be emphasized here that the strain energy release rate in the stress-free condition ($\sigma_a = 0$) increases with temperature, which means the potential energy stored in constituents due to recovery action can be increased by the SMA actuation. If the temperature is further increased ($T > 90$°C) without applied load, the critical strain energy release rate can be attained and initiate interfacial debond at the free embedded end. This problem is definied as 'over-actuation' of the SMA in the current study, and it has to be avoided in all the practical applications as well as pullout tests for experimental studies. The N_{ic} diminishes monotonically with the increase of the applied stress and climbs up again until the critical stress at turning point is attained. The improvement of initial debond stress, σ_d^o is also presented in the figure. Obviously, σ_d^o

is not increased in linear proportion with actuation temperature. Substantial improvement will only be obtained for $T > 50^{\circ}$C. However, initial debond stress can never be increased to infinity with two major reasons. The first one is the limitation of the SMA wire for which the extremely high temperature may cause plastic deformation (overshoot into the plastic zone (Fig. 3.5)) and hence the relaxation of the SMA wire may occur and the shape memory effect disappears eventually. The second one is the problem of over-actuation with which the interfacial debond may start at the free end instead of the loading end.

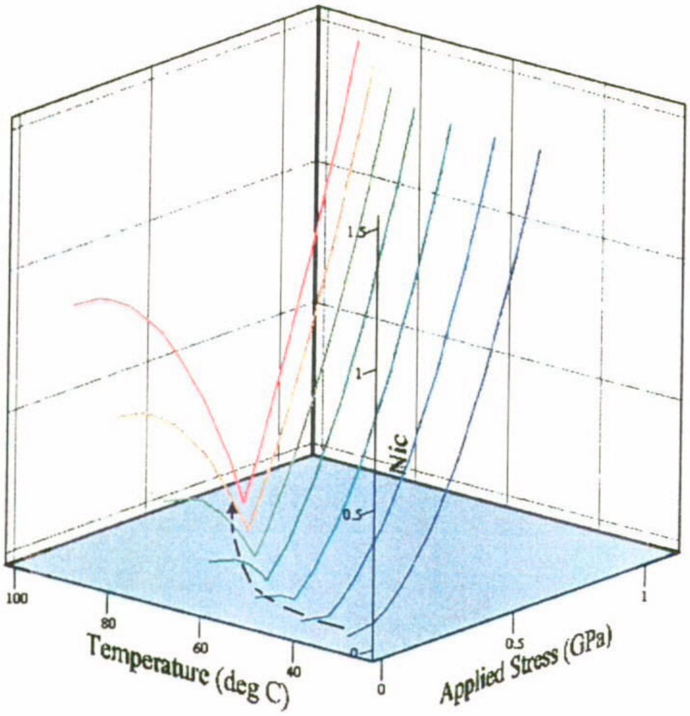

Figure 5.3 3-D plots of normalized strain energy release rate, N_{ic} ($= dU_t/dl/2\pi aG_{ic}$) for type-III loading condition in mode-b actuation.

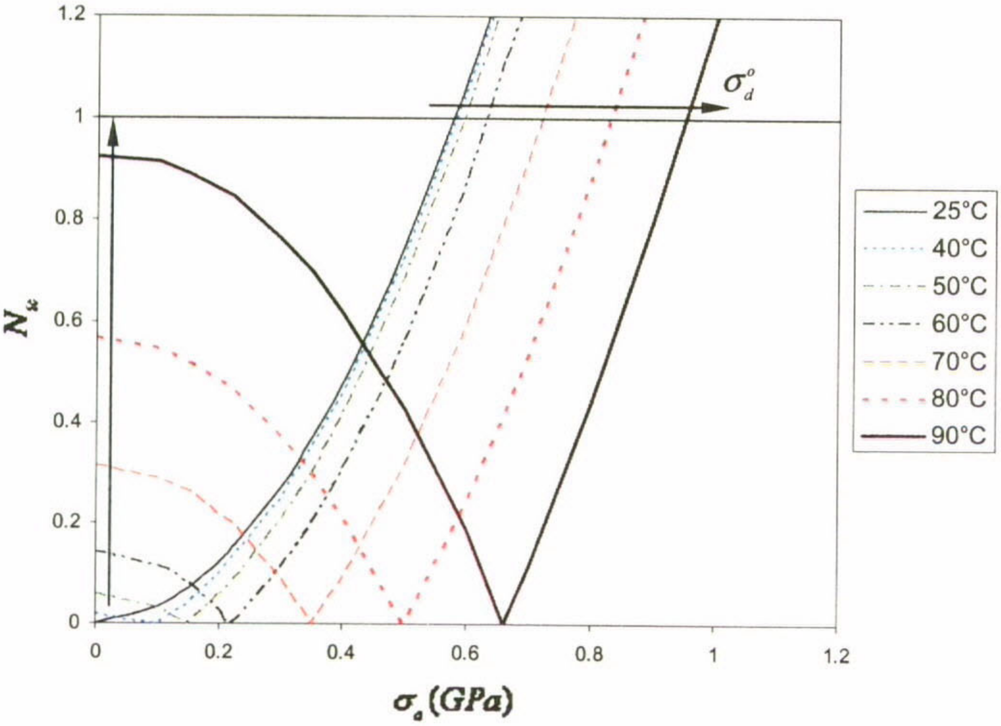

Figure 5.4 Plots of N_{ic} for type-III loading condition as function of externally applied stress, σ_a at different actuation levels.

5.4 Debonding Behaviour of SMA-Matrix Cylinder

5.4.1 Partial Debonding Stress

Using Eqn. 5.96, solutions of partial debond stress, σ_{d3}^{p} for type-III loading condition are plotted against debonded length, l as shown in Fig. 5.5. Stress value at $l = 0$ represents the initial debond stress, σ_{d3}^{o} in the corresponding actuation temperature while the value of σ_{d3}^{p} for $l > 0$ represents the required axial stress acting on SMA wire that leads to the partial debond at l. Using the location of σ_{d3}^{*} as cutting line, the debonding process can be divided into two parts: stable debonding and unstable debonding regions. In general, the partial debonding stress, σ_{d3}^{p} increases stably as the debond crack propagates. However, it decreases after reaching the maximum level, σ_{d3}^{*}.

When the SMA wire is heated up to 40°C, minor increase of σ_{d3}^{o} can be obtained but σ_{d3}^{*} will be improved substantially. Considerable improvement of these two stresses will be achieved until $T > 40$°C. This phenomenon can be easily identified from the surface plot as shown in Fig. 5.6. When the austenitic transformation starts at about 60°C in strain-constrained condition, both the elastic modulus of SMA and recovery stress will be increased instantaneously. As a result, strain energy stored in constituents due to recovery stress is increased at the instant and therefore the rate of change of debond stresses against temperature is dramatically increased.

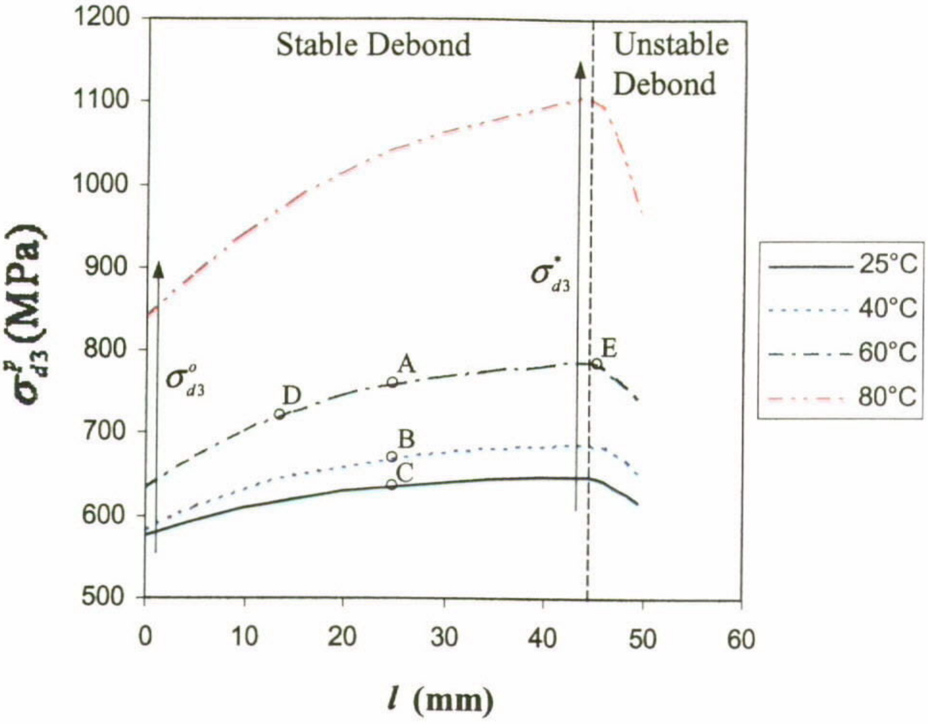

Figure 5.5 Plots of partial debond stress, σ_{d3}^{p} as a function of debonded length, l for type-III loading condition at different actuation temperatures. ($\varepsilon_p = 2\%$)

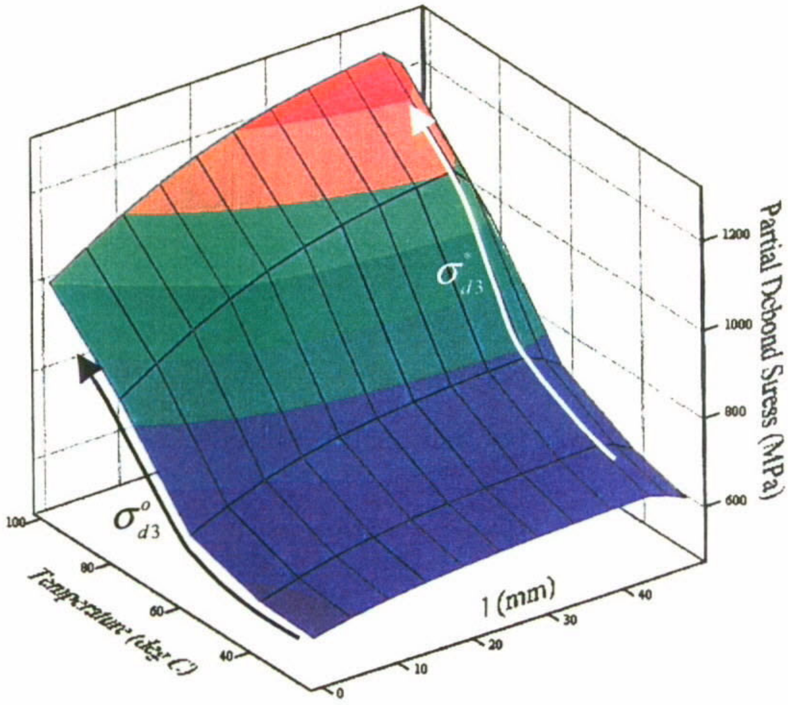

Figure 5.6 Surface plot of partial debond stress, σ_{d3}^{p} for type-III loading condition.

5.4.2 Influence of Prestrain Values on Debonding Behaviour

Figures 5.7a and b show the effect of prestrain value, ε_p on the development of partial debond stress at 60°C and 80°C respectively. Referring to Eqn. 3.4 for the solution of constrained recovery stress σ_r, one may notice that σ_r should be linearly increased with temperature before the austenitic transformation start. ε_p is simply a variable which governs the maximum recovery stress and the increasing rate of σ_r. In the other words, before the phase transformation, recovery stress generated inside a composite is independent of ε_p. Influence of prestrain value is therefore reasonably insignificant in a low actuation level as shown in Fig. 5.7a. However, when the SMA wire is heated up to 80°C, ε_p takes up the major role in recovery action. Considerable improvement of both the initial and maximum debond stresses could be obtained and the effect of ε_p becomes significant as shown in Fig. 5.7b. The initial debond stresses at 1% and 2% prestrained levels are 826MPa and 839MPa respectively. However when ε_p has been further increased up to 4%, much high applied stress is required to satisfy the debonding criterion and as a result, interfacial debond starts at 932MPa which is 12.8% higher than that at 1% prestrained level.

5.4.3 Internal Stress Distributions in a Partial Debonded Condition

Referring to Fig. 5.5 for the partial debonding stresses at 25°C, 40°C and 60°C, when the interfacial debond propagates to half of total embedded length (point A, B and C), the instantaneous axial stress distributions on SMA wire, σ^{z}_{f3} are shown in Fig. 5.8. Using the stress solutions derived in Section 5.2.1, σ^{z}_{fd3} and σ^{z}_{fb3} can be obtained for the

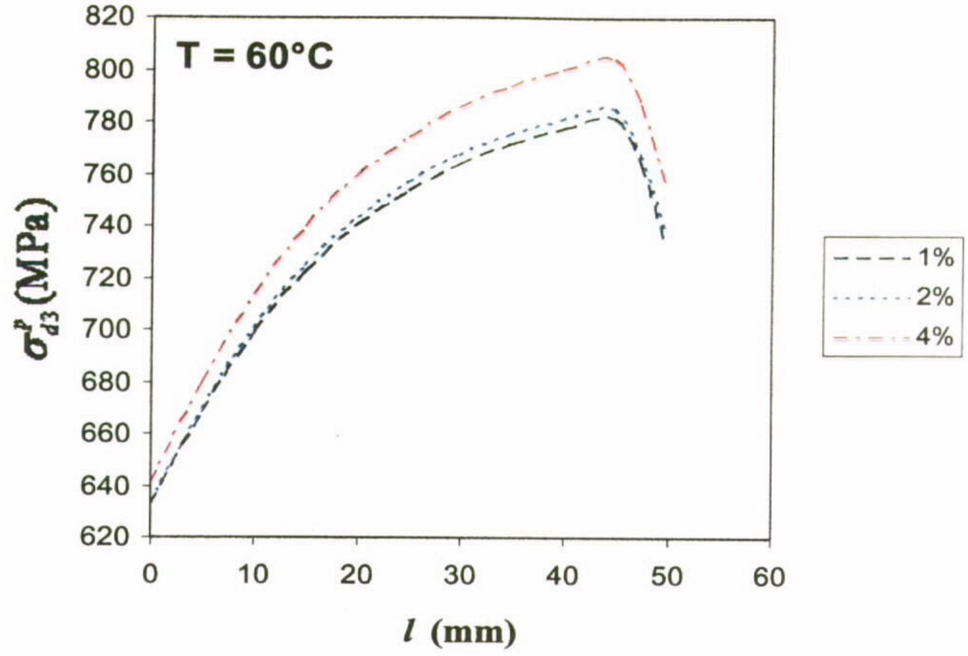

(a)

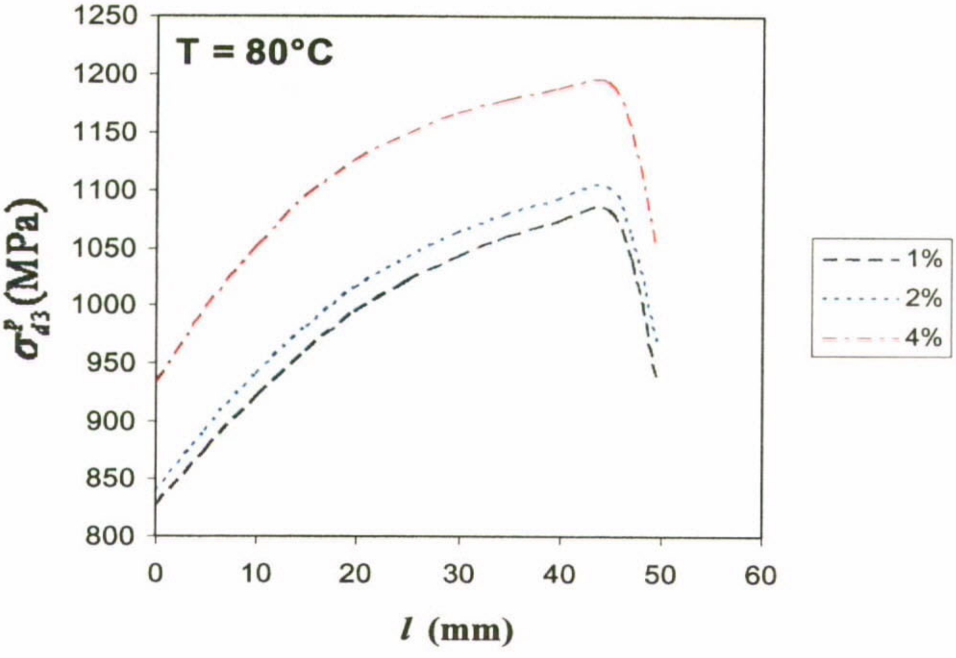

(b)

Figure 5.7 Influence of prestrain values, ε_p on partial debond stress, σ^p_{d3}. (a) Actuation temperature $T = 60^{\circ}$C and (b) Actuation temperature $T = 80^{\circ}$C.

debonded and bonded regions during debonding process and the junction point between the two regions is considered as crack tip debond stress, σ_{t3}. In Fig. 5.8, points A, B and C represent the initial debond stresses at 25°C, 40°C and 60°C respectively. The stress levels slightly decrease in the debonded region toward the crack tip at $L - z = 25$mm but drop down immediately after entering the bonded region. This implies that the internal stresses are not able to transmit through the interface effectively in the debonded region, only a weak frictional shear, τ_f takes up the role for stress transmission and hence the axial stress on SMA wire remains at high level in the debonded region.

At T = 60°C, when the interfacial debond propagates through 0.25L, 0.5L and 0.95L as illustrated in Fig. 5.5, σ_{d3}^{p} increases with l and drops in the unstable debonding region. This phenomenon is reproduced in Fig. 5.9 and the corresponding stress levels are denoted by the points E, A and D respectively. When l increases from 0.25L to 0.5L, σ_{d3}^{o} increases accordingly, while the σ_{f3}^{z} remains at a constant level in the bonded region. However, σ_{f3}^{z} drops to zero immediately in the bonded region at l = 0.95L, which means the effective internal stress transmission between the SMA wire and matrix is no longer maintainable. Therefore, the wire-matrix interface will be totally debonded at the instant.

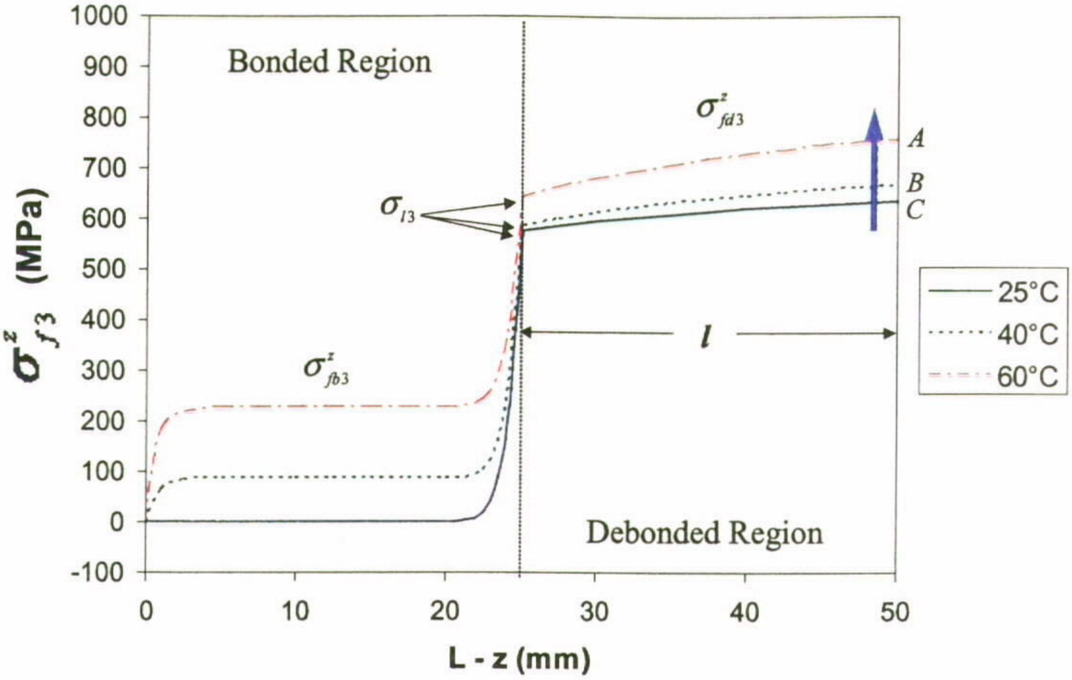

Figure 5.8 Axial stress distributions on SMA wire, σ^z_{f3} in partially debonded condition ($l = 0.5L$) at 25°C, 40°C and 60°C.

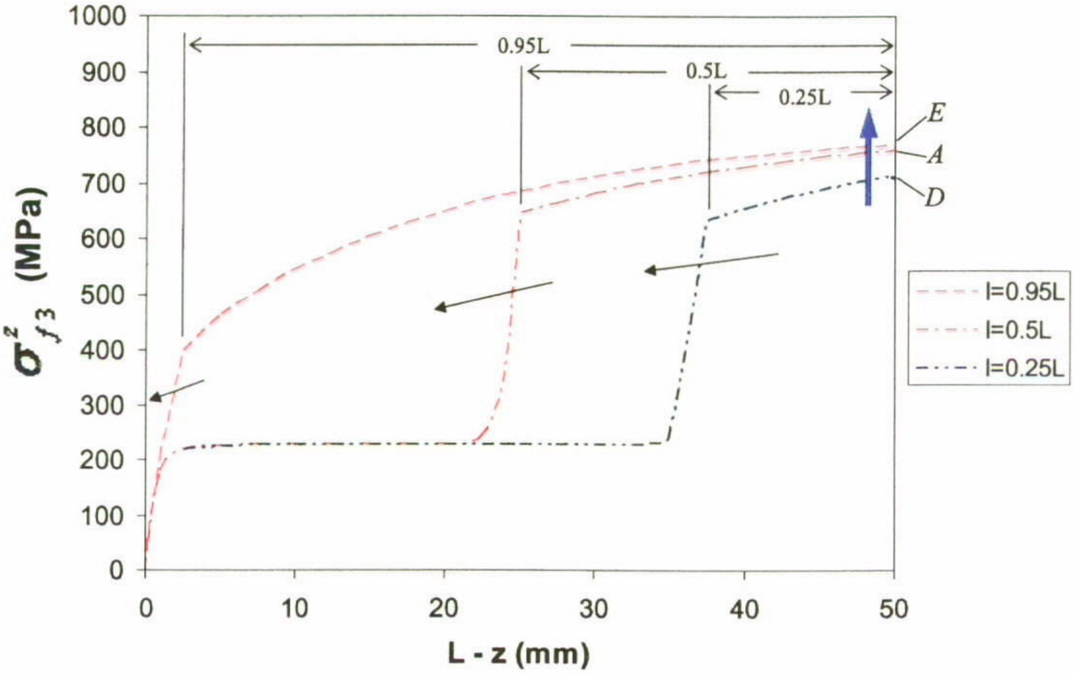

Figure 5.9 Evolution of axial stress along the SMA wire during debonding process at 60°C.

5.5 Summary

The total elastic strain energy on both the SMA wire and matrix cylinder is taken into account to formulate the interfacial debonding criterion for the SMA-composites. Solutions of stress distributions in the debonded and bonded regions are derived for the SMA wire and its surrounding matrix respectively. These solutions are then substituted into the debonding criterion that results in the numerical solutions of normalized strain energy release rate against the applied load. The substantial improvement of the initial debond stress is predicted with the increase of the actuation temperature. It has been found that the initial applied stress is required to compensate the additional recovery stress arising from SMA actuation before the further development of the strain energy release rate.

Chapter 6

Pullout Test of SMA Wire/Epoxy Matrix Cylinder

6.1 Introduction

A great deal of effort was expanded over the past decade in developing the applications of shape memory alloys in composite materials. Numerous designs and fabrication processes of composite structures built-in with SMA inclusions have been proposed by different research groups [60,102,118]. Using the concepts of active control, structure acoustic control [111] or shape control [82] can be accomplished with SMA reinforced composites utilizing a novel technique termed 'Active Modal Modification' [119]. However, there is a lack of experimental findings on the interfacial behaviour of this 'novel' material system, which governs the mechanical limitation of the composite structures.

As discussed in the previous chapter for the evaluation of interfacial properties of typical fiber-matrix composites using single-fiber pullout test, it is believed that the basic interfacial properties of SMA-composites such as residual clamping stress q_o, friction coefficient between constituents μ, interfacial fracture toughness G_{ic} as well as the critical debonding stresses σ_d^o and σ_d^* can be determined from the pullout tests. However, the basic equations for those critical properties are valid for the models with constant material properties in a well defined loading condition. Due to phase transformations in different loading-actuation scenarios, the martensite volume fraction and hence the material properties of embedded SMA wire may change along the wire direction. Certainly, the interfacial properties evaluated from the pullout tests are valid for the model before actuation. Even though a long embedded length and relatively high matrix-to-wire radius ratio are considered in pullout tests, which implies the constant material properties can be achieved in a large portion of embedded length (as discussed in Chapter 4), there is no effective measurement for the status of SMA inclusions at a instant. Therefore, even though the basic interfacial properties (q_o, μ and G_{ic}) can be obtained from the tests before SMA actuation occurs, due to the absent of instantaneous material properties, it is difficult to determine the interfacial properties of the SMA composite during actuation.

Based on the captioned difficulties on material properties measurement, only the pullout test results in zero-actuation condition are employed for the evaluation of interfacial properties in the current study. Referring to Chapter 5 for the stress solutions and total elastic strain energy stored in constituents, only the material constants and interfacial properties at initial state (when $T = T_o$) are required while the critical debonding stresses can be predicted for any given actuation temperature. Therefore, the results from pullout tests are still applicable to validate the previously developed theoretical models and the debonding stresses at different temperatures could be employed to compare directly with the theoretical results.

6.2 Experiments

This chapter focuses on the experimental studies of interfacial properties and debonding behaviour of SMA reinforced epoxy matrix composites. Experimental setup and fabrication of specimens are described in the following sections. The embedded wires were subjected to electrical resistive heating for the generation of shape memory effect (SME) inside an epoxy matrix cylinder. For simplicity, type-III and mode-b loading-actuation condition is considered in the SMA-wire pullout test. Actuation temperature is limited from 20°C to 60°C so as to avoid the unwanted interfacial debond to occur at free end ($z = L$) due to over-actuation of embedded SMA.

6.2.1 Experimental Setup

The SMA-epoxy cylinders embedded with NiTi wires of diameter 0.25mm and 0.4mm were fabricated for the pullout tests so as to exam the critical stresses in debonding processes. In order to increase the reliability and stability of the NiTi SMA wires, a thermal-mechanical cycle treatment was performed until no variation in stress-strain characteristic was observed. Material properties of the SMA wires and epoxy matrix cylinder are summarized in Table 6.1. The NiTi wires were elongated to the targeted residual strain, ε_p and then embedded into the epoxy matrix cylinder during the lay up process. Wire's ends were fixed (Fig. 6.1) to guarantee the alignment inside a matrix cylinder, that can also prevent shape change during the curing process of epoxy matrix. Dimensions and the corresponding quantities of specimens are summarized in Table 6.2. Pullout tests for the specimens at room temperature ($T = T_o = 20°C$) provide important information to determine interfacial properties of SMA-composites. In

Table 6.1 Material properties and dimensional constants of epoxy matrix cylinder and SMA wires.

Epoxy Matrix	b(mm)	E_m(GPa)	β_m(°C^{-1})	ν_m
	5	2.12	4x10^{-7}	0.35

SMA Wires		a (mm)	E_A (GPa)	E_M (GPa)	C_A (MPa/°C)	C_M (MPa/°C)	σ_s^{cr} (MPa)	σ_f^{cr} (MPa)
	#1	0.125	37.4	19.1	19.6	25.4	200	250
	#2	0.2	47.2	13.7	28	20	290	280
		T_{so}^{A} (°C)	T_{fo}^{A} (°C)	T_{so}^{M} (°C)	T_{fo}^{M} (°C)	θ (MPa/°C)	ν_f	ε_L (%)
	#1	40	75	33	18	5.5	0.33	8
	#2	38	75	35	20	5	0.33	8

Table 6.2 Dimensions and quantities of SMA epoxy-matrix cylinders. (*1* or *2* represents quantity of the particular type of specimens.)

		Wire Embedded Length											
		2mm			5mm			30mm			50mm		
Wire Dia.	T(°C) / ε_p	20	40	60	20	40	60	20	40	60	20	40	60
0.25mm (#1)	4%	*2*	*2*	*2*	*1*	*2*	*2*	*2*	*1*	*2*	*1*	*2*	*2*
0.4mm (#2)	0%							*1*	*2*	*2*	*1*	*2*	*2*
	4%	*2*	*2*	*1*	*2*	*1*	*2*	*2*	*2*	*2*	*2*	*2*	*2*
	8%							*1*	*2*	*2*	*1*	*2*	*2*

addition, they are considered as basic samples to clarify the influences of SMA actuation in the debonding process.

Experimental setup for the SMA-wire pullout test is schematically illustrated in Fig. 6.3. Both debonding process and pullout test data (including pullout force, displacement, partial debonded length and corresponding time taken) were captured by using the high resolution digital video camera and MTS Tytron-250 micro-force testing machine respectively. The embedded SMA wires were firstly heated to the target temperatures (20°C, 40°C or 60°C) and then the pullout test started under the constant

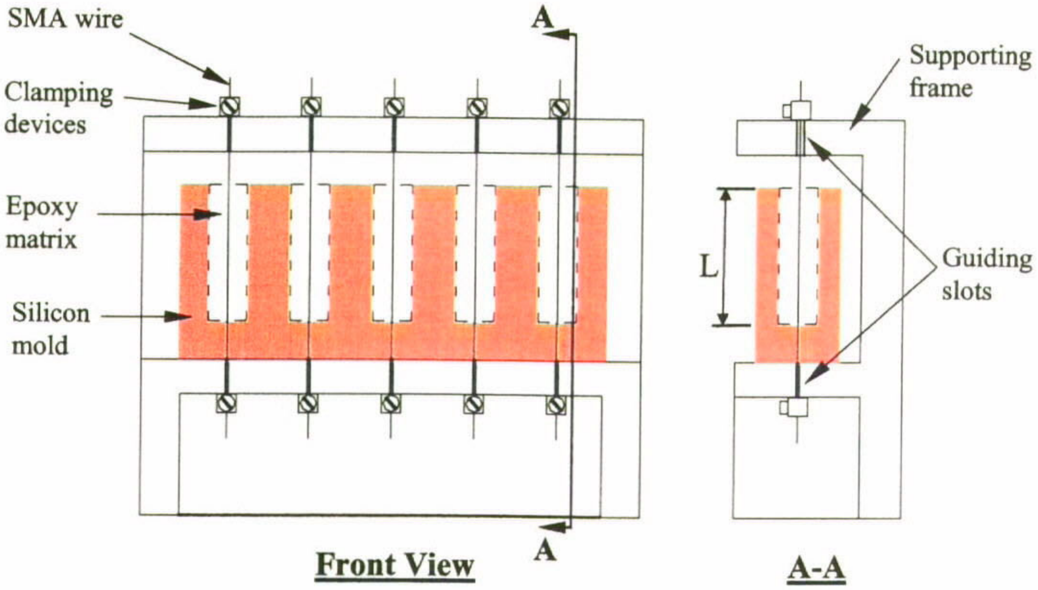

Figure 6.1 Experimental setup for the fabrication of SMA-epoxy cylinder

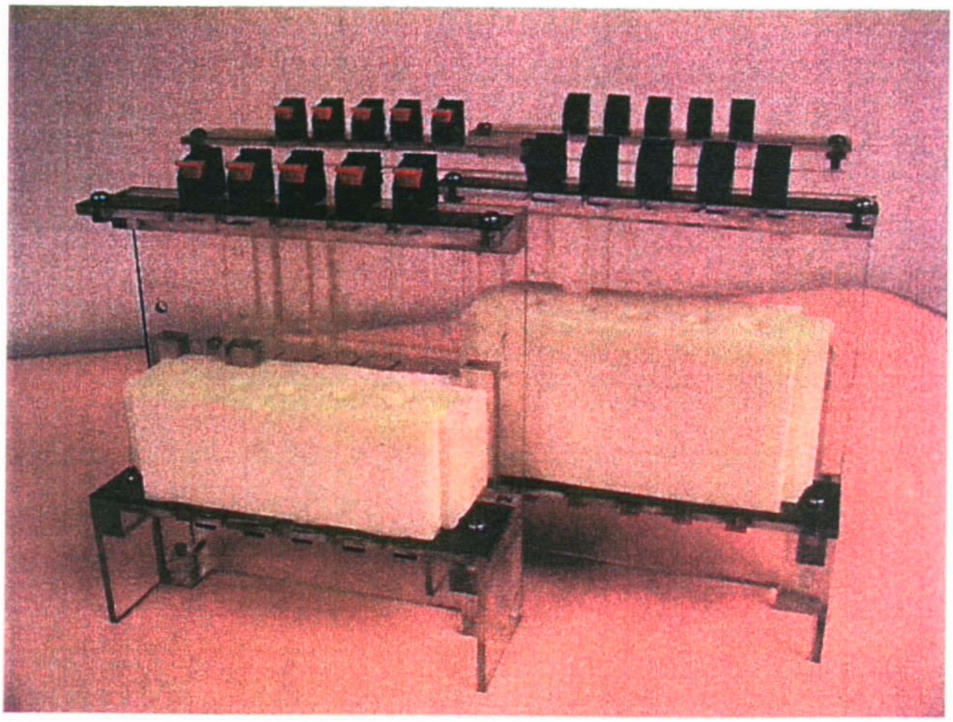

Figure 6.2 Fixtures for the specimen fabrication.

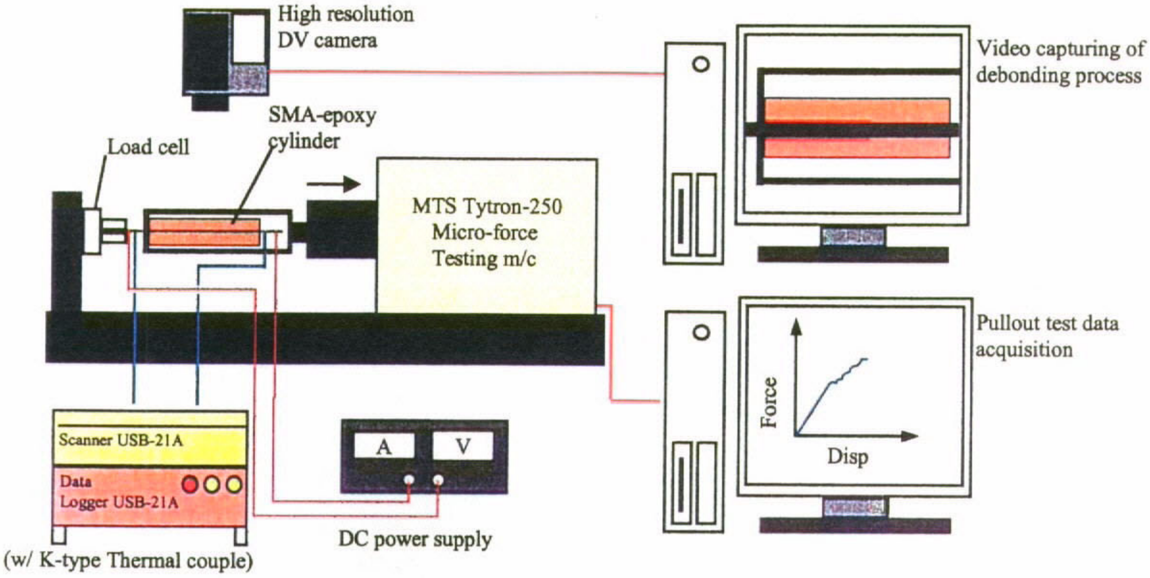

Figure 6.3 Schematic diagram of wire pullout experiment.

actuation temperature (mode-b actuation). It should be note that as electric resistive heating is applied for SMA actuation, fine-tuning of applied current may be required to achieve target temperature on wires. However, SMA exhibits non-linear thermal-mechanical cycles in the fine-tuning process (heating and cooling alternatively), that may derivate the actual properties of the SMA from the predicted status basing on monotonic heat up process. Therefore, the SMA was heated up monotonically to ±3°C of the target temperatures and then maintained constant during the pullout test. The loading end of the wire was clamped on load cell and the cylinder was slowly pulled away from the loading end at 0.5mm/min. Temperature on wire was continuously measured by using KYOWA USB-21A scanner and UCAM-20PC data logger equipped with K-type thermal couple.

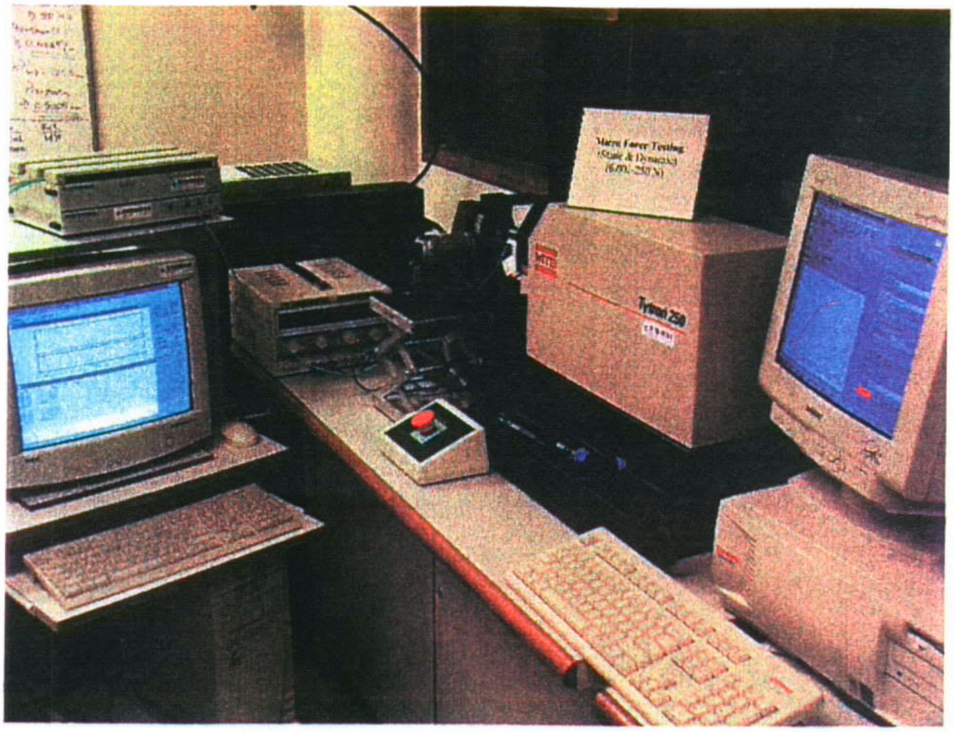

Figure 6.4 Experimental setup.

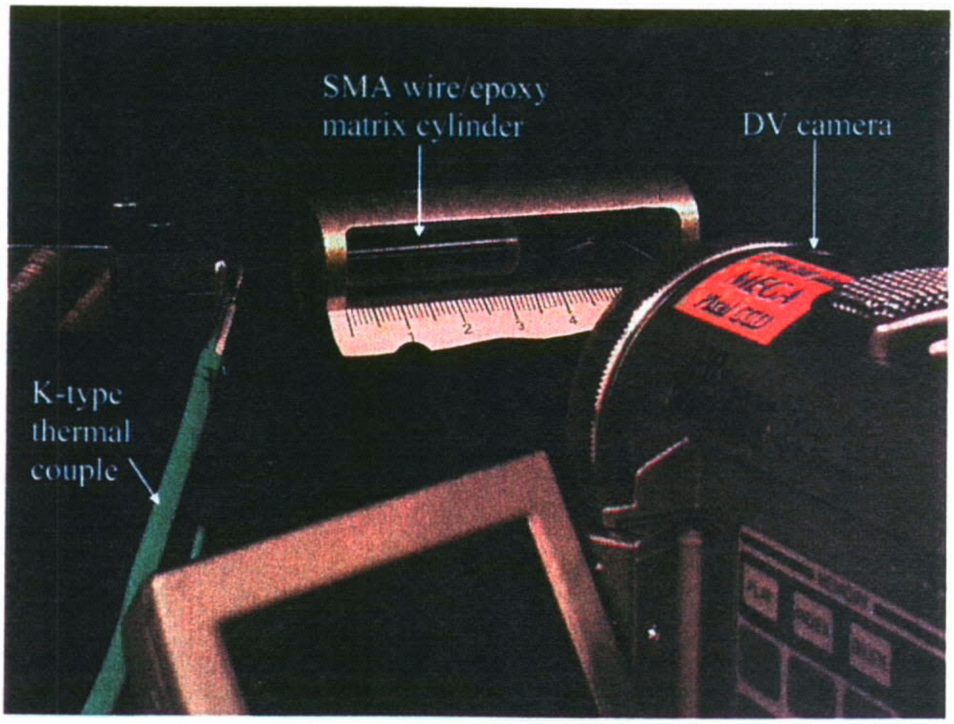

Figure 6.5 Debonding process is recorded by high resolution digital video camera.

6.2.1.1 Debonding Stress Analysis

Figure 6.6 shows the typical pullout test results for the SMA-epoxy matrix cylinders subjected to different actuation temperatures. It should be noted that both the maximum debond stress, σ_d^* and initial frictional pullout stress, σ_{fr} can be easily observed from the plots while the initial deobnd stress, σ_d^o is relatively difficult to be identified. The two major reasons include the risk of over-actuation and stress-induced martensitic transformation (SIM) occurred during the test. Over-actuation is able to initiate interfacial debond at free end instead of loading end [56]. In the other words, even though σ_d^o can be clearly identified, it is may not represent the normal debonding behaviour with interfacial debond starts from loading end ($z = 0$) and propagates toward the free end ($z = L$). On the other hand, the SIM yields sudden slope change of stress-

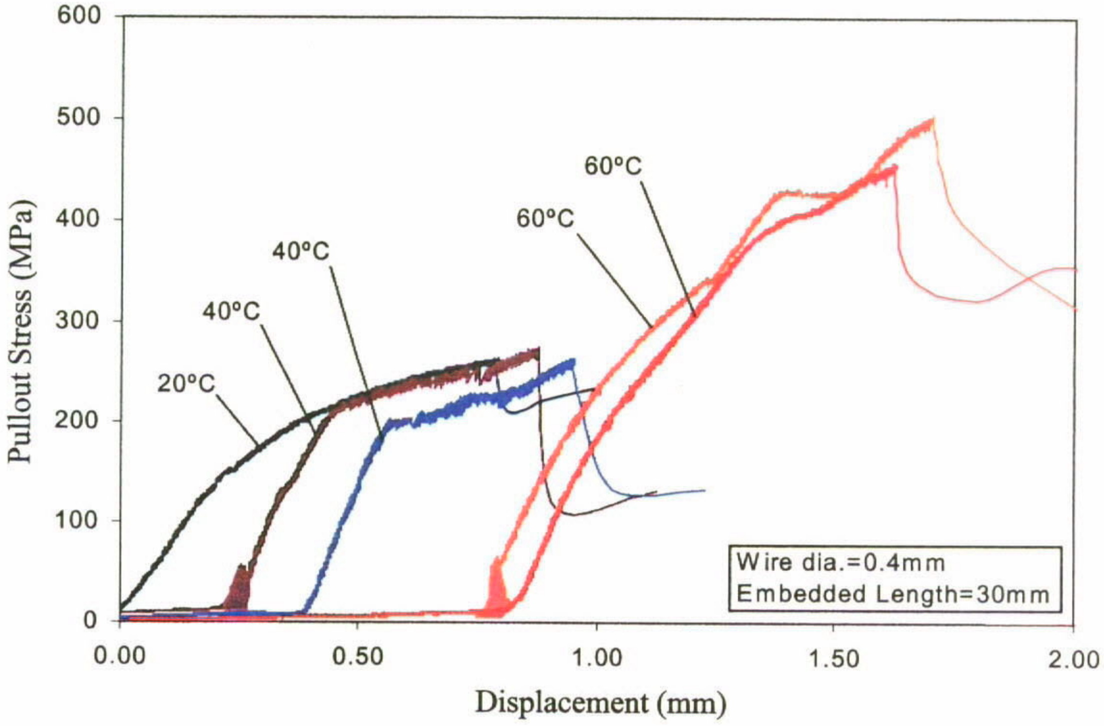

Figure 6.6 Typical Pullout test results for SMA-epoxy matrix cylinders subjected to different actuation temperatures.

displacement curve. The initial debond, which is normally identified by sudden slope change, may be covered up by the SIM.

6.2.1.2 Digital Video Monitoring of Debonding Processes

Due to the problems on the identification of initial debond stress, σ_d^o, in this study, the measured pullout stresses in partial debonded condition were plotted against the debonded lengths, l, which were captured by a high resolution digital video camera at the instant. As an example, if the debonded length observed in video is 5mm from loading end and the corresponding time frame is 50sec, the instantaneous value of applied stress can be traced back from the pullout test data for the same time frame. Depending on the wire embedded length and the transparency of epoxy matrix cylinder, two to eight sets of $\sigma_d^p(l)$ and l results can be obtained from video. Figures 6.7a to c show the images of partial debond extracted from pullout test video for the debonded lengths, l at 5mm, 15mm and 25mm respectively. Using the instantaneous time frame as shown at right bottom corners, the corresponding pullout stresses are readily obtained from pullout test data recorded by the MTS machine.

6.3 Determination of Interfacial Properties

6.3.1 Stress Drop Analysis

In pullout test for the conventional types of fibre-matrix cylinder with constant material properties of both constituents, the maximum debond stress, σ_d^*, is obtained when the remaining bonded length, $L - l$, reaches the critical value g^*. The previously developed stress drop analysis [120] considers the difference between the maximum debond stress, σ_d^* and initial frictional pullout stress, σ_{fr} as given below,

$$\begin{aligned}\Delta\sigma &= \sigma_d^* - \sigma_{fr} \\ &= \exp\left[-\lambda\left(L-g^*\right)\right]\left\{\sigma_{3l} + \sigma_3^*\left[\exp\left(-\lambda g^* - 1\right)\right]\right\}\end{aligned} \tag{6.1}$$

where g^* the critical bond length, is considered as a material constant which is independent of embedded fibre length, L for any given composite system [120]. σ_{3l} is the crack tip stress in type-III loading condition as given in Eqn. 5.15 for $z = l$. Further differentiating the logarithm of $\Delta\sigma$ with respect to L yields

$$\frac{d\ln\Delta\sigma}{dL} = -\lambda \tag{6.2}$$

One may notice that $-\lambda$ represents the slope of $\ln\Delta\sigma$ -L curve. Therefore, using the experimental data of σ_d^*, σ_{fr} and L, plot of $\ln\Delta\sigma$ versus against L can be obtained and hence to evaluate λ.

As previously discussed for the study of debonding behaviour, it is crucial to determine the three parameters including μ, q_o and G_{ic}. After the evaluation of λ from stress drop analysis, these parameters can be easily determined as summarized below.

Determination of μ :

Substituting λ into Eqn. 5.25 gives,

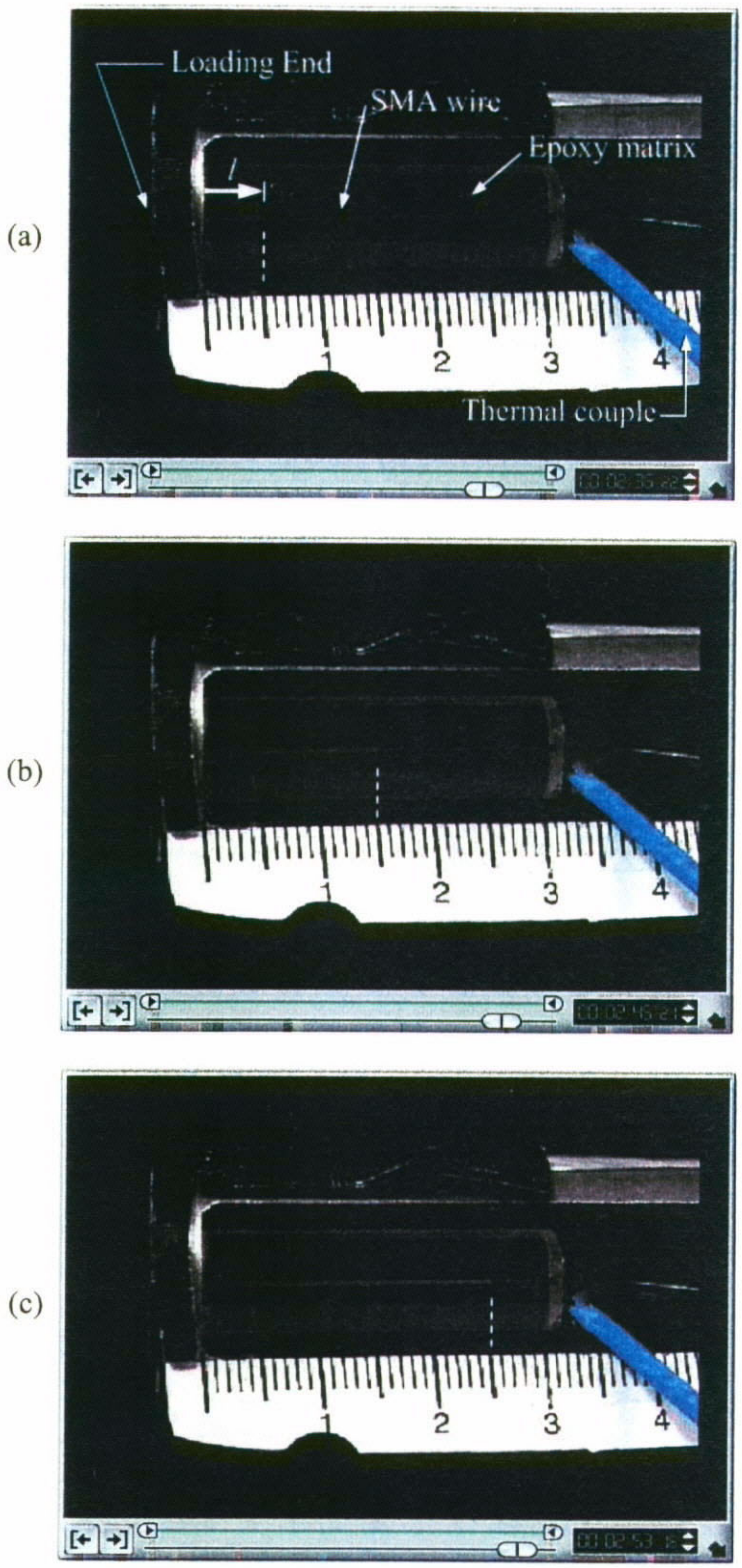

Figure 6.7 Images of crack propagation along interface between SMA wire and epoxy matrix. The measured debonded lengths, *l* are (a) 5mm, (b) 15mm and (c) 25mm respectively.

$$\mu = \frac{a\lambda}{2k} \tag{6.3}$$

where k is a constant value before SMA actuation.

Determination of q_o :

From the force balancing condition, partial debond stress, σ_d^p can be considered as the sum of crack tip stress, σ_{3l} and the stress components due to frictional shear in debonded region

$$\sigma_d^p = \sigma_{3l} + \frac{2}{a}\int_0^l \tau_f dz \tag{6.4}$$

The initial frictional pullout stress, σ_{fr} can be obtained for $l = L$ and the crack tip stress, σ_{3l} becomes zero at the instant. Therefore

$$\begin{aligned} \sigma_{fr} &= \frac{2}{a}\int_0^L \tau_{fr} dz \\ &= \sigma_3^*\left[1 - e^{-\lambda l}\right] \end{aligned} \tag{6.5}$$

where σ_3^* and λ are constants at $T < T_{so}^A$. Using a simple mean value method, the asymptotic debond stress σ_3^* can be obtained as shown below,

$$\sigma_3^* = \frac{1}{n}\sum_{j=1}^{m} \frac{(\sigma_{fr})_j}{1 - e^{-\lambda L_j}} \tag{6.6}$$

where $\left(\sigma_{fr}\right)_j$ (j = 1 to m) represent the experimental data of initial frictional stress corresponding to different embedded length, L_j. Finally, the residual clamping stress q_o can be obtained from Eqn. 5.20

$$\begin{aligned} q_o &= -\left(\sigma_3^{\bullet} + \eta E_T\right)k \\ &= -\sigma_3^{\bullet}k \qquad \text{for } T = T_o \end{aligned} \tag{6.7}$$

Determination of G_{ic} :

Substituting the experimental results of $\sigma_{dj}^{\bullet}$ and L_j into Eqn. 5.39, the interfacial fracture toughness can be determined by using the mean value method as given below

$$G_{ic} = \frac{1}{2\pi am}\sum_{j=1}^{m}\left[\tilde{B}_3\sigma_{dj}^{\bullet\,2} + \tilde{C}_3\left(\tilde{\sigma}_{3j}^{\bullet} - \sigma_{dj}^{\bullet}\right)\sigma_{dj}^{\bullet} + \tilde{D}_3\left(\tilde{\sigma}_{3j}^{\bullet} - \sigma_{dj}^{\bullet}\right)^2\right] \tag{6.8}$$

It should be noted that the coefficients $\tilde{L}_3$, $\tilde{M}_3$ and $\tilde{N}_3$ arising from SMA actuation become zero at $T = T_o$. This implies that the total elastic strain energy stored in constituents is independent of shape memory effect but due to externally applied load only. Interfacial properties of SMA-epoxy matrix cylinders embedded with type #1 and #2 SMA wires are summarized in Table 6.3.

6.4 Analysis of Debonding Stresses in SMA Actuation

6.4.1 Stress Development in Partial Debonded Condition

Referring to Fig. 6.6 for the typical pullout test results of dia.0.4mm SMA wire in 30mm epoxy matrix cylinder; it is no doubt that the higher the actuation temperature, the higher the maximum debond stress can be attained. The recovery stress acting in the opposite direction of the applied load moderates the interfacial shear at loading end – the potential crack tip. As a result, higher applied load is required to initiate interfacial debond in the actuated SMA-composites. It should be noted that a 'minor' improvement of maximum debond stress can also be observed at 40°C, which is supposed immediately higher than austenitic transformation start temperature, T_{so}^{A}. The recovery stress for $T < T_{so}^{A}$ increases linearly with temperature under a strain-constrained condition and it is generally governed by a thermal coefficient of expansion, θ. Therefore, it is not surprised for having improvement of maximum debond stress in such low actuation temperature. Using the data obtained from the video capturing system, relations between the pullout stress at partial debond condition, σ_d^p and the debond length, l at 20°C, 40°C and 60°C can be clarified. Figure 6.8 shows the data plots of σ_d^p against l for dia.0.4mm SMA wire with 30mm embedded length at different temperatures, where the plots for all specimens with different dimensions are more or less the same under the identical loading-actuation condition. Therefore Fig. 6.8 represents the typical experimental results for illustration purpose.

In addition, the plots of theoretical solution, σ_d^p (Eqn. 5.96) against l are compared with experimental results in Fig. 6.8. Both the pullout test results and theoretical predictions agree that the higher the actuation temperature, the higher the debond stresses are attained. This improvement is not only limited to maximum debond stresses, but also

Table 6.3 Interfacial properties for epoxy matrix cylinder embedded with type #1 and #2 SMA wires.

Interfacial Properties SMA Wire Type	λ	μ	q_o (MPa)	G_F (J/m^2)
#1 (Dia. 0.25mm)	13.75	0.031	-16.50	126
#2 (Dia. 0.4mm)	9.5452	0.035	-9.85	96

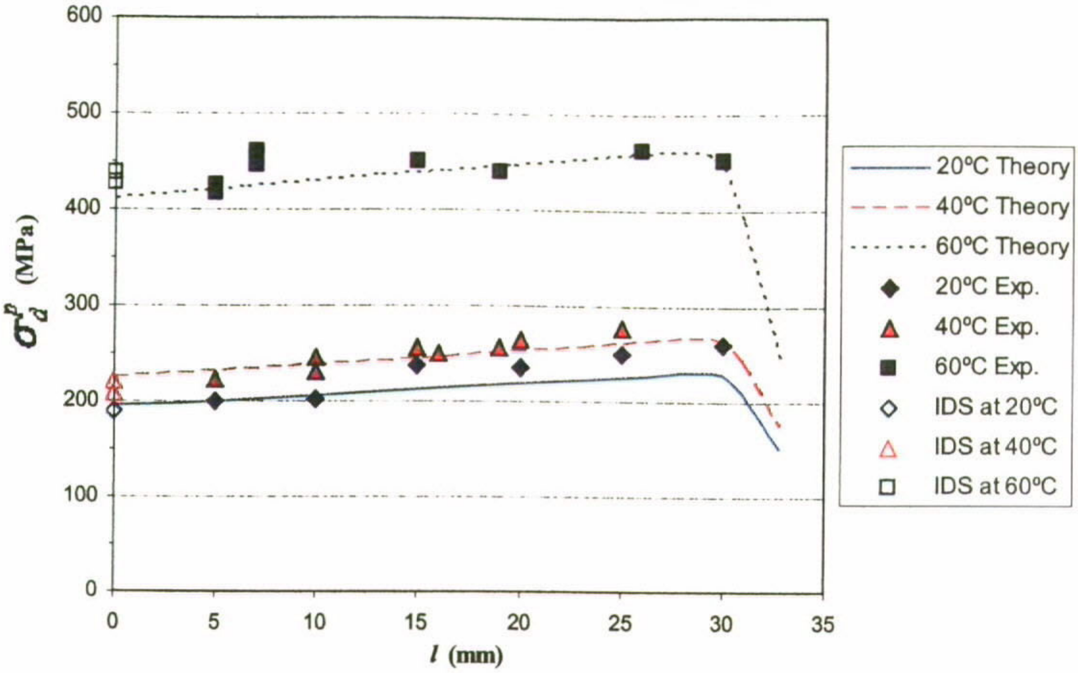

Figure 6.8 Comparison between theoretical solutions and pullout test results of partial debond stress, σ_d^p against debond length, l.

the initial values. Initial debond stresses were estimated by using extrapolation on the experimental data of σ_d^p. Results indicate outstanding improvement in debond stresses occurred at 60°C. However substantial increases of debond stresses can only be observed for 40°C during the initial debonding process. Theoretical solution reproduces all these changes due to shape memory effect. It confirms that both the initial and maximum debond stresses as well as the slope of stress development in the debonding process can be predicted in a good manner which means that the theoretical solutions are valid for actuation temperature above or below the phase transformation temperature – T_{so}^A.

6.4.2 Improvement of Bond Strength

Again, solving Eqn. 5.96 for σ_d^p at $l = 0$, solution of initial debond stress, σ_d^o at different actuation temperatures can be obtained. Figures 6.9 and 6.10 show the influences of the SMA actuation on σ_d^o for the matrix cylinders embedded with dia.

0.25mm and 0.4mm NiTi wires respectively. The two types of wire were prestrained by 4% and the material properties applied for the theoretical solutions are summarized in Table 6.1. Since the experimental data of σ_d^o were estimated from video captured results, due to the small dimensions and unclear matrix cylinder of several specimens, some of the initial debond stresses could not be clearly identified due to lack of data for extrapolation. This problem restricts the accuracy of σ_d^o estimation for L = 2mm. Therefore, only the solutions for L = 5mm, 30mm and 50mm are presented here to compare with experimental data. Obviously, both the theoretical and experimental findings confirm the improvement of initial and maximum debond stresses due to the SMA actuation.

When the wire embedded length increases to 50mm, both the experimental results for 0.25mm and 0.4mm SMA wires demonstrate outstanding improvement of σ_d^o at 60°C as shown in Figs. 6.9 and 6.10 respectively. The maximum value of σ_d^o for 0.25mm wire with L = 50mm is 730MPa, which is about 200% higher than that before actuation (T = 20°C). Similar result is obtained for the case with 0.4mm SMA wire and L = 50mm (σ_d^o = 504MPa at 60°C), the improvement of initial debond stress is almost 160%. It can be found that the theoretical results reproduce the effect of SMA actuation on σ_d^o improvement in a generally good manner in the two cases (0.25mm and 0.4mm SMA wires) for different embedded lengths. The predictions are particularly accurate for L = 30mm and 50mm, while the considerable derivations of experimental data were found for L = 2mm and 5mm. In addition to the problem of over-actuation which leads to sudden drop of pullout stress, fail to predict appropriate material properties of the SMA inclusions may also reduce the prediction accuracy. As previously discussed in the

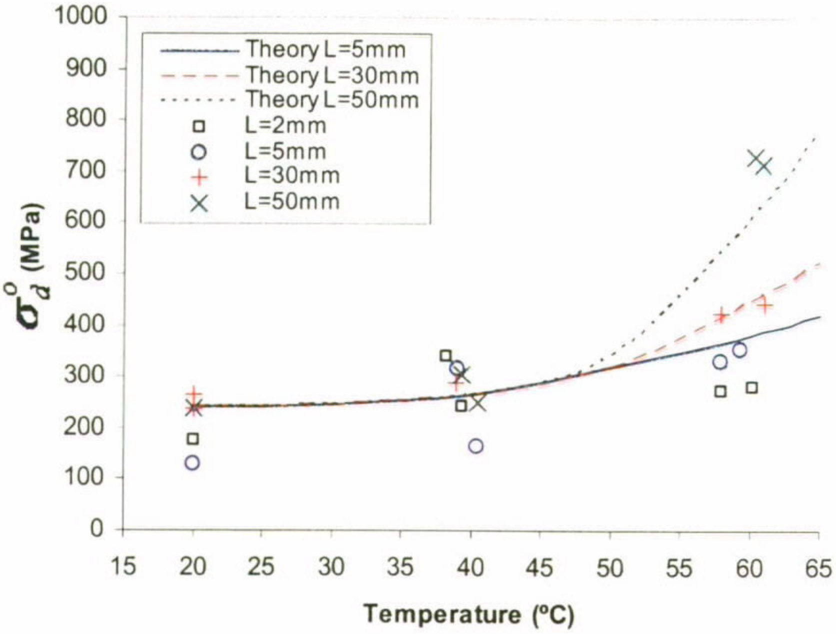

Figure 6.9 Influence of wire embedded length, L on the initial debond stress, σ_d^o under SMA actuation (for Dia. 0.25mm SMA wire).

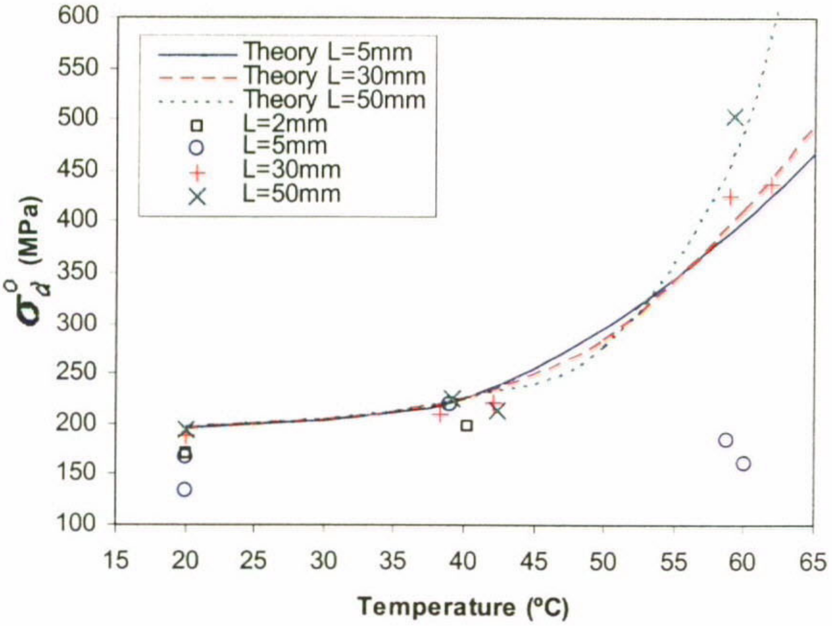

Figure 6.10 Influence of wire embedded length, L on the initial debond stress, σ_d^o under SMA actuation (for Dia. 0.4mm SMA wire).

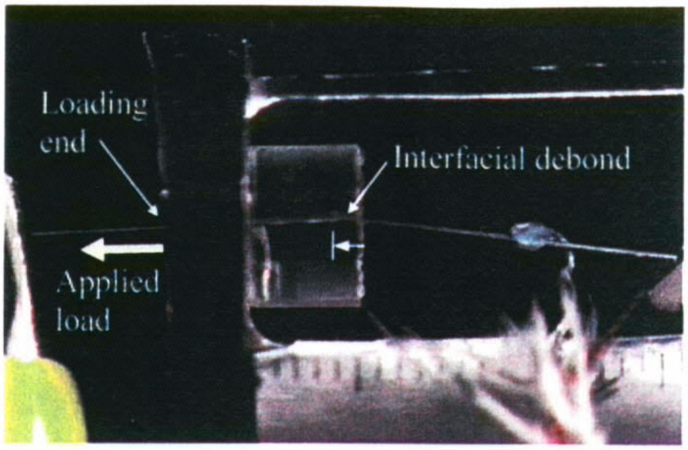

Figure 6.11 Interfacial debond occurred at free end for $L = 5$mm at $T = 60^{\circ}$C.

Chapter 5 for the application of equivalent material properties in the interfacial debond criterion (Eqn. 5.39), the critical embedded length, L_c is required to be satisfied for achieving the 'constant martensite volume fraction region' (CMR) on the SMA wire (Section 4.2.2.3). Otherwise Eqn. 5.38 becomes invalid for the short embedded length. As a result the ξ value could be over-estimated and hence the calculation of total elastic strain energy stored in constituents cannot be based on the constant material properties in a given temperature.

Considering the results for the specimens with embedded length 5mm, both the initial and the maximum debond stresses for 60°C are lower than that for 40°C. This observation contradicts to the outstanding improvement of debond stresses for 60°C as found in all other pullout test results or even the theoretical predictions. Referring to captured videos for those particular cases, it was found that the interfacial debond initiated at free end instead of loading end as shown in Fig. 6.11 . It is probably the problem of over-actuation on SMA wire for ε_p = 4%, which means recovery stress induced at free end may be too high to damage the interfacial bond. When the wire has been heated up to a relatively high temperature ($T > 60^{\circ}C$), interfacial shear at loading end could be moderated. However, at the free end, both the shear stress components arising from recovery action and applied load act in the same direction. As a result, the resultant interfacial shear becomes higher and eventually damages the interface.

6.4.3 Influence of Prestrain Value on Interfacial Debond

Referring to Eqn. 3.4 for the governing equation of constrained recovery stress, σ_r. prestrain value, ε_p is the critical parameter which determines the maximum recovery stress of a SMA wire in composite material. Therefore, it is crucial to clarify the effects of ε_p in the SMA reinforced composites by comparing the pullout test results for different ε_p–values. However, the accuracy of prestrained level of the SMA inclusions depends on the amount of unwanted cold works applied on wire during the fabrication process, such as the installation of prestrained SMA wires into the fabrication mold (Fig. 6.1) and the preload applied for holding the SMA wire in the curing process of epoxy matrix. All these unavoidable cold works may change the final value of ε_p inside a composite structure. In order to minimize these potential errors in the experimental studies, in addition to the specimens handling with extra care, prestrain values of 0%, 4% and 8% are chosen so as to ensure substantial differences between the results.

Plots of experimental data and theoretical predictions of 0%, 4% and 8% prestrain for L = 30mm and 50mm are shown in Figs. 6.12a and b respectively. One may notice that the fairly good agreement between experimental data and theoretical solutions is obtained for 4% and 8% prestrains. However, the experimental results for 0% prestrain are always lower than those for higher prestrain values even in the low temperature condition. When $T < T_{so}^{A}$, the constituents are supposed suffering thermal expansion only, and no considerable changes of initial debond stress should be observed. However, in order to fabricate the specimens with ε_p close to 0%, it is required to install SMA wires on the fixture slightly. As a result, the wires' alignment may not be controlled as good as those for higher ε_p–values. Therefore, the effective internal stress transmission across wire-matrix interface may not be achieved and as a result the interfacial shear at loading end becomes relatively high. Eventually, interfacial debond may start at a lower stress level. Except the unexpected pullout test results for 0% prestrain due to the captioned problems, relations between initial debond stress and actuation temperature for other prestrain levels can be predicted with reasonable accuracy in both low temperature region ($T < T_{so}^{A}$) and high actuation condition ($T > T_{so}^{A}$). The theoretical model successfully predictes the dramatic improvement of σ_d^o as actuation temperature increased over T_{so}^{A}. Since the ε_p–value governs the maximum recovery stress inside, which works against the externally applied load on wire, it is reasonable for having the highest debonding stress at 8% prestrain within each given temperature regions (i.e. 20°C, 40°C and 60°C). In case of 4% prestrain, both the experimental data and theoretical predictions are always lower than or equals to those for 8% prestrain. In Fig. 6.12b, the maximum value of σ_d^o obtained from pullout test for 8% prestrain is 784MPa at 68°C, which is almost 300% higher than the one without actuation.

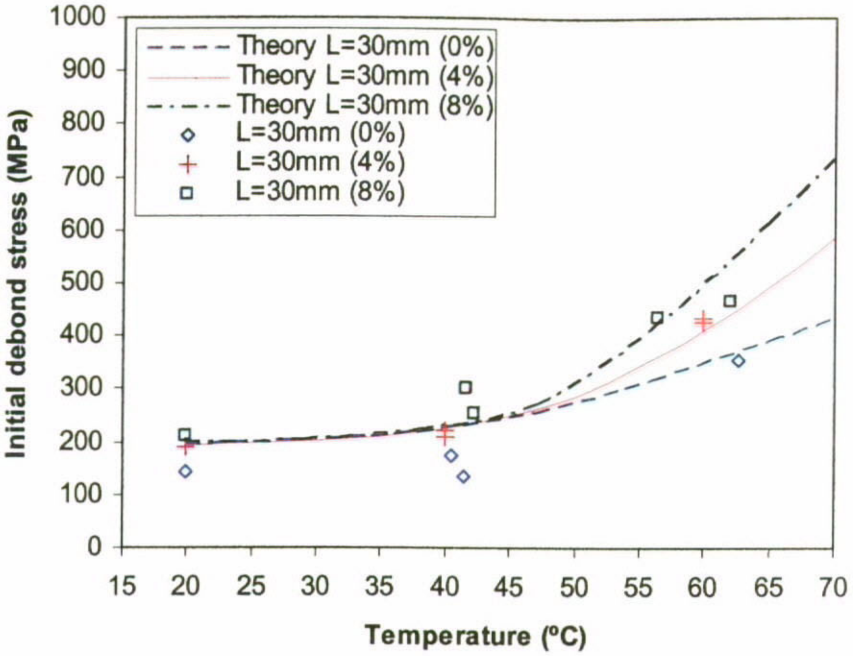

(a)

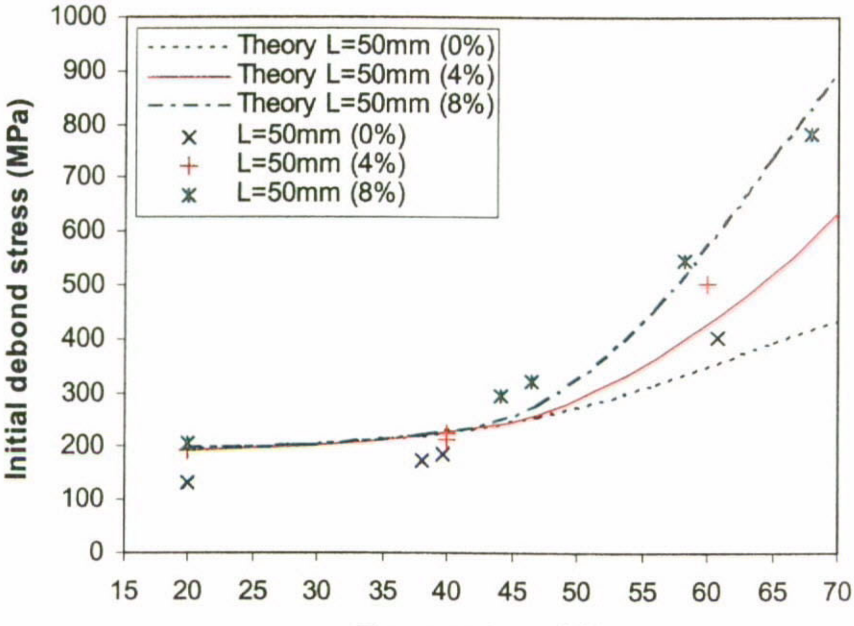

(b)

Figure 6.12 Influence of prestrain value, ε_p on the initial debond stress, σ_d^o in SMA actuation for (a) $L = 30$mm and (b) $L = 50$mm.

6.5 Summary

The previously developed theoretical model for the prediction of debond stresses has been validated by using a hybrid-experimental method in this study. Except the stress-displacement relation obtained from the single fiber pullout test, a digital video capturing system was also employed to identify the direction of debond propagation and the partial debonded length during the pullout test. This newly proposed experimental method is particularly useful to study the fracture mechanics in the partially debonded condition. Pullout test results confirm that both the initial and maximum debond stresses are improved with the increase of actuation temperature. The results obtained from video monitoring system clarified the relationship between partial debond stress and the corresponding debonding length. It has been found that the initial debond stress under the same actuation temperature was increased with wire embedded length.

Chapter 7

Optimum Actuation Condition

7.1 Introduction

Techniques of using Shape Memory Alloy (SMA) wires as actuators inside the hybrid composites have been studied extensively for improving mechanical properties of structures. There were many experimental findings and theoretical predictions agreed that the higher the actuation temperature on built-in SMA wires, the greater the improvement in mechanical response of a composite due to recovery action of wires. However, because of the limitation of interfacial shear strength, over-actuation (by means of electrical resistive heating) of the SMA wire is able to induce the development of interfacial crack inside the composite structure. When the maximum interfacial shear strength is attained due to vigorous recovery action of the SMA wire under relatively high temperature, interfacial debonding may occur. In this chapter, a typical SMA-matrix cylinder model is employed to study the captioned risk of SMA actuation. The concept of optimum actuation condition (OAC) is therefore proposed in the current study so as to predict an appropriate actuation level to prevent structural failure due to over-actuation. Influence of prestrain values as well as the geometric factors will be discussed in the following sections so as to present an over-view on the feasibility of the OAC control for the SMA-reinforced composites.

7.2 Theoretical Analysis

In this chapter, the SMA-matrix cylinder model is employed again to evaluate effects of the SME and thermal expansion on the interfacial debonding during the actuation process. Figure 7.1 shows the Type I loading condition for the SMA-matrix cylinder with fixed matrix bottom. The SMA wire end is subjected to a pull-out stress in axial direction. Using Eqn. 5.29 for the solution of interfacial shear stress τ_{i1} in the type-I/mode-b loading-actuation scenario,the surface plot of interfacial shear stress of the SMA-matrix cylinder is obtained and shown in Fig. 7.2. The plot presents the effect of actuation temperature on the interfacial shear stress distribution for L = 3mm, b/a = 40 and prestrain value, ε_p = 2%. When the wire end is subjected to an axial pull-out stress, σ = 500MPa but no electric current is supplied to heat up the wire, the interfacial debond tends to start from loading end due to the highest interfacial shear stress. However, it is clearly shown that the stress value at $z = 0$ (loading end) is decreased with increase of the temperature.When the SMA wire is heated up, the stress level raises up at $z = L$. This implies that, under a high actuation temperature, interfacial debond is able to start at the free end even though an external stress is applied at loading end. Using Eqn. 5.29, interfacial shear stress distributions are plotted for different embedded wire lengths and shown in Fig. 7.3a. The figure shows how the interfacial shear stress levels at free end ($z = L$) for a given applied load are affected by the embedded length, L in a zero-actuation condition. Under a constant ratio of b/a = 40, σ = 500MPa and $T = T_o$, stress distribution curves for composites with shorter embedded length, L are always located at a higher position. The predicted shear stresses at loading end, $\tau_i(0, \sigma, T_o)$ are almost the same for all curves. Substantial derivation of stress values at wires' free end, $\tau_i(L, \sigma, T_o)$ for

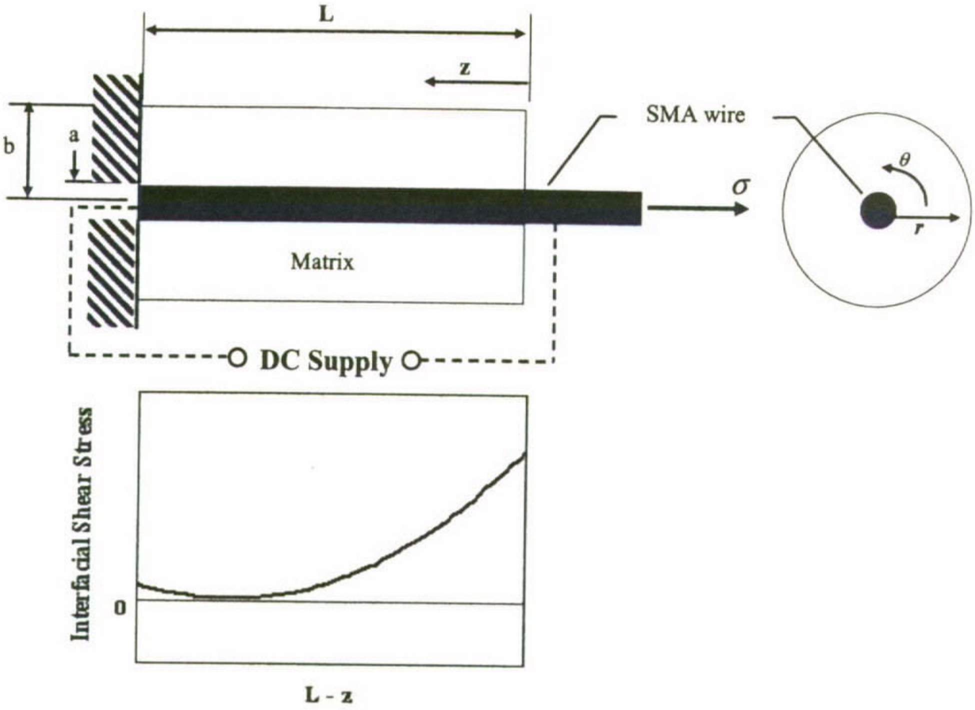

Figure 7.1 Loading configuration on the SMA-matrix cylinder model.

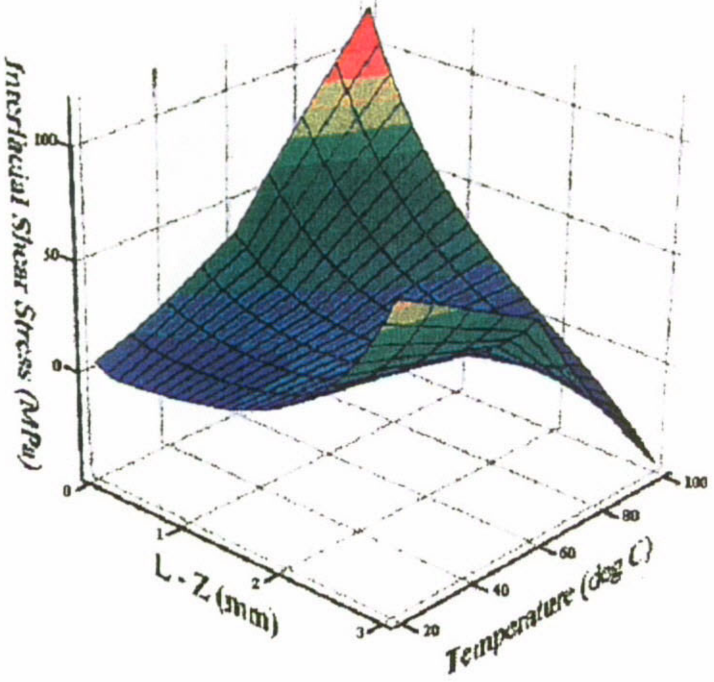

Figure 7.2 Surface plot of interfacial shear stress inside a SMA-matrix cylinder. ($\sigma = 0.5$GPa, $L = 3$mm, $b/a = 40$, $\varepsilon_p = 2\%$.)

L = 2mm and 3mm is also found. This observation implies that the axial stresses on SMA wire are not effectively transferred to its surrounding matrix through the interface. Therefore interfacial shear stress at free end is still reasonably high in the case of short embedded length.

In addition to the effect of the wire embedded length, L on stress distribution profiles inside the SMA-composites, b/a ratio is another important parameter affecting the shear stress distribution. Figure 7.3b shows the effect of matrix-to-wire radius ratio, b/a on the interfacial shear stress distributions for L = 4mm, $T = T_o$ and σ = 500MPa at $z = 0$. It is noted that for b/a = 10, interfacial shear stress decreases as z increases in the first half of the embedded length. However, $\tau_i(L,\sigma,T_o)$ increases to reach a finite value (approx. 20MPa) at the free end. If the b/a ratio is further decreased, increases of interfacial shear stress at free end can be observed. These shear stresses at free end become negligible for $b/a \geq 20$. This implies that a considerable high interfacial shear stress at free end can be generated by the applied load, σ without contribution of SME. This phenomenon is actually due to the stress-free condition at wire end [114,115].

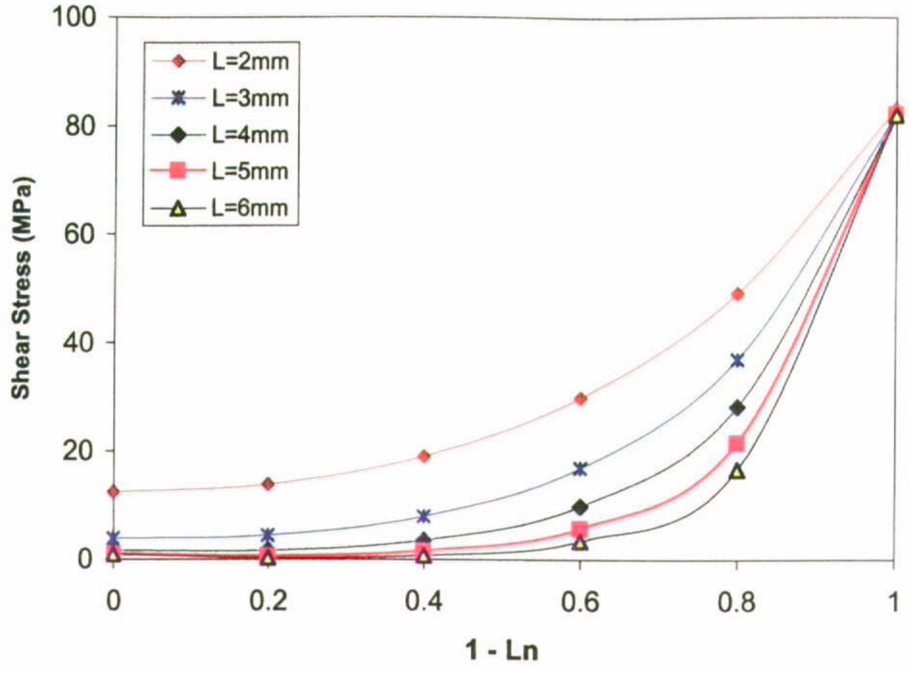

(a)

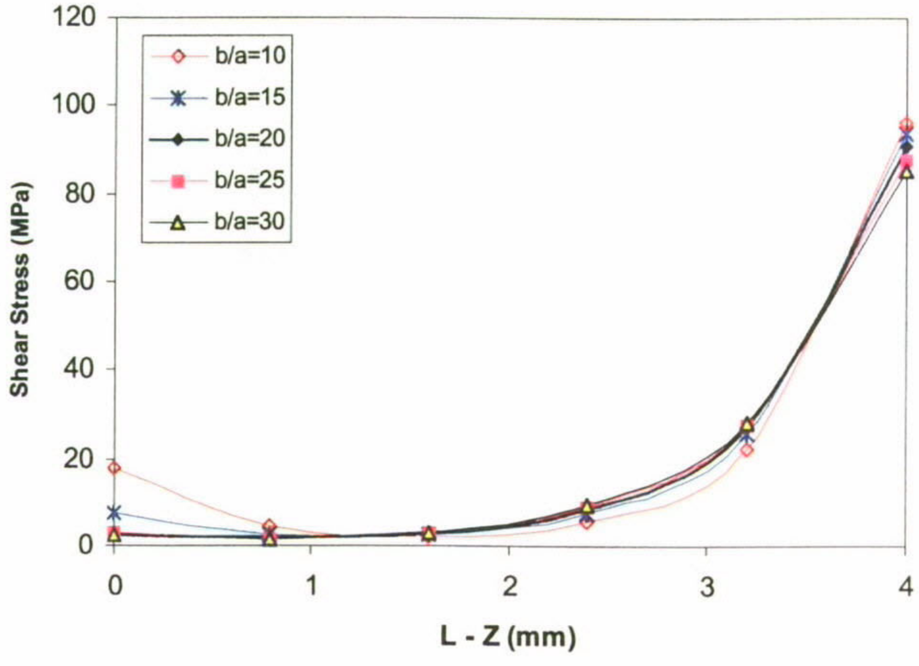

(b)

Figure 7.3 Plots of interfacial shear stress distributions for a) different wire embedded length, L. and b) different matrix-to-wire radius ratio, b/a. (where $L_n = z/L$)

7.2.1 Definition of Optimum Actuation Condition

Figure 7.4 schematically demonstrates the changes of stress distribution in different temperatures. Dotted lines in figures specify the maximum interfacial shear strength, τ_M, which is considered as a material constant. Whenever a curve reaches the line, interfacial debond starts immediately. It is assumed that when $T = T_o$ and applied axial stress at loading end is σ_d^o, the maximum interfacial shear strength, τ_M is just satisfied ($\tau_{i1}(0, \sigma_d^o, T_o) = \tau_M$). However, if the SMA wire is heated up to T_1 or even T_2, the maximum interfacial shear stress at loading end is moderated ($\tau_{i1}(0, \sigma_d^o, T_1)$ or $\tau_{i1}(0, \sigma_d^o, T_2) < \tau_M$) and extra amount of axial load $+\Delta\sigma$ is thus required to increase the shear stress again until τ_M is satisfied to initiate interfacial debond. In the worst scenario as shown in Fig. 7.4d, the highest stress moderation at loading end is obtained. However, the maximum bond strength is satisfied at free end without any further increase of the applied load. Since the interfacial shear stress at free end is induced by applied load as discussed previously, the reduction of applied load $-\Delta\sigma$ may be required to lower the stress level at $z = L$ for avoiding the interfacial debond.

If the actuation temperature is relative low, maximum shear stress will always appear at the loading end. However, as being shown in Figs. 7.2 and 7.4, further increase in actuation level increases the interfacial shear stress at the free end accordingly. When the critical actuation level ($T = T_{OA}$ as illustrated in Fig. 7.4c) is achieved, the interfacial shear stress at both ends becomes the same ($\tau_i(0, \sigma_d^o, T_{OA}) = \tau_i(L, \sigma_d^o, T_{OA})$). The optimum actuation condition (OAC) requires the equivalent shear stress at both the free end and loading end for any particular level of axial stress acting on SMA wire. This criterion can

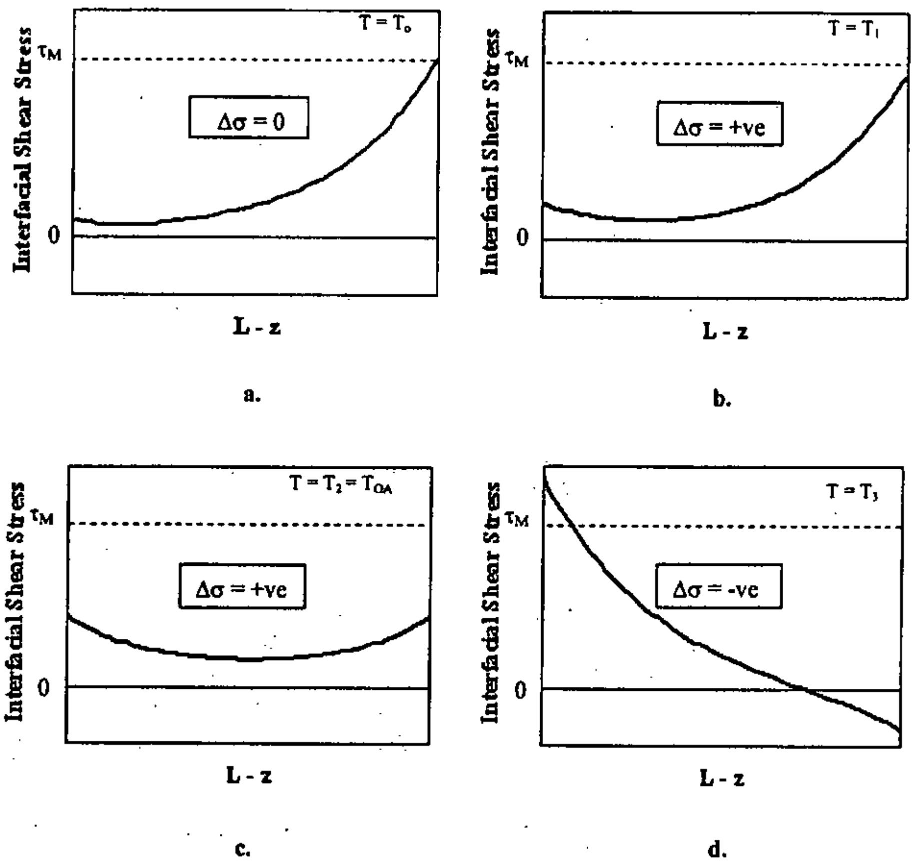

Figure 7.4 Schematic illustrations of stress variations under constant applied load but different actuation temperatures: a.) $\sigma = \sigma_d^o$, $T = T_o$; b.) $\sigma = \sigma_d^o$, $T = T_1$; c.) $\sigma = \sigma_d^o$, $T = T_2 = T_{OA}$ and d.) $\sigma = \sigma_d^o$, $T = T_3$ (Assuming that $T_o<T_1<T_2<T_3$ and T_{OA} is an ideal actuation temperature for optimum actuation condition.)

be simulated mathematically by setting the following condition

$$\tau_{i1}(0,\sigma,T) = \tau_{i1}(L,\sigma,T) \tag{7.1}$$

It should be noted that the Eqn. 7.1 is actually the relation between applied stress and the actuation temperature. Therefore, using this OAC criterion for the equivalent values of τ_{i1} at both $z = 0$ and $z = L$, the specific relationship between applied stress, σ and the target actuation temperature, T can be numerically determined.

7.2.2 Numerical Solutions of OAC at Different Prestrain Values

Numerical solutions of OAC for the SMA-composites embedded with the SMA wire prestrained by 1%, 2%, 3%, 5% and 10% are shown in Fig.7.5. Plots of critical relations between applied stress σ and actuation temperature T for satisfying the criterion of optimum actuation condition Eqn. 7.1 is known as OAC plots in the current study. Results indicate that the increase in actuation temperature increases the slopes of OAC plots for the pre-strained value $\varepsilon_p > 2\%$. If the pre-strained values are controlled at relatively low levels, $\varepsilon_p < 2\%$, slope of OAC plots will decrease or even tend to zero when the actuation temperature is further increased.

7.3 Evaluation of Simplified Optimum Actuation Condition

Substituting Eqn. 5.29 into Eqn.7.1 yields,

$$\frac{(\psi_{30}\sigma+\psi_{40})\sqrt{\psi_{10}}+(\sigma+\psi_{30}\sigma+\psi_{40})\sqrt{\psi_{10}}\cosh(\sqrt{\psi_{10}}L)}{\sinh(\sqrt{\psi_{10}}L)}=\frac{(\psi_{3L}\sigma+\psi_{4L})\sqrt{\psi_{1L}}\cosh(\sqrt{\psi_{1L}}L)+(\sigma+\psi_{3L}\sigma+\psi_{4L})\sqrt{\psi_{1L}}}{\sinh(\sqrt{\psi_{1L}}L)} \tag{7.2}$$

where the subscript '*0*' and '*L*' represent the corresponding parameters at $z = 0$ and L respectively. Since all those parameters are complex functions of both σ and T, no explicit solution can be derived for either $\sigma(T)$ or $T(\sigma)$ and only numerical solutions are available for the relation between σ and T. As discussed previously, if the value of L and b/a ratio are sufficiently large under a zero-actuation condition, interfacial shear stress at free end becomes negligible and hence the criterion of OAC can be greatly simplified by using a

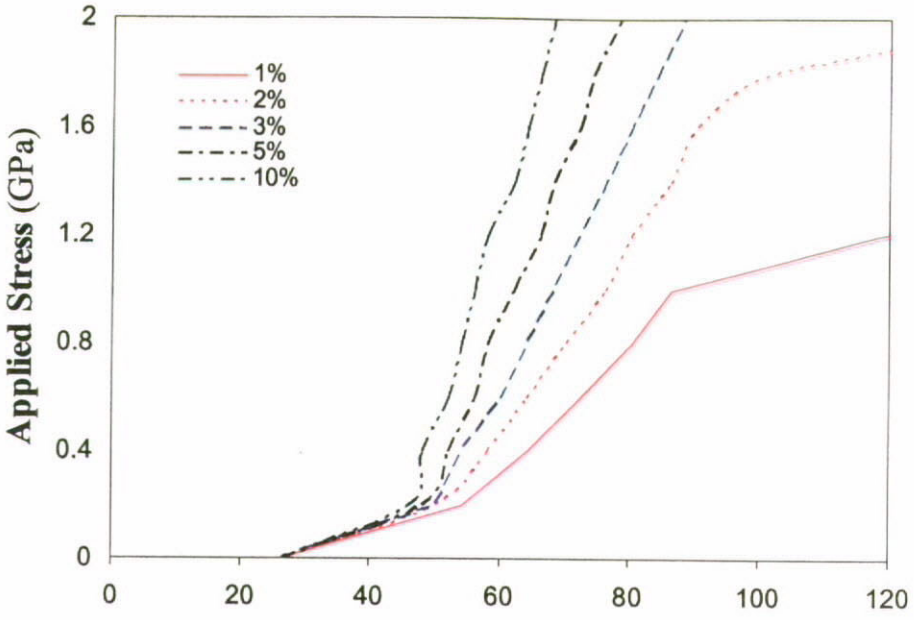

Figure 7.5 Plots of specific relations between applied normal stress, σ and target actuation temperature, T under the optimum actuation condition (OAC) for different pre-strain values (1%, 2%, 3%, 5% and 10%).

simple superposition method as following,

$$\tau_i(L,0,T) = \tau_i(0,0,T) + \tau_i(0,\sigma,T_o) \quad (7.3)$$

where $\tau_i(z,0,T)$ refers to the interfacial shear stress due to recovery action only and is independent of the applied stress, σ. $\tau_i(0,0,T)$ and $\tau_i(L,0,T)$ represent the corresponding recovery stresses at the free end and loading end respectively. $\tau_i(0,\sigma,T_o)$ represents the interfacial shear stress at loading end arising from externally applied axial load before actuation and it can be formulated as a function of σ for given geometric factors and material properties from Eqn. 5.29 as shown below,

$$\tau_i(0,\sigma,T_o) = Q_1\sigma + Q_2 \quad (7.4)$$

in which, Q_1 and Q_2 are constants for the given material properties and geometric factors. Applying Eqn. 5.29 again for the stress free condition at the wire's end ($\sigma = 0$ at $z = L$), $\tau_i(L,0,T)$ is given as following,

$$\tau_i(L,0,T) = \frac{a\sqrt{\psi_{1L}}\psi_{4L}}{2\sinh(\sqrt{\psi_{1L}}L)}[1 - \cosh(\sqrt{\psi_{1L}}L)] \tag{7.5}$$

where ψ_{1L} and ψ_{4L} are independent of σ due to the boundary condition for stress free requirement at the free end ($\sigma = 0$ at $z = L$). In addition, it is necessary to specify that $\tau_i(0,0,T)$ is actually equals to $\tau_i(L,0,T)$ in magnitude but act in opposite direction. Therefore, Eqn. 7.5 can be further reduced to

$$\tau_i(0,\sigma,T_o) = 2\tau_i(L,0,T) \tag{7.6}$$

It should be noticed that the left-hand side of Eqn. 7.6 is governed by applied stress only, while the stress component in right hand side is simply a function of actuation temperature. Due to the simplicity of Eqn. 7.6, this specific relationship is defined as simplified optimum actuation condition (SOAC) in this study.

Finally, substituting Eqns. 7.4 and 7.5 into Eqn. 7.6 yields,

$$\sigma(T) = \frac{a\sqrt{\psi_{1L}}\psi_{4L}(1 - \cosh(\sqrt{\psi_{1L}}L)) - Q_2}{\sinh(\sqrt{\psi_{1L}}L)Q_1} \tag{7.7}$$

Eqn. 7.7 is an analytical solution of σ with respect to T. The ideal relations between applied loads and actuation temperatures for achieving the OAC are therefore readily determined by using this simple equation.

7.4 Size Effect

7.4.1 Effect of Wire Embedded Length on the OAC

Comparisons between analytical solution of SOAC and numerical solution of OAC for different wire embedded lengths are illustrated in Fig. 7.6. It is noted that the substantial derivations from numerical solutions are observed for analytical solutions of SOAC for short embedded length (L < 4mm). Considering the results for L = 3mm as shown in Fig. 7.6b, as actuation temperature is gradually increased from initial temperature T_o = 25°C, the dotted line climbs up in sync with the solid line. When temperature is further increased to around 53°C, the dotted line starts to derivate from solid line. This derivation is continuously increased as temperature increases. A more obvious derivation can be found for shorter embedded length (L = 2mm) as shown in Fig. 7.6a. The predicted actuation temperature of SOAC for an analytical solution is always underestimated. Analytical solutions of SOAC are compatible with numerical solutions of OAC when long embedded lengths are being considered as shown in Fig. 7.6c and d. Developments of both the numerical and analytical solutions are in sync for L ≥ 4mm.

7.4.2 Effect of Matrix-to-wire Ratio on the OAC

Figure 7.7 shows the effect of *b/a* ratio on solution of OAC. With reference to the results shown in Fig. 7.6, it is not surprise for having similar effect on compatibility of analytical solutions of SOAC by varying the *b/a* ratio only. As what was predicted in Fig. 7.3b for the effect of *b/a* on interfacial shear stress distribution, when a small b/a ratio (< 10) is used, a finite value of shear stress at wire's free end is able to derivate the analytical solutions of SOAC from the numerical solutions. As discussed above, the interfacial shear stress appeared at free end before actuation is due to stress-free condition. Therefore the effect of reducing *b/a* ratio is similar to that of reducing wire embedded length *L*. Both of them result in the increase of interfacial shear stress at $z = L$.

7.5 Feasibility Study

Application of the concept of OAC requires the feed back of measured normal stress σ, so as to determine the target actuation temperature *T* by using Eqn. 7.1. Assuming that the same level of normal stress σ, is acting on the SMA-composites with ε_p = 1% and 5% respectively, and if the normal stress is increased by $\Delta\sigma$ the temperature changes of ΔT_1 and ΔT_2 as indicated in OAC plots (Fig.7.8) are required for maintaining the optimum condition. If $\Delta\sigma$ is considered as the precision of stress measurement, then ΔT will be regarded as the minimum required step size of actuation temperature. Therefore, the smaller value of ΔT_2 implies that the smaller step size of actuation temperature is required to maintain at OAC. This actuation requirement directly indicates the feasibility of achieving OAC by using the available actuation system. In order to facilitate the feasibility study, it is essential to define an actuation index Λ as shown below,

$$\Lambda = \frac{\Delta T}{\Delta \sigma} \tag{7.8}$$

where Λ is the ratio of required temperature change ΔT to the variation of applied stress $\Delta\sigma$. The higher the actuation index, the lower the accuracy and stability requirement for actuation control. Hence it is relatively easy to maintain at OAC.

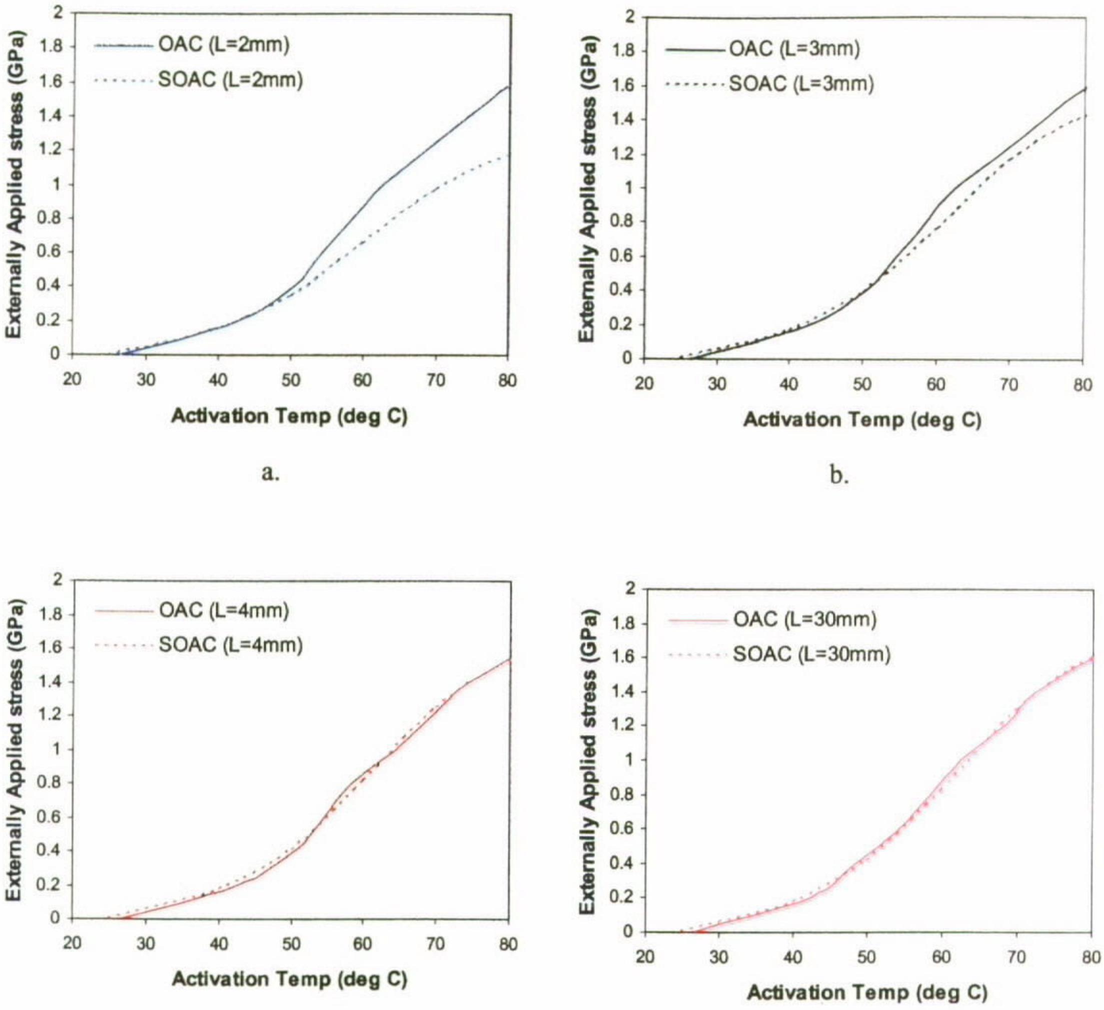

a.

b.

c.

d.

Figure 7.6 Comparisons between numerical solutions of OAC and analytical solutions of SOAC for different wire embedded lengths: a.) $L = 2$mm; b.) $L = 3$mm; c.) $L = 4$mm and d.) $L = 30$mm.

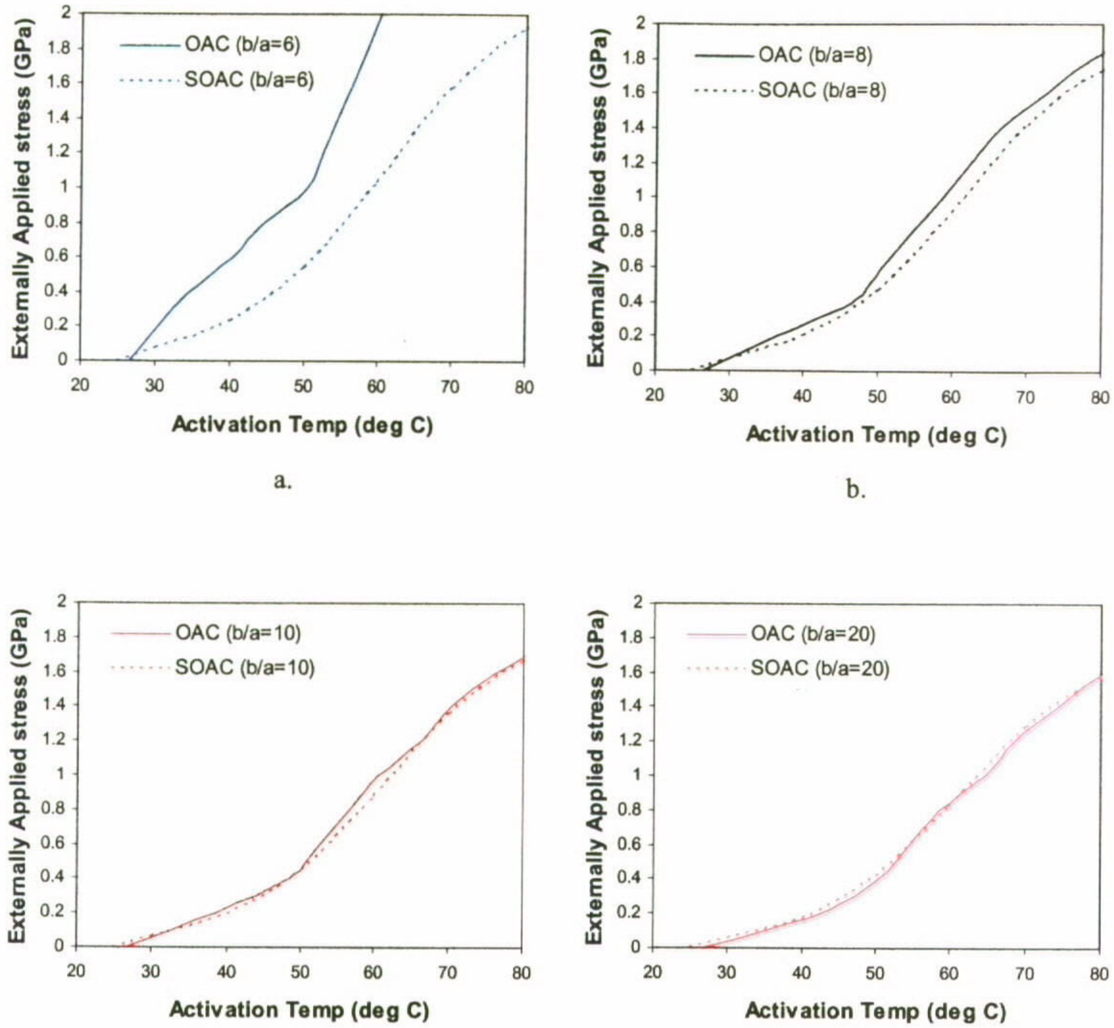

a.

b.

c.

d.

Figure 7.7 Comparisons between numerical solutions of OAC and analytical solutions of SOAC for different matrix-to-wire ratio: a.) *b/a* = 6; b.) *b/a* = 8; c.) *b/a* = 10 and d.) *b/a* = 20.

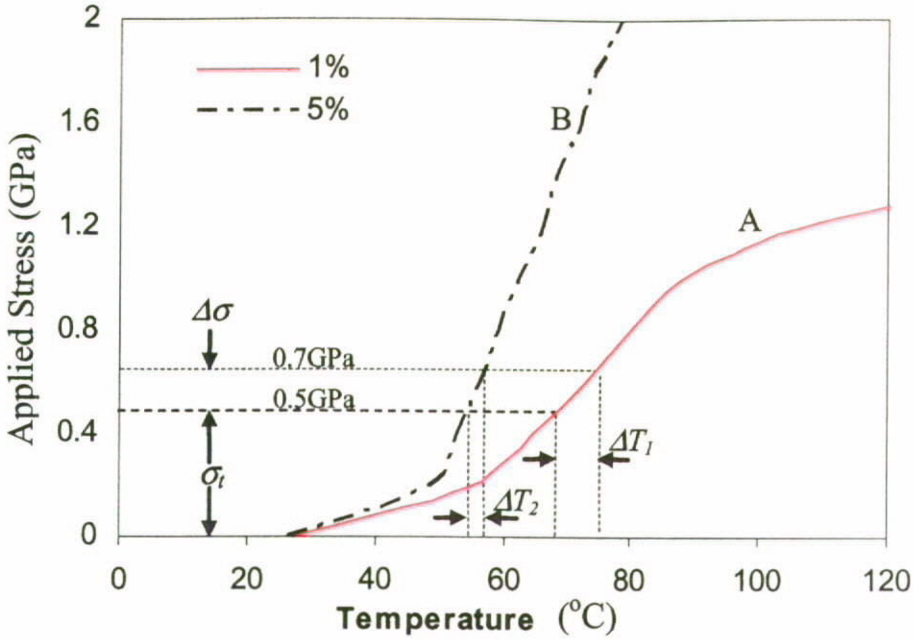

Figure 7.8 OAC plots for $\varepsilon_p = 1\%$ and 5% illustrate the concept of actuation index $\Lambda = \Delta T / \Delta\sigma$ for the feasibility assessment.

7.6 Example for the Feasibility Study of OAC

Assuming that there are two SMA-composites A and B with $\varepsilon_p = 1\%$ and 5% respectively And if the two composites are operated between the stress levels of 0.5GPa and 0.7GPa, the average actuation index should be $\Lambda_A \sim 30$°C/GPa and $\Lambda_B \sim 100$°C/GPa as shown in Fig.7.8. It implies that the composite B is much more sensitive (~6.67 times of that of composite A) to the temperature change. Therefore, if the precision of temperature control is assumed to be ±1°C, the maximum derivation from the targeted normal stress σ_t will be ± 0.0125GPa and ±0.0833GPa for composite A and B respectively. It can be concluded that a SMA-composite with higher value of ε_p is more difficult to be maintained at OAC or otherwise the temperature control system with higher precision and accuracy is required.

7.7 Summary

In this Chapter, the Optimum Actuation Condition (OAC) has been clearly defined which specifies the relation between applied load σ_a and the target level of actuation temperature T_t. Numerical results indicated that the prestrain value ε_p governs the manipulation (actuation index) of the SMA-composites. In addition, a simple equation for the determination of optimum actuation condition (OAC) was successfully developed. Using the fundamental knowledge of size effect on stress distributions obtained in this study, criterion of OAC (Eqn. 7.1) has been reduced to a simple relation between purely load-induced and purely temperature-induced interfacial shear stresses at different ends by using superposition method. This specific relation has been defined as simplified optimum actuation condition (SOAC). The effects of geometric factors including wire embedded length L and matrix-to-wire radius ratio b/a on the interfacial shear stress distribution under the zero-actuation condition have been studied. It has been found that the interfacial shear stress at free end is negligible for high values of L or b/a. An analytical solution for SOAC (Eqn. 7.7) clarifies the ideal relation between externally applied stress and the corresponding actuation temperature. It provides an explicit solution for OAC for the SMA-composite with sufficiently large of b/a ratio and/or L and hence to promote the application of OAC in the design optimization of the SMA-composites.

Chapter 8

Finite Element Analysis of Internal Stress Distributions

8.1 Introduction

As discussed in Chapter 3, even though the embedded SMA wire is subjected to a constant actuation temperature and the temperature distribution is assumed uniform, material properties of the SMA wire may still vary along the embedded length. Due to the stress transmission from the SMA wire to its surrounding matrix across their interface, stress distributions on both constituents may not be uniform. This problem is particularly serious in the SMA-composites with short wire embedded length as discussed in Chapter 4. When the prestrained SMA wire is heated up to the transient temperature T_{so}^{A}, austenitic phase transformation starts inside a composite and hence the martensite volume fraction ξ decreases with temperature increase. However, depending on the given boundary condition, non-uniform axial stress distribution on the SMA wire governs the evolution of ξ during the SMA actuation. Referring to the numerical results obtained in Chapter 4, depending on the given loads and boundary conditions, the ξ-values at the first-half ($0 < z < L/2$) and second-half ($L/2 < z < L$) of the embedded wire can be totally different. In certain extreme cases, the ξ-value may increase or decrease monotonically along the embedded length. Therefore, without the comprehensive studies on the criteria for achieving uniform distributions of ξ-value, one cannot simplify the problem of ξ-evolution by using a constant ξ-value throughout the embedded wire.

This Chapter focuses on the analysis of internal stress distributions in the SMA composite using the finite element method (FEM). Due to the limitation of finite element analysis (FEA) software package, the material property assignment function does not support the constitutive model of shape memory alloy that allows the change of the material properties with temperature and stress. Because of the non-uniform stress distributions on the SMA wire, the ξ-evolution in the wire direction yields the inconsistence of elastic modulus E_f along the embedded wire. In order to facilitate the finite element analysis for the SMA-composites, it is crucial to input the appropriate material constants for the SMA component in the finite element model. In the current Chapter, the concept of 'constant martensite volume fraction region (CMR)' is employed to estimate the equivalent E_f-values for the SMA wire at different specified actuation temperatures.

In addition to the assignment of appropriate material constants for the FE model, the success of the FEA also strongly relies on the appropriate assignment of loads and boundary conditions, development of geometric models as well as the meshing techniques. In order to simulate the effect of SMA actuation on the partially debonded two-cylinder model, a contact surface subjected to frictional shear is created at the predefined section of the interface between the SMA wire and matrix. For the simulation of perfectly bonded SMA wire/matrix cylinder, the simple linear static type of FEA solutions is used to calculate the internal stress distributions in constituents. However, when the interfacial debonding occurs and sliding starts at the debonded region, the nonlinear static type of FEA is required to solve the frictional contact problems.

All the captioned concerns regarding FEA of the stress distributions in the partially debonded SMA composite structure are addressed in the current chapter. The FEA results are then employed to validate the theoretical solutions of stress distributions as well as the application of equivalent martensite volume fraction $\tilde{\xi}$ proposed previously in Chapter 4 and 5 respectively.

8.2 Selection of Material Properties for the SMA Wire

Using the concept of CMR proposed in Chapter 4, if the critical values of the wire embedded length L_c and the matrix to wire radius ratio b_c/a are satisfied, an equivalent martensite volume fraction $\tilde{\xi}$ can be obtained. In the other words, the $\tilde{\xi}$ at $z = L/2$ for $L > L_c$ and $b/a > b_c/a$ is considered as a constant throughout the embedded SMA wire and is given in Eqn. 5.38. The equivalent elastic modulus of the SMA wire $\tilde{E}_f$ $(= E_f(\tilde{\xi}))$ at the given loading and actuation conditions can then be obtained by substituting $\tilde{\xi}$ into Eqn. 3.3. Therefore, a constant value of elastic modulus can be used in the FE model to simulate the mechanical response of SMA component. In this Chapter, only the mode-b actuation scenario is considered and all the material properties of SMA employed for the numerical studies are listed in Table 3.1 unless otherwise specified.

Since the FEA results will be employed to validate the theoretical solutions of stress distributions in the SMA composite, the FE models are assumed to be subjected to the specific applied stresses and actuation temperatures as shown in Figs. 5.8 and 5.9. The maximum applied stress σ_a employed in the current study is therefore limited

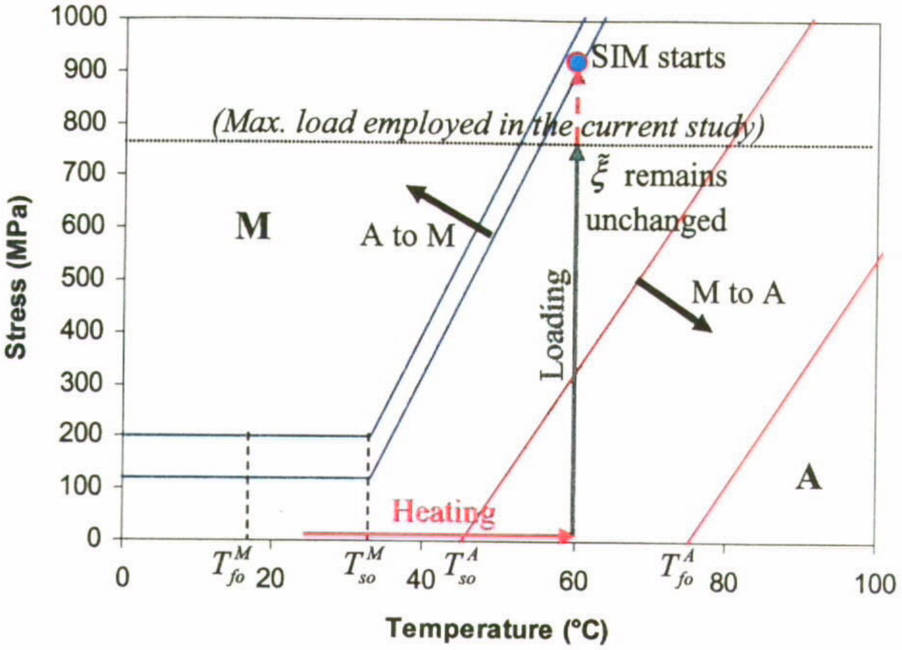

Figure 8.1 Plots of critical transformation stresses using the material properties of SMA listed in Table 3.1.

to 768MPa as illustrated in Fig. 5.9 for the partial debonded length l that equals to $0.95L$. Figure 8.1 shows the critical stresses of phase transformations at different actuation temperatures. It indicates that the stress-induced martensitic transformation (SIM) will not occur at the limited stress level (up to 768MPa), the $\tilde{\xi}$ is therefore remains unchanged after the actuation of the SMA at the stress-free condition. As a result, the equivalent elastic modulus is independent of applied load but varies with actuation temperature as given in Table 8.1.

In addition to the equivalent martensite volume fraction $\tilde{\xi}$ and the elastic modulus $\tilde{E}_f$, it is critically important to simulate the recovery action of the prestrained SMA wire inside the matrix. Since the recovery action of SMA material is similar to the thermal expansion or contraction of natural materials subjected to temperature changes, the strain recovery of the SMA can be considered as a result of thermal

Table 8.1 Predicted values of $\tilde{\xi}$ and $\tilde{E}_f$ at different loading and actuation condition.

			Applied Stress - σ_a (MPa)						
			0	500	636	668.1	713.35	757.5	768
Temperature - T (°C)	25°C	$\tilde{\xi}$	1	1	1				
		$\tilde{E}_f$ (GPa)	19.14	19.14	19.14				
	40°C	$\tilde{\xi}$	1	1		1			
		$\tilde{E}_f$ (GPa)	19.14	19.14		19.14			
	60°C	$\tilde{\xi}$	0.9438	0.9438			0.9438	0.9438	
		$\tilde{E}_f$ (GPa)	20.17	20.17			20.17	20.17	
	80°C	$\tilde{\xi}$	0.7051	0.7051					0.7051
		$\tilde{E}_f$ (GPa)	24.53	24.53					24.53

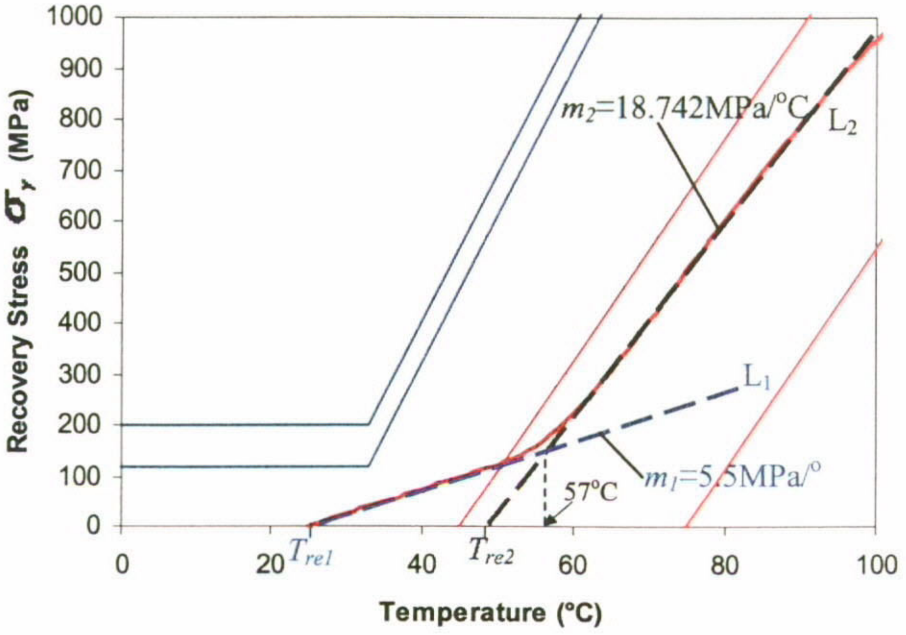

Figure 8.2 Identification of reference temperatures (T_{re1} and T_{re2}) and stress increasing rate (S_1 and S_2) from the plot of recovery stress versus against actuation temperature.

Table 8.2 List of the reference temperatures T_{re} and the thermal expansion coefficients β_{SMA} identified from the curve-fitting method.

	L_1 for $T \leq 57^{\circ}C$	L_2 for $T > 57^{\circ}C$	
		60°C	80°C
T_{re} (°C)	25	48.128	
S (MPa/°C)	5.5	18.742	
$\tilde{E}_f$ (GPa)	19.14	20.17	24.53
$\beta_{SMA} = -S/\tilde{E}_f$ (/°C)	$-2.874\text{x}10^{-4}$	$-9.292\text{x}10^{-4}$	$-7.64\text{x}10^{-4}$

contraction of a material. However, such coefficient should not be a constant for the simulation of shape memory effect during the heating up process.

Recalling Eqn. 3.4 for the prediction of recovery stress σ_r under the strain-constrained condition, the plot of recovery stress against actuation temperature can be obtained as shown in Fig. 8.2. U straight-lines and hence the reference temperatures (T_{re1} and T_{re2}) and the corresponding slopes (m_1 and m_2) can be obtained as illustrated in Fig. 8.2. The data obtained for different temperature ranges are summarized in Table 8.2. Using the curve fitting method, the recovery-stress curve can be fitted in with two straight-lines and hence the reference temperatures (T_{re1} and T_{re2}) and the corresponding slopes (m_1 and m_2) can be obtained as illustrated in Fig. 8.2. The data obtained for different temperature ranges are summarized in Table 8.2.

8.3 Development of 2D-Axisymmetric Models

8.3.1 Arrangement of 2D-Surfaces

Figure 8.3 shows the loading configuration of a SMA wire/matrix cylinder model during the pullout test. Based on the simple geometry and loading method with single applied load acting on the end of the SMA wire in axial direction, the influence of the SMA actuation on stress distribution inside this specific two-cylinder structure can be simulated by using a simplified two-dimensional axisymmetric model in the finite element package for the sack of simplicity. Assuming that the constituents are isotropic and the interface between the SMA wire and matrix is either remains perfectly bonded or pre-existed with a constant debonded region (i.e. the debonded length will not be further increased in the simulation), the simplified axisymmetric 2D-solid models for the corresponding configurations are shown in Figs. 8.4a and b respectively.

One may notice that the fixture for holding the two-cylinder model reserves an opening with sufficient clearance for the SMA wire to pass through as illustrated in Fig. 8.3. The opening size of the tailor-made fixture for this pullout test is approximately equals to 1mm in diameter which means the clearance between the 0.25mm dia. wire and the edge of the circular opening is 0.375mm. The matrix body is therefore divided into two groups (3 and 4 in Fig. 8.4a, and 3-4-5 and 6-7-8 in Fig. 8.4b respectively) which allow the easier identification of restricted end for the load and boundary conditions assignments. In addition, the SMA wire in each model is created with 10mm extension from the matrix body, it is composed with two surfaces (1 and 2) so as to define the bond and debonded region at the interface.

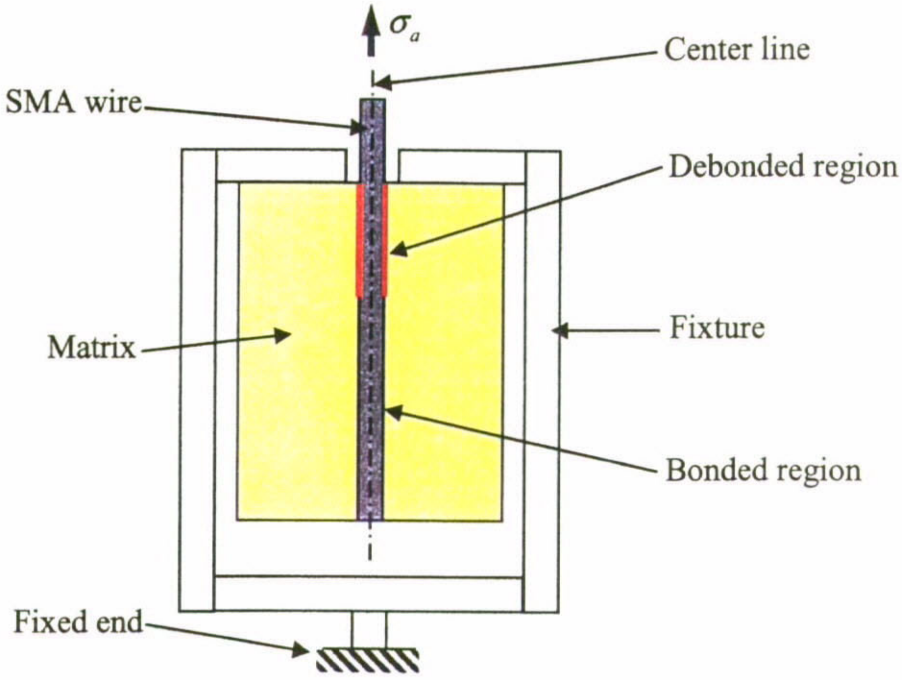

Figure 8.3 Identification of loads and boundary conditions in the wire-pullout test configuration.

8.3.2 Surface Meshing

In addition to the development of the 2D geometries, it is crucial to select an appropriate mesh type as well as the mesh density which governs the accuracy of the FEA results. To satisfy the requirement of axisymmetric solid modeling, the 2D-solid meshing with 'Tria' element shape is used, while the element size at the interest zone is controlled by means of seed assignment. The curve or an edge of surface created with mesh seed definition is considered as a boundary predefined with mesh nodes that forces the development of 2D-mesh to follow the required pattern and density. The MSC Patran provides several types of mesh seed to satisfy the captioned requirement. In the current study, the three basic types of mesh seed arrangement including 'uniform', 'one-way bias' and 'two-way bias' are employed to increase the mesh density nearby the interface between the SMA wire and matrix as well as the crack tip,

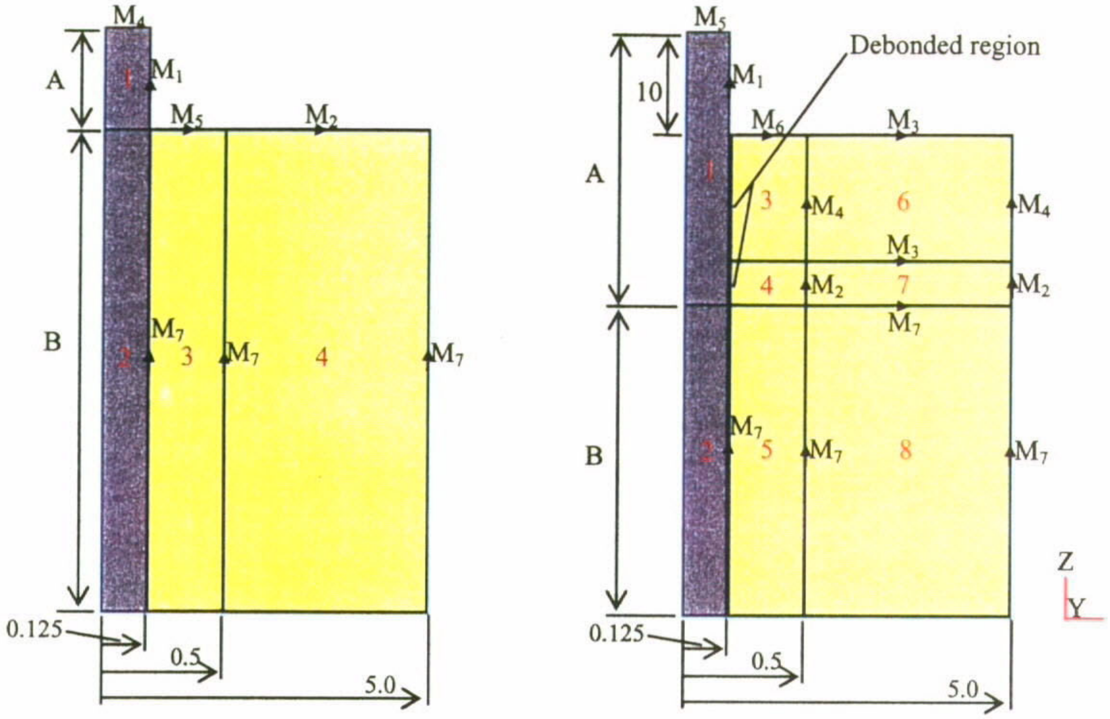

(a) (b)

Figure 8.4 Mesh seed assignments on the axisymmetric 2D-solid models for a) the fully bonded (model #1) and b) partially debonded SMA wire/matrix cylinders (model #2 – #4).

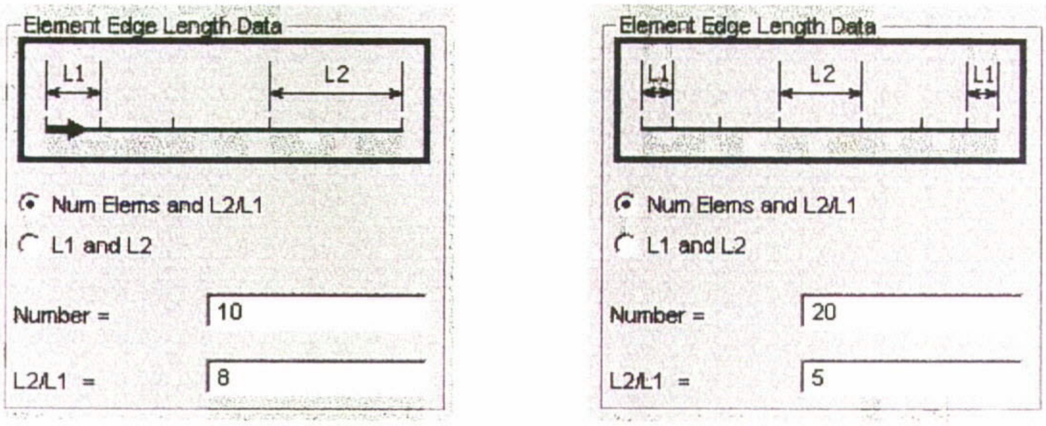

Element Edge Length Data

● Num Elems and L2/L1

○ L1 and L2

Number = 10

L2/L1 = 8

Element Edge Length Data

● Num Elems and L2/L1

○ L1 and L2

Number = 20

L2/L1 = 5

(a) (b)

Figure 8.5 Definitions of a) one way bias - and b) two way bias - mesh seed assignments in MSC. Patran 2003r3.

Table 8.3 Mesh seed assignment on the corresponding edges of surfaces.

				Types of Mesh Seed						
				Uniform			One-way Bias $\left({}^{n}/_{L2/L1}\right)$			Two-way Bias $\left({}^{n}/_{L2/L1}\right)$
Model #	*l*	A	B	M_1	M_2	M_3	M_4	M_5	M_6	M_7
1	0	10	50	20	10		8/0.2	10/8		100/20
2	12.5	22.5	37.5	30	1	20	20/10	8/0.2	10/9	75/20
3	25	35	25	40	1	20	30/10	8/0.2	10/8	50/10
4	47.5	57.5	2.5	50	1	20	60/10	8/0.2	10/8	20/5

('*l*' : debonded length; '*n*' : number of node)

loading end and embedded end. Definition of one-way and two-way bias types of mesh seed are schematically illustrated in Fig. 8.5. Figure 8.4 shows the mesh seed assignment applied on the four 2D axisymmetric models for the partial debonded length *l* = 0, 12.5, 25 and 47.5mm (named as model #1, 2, 3 and 4) respectively and the information for the corresponding types of mesh seed are listed in Table 8.3.

8.3.3 Loads and Boundary Conditions

Figure 8.6 and **8.7** demonstrate the assignment of the loads and boundary conditions on the perfectly bonded and partially debonded interfaces respectively. Due to the result of shrinkage arising from the curing process of matrix material, a residual clamping stress q_o is reasonably applied on the surface edge 3.4 which represents the inner surface of the matrix body.

For the 2D axisymmetric problem, surface edges 1.4 and 2.4 form the centerline of the model. Therefore, a specific displacement constrain with '12456' (freeze the transverse displacement in X- and Y- axis, and rotation about X-, Y- and Z-axis respectively) should be assigned to such centerline. In order to simulate the condition without externally applied load but SMA actuation only, the center node on surface edge 2.4 is not allowed to move in all the six degrees of freedom (DOF) as shown in Fig. 8.6a. However, in the case with pullout stress σ_a applying on the wire's end, the surface edge 4.3 should be froze in five DOF except the transverse displacement in X-axis (i.e. '23456') instead of a single fixed node on surface edge 2.4. In addition to these kinds of displacement constrains, all other nodes on the model are assigned with the special attributes that allow the transverse motions in X- and Z-axis, and rotations about the Y-axis only (i.e. '246').

Finally, during the SMA actuation, the embedded SMA wire and its surrounding matrix are assumed to be subjected identical and constant temperature in the steady state. Therefore, all elements in the models are defined as subjecting to a constant temperature in different actuation levels.

8.3.3.1 Special Meshing Assignment for the Nonlinear Contact Problem

Models #2 to 4 simulate the SMA wire/matrix cylinder in the partially debonded conditions with different debonded length *l*. Since the debonded surfaces remain in contact throughout the pullout process, frictional shear on the debonded surfaces is responsible to the stress transmission from the SMA wire to the surrounding matrix. However, the SMA wire slides on the matrix surface results in a large relative displacement between the nodes on surface 1.2 and 3.4. Therefore, nonlinear

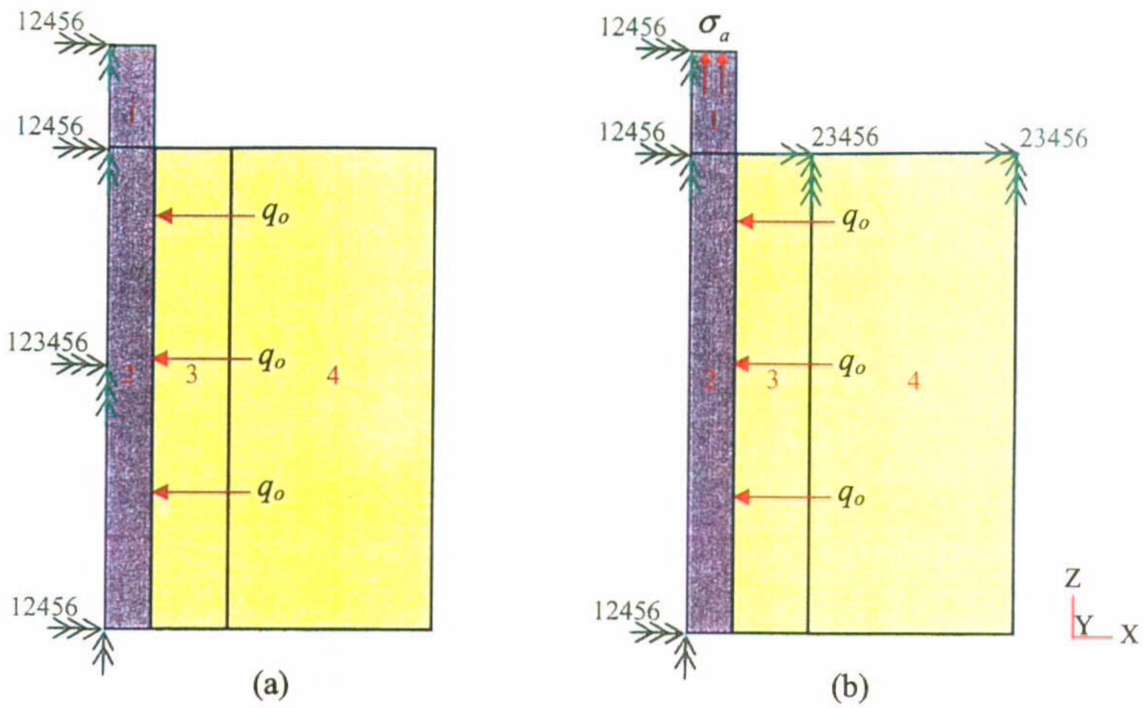

Figure 8.6 Assignment of loads and boundary conditions on the axisymmetric 2D-solid models for the simulations of a) SMA actuation without applied pullout stress and b) SMA actuation with applied pullout stress in model #1 – perfectly bonded condition.

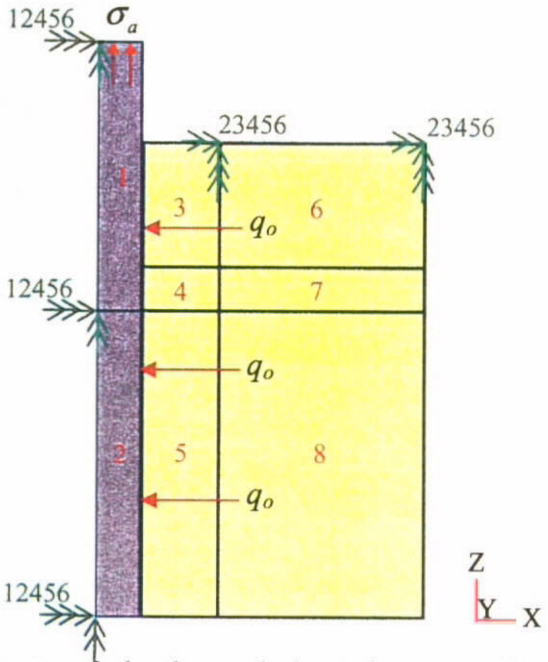

Figure 8.7 Assignment of loads and boundary conditions on the axisymmetric 2D-solid models for the simulations of SMA actuation with applied pullout stress in the model #2, #3 and #4 – partial debonded condition.

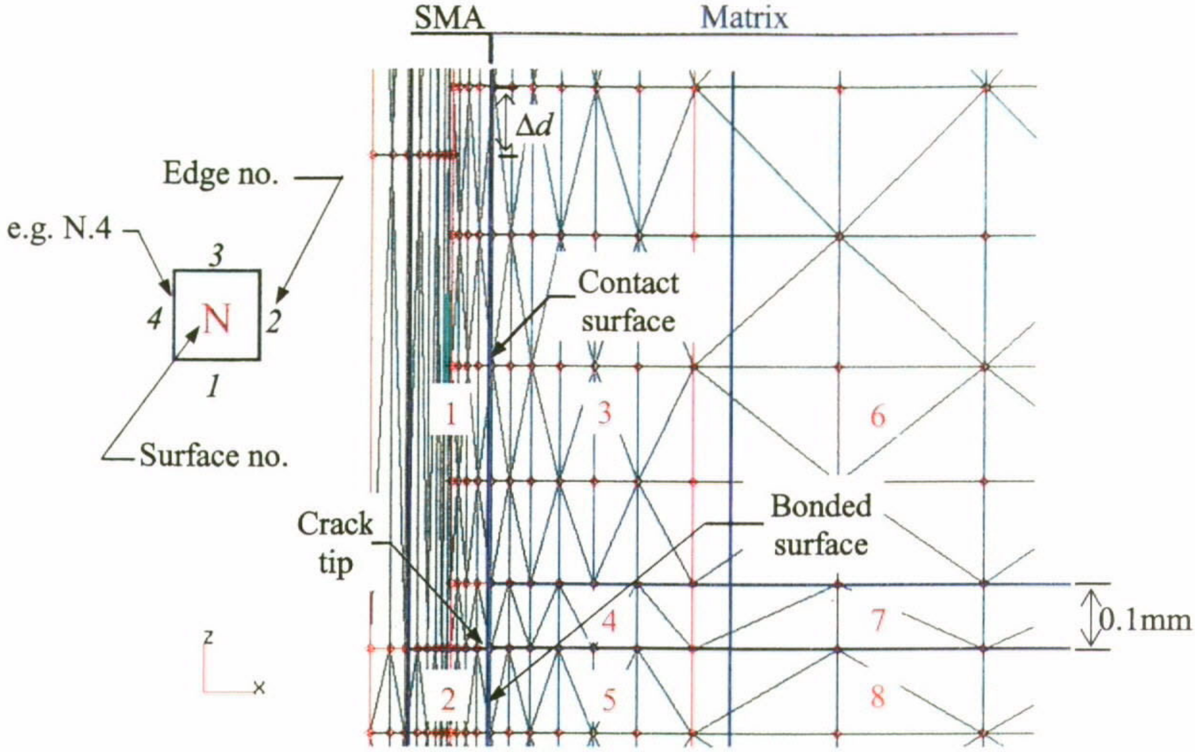

Figure 8.8 Special arrangement of surface meshing for satisfying the 'contact' assignment between the surface edges 1.2 and 3.4.

static analysis is employed for the partially debonded condition. Any two adjacent surfaces or edges of 2D axisymmetric surfaces can be defined as in contact with each other. However, if the displacement Δd between any two nodes on the adjacent surfaces is smaller than the global model tolerance (defaulted as 0.005mm in the current studies), the associated nodes will be considered as equivalent and the 'contact' attribute cannot be created successfully. One may notice that the surfaces of the SMA wire and matrix along the debonded region are sharing the same point at crack tip, which means they cannot be directly defined as in contact for having the common node at the same position. The extremely small surfaces 4 and 7 were therefore inserted immediately above the crack tip for separating the bonded and debonded regions in the matrix. These small pieces of surface can offset the end point of surface edge 3.4 away from the crack tip. Using this special arrangement of 2D geometries and careful selection of mesh density and pattern on the surface edge 1.2 and 3.4, the contact surface can be successfully defined in the model #2 to 4.

8.4 Comparison between FEA and Theoretical Results

8.4.1 FEA Results

After the input of relevant material properties for SMA and epoxy matrix, the created models were then submitted to the MSC.Nastran for the nonlinear static calculations. Figure 8.9 shows the typical result of resultant deformation in a partially debonded condition with $l = 25$mm, $T = 60^{\circ}$C and $\sigma_a = 757.5$MPa. It can be found that the deformation of matrix in the debonded region is much smaller than that in the bonded region. It is a result of sliding on the debonded surface, where the frictional shear stress remains and hence generates minor deformation in the debonded region. In addition to the deformation of the surface edges 3.4, 4.4 and 5.4 (inner surfaces of matrix) in +Z direction, the matrix body is found to be deformed in the –Z direction. That should be the result of thermal expansion of the matrix cylinder.

Figures 8.10a and b show the fringe plots of axial stress and interfacial shear stress distributions respectively. Under the relative high applied load and actuation temperature ($\sigma_a = 757.5$MPa and $T = 60^{\circ}$C), the axial stress distribution on the SMA wire is found to have a dramatic drop within a short wire length immediately in behind the crack tip. The wire in the debonded region is continuously maintain at the high

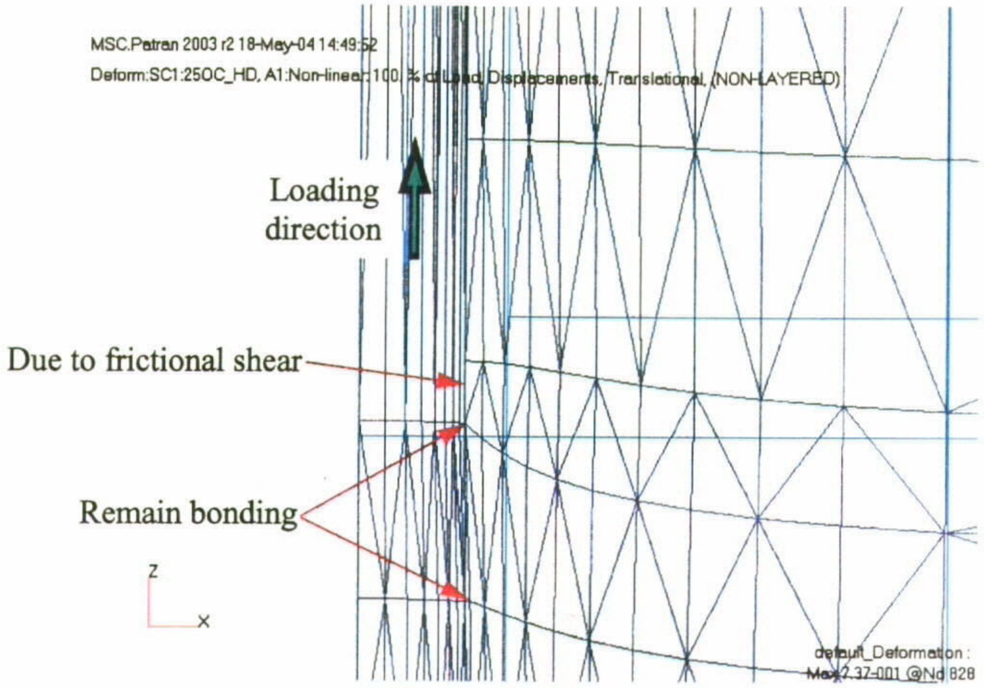

Figure 8.9 Deformation at the junction point between the bond and debonded regions. ($T = 60^\circ$C and $\sigma_a = 757.5$MPa)

stress level because of the poor stress transmission across the interface where the frictional shear can serve a minor stress reduction only. As a result, the SMA wire takes up most of the applied load in the debonded region.

Figure 8.10b confirms the sudden increase of interfacial shear stress behind the crack tip. It explains the effective stress transmission in the bonded region where the applied load transfers to the matrix effectively and hence the sudden drop of axial stress is observed in Fig. 8.10a.

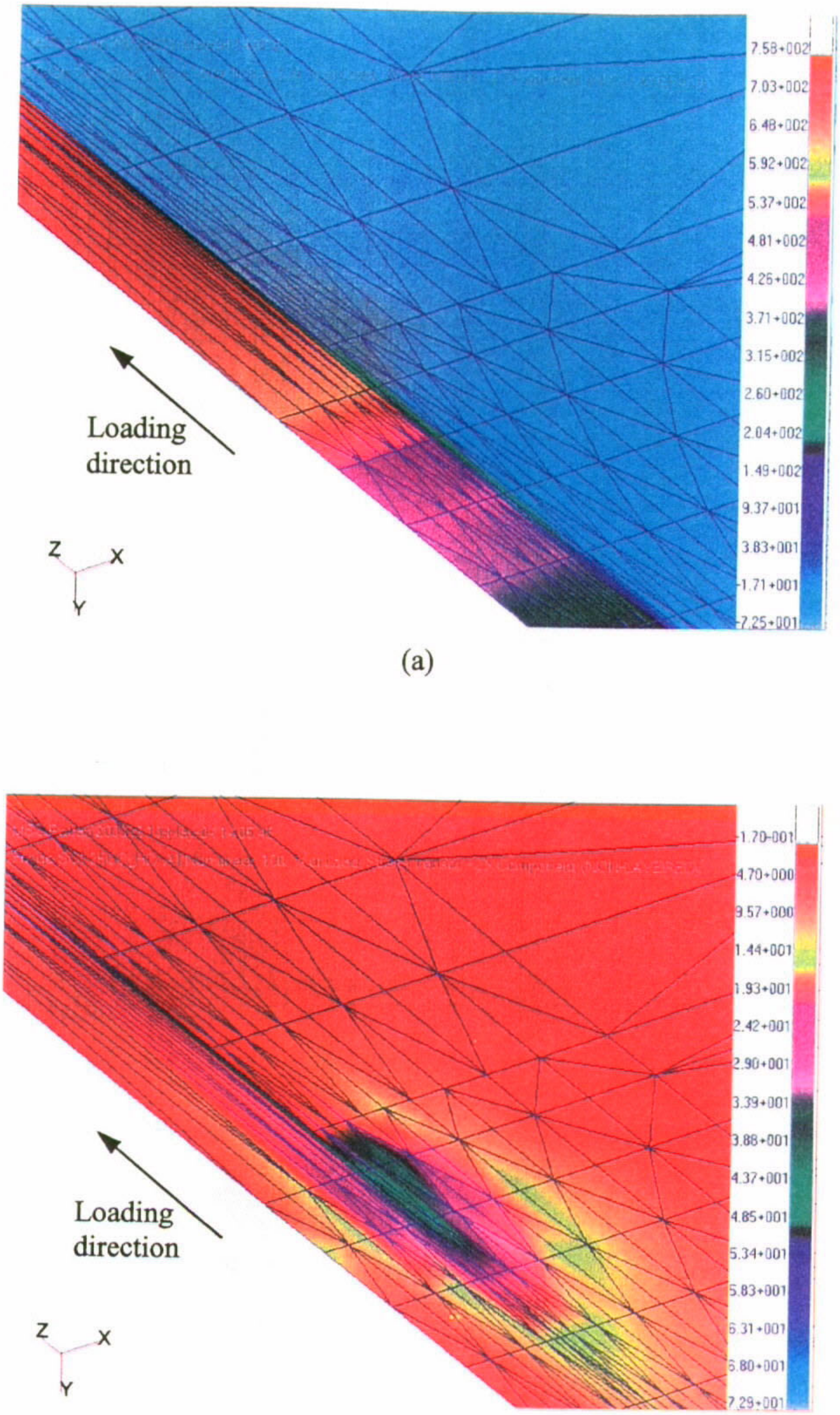

(a)

(b)

Figure 8.10 Fringe plots show the distributions of a) axial stress (Z – component) and b) shear stress (ZX - component) around the defined crack tip on the 2D-axisymmetric model. The applied load and actuation temperature are 757.5MPa and 60°C respectively.

8.4.2 Internal Stress Distributions in the Perfectly Bonded Condition

This section focuses on the comparison between the FEA results and theoretical solutions developed in Chapters 3 to 5. All the models are assumed to be subjected to the mode-b actuation which means the embedded SMA wire is actuated to the target temperature prior to the application of pullout load. The first comparison is performed for the SMA wire/matrix cylinder under the perfectly bonded condition and zero applied stress. Figures 8.11a and b show the influence of the SMA actuation on the axial stress and interfacial shear stress distributions respectively. In Fig. 8.11a, the negative but minor axial stress is obtained from the FEA result at $T = 25°C$, while the zero stress level is predicted by the theoretical solution (Eqn. 5.34). It could be the result of residual clamping stress applying on the inner surface of matrix cylinder where the matrix body is deformed in the axial-direction. Unlike the thermal expansion of the matrix cylinder, since the residual stress (compressive) is assumed applying in the radial direction and the elements (except the center point as illustrated in Fig. 8.6a in FE model) are allowed to move in X-Z plane and rotate about Y-axis, the elements adjacent to the interface are tends to compress toward the wire's center point in both X and Z direction. As a result, the negative axial stress is found in the FEA result. Except the effect of residual clamping stress observed form FEA results, all the results demonstrate a fairly good agreement between the FEA results and theoretical predictions. The differences below 10% are obtained for the actuation temperature increased as high as 80°C.

Similarly, fairly good agreement between the FEA and theoretical results are also found in the plots of interfacial shear stress τ_3 as shown in Fig. 8.11b. It shows that the

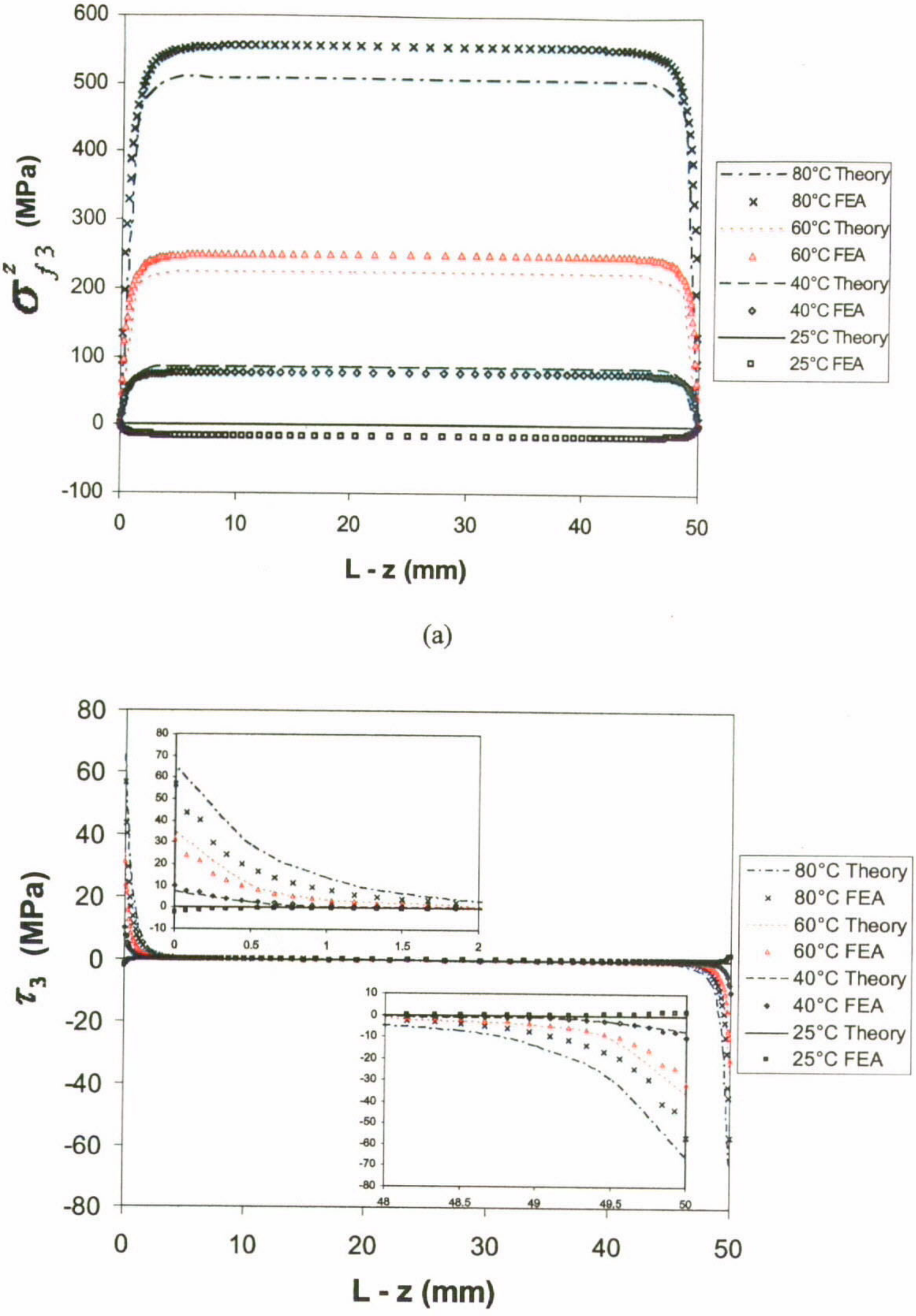

(a)

(b)

Figure 8.11 Comparison between theoretical and FEA results for the a) axial stress distributions and b) interfacial shear stress distributions for $\sigma_a = 0\text{MPa}$.

theoretical results obtained from Eqn. 5.37 predict the similar distribution profiles along the whole embedded length including two embedded ends. However, substantial derivation is found when the actuation temperature is increased upon 80°C. One may notice that the equivalent elastic modulus is employed for the SMA material in the FEA. However, as previously discussed for the evolutions of material properties of the embedded SMA wire, such evolution mechanism cannot be reproduced in the analysis which considers an equivalent (constant) value of elastic modulus only. This phenomenon becomes more significant at high actuation temperature. Since the wire's embedded ends (z = 0 and L) are subjected to zero axial stress, the martensite volume fraction ξ at the low-stress regions (nearby the embedded ends) should be much lower than the equivalent value. In the other words, the elastic modulus is underestimated. The effectiveness of stress transmission between the SMA wire and matrix is reasonably low in the FEA and hence the calculated interfacial shear stress is lower than the theoretical prediction.

Considering that the SMA wire is subjected to a constant applied stress σ_a = 500MPa as shown in Figs. 8.12a and b, the plots of axial stress and interfacial shear stress distributions also present a good agreement between the FEA results and theoretical predictions. Comparing to the results obtained for case with zero applied stress (Fig. 8.11a), no substantial difference on the axial stress is found at the middle section of wire embedded length.

Figure 8.12b shows the results of interfacial shear stress distributions. It should be noted that both the FEA and theoretical results predict the reduction of shear stress at loading end with temperature increase. However the derivation between the FEA and theoretical results is much smaller than that obtained in the Fig. 8.11b which means the externally applied load will minimize the prediction error due to the application of equivalent elastic modulus.

Figure 8.13 shows the comparison between the FEA and theoretical results for the prediction of interfacial shear stress τ_{i3} at free end ($z = L$) for the case with the SMA actuation only. Certainly, the theoretical predictions can match fairly well with the FEA results, especially for the temperature increased up to 60°C. The derivation increases with temperature due to the application of equivalent elastic modulus in the FE model where the effectiveness of stress transmission is underestimated and hence the shear stress calculated from the FEA is lower than that obtained from the theoretical model.

As discussed previously for the case with applied load σ_a = 500MPa, the predictions of interfacial shear stress at loading end obtained from the FEA and the theoretical model can match very well even for the relatively high actuation temperature as shown in Fig. 8.14a. However the results derivate at the free end ($z = L$) when temperature is increased upon 60°C as shown in Fig. 8.14b. It seems to be the result of effective transmission along the wire-matrix interface that minimizes the influence of applied load on stress distribution at the free end. Therefore, the prediction is similar to the case without applied load but the SMA actuation only.

The comparison of axial stresses, σ_{fb3} on the SMA wire at $z = L/2$ obtained from the FEA results and theoretical predictions is shown in Figs. 8.15a and b. Unlike the results obtained for interfacial shear stress τ_{i3} at the embedded ends, both of the FEA and theoretical results demonstrate the consistence development profile within the

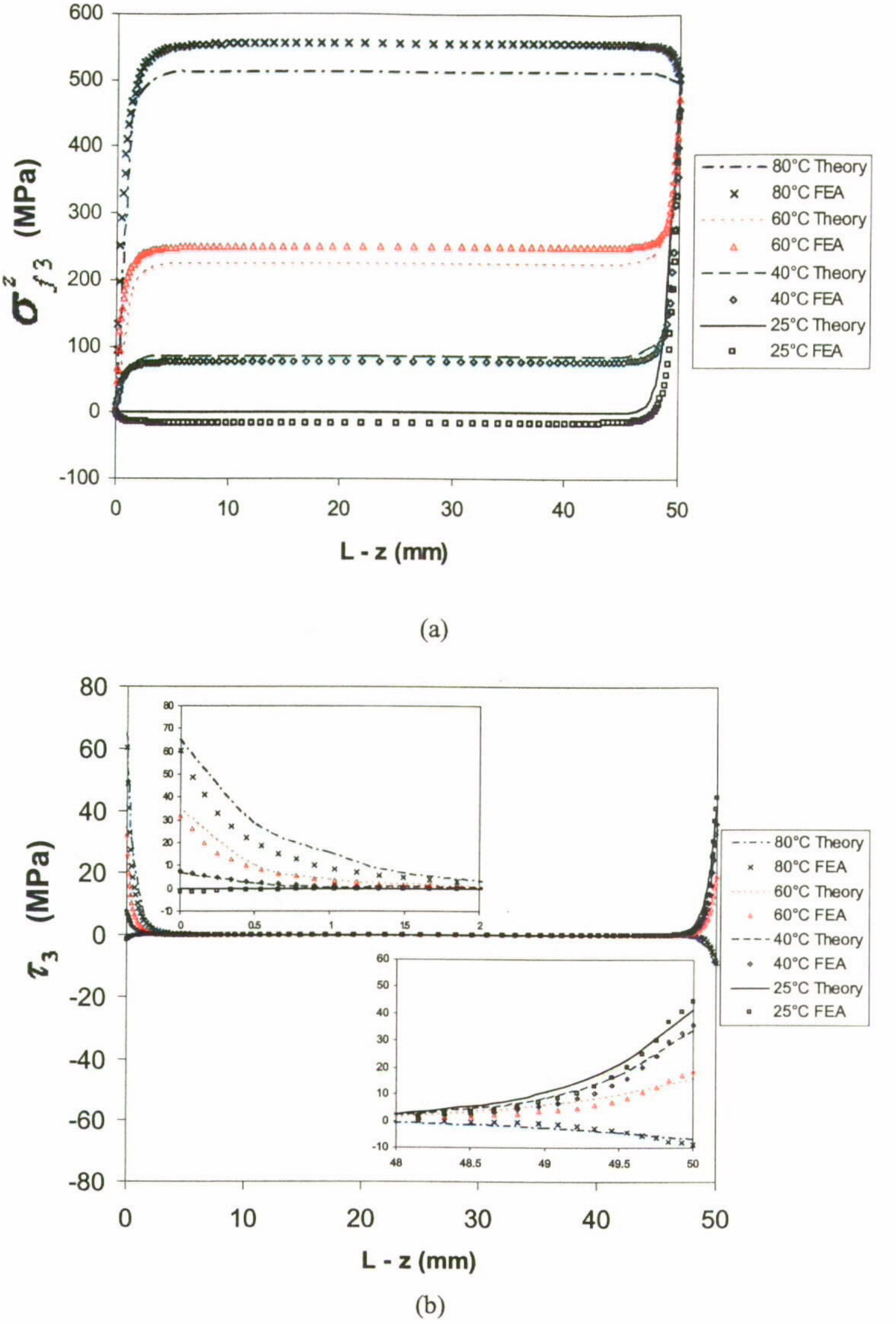

Figure 8.12 Comparison between theoretical and FEA results of the a) axial stress distributions and b) interfacial shear stress distributions for $\sigma_a = 500\text{MPa}$.

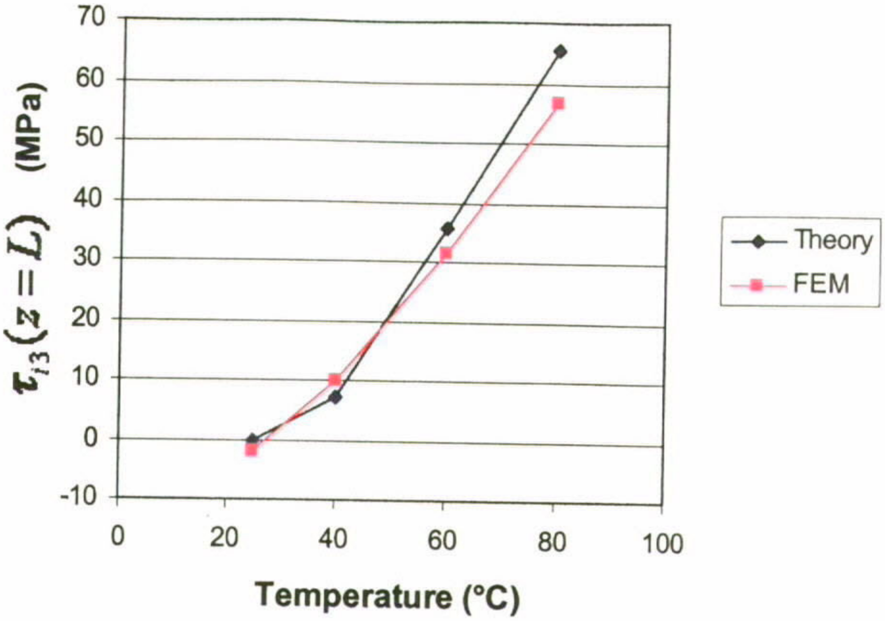

Figure 8.13 Development of interfacial shear stress τ_{i3} at free end (z = 50mm) due to SMA actuation only.

targeted temperature range. The influence of applied stress on axial stress distributions along the center portion of the SMA wire is relatively insignificant as presented in the two plots. It confirms that the application of equivalent elastic modulus is appropriate for the simulation of shape memory effect inside a composite.

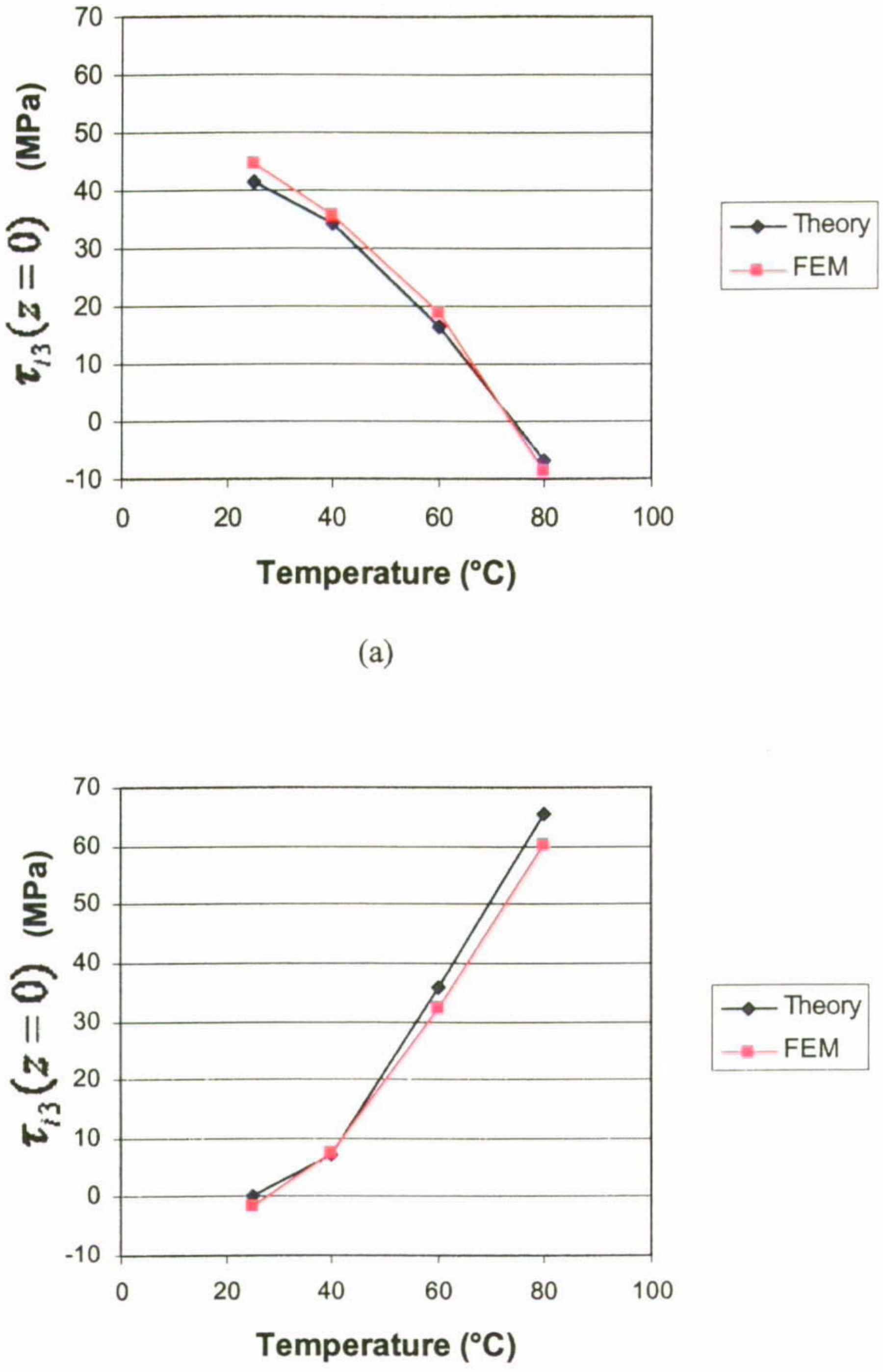

(a)

(b)

Figure 8.14 Reduction of interfacial shear stress τ_{i3} at a) loading end (Z = 0mm) and b) free end (Z = 50mm) for σ_a = 500MPa.

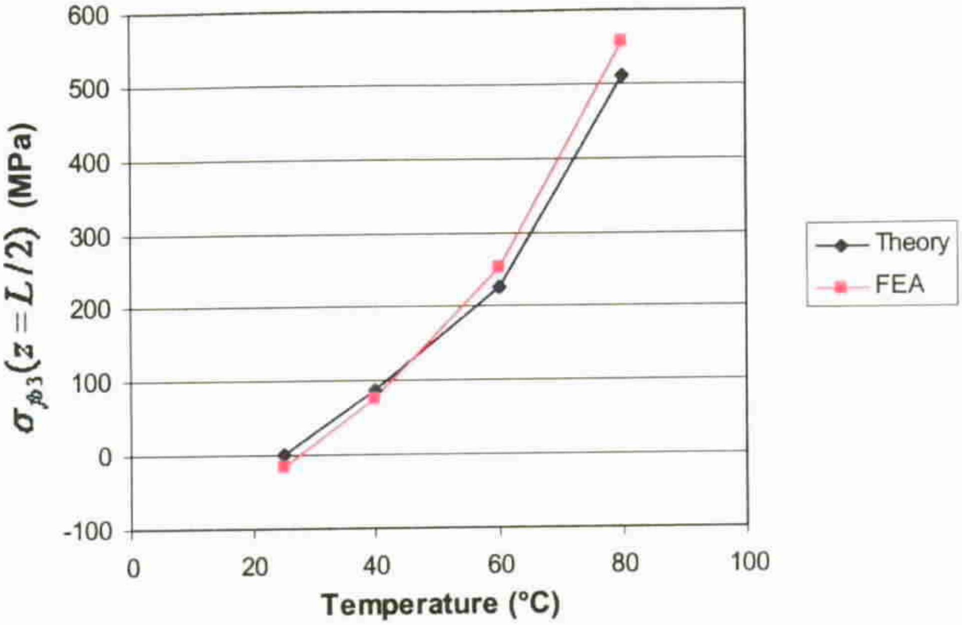

(a)

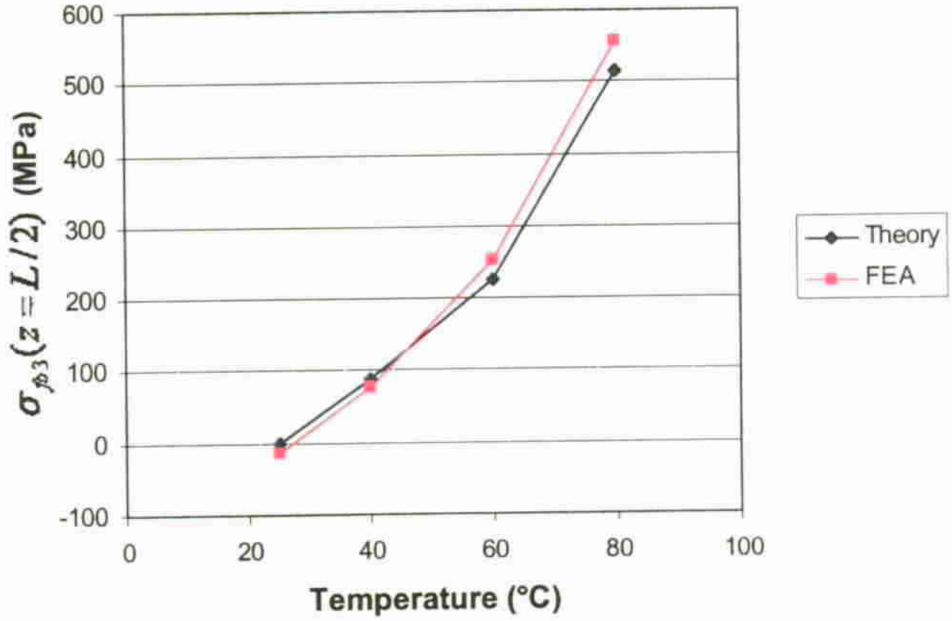

(b)

Figure 8.15 Development of axial stress on SMA wire σ_{fb3} at the middle of wire embedded length (z = L/2) for a) σ_a = 0MPa and b) σ_a = 500MPa respectively.

8.4.3 Internal Stress Distributions in the Partially Debonded Condition

Referring to Fig. 8.10 for the fringe plots of stress distributions on the ZX-plane, one may notice that the sharp changes (within a very short length) of axial and shear stresses were found adjacent to the crack tip. The stress data obtained from the FEA for such nonlinear problem, including the calculations of frictional shear in the debonded surface, are plotted against the wire embedded length as shown in Fig. 8.16. Figure 8.16a shows the plots of axial stress distributions at different actuation temperatures for the partial debonded length l = 0.5L. It should be noted that all the corresponding applied stresses σ_a are calculated by using Eqn. 5.96 for the given debonded length and actuation temperature. It can be found that both FEA and theoretical model predict the similar results with minor difference at the critical position – crack tip. Due to the application of 'one-way bias' for the mesh seed assignment on the debonded region of the SMA wire, the relative low density of surface meshing at loading end yields the zip-zap shape of data plots for 60°C in the debonded region. The stress drop immediate after the crack tip is found to be perfectly predicted by using the theoretical model. The stress levels at different actuation temperatures in the bonded region also agree well with the FEA results.

Considering the comparison of interfacial shear stress distributions as shown in Fig. 8.16b, the predicted values at the crack tip match fairly well with those obtained from the FEA. It confirms the validity of shear stress prediction by using the theoretical model even for the interfacial debond developed upon half of the wire embedded length. However, due to the application of equivalent elastic modulus in such case with short bonded length (25mm < L_c, where L_c = 42mm), the modulus should be underestimated. Beside, the influence of crack tip stress σ_{l3} at z = L/2 becomes significant toward the stress distributions at the free end. Therefore, the derivation between the FEA results and theoretical predictions is found substantial at the end of bonded region.

Fairly good predictions of axial stress distributions for l = 0.25L and 0.5L can be obtained as demonstrated in Fig. 8.17a. However, when the debonded length is increased upon 95% of the wire embedded length, a serious derivation between the results of the FEA and theoretical solution is found. In addition, Fig. 8.17b shows a good agreement between the two results for the prediction of τ_3 for the debonded length l which is increased up to 0.5L. When a very short wire length still remains bond with the surrounding matrix (L – z = 2.5mm or 0.05L), the interfacial shear stress at crack tip obtained from the FEA is much higher than that from the theoretical prediction. Based on the captioned findings for the cases with different debonded lengths, it is confirmed that the internal stress distributions for the condition with short debonded length can be predicted well with the theoretical model. The substantial derivation between the results of the FEA and the theoretical prediction will be obtained as a result of underestimated equivalent modulus in the very short deboned length.

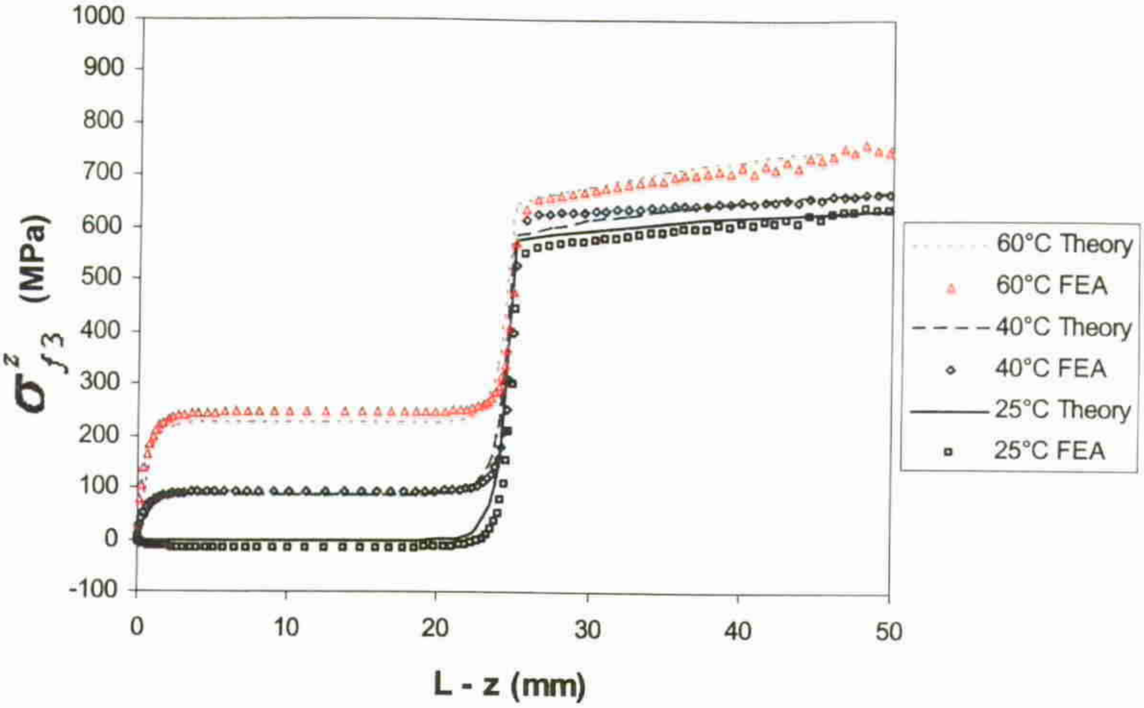

(a)

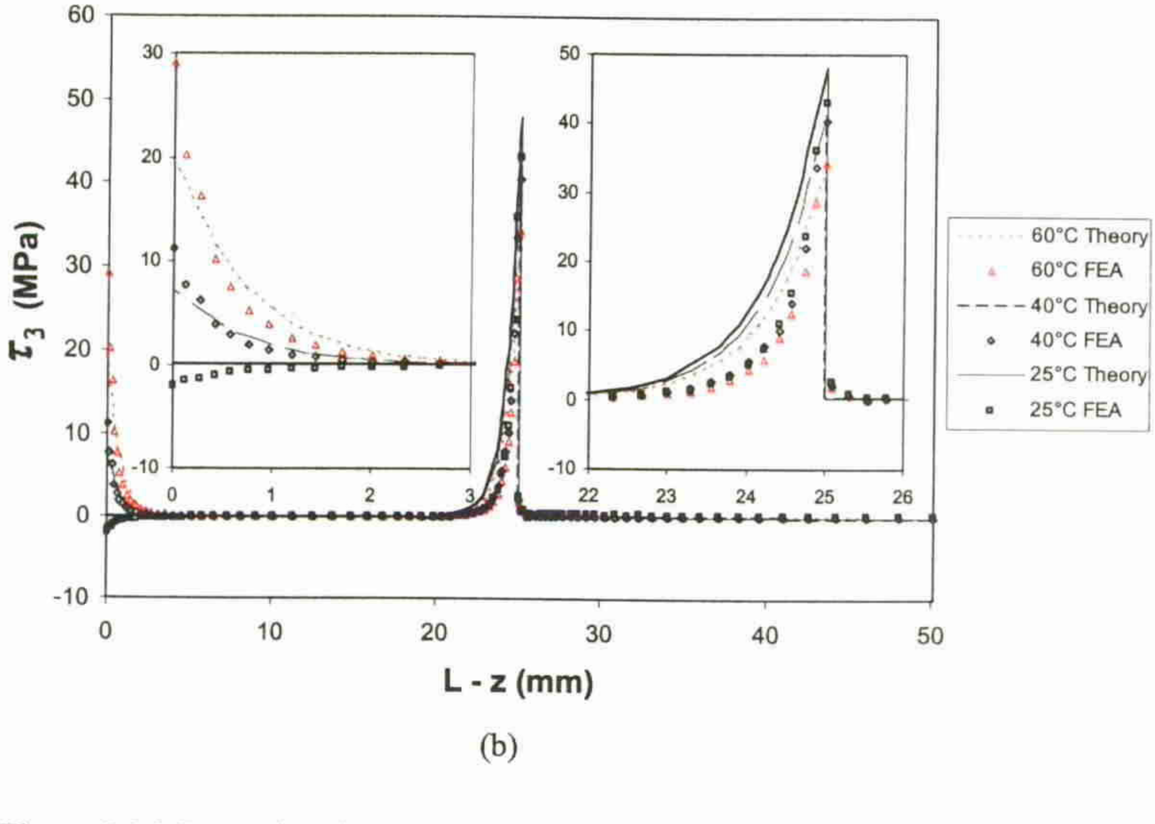

(b)

Figure 8.16 Comparison between theoretical and FEA results of the a) axial stress distributions and b) interfacial shear stress distributions for $l = 0.5L$.

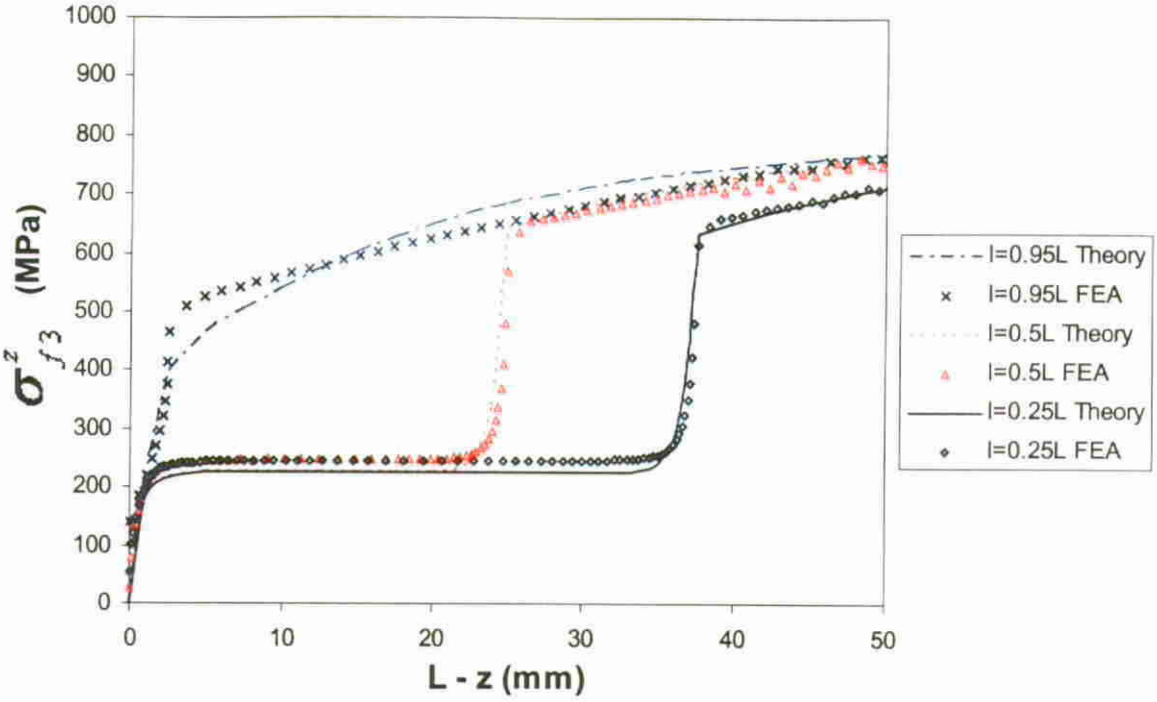

(a)

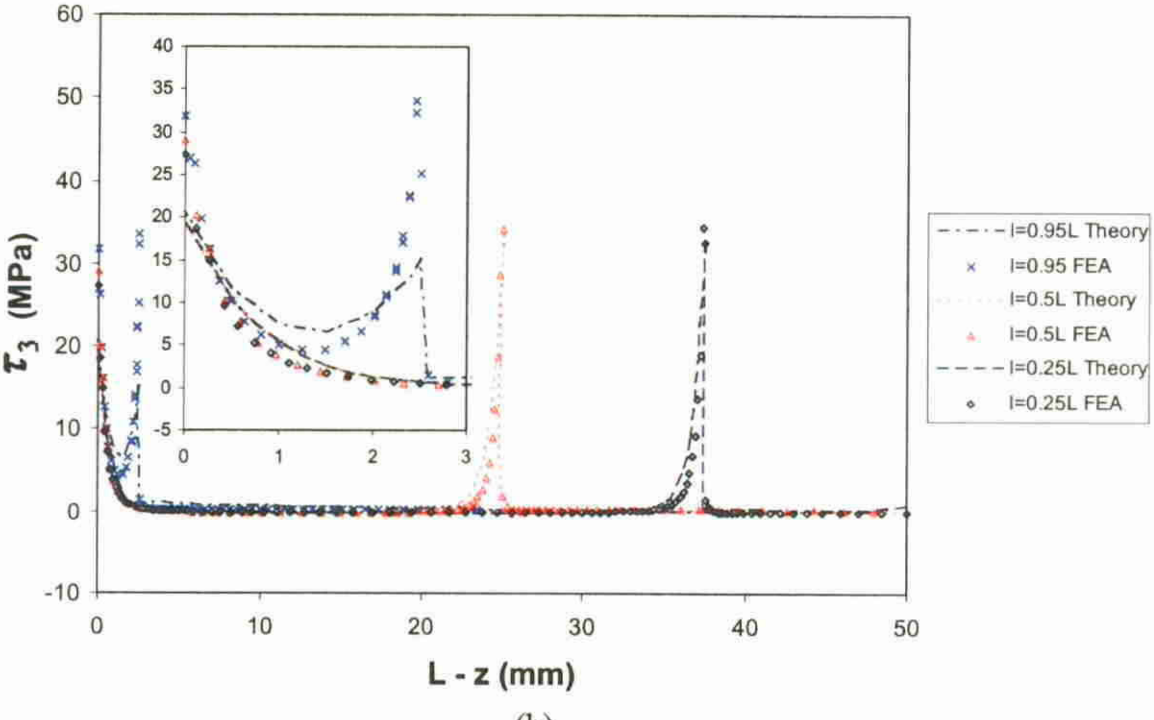

(b)

Figure 8.17 Comparison between theoretical and FEA results of the a) axial stress distributions and b) interfacial shear stress distributions at 60°C for different debonded length *l*.

8.5 Summary

In this chapter, the finite element method was employed to study the internal stress distributions within the SMA wire/matrix cylinder. The results were compared with the theoretical solutions in order to validate the theoretical model proposed in the current study. The FE models with predefined deboned surface were developed for the simulation of stress distributions in a partially debonded SMA composite. Nonlinear static analysis was used for the calculation of frictional shear stresses on the debonded surface. In addition, the concept of constant martensite volume fraction region (CMR) was employed to estimate the equivalent material properties of the embedded SMA wire in the FEA. A series of stress distribution comparison confirmed that both the FEA and theoretical results are matched in a fairly good manner especially for the models in the perfectly bonded condition.

Chapter 9

Buckling Control of SMA-reinforced Laminated Beam

9.1 Introduction

The fiber-reinforced composite (FRC) laminate has been widely used in various engineering structures because of the high stiffness-to-weight ratio. However, the buckling resistance has been a major issue for the design of a composite structure. The FRC laminates react passively to the buckling load which depends on the geometry and material properties of the composite structure. In order to improve the buckling resistance and enhance the stability of overall structure, research has increasingly focused on the designs and reliability studies of the smart composite structures that equip with the sensing and actuation systems to work against external stimuli [107].

This chapter will focus on the study of additional buckling resistance arising from the shape memory effect of the SMA wire actuators embedded inside a laminated beam. The recovery action exploited in the conventional laminated beams enhances the buckling response without the application of surface-mounted type actuators. Phase transformations accompanied by the changes of stiffness and strength of this novel actuator provide the means to generate additional bending moment and hence to increase the critical buckling load. Buckling test of the laminated beams with different number of layers and wire diameters were conducted so as to study the influences of geometric factors and material properties toward buckling resistance. A theoretical model incorporated with the SMA's constitutive law will be developed for the prediction of buckling resistance.

9.2 Modeling of Buckling Resistance of the SMA-reinforced Laminated beam

To improve the buckling resistance of a laminated beam, prestrained SMA wires were employed as the built-in actuators. In the current study, five pieces of SMA actuator were embedded in the beam as shown in Fig. 9.1. The wires were all embedded in the x-y plane and align in the direction of buckling (along x-direction) of the beam. In addition to the wires' orientation, the boundary conditions have to be clear defined for either the experiment and theoretical analysis of buckling response. Considering the typical loading configurations for buckling tests, the two major boundary conditions can be categorized as clamped-clamped (CC) and simply supported-simply supported (SS) conditions.

9.2.1 Loading Configurations

The buckling mode shapes of the SS- and CC- conditions are differed according to whether the rotation about the y-axis is fixed. The laminated beam subjected to the SS boundary condition showed greater lateral deflection than that with CC boundary condition. The two mode shapes are shown in Figs. 9.2a and b.

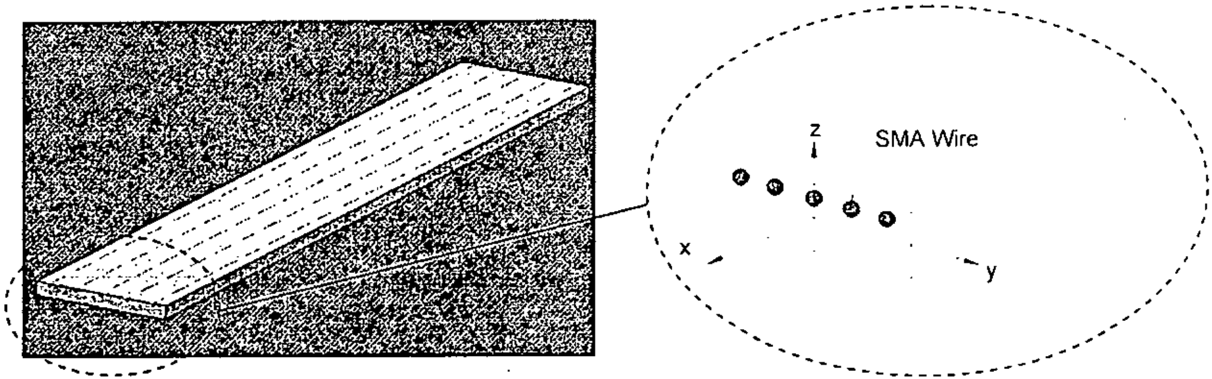

Figure 9.1 SMA wires embedded in a FRC slender beam.

(a) Simply Supported - Simply Supported

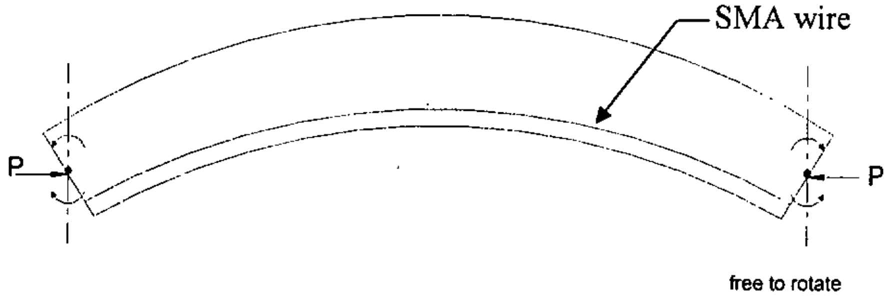

(b) Clamped - Clamped

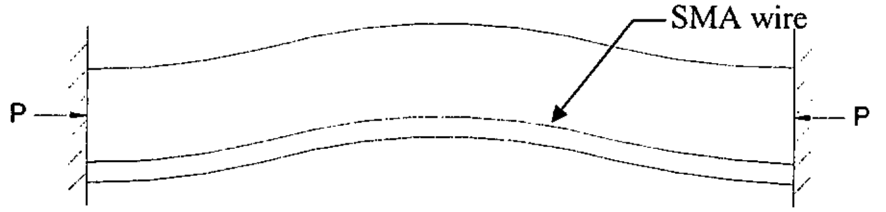

Figure 9.2 The first buckling mode shape of a) simply supported-simply supported (SS) and b) clamped-clamped (CC) condition.

9.2.1.1 Simply Supported – Simply Supported Boundary Condition

When a laminated beam is supported by hinge-joints at the two ends as shown in Fig. 9.2a, it is considered as a simply supported beam. This configuration allows the whole laminated beam to bend in the continuous curved shape (purely curved upward or downward). Figure 9.3 illustrates two possible arrangements of the SMA actuators in the laminated beam for achieving different buckling responses. In the case that the wires embedded eccentrically in the buckling direction and when the SMA actuators are heated up, recovery force $\bar{F}_{sma}$ will be generated. The additional bending moment M_{sma} generated by such SMA actuation will occur in the opposite direction of M_b, which is the bending moment arising from the buckling load P. As a result, additional buckling load will be required to maintain the same lateral deflection v_a. However, if the SMA actuators are embedded in the opposite direction of buckling, the additional bending

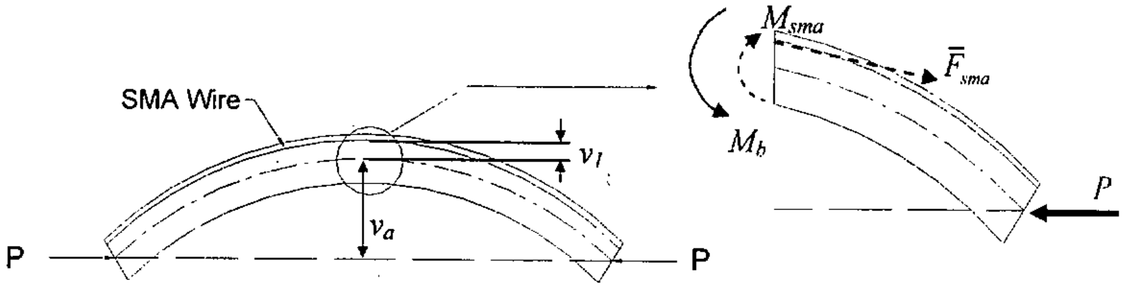

(a) SMA Wires Embedded in the Direction of Buckling

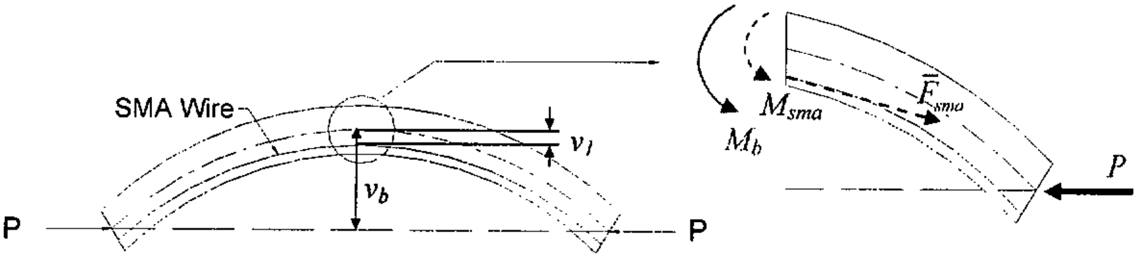

(b) SMA Wires Embedded in the Opposite Direction of Buckling

Figure 9.3 Influence of actuator arrangements on buckling behaviour. a) SMA wires embedded in the buckling direction for additional buckling resistance, while b) the wires embedded in the opposite direction enhances the buckling.

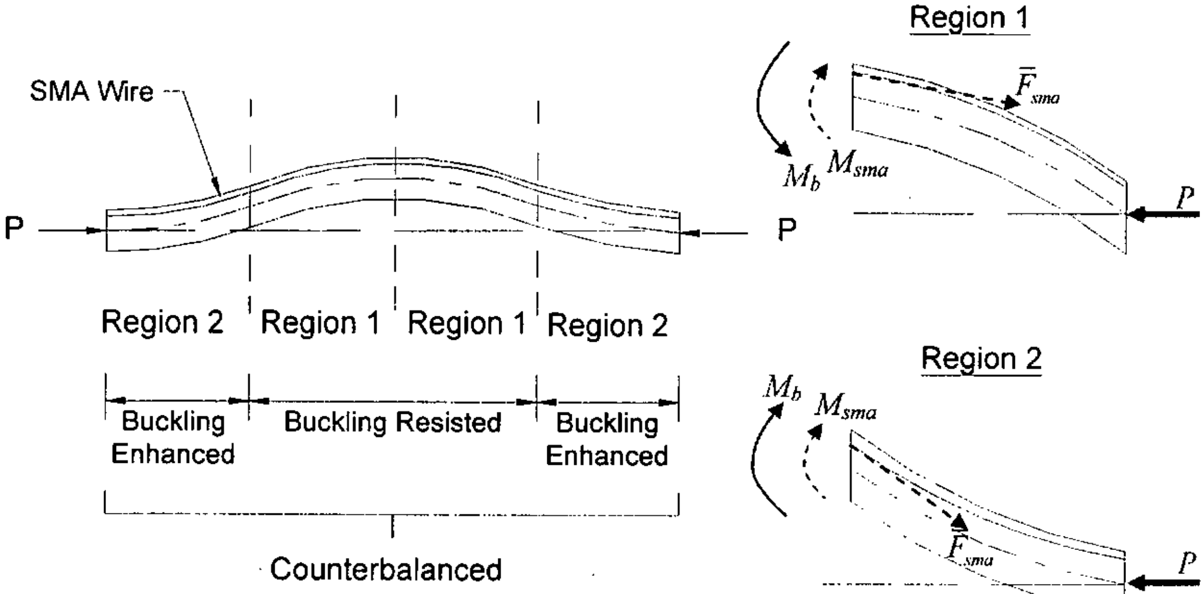

Figure 9.4 Embedded SMA wire in the direction of Buckling under clamped – clamped (CC) boundary condition.

moment M_{sma} will work together with M_b in the same direction. Therefore, the lateral deflection should be increased (i.e. $v_b > v_a$) under the same buckling load.

9.2.1.2 Clamped – Clamped Boundary Condition

Figure 9.3 shows the loading configuration of the SMA reinforced laminated beam under the clamped – clamped (CC) boundary condition. It should be noted that the model is divided into four parts. The loading condition in Region 1 is similar to that of SS. When the SMA wires are actuated, additional buckling can be obtained in such region. However, the bending moment M_p acts in the opposite direction in Region 2. In the other words, the buckling is enhanced in this region and the additional buckling resistance obtained in region 1 is counterbalanced. Therefore, the influence of the SMA actuation in the CC condition is reasonably lower than that achieved in SS condition. Since the SMA actuation in the CC boundary condition will not provide significant improvement of buckling resistance as discussed in the previous section, only SS boundary condition is considered in the current study.

9.2.2 Formulation of the Theoretical Model for Buckling Resistance

9.2.3.1 Basic Assumptions

In order to make sure that the buckling occurs in the designed direction, an initial compressive load P_o (also known as bias load) is applied on the both ends of laminated beam as schematically illustrated in Fig. 9.5a. When the applied compressive load is

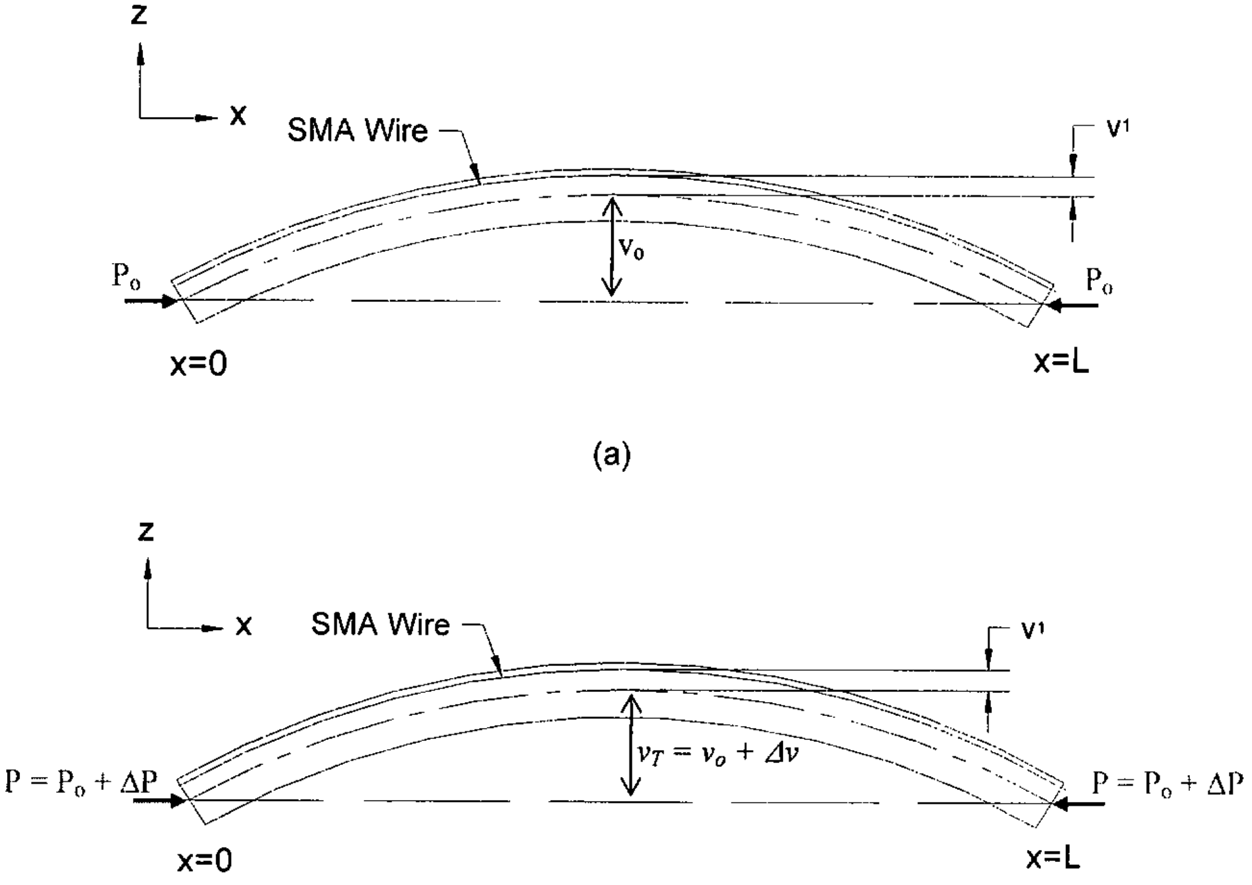

(b)

Figure 9.5 Schematic diagram of laminated beam embedded SMA wires subjected to a) the initial compressive load P_o and b) the total compressive load P respectively.

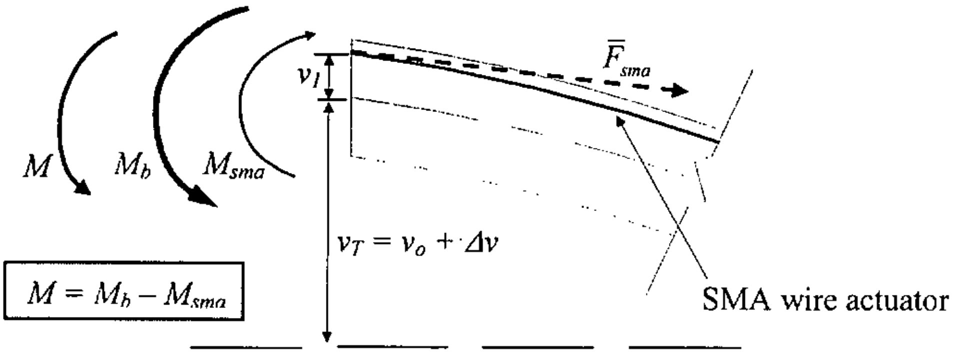

Figure 9.6 Free body diagram

increased by ΔP, the total lateral deflection v_T (= v_o + Δv) is obtained as shown in Fig. 9.5b. Figure 9.6 is the free body diagram which explains the mechanism for achieving additional buckling resistance due to the activation of the SMA wire actuators. As discussed in the previous section, the additional bending moment M_{sma} arising from SMA actuation is able to moderate the overall bending moment. Therefore, the formulation of theoretical model for the buckling resistance prediction can be started from this novel mechanism. However, several basic assumptions have to be clearly defined. They are summarized as following:

- The lateral deflection v_T should be small; therefore the laminated beam is within the elastic region and no fracture developed when buckling occurs.
- The cross section area of the beam is uniform in the entire length.
- The elastic modulus of the laminated beam is independent of temperature change during the SMA actuation.
- The SMA wire actuators are activated prior to the application of compressive load.
- The flexural stiffness is assumed constant and uniformly distributed across the width (along the y – axis) the laminated beam.
- The externally applied compressive force is assumed to be uniformly distributed at the ends of the laminated beam and maintain its original line of action after onset of buckling.
- The bias load P_o is assumed very small.
- The embedded SMA wires are equally spaced, and the recovery stress generated by the SMA wire actuators is assumed uniformly distributed across the width of laminated beam as schematically illustrated in Fig. 9.7.

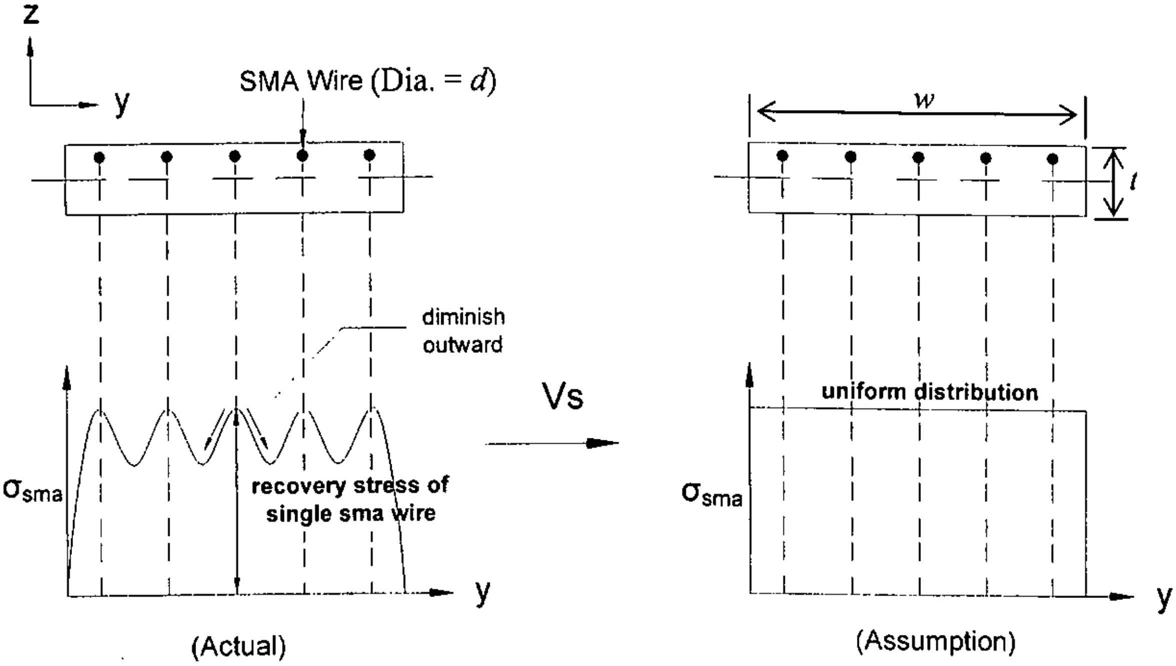

Figure 9.7 Assumption of uniformly distributed recovery stress across the width of laminated beam.

9.2.3.2 Model Development

Referring to the Fig. 9.6, the resultant bending moment M – for achieving additional lateral deflection Δv under the SMA actuation, can be formulated as given below:

$$M_b = \Delta P(v_o + \Delta v) \tag{9.1}$$

$$M_{sma} = N \cdot F_{sma} v_1 = \overline{F}_{sma} v_1 \tag{9.2}$$

$$M = M_b - M_{sma} = \Delta P(v_o + \Delta v) - \overline{F}_{sma} v_1 \tag{9.3}$$

where M_b and M_{sma} represent the bending moment due to the additional compressive load ΔP and the SMA actuation respectively. v_o is the initial lateral deflection while Δv is the additional lateral deflected arising from the application of compressive load ΔP and

SMA actuation. N is the number of embedded actuators while $\bar{F}_{sma}$ is the total recovery force generated by the SMA wire actuators. Recalling Eqn. 3.4 for the constrained recovery stress σ_r, the recovery force F_{sma} is readily obtained as

$$F_{sma} = \sigma_r A_{sma} = \left[E_f(\xi)\left(\varepsilon_p - \varepsilon_L \xi_s\right) + \theta\left(T - T_o\right)\right]\pi d^2/4 \tag{9.4}$$

Since the SMA wire actuators are assumed subjected to a constant actuation level prior to the application of compressive load on the two ends, ξ and ξ_s at any given temperature can be estimated by using Eqn. 3.30 and 3.32 respectively.

Considering the basic moment-curvature relation between M and Δv,

$$M = -EI_{yy}\frac{d^2\Delta v}{dx^2} \tag{9.5}$$

and then substituting the Eqn. 9.3 into Eqn. 9.5 yield

$$EI_{yy}\frac{d^2\Delta v}{dx^2} + \Delta P(v_o + \Delta v) - \bar{F}_{sma}v_1 = 0 \tag{9.6}$$

where I is the second moment of area of the y-axis. The elastic modulus of the SMA composite E is given as following

$$E = E_c\left(1 + \phi\right) + E_{sma}\phi \tag{9.7}$$

where ϕ $(= N\pi d^2/(4tw - N\pi d^2))$ is the volume ratio of the SMA wires to composite matrix. E_c and E_{sma} are the elastic modulus of the FRC and the SMA respectively.

Assuming that the initial lateral deflection v_o is a sinusoidal function in the x-direction (i.e. $v_o = a\sin(\pi x/L)$), the Eqn. 9.6 can be rewritten as

$$EI_{yy}\frac{d^2\Delta v}{dx^2}+\frac{\Delta P}{EI_{yy}}\Delta v=\frac{NF_{sma}}{EI_{yy}}v_1-k^2 a\sin(\pi x/L) \tag{9.8}$$

where a is the initial lateral deflection at the mid-point of laminated beam. Finally, solving Eqn. 9.8 by using the boundary conditions of $\Delta v = 0$ at $x = 0$ and L, the general solution of Δv along the x-direction can be obtained by

$$\Delta v=\frac{a}{(\pi/kL)^2-1}\sin(\pi x/L)+\frac{NF_{sma}v_1}{\Delta P}(1-\cos kx-\frac{(1-\cos kL)}{\sin kL}\sin kx) \tag{9.9}$$

Therefore, the lateral deflection Δv_m at mid-point ($x = L/2$) of the laminated beam is given below

$$\Delta v_m=\frac{a}{(\pi/kL)^2-1}+\frac{NF_{sma}v_1}{\Delta P}(1-\frac{1}{\cos(kL/2)}) \tag{9.10}$$

9.3 Experiment

9.3.1 Fabrication of SMA-reinforced Composite Slender Beam

Table 9.2 shows the quantities of the corresponding specimens with embedded SMA wires of different diameters, while the arrangement of those wire actuators is schematically illustrated in Fig. 9.8. Material properties of the SMA wire actuators are listed in Table 9.1. One may notice that the material properties of a composite structure are normally sensitive to the curing temperature. In order to minimize the experimental errors due to variation of the material properties of the specimens, eight pieces of FRC slender beam were cropped off from one single composite plate as shown in the figure. As a result, the material properties of the eight pieces of FRC structures should be more or less the same. Except the specimens with embedded SMA wires, the other two were used for tensile test of the FRC beams with different numbers of layer so as to clarify the mechanical properties of the specimens without the SMA reinforcement.

To increase the reliability and stability of the SMA wires that were used to fabricate the SMA-reinforced laminated beam, a thermomechanical cycle treatment was first conducted until no variation in the stress-strain characteristic was observed. All the wires were then prestrained by 6% before embedding inside the composites. One may notice that the effectiveness of the SMA actuation on the buckling resistance strongly relies on the orientation of the SMA wires inside the composite structure. Therefore, an Aluminum framework as shown in Fig. 9.9 was used to maintain the alignment of the wires during the fabrication process. Figure 9.10 shows the strain gauges installed on the surface of a laminated beam. The measured surface strain at the middle point will be employed for the calculation of lateral deflection due to the applied compressive load.

Table 9.1 Material constants of SMA wire actuators.

Constants	Values			Units
	Ø0.35mm	Ø0.40mm	Ø0.51mm	
T_{so}^{M}	43	35	41	°C
T_{fo}^{M}	22.5	20	21.5	°C
T_{so}^{A}	45.5	38	40	°C
T_{fo}^{A}	90.5	75	63	°C
C_A	50.0×10^{6}	28×10^{6}	19.5×10^{6}	Pa
C_M	38.0×10^{6}	20×10^{6}	30.0×10^{6}	Pa
σ_s^{cr}	65.5×10^{6}	190×10^{6}	93.5×10^{6}	Pa
σ_f^{cr}	351.4×10^{6}	280×10^{6}	208.8×10^{6}	Pa
E_M	17.7×10^{9}	13.7×10^{9}	22.2×10^{9}	Pa
E_A	40.6×10^{9}	47.2×10^{9}	42.4×10^{9}	Pa
ε_L	0.08			-

9.3.2 Experimental Setup

In order to satisfy the requirement of simply supported-simply supported (SS) boundary condition in the buckling test, a pair of tailor-made testing rigs was designed as shown in Fig. 9.11. One may notice that the clamping head is allowed to rotate freely about the hinge- joint. Therefore, the bending moment at the two loading ends rare negligible. In addition, since the electrical resistive heating is employed for the SMA actuation, it is crucial to ensure that identical electric current passes through each piece of the SMA wire. Therefore, the wire actuators are connected in series as shown in Fig. 9.12. Figure 9.13 demonstrates the installation of the tailor-made testing rig on the MTS Alliance RT/50 testing machine while the overall experimental setup is schematically illustrated in Fig. 9.14.

No. of layers	Diameter of SMA wire	Quantity
6	Nil	2
	0.35mm	2
	0.40mm	2
	0.51mm	2
10	Nil	2
	0.35mm	2
	0.40mm	2
	0.51mm	2
14	Nil	2
	0.35mm	2
	0.40mm	2
	0.51mm	2

Table 9.2 Quantity of slender-shape specimens.

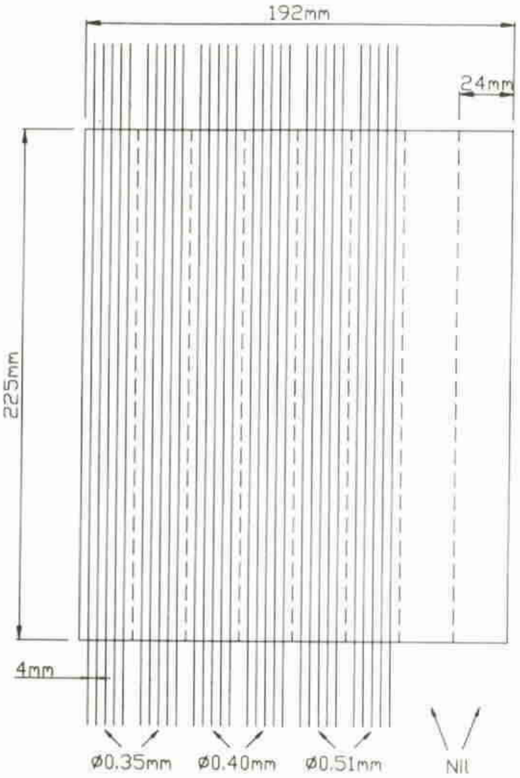

Figure 9.8 Dimension of composite with embedded SMA wires.

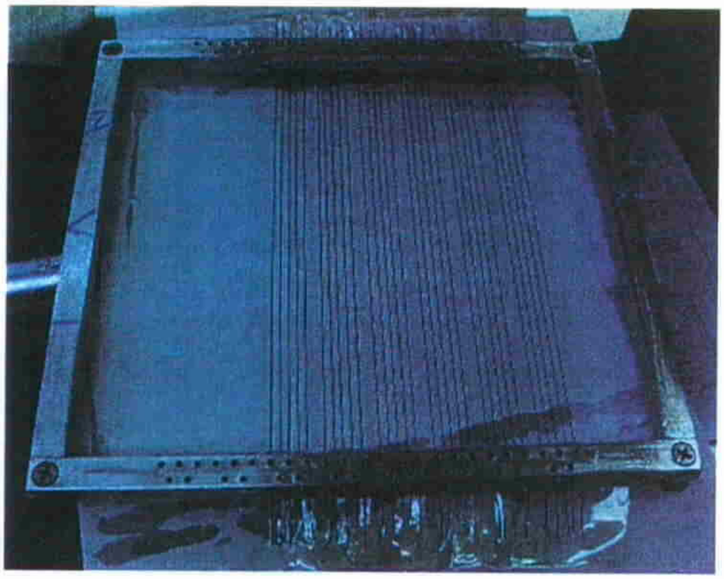

Figure 9.9 A tailor-made fixture for the control of wires alignment during fabrication.

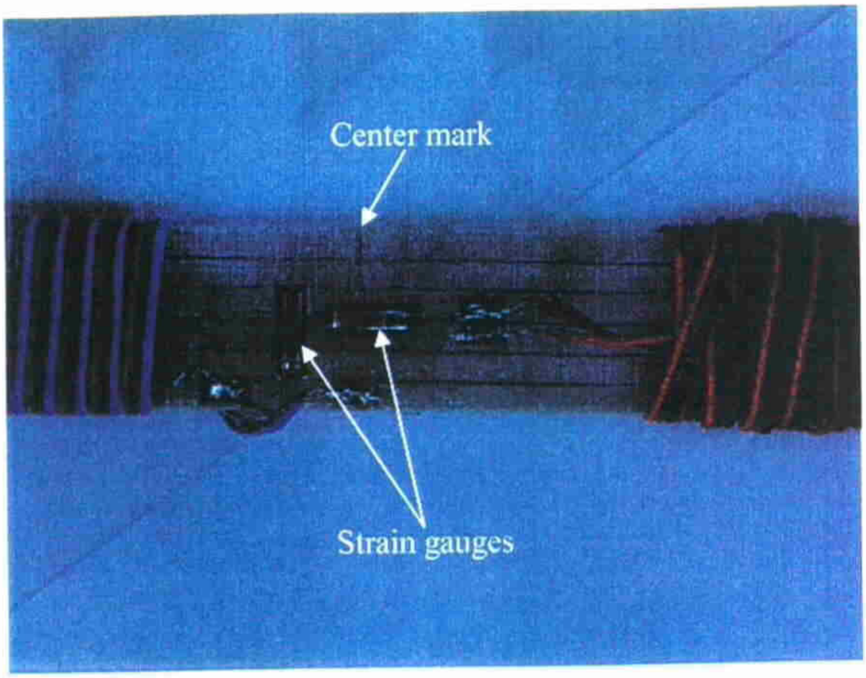

Figure 9.10 Strain gauges were used to measure the surface strain during the buckling test.

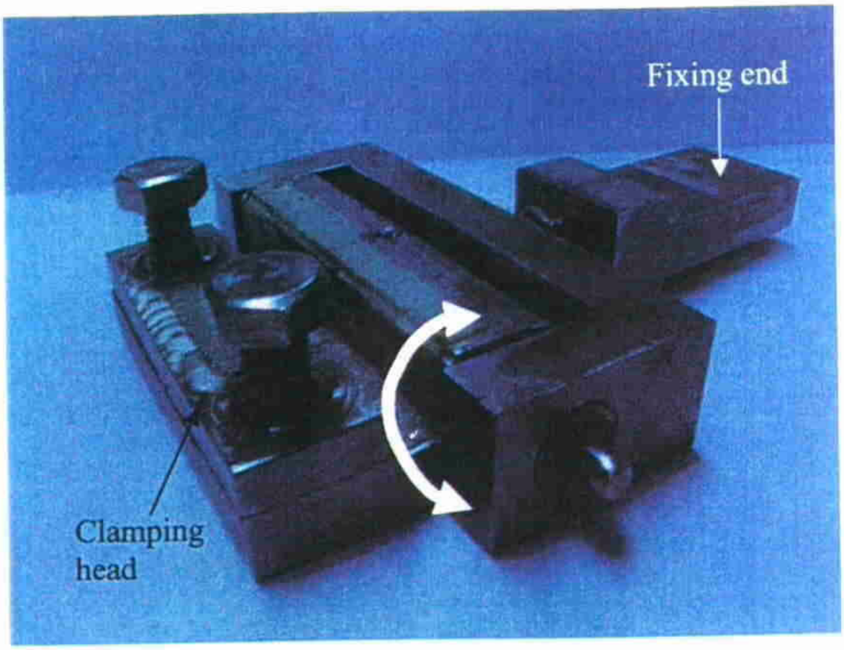

Figure 9.11 Tailor-made testing rig (x2 pieces) for satisfying the requirement of simply supported-simply supported (SS) boundary condition.

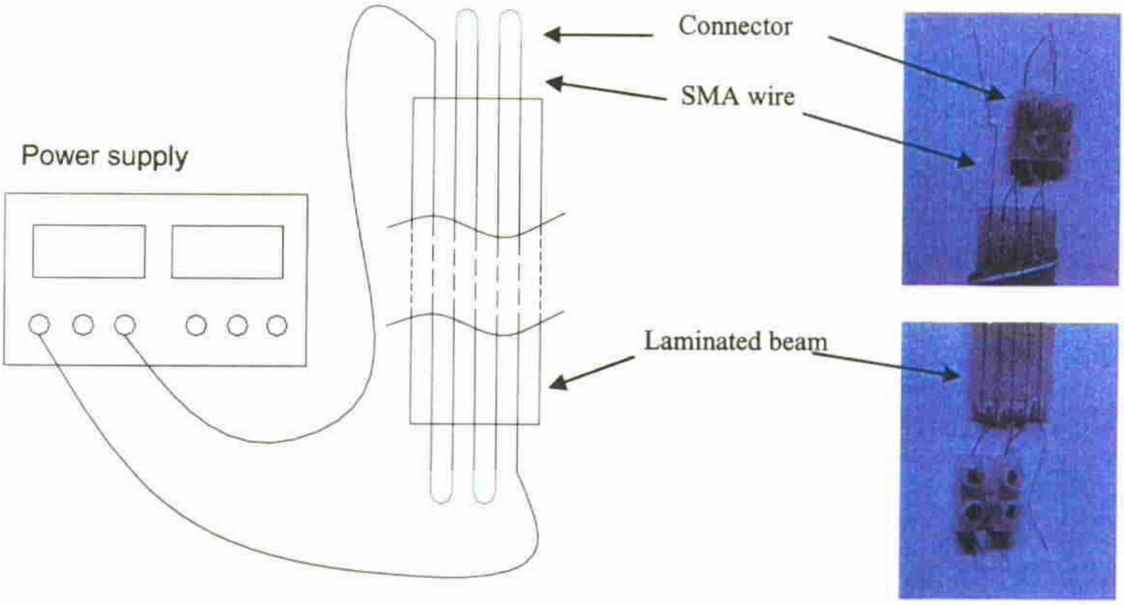

Figure 9.12 The SMA wire actuators are connected in series inside the laminated beam.

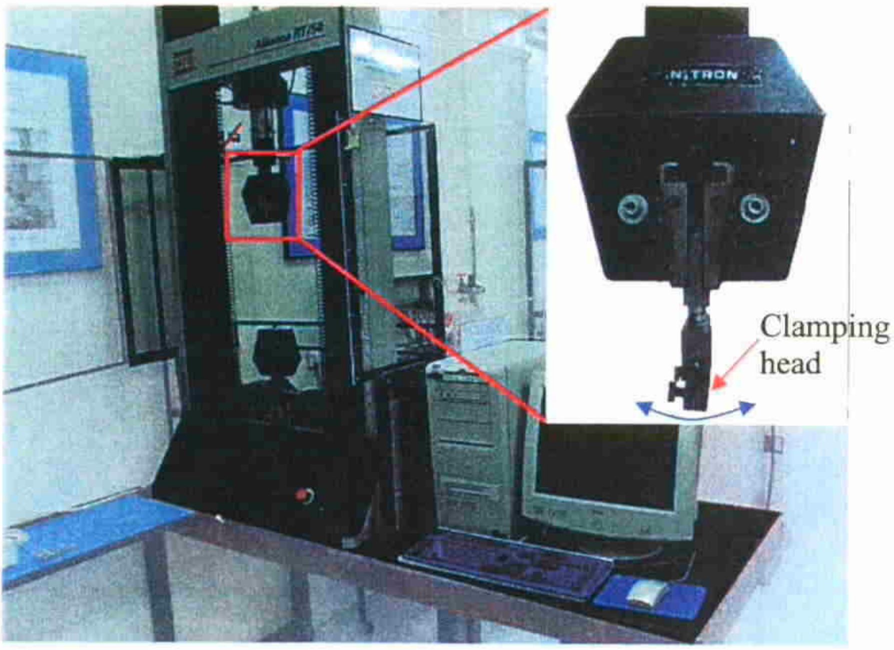

Figure 9.13 Installation of the tailor-made testing rig on the MTS Alliance RT/50 testing machine.

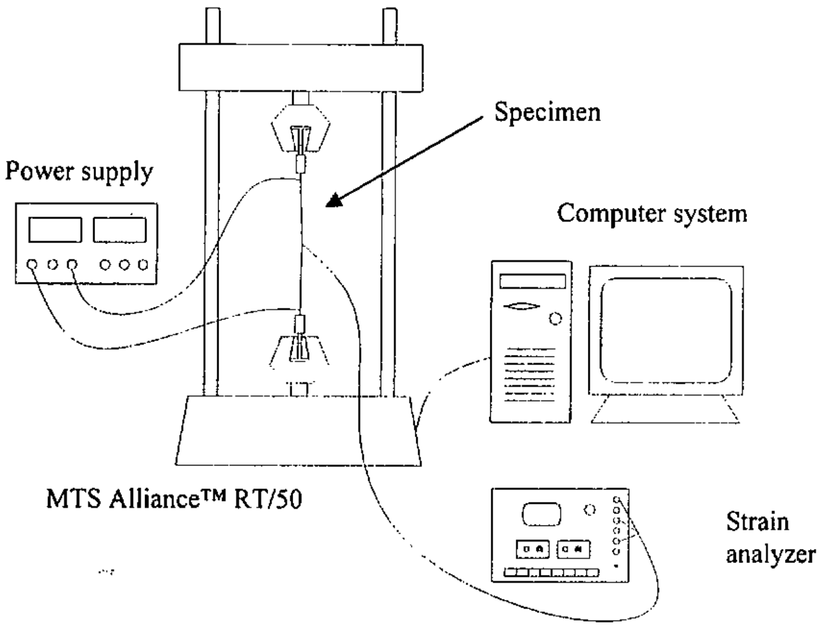

Figure 9.14 Schematic diagram of experimental setup for the buckling test.

9.4 Experimental Results

Figure 9.15 shows the plots of the wire temperature against the applied electric current for 0.35, 0.4 and 0.51mm SMA wire actuators. It should be noted that the plot of 0.51mm wire derivates from others when the temperature is increased upon 30°C while the temperature of 0.35 and 0.4mm wires are increased steadily with applied current and the substantial derivation occurs until the current increases upon 0.7A. As discussed previously in Chapter 4 for the evolution of martensite volume fraction along the embedded SMA wire, it is basically not practical for the SMA wire actuator, which is subjected to the strain-constrained condition inside the matrix, to achieve 100% austenitic phase transformation. Due to the increase of the phase transformation temperature with the internal stress on the SMA, extremely high temperature may be required to complete the austenitic transformation. During the buckling test of different SMA-reinforced laminated beams, interfacial debond was found in some of the trial samples when the wire actuators had been heated up upon 58°C~60°C. In order to avoid the problem of interfacial debond due to over-actuation, the target temperature range for each specimen is therefore restricted to 50°C. Based on the temperature-current relationships for the different SMA actuators, the appropriate current ranges are applied on the corresponding specimens for the actuation purpose.

Figures 9.16 to 9.18 present the buckling test results for the 6, 10 and 14-layers SMA-reinforced laminated beams respectively. Obviously, the improvement of buckling resistance by means of the SMA actuation is relatively less significant for the 6-layer laminated beams while the best performance was found on the 14-layers specimens. Referring to the Figs. 9.18a and b, substantial improvements of buckling resistance were obtained for the laminated beams embedded with 0.4mm and 0.51mm SMA wire actuators. The compressive force is increased linearly with the additional buckling deflection Δv_m and dropped steadily from the highest force levels. However, for the 14-layer specimen embedded with 0.35mm SMA wire actuators, except the minor increment at the initial buckling stage, the compressive forces dropp below the initial values immediately after the peak levels and decrease monotonically with the further increase of Δv_m. The similar results are also obtained for the 10-layer specimens as shown in Fig. 9.17. The specimen embedded with 0.35mm SMA actuators demonstrates poor performance again in the buckling test. Although the increases of initial compressive force were measured during the actuation, the force level dropped in the early stage of buckling. Substantial improvement of buckling resistance can be found for the 10- and 14 layers laminated beams as shown in Figs. 9.17b and c. Similar to the results obtained for 14-layers specimen, the compressive force is increased steadily with the lateral

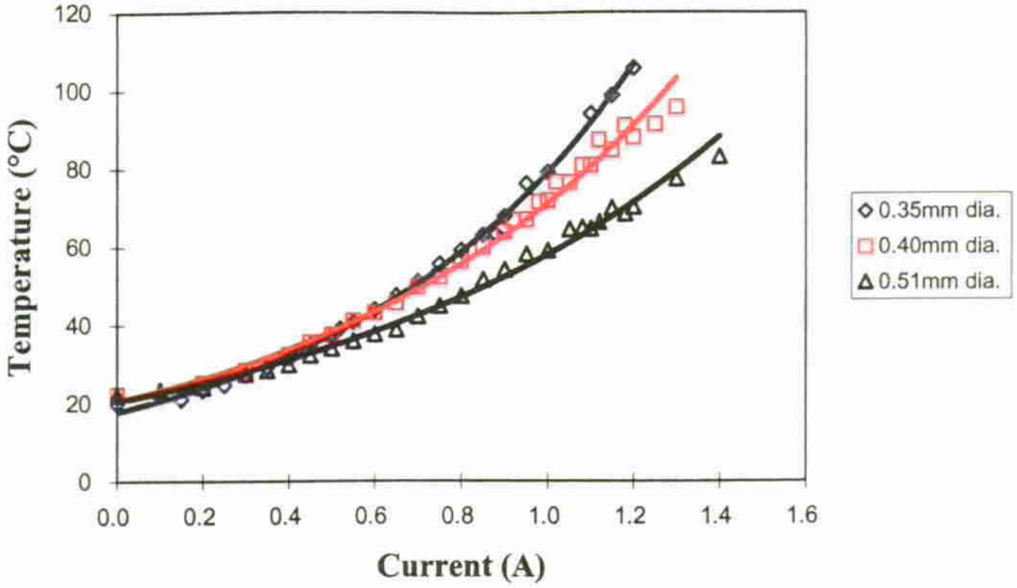

Figure 9.15 Relations between electric current and wire temperature for different SMA wire actuators.

deflection Δv_m in the initial buckling stage. However the force-drop starts earlier for the 10-layers specimen.

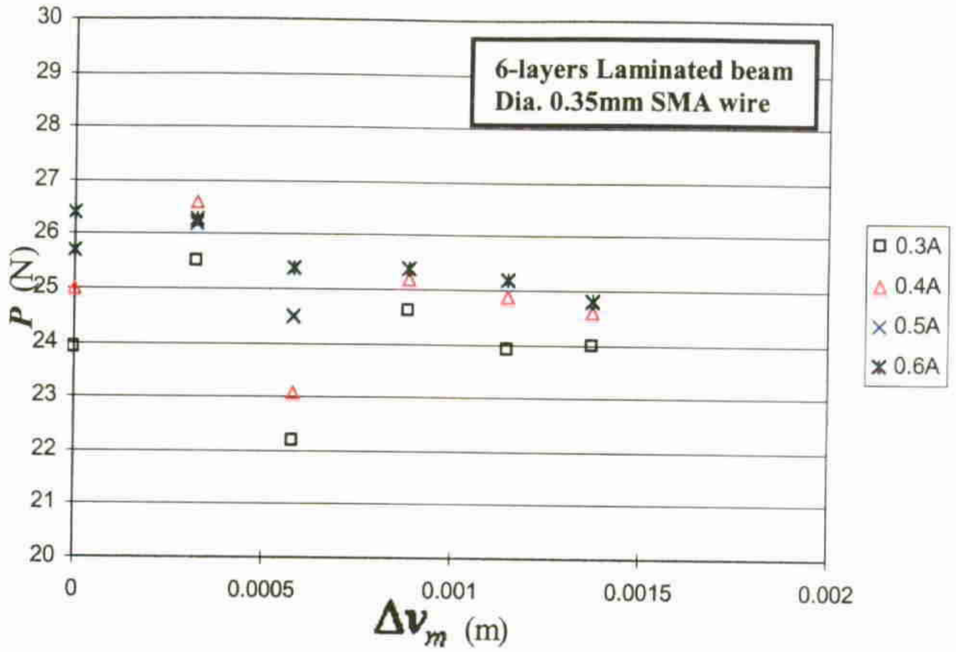

Figure 9.16a Buckling test results of 6 layers composite with embedded Dia 0.35mm SMA wires.

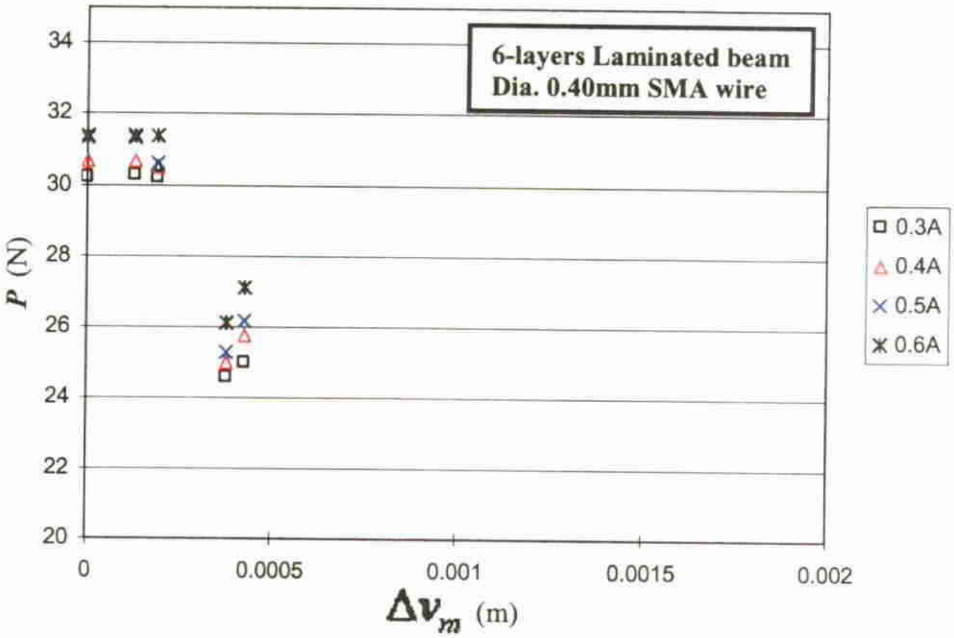

Figure 9.16b Buckling test results of the 6-layers laminated beam embedded with Dia 0.40mm SMA wires.

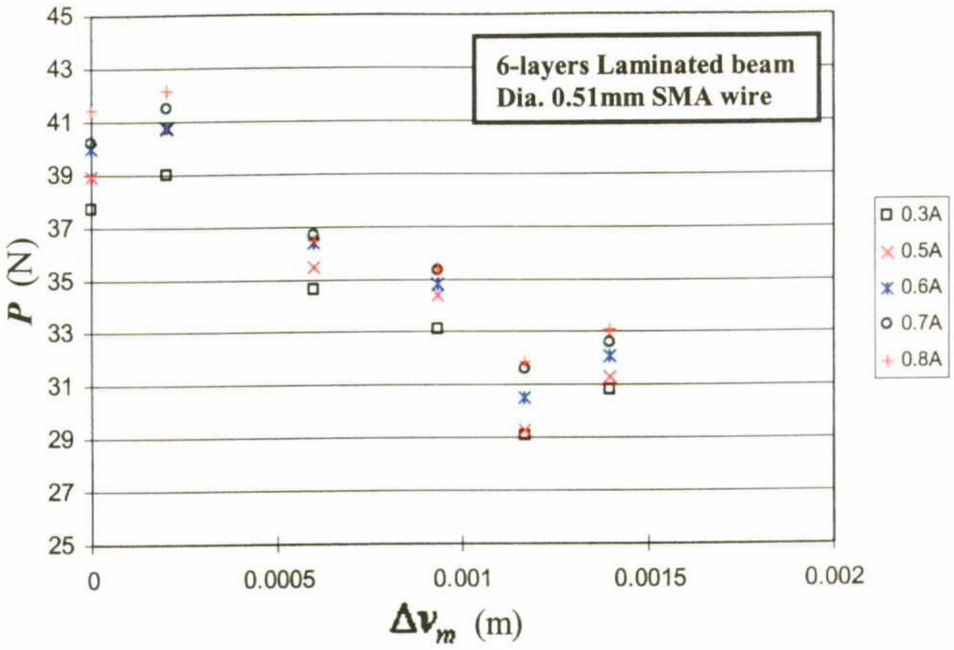

Figure 9.16c Buckling test results of the 6-layers laminated beam embedded with Dia. 0.51mm SMA wire actuators.

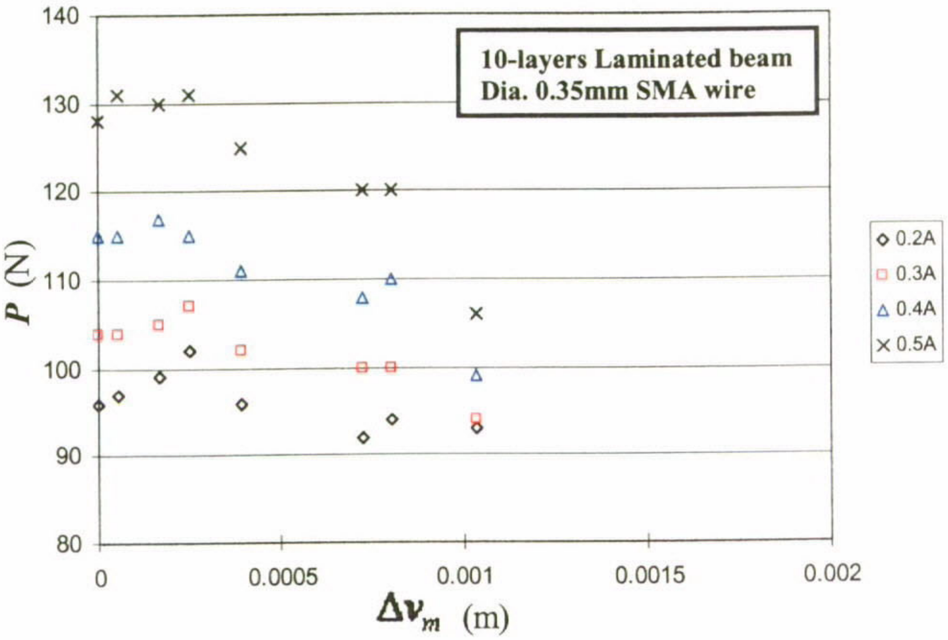

Figure 9.17a Buckling test results of the 10-layers laminated beam embedded with Dia 0.35mm SMA wire actuators.

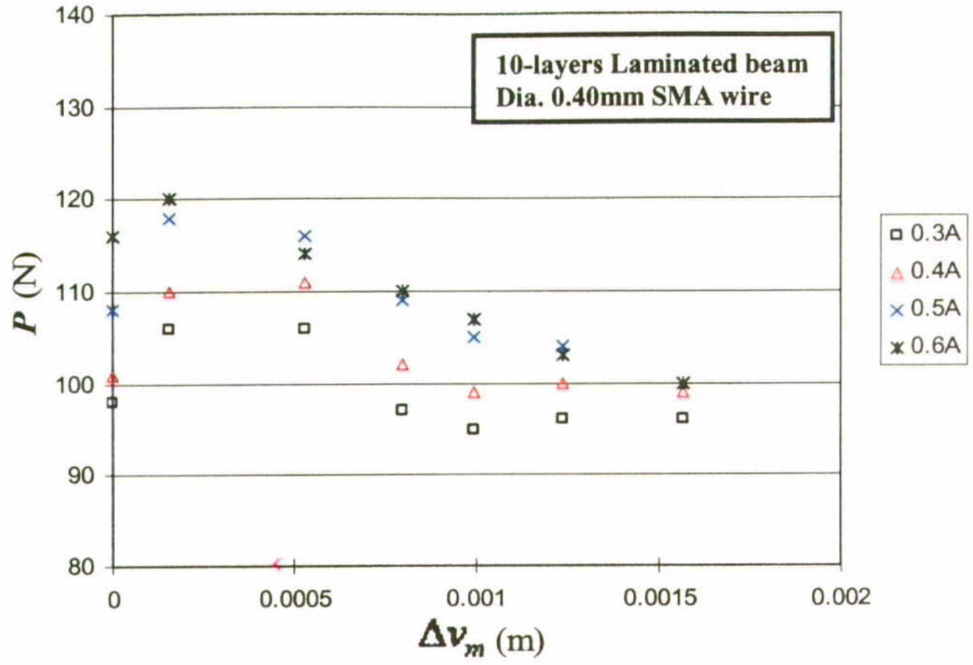

Figure 9.17b Buckling test results of the 10-layers laminated beam embedded with Dia 0.40mm SMA wire actuators.

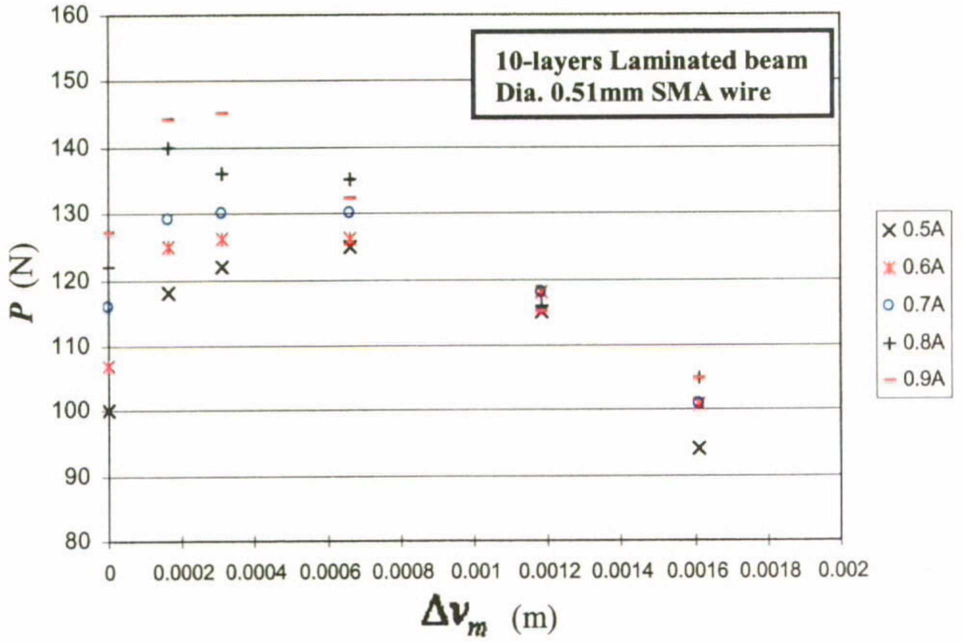

Figure 9.17c Buckling test results of the 10-layers laminated beam embedded with Dia 0.51mm SMA wire actuators.

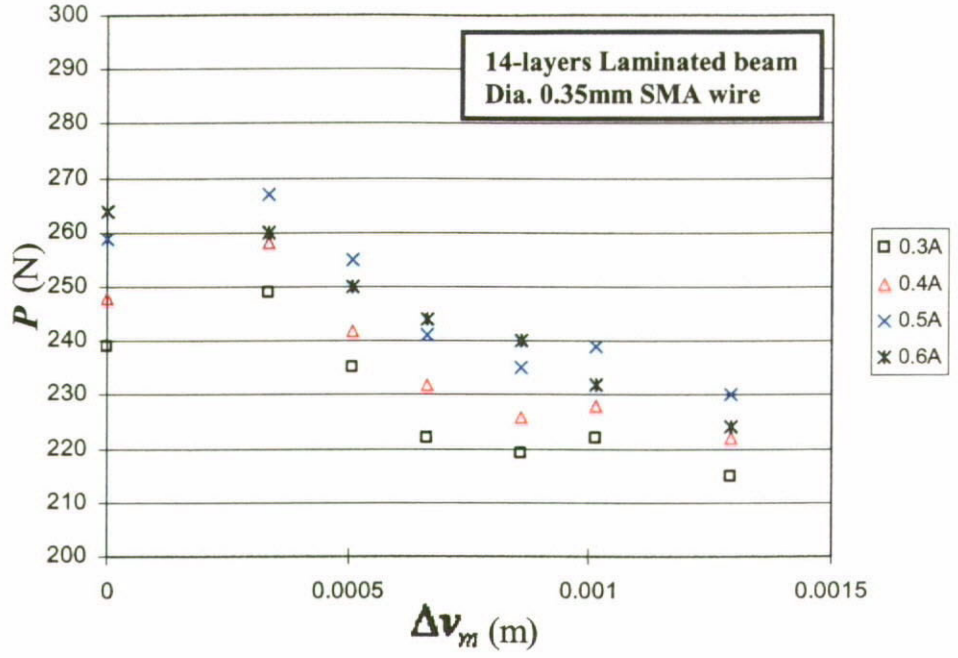

Figure 9.18a Buckling test results of the 14-layers laminated beam embedded with Dia 0.35mm SMA wire actuators.

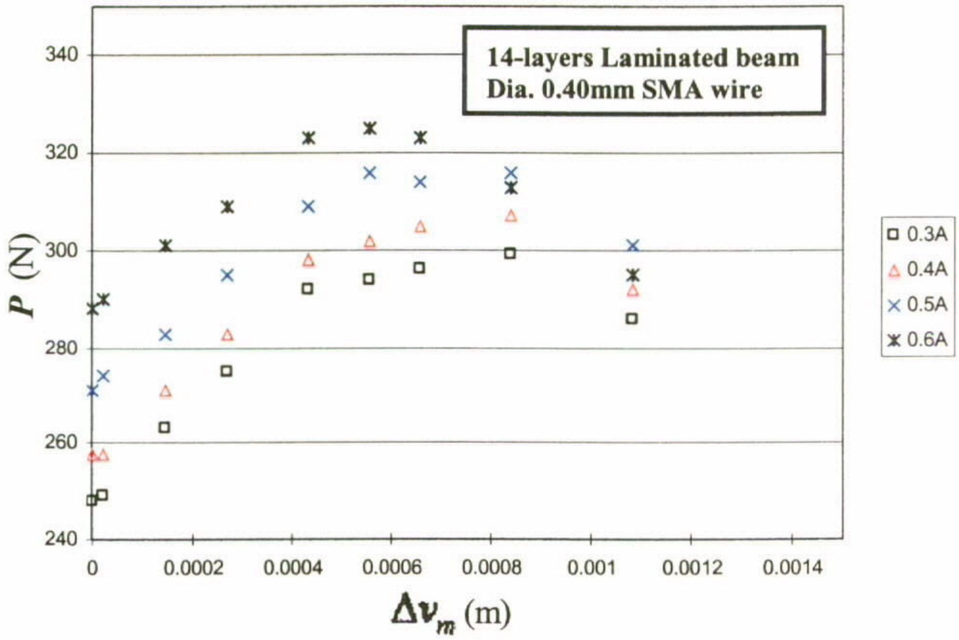

Figure 9.18b Buckling test results of the 10-layers laminated beam embedded with Dia 0.40mm SMA wire actuators.

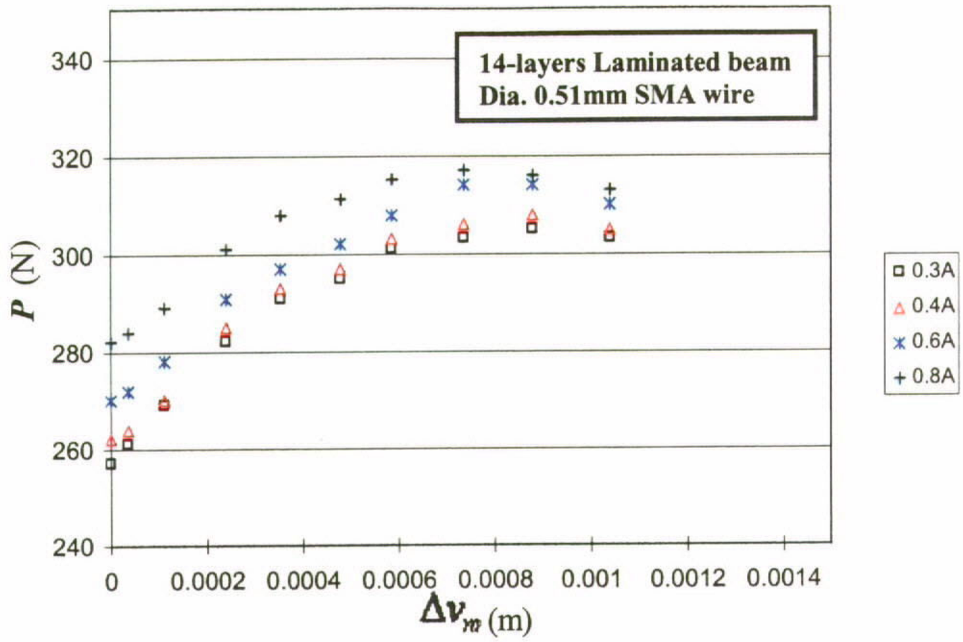

Figure 9.18c Buckling test results of the 14-layers laminated beam embedded with Dia 0.51mm SMA wire actuators.

9.5 Analysis of the Results

Considering the buckling test results presented in the previous section, one may notice that the effect of the SMA actuation for the enhancement of buckling resistance is not significant for the 6-layers laminated beam. This result can be explained by using the free-body diagram as shown in Fig. 9.6. Due to the geometric limitation for the SMA wire installation inside such a thin structure, the perpendicular displacement between the wires and the neutral axis (i.e. v_l) is too short to generate sufficiently high bending moment M_{sma} for the improvement of buckling behaviour. Similarly, the relatively thin SMA wire - Dia. 0.35mm seems unable to generate sufficiently high recovery force F_{sma} to work against the buckling load. Among the buckling test results for the nine combinations of wire diameter and number of layers, the most significant improvement is found for the 10-layers laminated beam embedded with 0.4mm SMA wires.

Base on the captioned preliminary conclusions on the buckling tests, the theoretical analysis for the influence of the SMA actuation on the buckling resistance will be focused on the 10-layers/0.4mm-wire laminated beam in the current study.

9.5.1 Analysis of Additional Buckling Resistance due to SMA Actuation

Recalling Eqn. 9.10 for the relation between additional lateral deflection Δv_m and the SMA actuation for a given compressive load P, one may notice that the initial lateral deflection a is required to be obtained. However, the deformation of a laminated beam during the buckling test was measured by using the strain gauge attached on the surface of the buckling side, it is therefore necessary to clarify the relation between surface strain

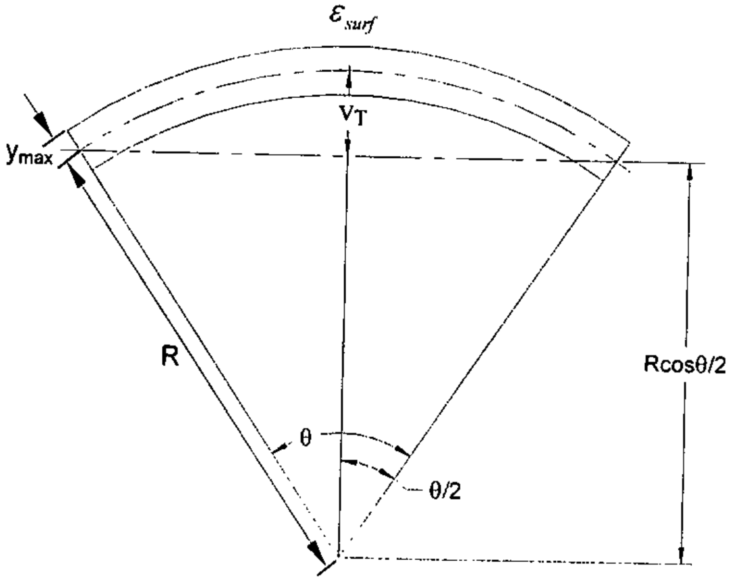

Figure 9.19 Geometric illustration for a buckled laminated beam.

and lateral deflection for the prediction of Δv_m.

Figure 9.19 illustrates the geometric relations of a buckled laminated beam. The general relations between the geometric variables are given as below:

$$\varepsilon_{surf} = y_{\max}/R \tag{9.11}$$

$$L = R\theta \tag{9.12}$$

$$v_T = R - R\cos(\theta/2) \tag{9.13}$$

Substituting Eqns. 9.11 and 9.12 into Eqn. 9.13 gives

$$v_T = \frac{y_{\max}}{\varepsilon_{surf}}\left[1-\cos\left(L\varepsilon_{surf}/2y_{\max}\right)\right] \tag{9.14}$$

where ε_{surf} is the surface strain on the buckling side and y_{max} is the thickness of the beam as illustrated in Fig. 9.19. If the beam is subjected to an initial compressive force P_o on the two ends, the initial lateral deflection a can be calculated by substituting the measured initial surface strain ε_{surfo} in Eqn. 9.13,

$$v_o = a = \frac{y_{max}}{\varepsilon_{surfo}}\left[1-\cos\left(L\varepsilon_{surfo}/2y_{max}\right)\right] \tag{9.15}$$

Finally, substituting Eqn. 9.15 into Eqn. 9.10 yields

$$\Delta v_m = \frac{y_{max}/\varepsilon_{surfo}\left[1-\cos\left(L\varepsilon_{surfo}/2y_{max}\right)\right]}{\frac{\pi^2}{4}\frac{EI_{yy}}{\Delta P}-1} + \frac{NF_{sma}v_1}{\Delta P}\left[1-\sec\left(\frac{L}{2}\sqrt{\frac{\Delta P}{EI_{yy}}}\right)\right] \tag{9.16}$$

Equation 9.16 is the solution for the additional lateral deflection of the SMA-reinforced laminated beam. It should be emphasized here that if a laminated beam without embedding the SMA actuators is subjected to the applied compressive force only, then the Eqn. 9.16 will be reduced as given below

$$\Delta v_m = \frac{y_{max}/\varepsilon_{surfo}\left[1-\cos\left(L\varepsilon_{surfo}/2y_{max}\right)\right]}{\frac{\pi^2}{4}\frac{E_c I_{yy}}{\Delta P}-1}$$

or

$$\Delta P = \frac{E_c I_{yy}\left(\pi/L\right)^2}{\left(y_{max}/\varepsilon_{surfo}\Delta v_m\right)\left[1-\cos\left(L\varepsilon_{surfo}/2y_{max}\right)\right]+1} \tag{9.17}$$

where E_c, the elastic modulus of the composite is employed instead of the equivalent value E for the SMA-reinforced composite structure.

9.5.1.1 Experimental and Theoretical Analysis of the Additional Buckling Resistance

The additional buckling resistance (ABR) can be easily identified from the experimental results by using the simple superposition concept as following,

$$\bar{P}_{act} = \Delta\bar{P} - \Delta\bar{P}\big|_{w/o} \tag{9.18}$$

where $\bar{P}_{act}$ is the additional compressive force required to overcome the reaction arising from the SMA actuation. $\Delta\bar{P}$ and $\Delta\bar{P}\big|_{w/o}$ are the measured values for a laminated beam with and without SMA actuation respectively.

Similarly, the ABR predicted from the theoretical model should also be identified as given below,

$$P_{act} = \Delta P - \Delta P\big|_{w/o} \tag{9.19}$$

where ΔP is the numerical result obtained from Eqn. 9.16 and $\Delta P\big|_{w/o}$ is the analytical result of Eqn. 9.17.

Figure 9.20 shows the comparison between the experimental results and theoretical predictions of the additional compressive force arising from the SMA actuation for the 14-layer laminated beam with embedded 0.4mm SMA wire actuators. The theoretical predictions agree fairly well with the experimental results. Both sets of the results indicate the decrease of P_{act} with the Δv_m increase. Referring to the Eqn. 9.3 for the resultant bending moment of a buckled laminated beam, the M_{sma} arising from the SMA actuation is considered as a constant while the M_b should be increased with the increase

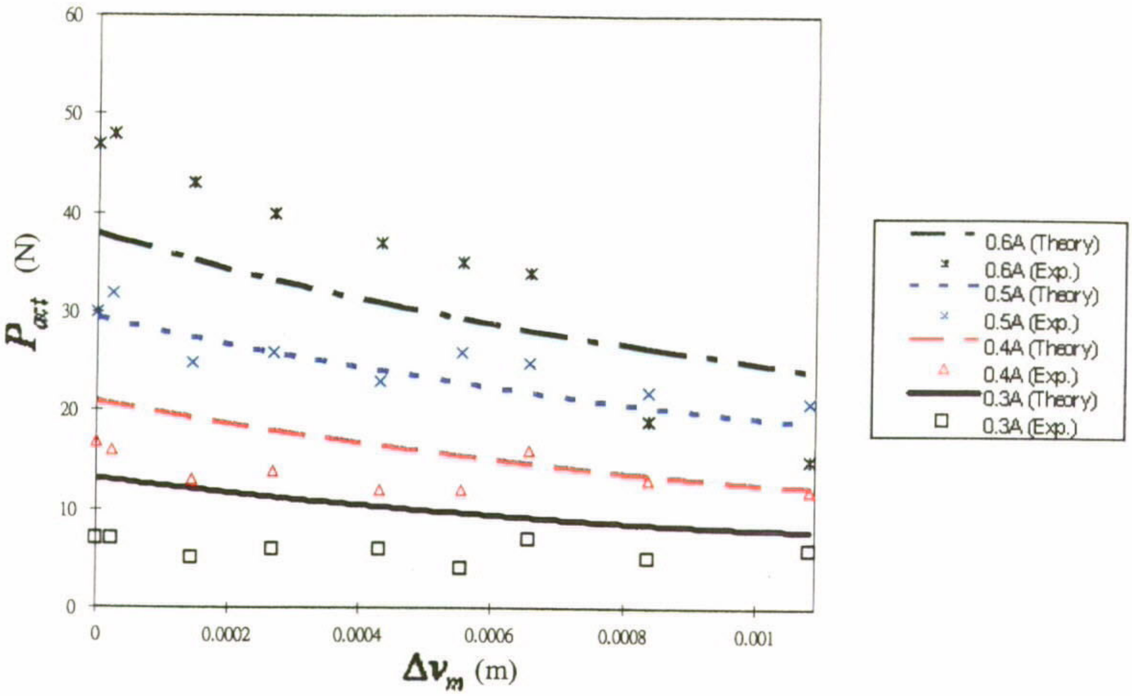

Figure 9.20 Comparison between theoretical and experimental results of the additional compressive force arising from SMA actuation for the 14-layers laminated beam embedded with 0.4mm SMA wire actuators.

of the lateral deflection Δv_m. In the other words, when Δv_m is getting higher and higher, the resultant bending moment M is dominated by the M_b and the influence of M_{sma} on the buckling resistance becomes less significant.

9.6 Summary

In this Chapter, the feasibility of using SMA wire actuators in the buckling control has been studied. The laminated composite beams embedded with 0.35, 0.4 and 0.51mm SMA wire actuators were tested for the buckling resistance under the SS boundary condition. In addition, the stress component arising from the recovery action of the SMA actuators was incorporated in the classical theory of buckling of slender beam. The martensite volume fraction has been estimated from the previously developed theoretical model (Eqn. 3.30) and hence the material properties of the embedded SMA were estimated and inputted into the model developed in this Chapter for the prediction of buckling resistance. The theoretical results were agreed fairly well with the experimental findings on the estimation of additional buckling resistance at different levels of lateral deflection. The improvement of buckling resistance was found significant for the initial buckling stage.

Chapter 10

Conclusions and Suggestions for Future Research

10.1 Conclusions

A comprehensive review of the literatures showed a great demand on the smart materials and structures for modern designs of medical devices, aircrafts and motor vehicles as well as the space structures. Numerous researches reported the success of using SMA actuators in various engineering structures, especially the fiber reinforced composites (FRC), for the modifications of mechanical responses towards many different external stimuli. However, there was a lack of theoretical models or even experimental findings for the designs and reliability studies of the SMA-reinforced composites.

In the present study, a great deal of work has been done on the characterizations of interfacial behaviours of the SMA-composites. The constitutive model of the SMAs has been successfully incorporated with the classical stress-strain relations to formulate the solutions of internal stresses. Martensite volume fraction ξ has been considered as a governing parameter which determines the material status of the SMA inclusions under the specific loading and/or actuation conditions. Solution of such critical parameter in the strain-constrained condition has been derived as a function of applied load, temperature and axial position along the SMA wire. Also, the recurrent relation between axial stress on the SMA wire and axial position at the given applied load and actuation temperature has been also developed to predict the ξ-evolution and hence the evolution of elastic modulus and axial stress on the SMA wire. Using the general stress-strain relations and equilibrium conditions between wire and matrix, the internal stress distributions were predicted. Results indicated that axial stress on the SMA wire could be increased substantially to improve the mechanical responses of a composite structure. However the interfacial shear stress at the two embedded ends could be also increased and cause the potential damage to the bonded interface at relatively high temperature. On the other hand, if the SMA wire is subjected to an externally applied load, the SMA actuation is able to moderate the interfacial shear and as a result, higher applied load is required to initiate the interfacial debond. Parametric studies of the influences of the SMA wire embedded length L and the matrix-to-wire ratio b/a on the axial stress distribution on the SMA wire were also performed. The results indicated that the maximum axial stress on the SMA wire during the SMA actuation could be achieved for the sufficient long embedded length and high matrix-to-wire ratio.

Since the evolution of the SMA properties strongly depends on the applied load and actuation temperature, three types of loading conditions and two modes of the SMA actuations have been defined as the typical loading-actuation scenarios for the SMA-composites. The parametric studies on the influence of geometric factors suggested that the competence of type III loading condition in the fiber pullout test could be achieved if the critical embedded length and matrix-to-wire ratio have been satisfied. Also, the shape memory effect (SME) was found more effective and the austenitic transformation could be initiated more easily in mode-b actuation. In addition, the important concepts of constant martensite volume fraction region (CMR) and constant axial stress region (CASR) have been proposed as a research and design basis for ensuring that the uniformly distributed material and mechanical properties can be attained at the targeted region on the SMA-composite. The critical values of L_c and b_c/a were therefore considered as the design guide line to ensure the required mechanical response can be achieved by the actuated SMA-composites.

The total elastic strain energy on both the bonded and debonded regions has been used to formulate the interfacial debond criterion of the SMA wire-matrix cylinder. The theoretical model predicted substantial improvement of debond stresses with the increase of actuation temperature. The numerical solutions indicated that the normalized strain energy release rate could be increased considerably due to the SMA actuation even at the no-load condition. This result explained the possibility of interfacial debond at the free embedded end induced by over-actuation of the embedded SMA wire. Effects of actuation temperatures and prestrain values of the SMA wire on the partial debond stresses were also studied. The results showed the substantial improvement of both initial and maximum debond stresses due to SMA actuation.

A series of pullout test have been conducted to obtain the critical debond stresses. The interfacial properties were then evaluated by using the stress drop analysis. The debonding behaviours of the actuated SMA wire-matrix cylinders were also closely monitored by using a high resolution digital camera. The comparisons of initial debond stress and stress development in a partial debonded condition between experimental findings and theoretical results were agreed well with each other. Therefore, the theoretical model developed in this study has been validated and the performance of the SMA actuation on the bond strength improvement was also confirmed. When the embedded SMA wire has been actuated to a relatively high temperature, the initial deobnd was found at the free-end instead of loading end. Therefore, the possibility of structural failure due to over-actuation of the embedded SMA actuators was also confirmed.

Based on the fact that the interfacial shear stress can be changed substantially at different actuation temperatures, the optimum actuation condition (OAC) has been clearly defined to specify the relation between applied load and the ideal actuation level. Numerical results indicated that the higher the prestrain value of the SMA, the more difficult the control of the OAC. The criterion of OAC has been further simplified to an analytical form which is known as SOAC in the current study. It provides an explicit solution of the OAC for the model with sufficient large geometric factors including wire embedded length and *b/a* ratio.

Finite element analysis (FEA) has been used to further clarify the internal stress distributions in the SMA-composites. The 2D-axisymmetric models have been developed with predefined debonded length. The frictional contact surfaces between the SMA wire and matrix cylinder at the debonded region were successfully simulated with the consideration of interfacial properties obtained from single fiber pullout test. Nonlinear static analysis was used to evaluate both the axial stress distribution on the SMA wire and the shear stress along the wire matrix interface. The equivalent elastic modulus of SMA has been estimated by using the proposed recurrence relation to simulate the instantaneous material status under different actuation levels. A series of stress distribution comparisons indicated that the theoretical predictions could match with FEA results in a good manner especially for the perfectly bonded condition.

Application of SMA wire actuators for the buckling control of laminated beam has been demonstrated to show substantial improvement in the buckling resistance. A model of buckling response of SMA-reinforced laminated beam has been also developed on the basis of classical buckling equation and the constitutive law of the SMA. The simply supported-simply supported boundary condition has been used for the buckling test to evaluate the additional buckling resistance obtained from the SMA actuation. The experimental results agreed fairly well with theoretical prediction in the estimation of buckling resistance at different actuation temperature and the significant improvement was found at the initial buckling stage.

10.2 Suggestions for Future Research

SMA-reinforced composite is a new class of novel material system which possesses various advantages over most of the existing engineering materials and structures. While some observations and correlations were made on the micro-mechanics between the SMA inclusions and the surrounding matrix, there are still some other researches that can fill up the remaining knowledge gaps regarding the design and application issues. For example, the influence of heat transfer between SMA, matrix and the ambience could be further analyzed to clarify the temperature distribution along the SMA. In the other words, incorporating the heat transfer component into the model developed in this study may help to estimate more practical actuation levels for satisfying the required mechanical responses.

As previously discussed in Chapter 2 regarding several plausible methods to improve the interfacial bond strength, embedment of twisted wire is one of the good candidates for achieving this specific task. The twisted wire possesses relatively high surface roughness and hence the bonding quality may be improved. However, the twisting process may induce non-uniform distribution of martensite volume fraction across the wire's cross section, the prestrained level on outer surface could be much higher than that at the center. Therefore, the one-dimensional constitutive model of SMA may need to be replaced by the one in three-dimensional form in order to reproduce the mechanical response of twisted SMA wire.

Some research suggested the use of novel speckle pattern recognition technique known as digital image correlation (DIC) to characterize the recovery action of the embedded SMA wires. However the accuracy of such measurement is not high enough for the quantitative analysis but only available for the qualitative assessment. In order to measure the stress distributions inside a SMA-matrix cylinder, it is suggested to install an optical fiber bragg grating (FBG) sensor at the interface between the SMA wire and matrix during the fabrication process, so that a specimen built-in with both SMA wire actuator and FBG sensor can be obtained and hence the internal stress distribution due to SMA actuation could be measured directly. Depending on the dimensions and material properties of the constituents, the stiffness of conventional type FEG sensor may be too high to derivate the stress distribution. Therefore, the application of polymer optical fiber sensor may be considered in the future experimental studies.

Publications Arising from the Thesis

1. C.K. Poon, K.T. Lau and L.M. Zhou, 2004, "Design of pullout stresses for prestrained SMA wire/polymer hybrid composites", Composites Part B: Engineering. 2004, accepted for publication.

2. C.K. Poon, L.M. Zhou and L.H. Yam, 2004, "Size Effect on the Optimum Actuation Condition for SMA-Composites", Journal of Composite Structures; 2004, accepted for publication.

3. C.K. Poon, L.M. Zhou and L.H. Yam, 2004, "Analysis of Internal Stresses in SMA Composites", Submitted to Composites Part B: Engineering, April, 2004

4. C.K. Poon, L.M. Zhou, W. Jin and S.Q. Shi, 2004, "Interfacial Debond of SMA Composites", Submitted to Smart Materials and Structures, April 2004

5. C.K. Poon, L.M. Zhou and W. Jin, 2004, "Optimum Actuation Condition for SMA-Composites", Submitted to Composite Sciences and Technology, May 2004

6. C.K. Poon, L.M. Zhou and W. Jin, 2004, "Finite Element Analysis of SMA Composites", to be submitted to Composites Part B: Engineering, June 2004

7. C.K. Poon and L.M. Zhou, 2004, "Shape Memory Effect on Interfacial Strength of SMA-reinforced Composites", Accepted for presentation at the 4th Asian-Australasian Conference on Composite Materials, Sydney, Australia, July 2004.

8. C.K, Poon, L.M. Zhou and L.H. Yam, 2004, "Determination of Optimum Actuation Condition for SMA-Composites", Presented at the International Workshop on Advanced Smart Materials and Smart Structure Technology, Hawaii, USA, Jan, 2004

9. C.K. Poon, L.M. Zhou and L.H. Yam, 2003, "Analytical Study of Internal Stress Distribution in SMA Composites", Presented at the International Symposium on Macro-, Meso-, Micro- and Nano- Mechanics of Materials (MM2003) on Dec, 2003, P182.

10. C.K. Poon, L.M. Zhou and W. Jin, 2003, "Prediction of Interfacial Debond for Smart Composites", Presented at the International Symposium on Macro-, Meso-, Micro- and Nano- Mechanics of Materials (MM2003) on Dec, 2003, P181.

11. L.B. Yuan, L.M. Zhou, W. Jin, K.T. Lau and C.K. Poon, 2003, "Effect of Thermal Induced Strain on Optical Fiber Sensors Embedded in Cement-based Composites", Optical Fiber Technology, 2003; 9 (2): pp. 95-106

12. K.T. Lau, C.K. Poon, L.H. Yam and L.M. Zhou, 2002, "Bonding Behaviour at a NiTi/epoxy Interface: SEM Observation and Theoretical Study", Materials Science Forum, 2002; 394-395: pp. 527-530.

References

[1] K. Tanaka, 1986, "A Thermomechanical Sketch of Shape Memory Effect: One Dimensional Tensile Behaviour", Res. Mechanica, 18: pp. 251-263

[2] C. Liang and C.A. Rogers, 1990, "One-Dimensional Thermo Mechanical Constitutive Relations for Shape Memory Material", J. Intelligent Mater. Syst. Struct., 1: pp. 207-234

[3] L.C. Brinson, 1993, "One-Dimensional Constitutive Behaviour of Shape Memory Alloys: Thermomechanical Derivation with Non-Constant Material Functions and Redefined Martensite Internal Variable", J. Intelligent Mater. Structu. 4: pp. 229-242

[4] W.J. Buehler and R.C. Wiley, 1965, "Nickel-Based Alloys", Technical Report, U.S.-Patent 3174851

[5] W.B. Cross, A.H. Kariotis, and F.J. Stimler, 1969, Technical Report. NASA SP 1433

[6] C.M. Jackson, H.J. Wagner and R.J. Wasilewski, 1972, "55-Nitinol – The Alloy with a Memory: Its Physical Metallurgy, Properties and Applications". Technical Report NASA SP 5110

[7] W. Cross, A. Kariotis and F. Stimler, 1969, "Nitinol Characteristic Study", NASA CR-1433

[8] F.E. Wang, 1968, Proceeding of Symposium of NiTi and Related Compounds, Technical Report. NOLTR 68-16

[9] C. Liang, J. Jia and C.A. Rogers, 1989, "Behaviour of Shape Memory Alloy Reinforced Composites (Part 2)", Proceedings of the 30th AIAA/ASME/ASCE/AHS/ASC Structures, Structural Dynamic and Material Conference, Mobile, AL, 3-5 April 1989 pp. 1504-1513

[10] C.A. Rogers, 1990, "Active Vibration and Structural Control of Shape Memory Alloy Hybrid Composites: Experimental Results", Journal of the Acoustical Society of America, 88(6): pp. 2803-2811

[11] E.C. Bain, 1924, Transaction AIME, 70: 25

[12] W. Buhrer, M. Zolliker and R. Gotthart, 1992, "Crystal Structures of the Shape Memory Alloy Adjustable Camber (SMAAC) Control Surfaces", First European Conference on Smart Structures and Materials, pp. 189-192

[13] K. Madangopal and S. Banerjee, 1990, "The Self Accommodation Morphology of Ni-Ti Shape Memory Alloy Martensite", Scripta Metallurgica et Materialia, 24: pp. 2291-2296

[14] K. Madangopal and S. Banerjee, 1992, "The Lattice Invariant Shear in ni-Ti Shape Memory Alloy Martensites", Scripta Metallurgica et Materialia, 26: pp. 1627-1632

[15] K. Madangopal and S. Banerjee, 1993, "The Nature of Self Accomodation in ni-Ti Shape Memory Alloys", Scripta Metallurgica et Materialia, 29: pp. 725-728

[16] K.N. Melton, 1990, "Ni-Ti Based Shape Memory Alloys", In T.W. Duerig, K.N. Melton, D. Stokel and C.M. Wayman, Editors, Engineering Aspects of Shape Memory Alloys, pp. 21-35

[17] X. Gao, X. Zhang and L.C Brinson, 2000, "SMA Single Crystal Experiments and Micromechanical Modeling for Complex Thermomechanical Loading", Proceedings SPIE: Active Materials: Behaviour and Mechanics, Volume 3992, pp. 516-523

[18] P.H. Adler, W. Yu, A.R. Pelton, R. Zadno, T.W. Duerig and R. Barresi, 1990, "On the Tensile and Torsional Properties of Pseudoelastic Ni-Ti", Scripta Metallurgica et Materialia, 24: pp. 943-947

[19] S. Miyazaki, 1990, "Thermal and Stress Cycling Effects and Fatigue Properties of Ni-Ti Alloys", In T.W. Duerig, K.N. Melton, D. Stokel and C.M. Wayman, Editors, Engineering Aspects of Shape Memory Alloys, pp. 394-413

[20] H. Tobushi, H. Iwanaga, A. Inaba and M. Kawaguchi, 1989, "Deformation Behaviour of Ni-Ti Shape Memory Alloy Under Thermo-mechanical Cycles", In A.S. Khan and M. Tokuda, Editors, Advances in Plasticity, pp. 365-368

[21] H. Tobushi, H. Iwanaga, Y. Ohashi, A. Inaba, M. Kawaguchi and H. Saida, 1990, "Cyclic Characteristic of the Shape Memory Effect in Ti-Ni Alloy Wires and Helical Springs", JSME international Journal, 33: pp. 256-262

[22] H. Tobushi, H. Iwanaga, K. Tanaka, T. Hori, and T. Sawada, 1991, "Deformation Behaviour of NiTi Shape Memory Alloy Subjected to Variable Stress and Temperature", Continuum Mechanics and Thermodynamics, 3: pp. 79-93

[23] M. Kawaguchi, Y. Ohashi and H. Tobushi, 1991, "Cyclic Characteristics of Pseudoelasticity of Ti-Ni Alloys (effect of maximum strain, test temperature and shape memory processing temperature)", JSME International Journal, 34: pp. 76-82

[24] T.J. Lim and D.L. McDowell, 1994, "Degradation of an Ni-Ti Alloys During Cyclic Loading", In Smart Structure and Materials 1994, Smart Materials, Proceedings of the SPIE – The International Society for Optical Engineering, Vol. 26: pp. 326-341

[25] D.A. Hebda and S.R. White, 1995, "effect of Training Conditions and Extended Thermal Cycling on Nitinol Teo-Way Shape Memory Behaviour", Smart Mater. Struct. 4: pp. 298-304

[26] D.A. Hebda, M.E. Whitlock, J.B. Ditman and S.R. White, 1995, "Manufacturing of Adaptive Graphite/Epoxy Structure with Embedded Nitinol wires. J. Intelligent Mater. Syst. Struct.

[27] L. Dalaey and J. Thienel, 1975, "Shape Memory Effects in Alloys", J. Perkins (New York: Plenum): pp. 341-350

[28] R.J. Wasilewski, 1971, "The effects of Applied Stress on the Martensitic Transformation in NiTi", Metallurgical Transactions, 2(11): pp. 2973-2981

[29] H.C. Liang and R. Kaplow, 1980, "Phase Transformation and Shape Memory in NiTi", Metallurgical Transaction A, 11A (1): pp. 77-83

[30] J. Ditman, S.R. White and L. Bergman, 1991, "Tensile Testing of Nitinol Wire", UILU-ENG-91-0508, University of Illinois Urban-Champaign, Urban, IL.

[31] K.N. Melton and O. Mercier, 1981, "The Mechanical Properties of NiTi-Based Shape Memory Alloys", Acta-Metallurgica, 29(2): pp. 393-398

[32] J. Perkins and D. Hodgson, 1990, "The Two-Way Shape Memory Effect", Engineering Aspects of Shape Memory Alloys, C.M. Wayman et al., Eds., Butterworth-Heinemann Ltd., London, England, pp. 195-206

[33] T.E. Dye, 1990, "An Experimental Investigation of the Behaviour of Nitinol", PhD Dissertation, Virginia of Polytechnic Institute and Stage University, Blacksburg, VA.

[34] D.S. Ford, D.A. Hebda and S.R. White, 1994, "Constitutive and Transformation Behaviour of Two-Way Shape Memory (TWSM) Nitinol", Proceeding of the 31st Society Cociety TX, 10-12: pp. 2427-2432

[35] D.A. Hebda, 1995, "Mechanical Behaviour of Active Composites with Embedded Nitinol"

[36] D.S. Ford and S.R. White, 1996, "Thermomechanical Behaviour of 55Ni45Ti Nitinol", Acta-Materialia, 44(6): pp. 2295-2307

[37] S. Miyazaki, K. Otsuka and Y. Suzuki, 1981, "Transformation Pseudoelasticity and Deformation Behaviour in a Ti-50.6 at % Ni Alloy", Scripta Metallurgica, 15(3): pp. 287-292

[38] P.H. Leo, T.W. Shield and O.P. Bruno, 1993, "Transient Heat Transfer Effects on the Pseudoelastic Behaviour of Shape-Memory Wires", Acta Metallurgica et Materialia, 41(8): 2477-2485

[39] J.A. Shaw and S. Kyriakides, 1995, "Thermomechanical Aspect of NiTi", Journal of Mechanics and Physics of Solids, 43(8): pp. 1243-1281

[40] Y. Furuya, H. Shimada, Y. Tanahashi, M. Matsumoto and T. Honma, 1988, "Evaluation of Recovery Bending Force of Shape Memory Ni-Ti Alloy", Scripta Metallurgia, 22(6): pp. 751-755

[41] P. Sittner, Y. Hara and M. Tokuda, 1995, "Experimental Study on the Thermoelastic Martensic Transformation in Shape Memory Alloy Polycrystal Induced by Combined Forces", Metallurgical and Materials Transactions, 26A(11): pp. 2923-2935

[42] K. Jacobus, H. Sehitoglu and M. Balzer, 1996, "Effect of Stress State on the Stress-Induced Martensitic Transformation in Polycrystalline Ni-Ti Alloy", Metallurgical and Materials Transactions 27A: pp. 3066-3073

[43] J.S. Paine and C.A. Rogers, 1993, "Characterization of International Shear Strength Between SMA Actuators and Host Composite Material in Adaptive Composite Material Systems", Proceedings of the 1993 ASME Winter Annual Meeting , New Orleans, LA, 28 November – 3 December 1993, pp. 63-70

[44] K.D. Jonnalagadda and N.R. Sottos, 1995, "Influence of Adhesion on Micromechanical Behaviour of SMA-composites", Proceeding of the 1995 SPIE Smart Structures & Materials Symposium: Mathematics and Control in Smart Structures, San Diego, CA, 27 February – 1 March 1995, 2442: pp. 143-151

[45] G.E. Kline, K.D. Jonnalagadda and N.R. Sottos, 1995, "Correlating Interfacial Properties with Stress Transfer in SMA-composites", Proceedings of the ASME Applied Mechanics and Materials Summer Meeting, Los Angeles, CA, 28-30 June 1995, pp. 121-128

[46] K.D. Jonnalagadda, 1997, "Local Displacements and Load Transfer of Shape Memory Alloys in Polymer Matrices" PhD Dissertation, University of Illinois Urbana-Champaign, Urbana, IL.

[47] A. Baz and J. Ro, 1992, "Thermodynamic Characteristics of Nitinol-Reinforced Composite Beams", Composite Engineering, 2(5-7): pp. 527-542

[48] Z. Chaudhry and C.A. Rogers, 1989, "Response of Composite Beams to an Internal Actuator Force", Proceeding of the 30th AIAA/ASME/ASCE/AHS/ASC Structures, Structual Dynamics and Materials Conference, Mobile, AL, 3-5 April 1989, pp. 186-193

[49] J.S. Paine and C.A. Rogers, 1994, "Improved Impact Damage Resistance in Adaptive Shape Memory Alloy Hybrid Composite Materials", Proceedings of the 1994 Smart Structures and Materials Meeting, Orlando, FL, 14-16 February 1994, 2190: pp. 402-409

[50] J.B. Berman and S.R. White, 1994, "A Three-Phase Cylinder model for Residual and Transformational Stresses in SMA-composites", Proceedings of the 2nd Internal Conference on Intelligent Materials, Williamsburg, VA, 5-8 June 1994, pp. 155-166

[51] J.B. Berman and S.R. White, 1996, "Theoretical Modeling of Residual and Transformational Stresses in SMA-composites", Smart Mater. Struct. 5(6): pp. 731-743

[52] K.D. Jonnalagadda, N.R. Sottos, M.A. Qidwai and D.C. Lagoudas, 2000, "In Situ Displacement Measurements and Numerical Predictions of Embedded SMA Transformation", Smart Mater. Struct. 9: pp. 701-710

[53] A. Shimamoto, J.S. Hawong and H.J. Lee, 2002, "Development of Shape Memory TiNi Fiber Reinforced Epoxy Matrix Composite and Its Properties", Transactions of the ASME, Vol. 124: pp. 390-396

[54] C.K. Poon, L.M. Zhou and L.H. Yam, 2003, "Analytical Study of Internal Stress Distribution in SMA-composites", Proceeding of the International Symposium on Macro-, Meso-, Micro- and Nano- Mechanic of Materials

[55] C.K. Poon, L.M. Zhou and L.H. Yam, 2003, "Size Effect on the Optimum Actuation Condition for SMA-composites", Journal of Composite Structures (Special Issue); Accepted for Publication

[56] C.K. Poon, L.M. Zhou and L.H. Yam, 2004, "Determination of Optimum Actuation Condition for SMA-Composites", (Accepted for presentation in the International Workshop on Advanced Smart Materials and Smart Structure Technology 2004)

[57] J.B. Berman, 2001, "Investigation of Residual Stresses in Shape Memory Alloy (SMA) Composites", PhD Dissertation, University of Illinois Urbana-Champaign, Urbana, IL.

[58] A. Baz, K. Imam and J. McCoy, 1995, "Active Vibration Control of Beams Using Shape Memory Actuators", J. Sound Vib. 140: pp. 437-455

[59] C.A. Rogers, C. Liang and D. Barker, 1990, "Dynamic Control Concepts using Shape Memory Alloy Reinforced Plates", Proc. Third ARO Workshop on Smart Materials, Structures and Mathematical Issues, VPI and SU

[60] J. Epps and I. Chopra, 1997, "Comparative Evaluation of Shape Memory Alloy Constitutive Models with Experimental test Data", Proc. AIAA/AHS/ASME/ASCE, Adaptive Structures Forum Kissemmee, FL.

[61] H. Prahlad and I. Chopra, 2000, "Experimental Characterization of Ni-Ti Shape Memory Alloy wires under Uniaxial loading Conditions", J. Intelligent Mater. Syst. Struct.: Special Issue – ARO Workshop on smart Structures, 11(4), pp. 272-283

[62] H. Prahlad and I. Chopra, 2000, "Development of an Adaptive Flexbeam for Rotorcraft Applications using embedded Shape Memory Alloy (SMA) Actuators", Proc. of the 41st AIAA/ASME/AHS Adaptive Structures Forum, Atlanta. G.A.

[63] K. Tanaka, 1986, "A Thermomechanical Sketch of Shape Memory Effect: One Dimensional Tensile Behaviour", Res. Mechanica, 18: pp. 251-263

[64] C. Liang and C.A. Rogers, 1990, "One-Dimensional Thermo Mechanical Constitutive Relations for Shape Memory Material", J. Intelligent Mater. Syst. Struct., 1: pp. 207-234

[65] L.C. Brinson, 1993, "One-Dimensional Constitutive Behaviour of Shape Memory Alloys: Thermomechanical Derivation with Non-Constant Material Functions and Redefined Martensite Internal Variable", J. Intelligent Mater. Structu. 4: pp. 229-242

[66] Steven G. Shu, D.C. Lagoudas, D. Hughes and John T. Wen, 1997, "Modeling of a Flexible Beam Actuated by Shape Memory Alloy Wires", Smart. Mater. Struct. 6: pp. 265-277

[67] S. Hanagud and R. Roglin, 1995, "Helicopter with Adaptive Rotor Blade for Collective Control", Smart Mater. Struct. 5: pp. 75-89

[68] Z. Chaudhry and C.A. Rogers, 1991, "Bending and Shape Control of Beams Using SMA Actuators", J. Intell. Mater. Struct. 2: pp. 581-602

[69] W. Brand, C. Boller, M.S. Huang and L.C. Brinson, 1994, "Introducing the Constitutive Behaviour of Shape Memory Alloys into Adaptive Engineering Structures", ASME Winter Annual Meeting: Symp. On the Mechanics of Phase Transformations and Shape Memory Alloys (Chicago, IL)

[70] S.S. Sun, G. Sun and J.S. Wu, 2002, "Thermo-viscoelastic Bending Analysis of a Shape Memory Alloy Hybrid Epoxy Beam", Smart Mater. Struct. 11: pp. 970-975

[71] A. Baz, J. Ro, M. Mutua and Gilheany, 1991, "Active Buckling Control of Nitinol-reinforced Composite Beams", Conf. Active Material and Adaptive Structures (Alexandra. VA) Nov. 1991 pp. 167-176

[72] G.Q. Song and Q.P. Sun, 1999, "Effect of Microstructure on the Mechanical Behaviour of NiTi Shape Memory Alloy Reinforced Aluminum Matrix Composite", Smart Mater. Struct. 9: pp. 693-700

[73] Y. Xu, K. Otsuka, N. Toyama, H. Yoshida, H. Nagai and T. Kishi, 2003, "A Novel Technique for Fabricating SMA/CERP Adaptive Composites Using Ultrathin TiNi Wires", Smart Mater. Struct. 13: pp. 196-202

[74] J.A. Balta, V.J. Michaud, M. Parlinska, R. Gotthard and J-A. E. Manson, 2000,

"Adaptive Composite Materials Processing", Proc. European Conference on Macromolecular Physics, Structure Development upon Polymer Processing: Physical Aspects, Sept 24-28, 2000, Vol. 241: pp. 33-34

[75] G.C. Psarras, J. Parthenios and C. Galiotis, 2001, "Adaptive Composites Incorporating Shape Memory Alloy Wires", J. Materials Science, 36: pp. 535-546

[76] C. Kim, B.S. Park and N.S. Goo, 2001, "The Bending and Twisting Control of SMA/Graphite/Epoxy Composite Beams" Proceeding of 13th ICCM Conference

[77] C. Kim, B.S. Park and N.S. Goo, 2002, "Shape Changes by Coupled Bending and Twisting of Shape-Memory-Alloy-Embedded Composite Beams", Smart Mater. Struct. Vol.11: pp. 519-526

[78] J. Schrooten, Kelly A. Tsoi, Rudy Stalmans, Y.J. Zheng and P. Sîttner, 2000, "Comparison between Generation of Recovery Stresses in Shape Memory Wires and Composites: Theory and Reality", SPIE's Smart Materials and MEMS, 13-15 December, 2000, Melbourne, Australia

[79] R. Stalmans, V. Michaud, J.-E. Bidaux, R. Gotthardt and J.-A. E. Månson, 1998, "Adaptive Composites with Embedded Shape Memory Alloy Wires", in Proceedings of the 4th European Conference on Smart Structures and Materials, ed. G. R. Tomlinson en W. A. Bullough, Institute of Physics Publishing, Bristol (England), pp.801-804

[80] G.K. Hu and Q.P. Sun, 2002, "Thermal Expansion of Composites with Shape Memory Alloy Inclusions and Elastic Matrix", Composites Part A: Applied Science and Manufacturing, 33: pp. 717-724

[81] D.C. Lagoudas and I.G. Tadjbakhsh, 1992, "Active Flexible Rods with Embedded SMA Fibers", Smart Mater. Struct. 1: pp; 162-167

[82] C.A. Rogers and D.K. Baker, 1990, "Experimental Studies of Active Strain Energy Tuning of Adaptive Composites", Proc. AIAA/ASME/AHS/ASC, 31st Structures, Structural Dynamics and Materials Conf. (Long Beach, CA, April 1990)

[83] Z. Chaudhry and C.A. Rogers, 1992, "Response of Composite Beams to an Internal Actuator Force", J. Mech. Design, 114: pp. 343-348

[84] J. Epps and R. Chandra, 1997, "Shape memory Alloy Actuation for Active Tuning of Composite Beams", Smart Mater. Struct. 6: pp. 251-264

[85] G.C. Psarras, J. Parthenios and C. Galiotis, 2001, "Adaptive Composites Incorporating Shape Memory Alloys Wires: Part 1 Probing the Internal Stress and Temperature Distributions with a Laser Raman Sensor", J. Material Science 36: pp. 535-546

[86] C.L. Moore and H.A. Bruck, 2001, "A Fundamental Investigation into Large

Strain Recovery of One-way Shape Memory Alloy Wires Embedded in Flexible Polyurethans", Smart Mater. Struct. 11: pp. 130-139

[87] de B.J. Blonk and D.C. Lagoudas, 1998, "Actuation of Elastomeric Rods with Embedded Two-way Shape Memory Alloy Actuators", Smart Mater. Struct. 7: pp. 771

[88] D.J. Lee and T.H. Jeong, 1997, "Deign of the Smart Components Based on Shape Memory Effect", ICCM 11 The 11th International Conference on Composite Materials Vol. 6: pp. 528-539

[89] X. Wang, 2002, "Shape Memory alloy Volume Fraction of Pre-stretched Shape Memory Alloy Wire-reinforced Composites for Structural Damage Repair", Smart Mater. Struct. 11: pp. 590-595

[90] Y. Li, L. Cui, P. Shi and D. Yang, 2000, "Phase Transformation Behaviour of Prestrained TiNi Shape Memory Alloy Fibers under the Constraint of a Hard Substrate", Material Letters 49: pp. 224-227

[91] K.T. Lau, W.L. Chan , S.Q. Shi and L.M. Zhou, 2001, "Interfacial Bonding Behaviour of Embedded SMA Wire in Smart Composites: Micro-scale Observation", Materials and Designs, 2002, 23: pp. 265-270

[92] K.T. Lau, C.K. Poon, L.H. Yam and L.M. Zhou, 2002, "Bonding Behaviour at a NiTi/Epoxy Interface: SEM Observation and Theoretical Study", Materials Science Forum, 394-395: pp. 527-530

[93] R. Gotthardt, 2001, "Vibrational Properties of Adaptive Polymer Matrix Composites with Embedded Shape Memory Alloy Wires", Proc. Of SMST-SMM, pp. 159

[94] V. Beckel and N.R. Sottos, 1998, "Application of Debond Length Measurements to Examine the Mechanics of Fiber Pushout", J. Mechanics and Physics of Solids, 46: pp. 1675-1697

[95] K. Jonnalagadda, G.E. Kline and N.R. Sottos, 1995, "local Displacements and Load Transfer in Shape Memory Alloy Composites", Theoretical and Applied Mechanics Report no. 805 UILU- ENG 95-6027: pp. 1-18

[96] B. Gabry, F. Thiebaud and C. Lexcellent, 2000, "Topographic Study of Shape Memory Alloy Wires Used as Actuators in Smart Materials", J. Intell. Mater. Syst. Struct, Vol 11: pp. 592-603

[97] E. Umezaki, 2000, "Improvement in Separation of SMA from Matrix in SMA Embedded Smart Structures", Materials Science and Engineering A285: pp. 363-369

[98] B. Budiansky, J.W. Hutchinson and A.G. Evans, 1986, "Matrix Fracture in Fiber-reinforced Ceramics", J. Mech. Phys. Solids 34: pp. 167-189

[99] B. Greszczuk, 1969, "Theoretical Studies of the Mechanics of the Fiber-matrix Interface in Composites", ASTM STP 452: pp. 42-58

[100] S.W. Tsai and H.T. Hahn, 1980, "Introduction to Composite Materials", (Lancaster, Pennsylvania: Technomic Publishing)

[101] S. Hanagud and R. Roglin, 1995, "Helicopter with Adaptive Rotor Blade for Collective Control", Smart Mater. Struct. 5: pp. 75-89

[102] J.E. Bidaux, N. Bernet, C. Sarwa, J.A.E. Manson and R. Gotthardt, 1995, "Vibration Frequency Control of a Polymer Beam Using Embedded Shape-Memory-Alloy Fibres", J. Physique 5: pp. 1177-1182

[103] J.G. Boyd and D.C. Lagoudas, 1994, "Thermomechanical Response of Shape Memory Composites" J. Intell. Mater. Sys. Struct. 5: pp. 333-346

[104] F. Gandh and D. Wolons, 1999, "Characterization of the Pseudoelastic Damping Behaviour of Shape Memory Alloy Wires Using Complex Modulus", Smart. Mater. Struct. 8: pp. 49-56

[105] K. Hamada, J.H. Lee, K. Mizuuchi, M. Taya and K. Inoue, 1997, "Mechanical Properties of Smart Metal Matrix Composite by Shape Memory Effects", Mater. Res. Soc. Symp. Proc. 459: pp. 143-148

[106] J.H. Lee, K. Hamada, K. Miziuuchi, M. Taya and K. Inoue, 1997, "Microstructures and Mechanical Properties of 6061 Al Matrix Smart Composite Containing TiNi Shape Memory Alloy Fibre", Mater. Res. Soc. Symp. Proc. 459: pp. 419-424

[107] B.J. de Blonk and D.C. Lagoudas, 1997, "Actuation of elastomeric rods with embedded two-way shape memory alloy actuators", Smart Mater. Struct. 7: pp. 771-783

[108] H.J. Lee and J.J. Lee, 2000, "A Numerical Analysis of the Buckling and Postbuckling Behaviour of Laminated Composite Shells with Embedded Shape Memory Alloy Wire Actuators" Smart Mater. Strudt. 9: pp. 780-787

[109] M. Tawfik, J.J. Ro and C. Mei, 2002, "Thermal Post-Buckling and Aeroelastic Behaviour of Shape Memory Alloy Reinforced Plates", Smart Mater. Struct. 11: pp. 297-307

[110] C.A. Rogers, C. Liang and J. Jia, 1991, "Structural modification of simply-supported laminated plates using embedded shape memory alloy fibers", Comput. Struct. 38: pp. 569-80

[111] S. Saadat, M. Noori, H. Davoodi, Z. Hou, Y. Suzuki and A. Masuda, 2001, "Using NiTi SMA Tendons for Vibration Control of Coastal Structures", Smart Mater. 10: pp. 695-704

[112] X. Wang, 2002, "Shape Memory Alloy Volume Fraction of Pre-stretched Shape Memory Alloy Wire-reinforced composites for Structural Damage Repair", Smart Mater. Struct. 11: pp. 590-595

[113] J.A. Shaw and S. Kyriakides, 1995, "Thermomechanical Aspects of NiTi", J. Mech. Phys. Solids 43: pp. 1243-1281

[114] L. M. Zhou, J.K. Kim and Y.W. Mai, 1992, "On the Single Fibre Pull-out ProblemL Effect of Loading Method", Composites Science and Technology 45: pp. 153-160

[115] L.M. Zhou, J.K. Kim, Y. W. Mai, 1992, "Interfacial Debonding and Fiber Pull-out Stresses: Part II. A new model based on the fracture mechanics approach", Journal of Materials Science 27: pp. 3155-3166

[116] Y. C. Gao, Y. W. Mai and B. Cotterell, 1988, "Fracture of Fiber-reinforced materials", J. Appl. Math. Phys. (ZAMP); 39: pp.550-572

[117] C. H. Hsueh, 1990, "Interfacial Debonding and Fiber Pull-out Stresses of Fiber-reinforced Composites", Mater. Sci. Eng.; A123: pp.1-11

[118] K. Hamada, J.H. Lee, K. Mizuuchi, M. Taya and K. Inoue, 1997, "Mechanical Properties of Smart Metal Matrix Composite by Shape Memory Effects", Mater. Res. Soc. Symp. Proc. 459, pp. 143-148

[119] C.A. Rogers, C. Liang and J. Jia, 1989. "Behaviour of SMA Reinforced Composites Plates Part I," Proceedings of the 30th Structures, Structural Dynamics and Materials Conference, Mobile, AL

[120] J.K. Kim, C. Baillie and Y.W. Mai, 1992, "Interfacial Debonding and Fibre Pull-out Stress: Part I. A Critical Comparison of Existing Theories with Experiments", J. Mater. Sci. 27, pp. 3143-3154